ABSTRACT

Title of Dissertation:	On The Computation Of Buoyancy Affected Turbulent Wall Flows Using Large Eddy Simulation
	Ayodeji Ojofeitimi, Doctor of Philosophy, 2013
Dissertation directed by:	Associate Professor, Arnaud Trouvé, Department of Aerospace Engineering (Affiliate Professor)

A high fidelity object-oriented C++ solver was developed in OpenFOAM® for the solution of low Mach number variable density Navier Stokes equations. Employing the Large Eddy Simulation (LES) methodology to compute the turbulent flowfield, the filtered LES equations were subsequently utilized to study buoyancy affected spatially developing boundary layers in natural and mixed convection spatially developing boundary layer flows. For the subgrid scale (SGS) closure, a locally dynamic Smagorinsky SGS model was implemented into OpenFOAM® to enable the backscatter phenomenon intrinsic to transitioning boundary layers.

As a precursor to simulating the intricate aero-thermal flowfield of an in-flight aircraft engine pool fire due to a fuel leak, detailed investigations of two canonical problems in the absence of flames were conducted to assess the robustness

of the C++ solver and to elucidate the turbulent flow physics; these test cases consisted of a natural convection turbulent boundary layer over an isothermal vertical plate without any forced flow and the mixed convection turbulent boundary layer over an isothermal vertical plate where the effects of a gradually increasing forced flow in the direction opposite to the gravitational vector were assessed. A third canonical case, the mixed convection over an isothermal horizontal plate, was also investigated as an extension of this thesis.

For the first two cases, wall-resolved LES computations were compared with experimental data for first and second order turbulent statistics, along with available experimental frequency spectra of temperature and streamwise velocity fluctuations. In an effort to reduce the computational cost, wall-layer modeled LES computations were performed by implementing new wall models into OpenFOAM®. The fidelity of the wall-resolved and wall-layer modeled LES successfully confirmed the ability of the solver in computing high Grashof number transitioning natural and mixed convection spatially developing boundary layers.

As it pertains to the third case, while experimental measurements in air of mixed convection over an isothermal horizontal plate is lacking in the literature, the fundamental structure of the boundary layer was qualitatively validated by examining the near-wall vortical flow topology and employing available empirical data. The accuracy of the results acquired for this flow configuration was deemed reliable due to the excellent agreement attained with the prior two test cases.

Overall, the level of fidelity illustrated in this thesis has not been previously demonstrated for spatially developing turbulent boundary layers in natural and mixed

convection wall flows, especially for LES. Thus, with the establishment of the methodology employed in this work, it can be further utilized as a reliable tool in computing buoyancy affected flame spread problems aboard in-flight aircraft engine fires to shed light upon the complex flow physics inherent to such flows.

On The Computation Of Buoyancy Affected Turbulent Wall Flows Using Large Eddy Simulation

By

Ayodeji Ojofeitimi

Dissertation submitted to the Faculty of the Graduate School of the
University of Maryland, College Park, in partial fulfillment
of the requirements for the degree of
Doctor of Philosophy
2013

Advisory Committee:

Dr. Arnaud Trouvé, Chair/Advisor
Dr. James D. Baeder,
Dr. Christopher Cadou,
Dr. Kenneth Yu,
Dr. Marino diMarzo, Dean's representative

Acknowledgements

I thank the LORD Christ Jesus for providing me with the health, means, mind and ability to accomplish this huge goal in my life. Without the LORD's mercy, none of this would have been possible.

The profound appreciation and gratitude towards my advisor Dr. Arnaud Trouvé has to be conveyed for making this research effort possible. His guidance and feedback in my research over the few years was incredibly helpful and insightful. I would like to thank all the professors of my doctoral committee for their suggestions and expert feedback in improving my research efforts.

During my tenure in the Aerospace engineering department, the mentorship of Dr. Darryll Pines and my M.Sc. advisor, Dr. James Baeder were immensely helpful and no words can measure up to express how appreciative I am. I would also like to thank Dr. Christopher Cadou and Dr. Kenneth Yu for the insightful discussions subsequent to the successful completion of my PhD qualifying exam in 2007.

I would be remiss if the support of NSWCIHD and NRL were not mentioned. The huge support, one of which was the computational resources, was crucial in the timely completion of this thesis.

Many thanks to all my colleagues in the CFD group (Dr. Vivien Lecoustre, Dr. Luis Bravo, Andrew Voegele, Sebastien Vilfayeau and Zohreh Gorbani) for their interesting and helpful technical discussions that took place over the past year. To all the friendships I made within the Aerospace engineering department, I certainly do have the greatest sense of appreciation.

All my academic aspirations were instilled me at a fairly young age and for that, I surely do thank my dear parents, Prof. and Mrs. Ojofeitimi. In addition, I would also like to express my gratitude to all my brothers and sister for their support over the years. Being raised as a child in such an environment helped me to realize it was fun to challenge one's self intellectually and academically.

Lastly, I would like to thanks the friendships that I made outside of school for their support and concerns regarding the completion of my Aerospace engineering PhD degree. Thanks so much to all the dear friends that I met while on this intellectual voyage.

Table of Contents

List of Tables

List of Figures

Chapter 1: Introduction

1.1 Buoyancy Affected Flows

Many fluid transport processes encountered in nature are strongly affected by the presence of buoyancy. The buoyancy effect can be largely a consequence of temperature gradients within the flowfield. The flowfield may be driven primarily by the buoyancy force or it can be a combination of the buoyancy and a weakly forced ambient flow induced via some mechanical means. In the former flow, it is essentially a natural convection and in the latter, it is a mixed convection type flow. Nonetheless, both flows are profoundly affected by buoyancy. For both types of flows, the structural characteristics of the boundary layer is profoundly intricate and is a consequence of the non-linear effects and mutual coupling of the velocity and thermal flowfields. Moreover, many such strongly affected buoyancy flows are largely unstable and the flow mechanism becomes turbulent. In the case of a purely natural convection boundary layer flow, the turbulent heat transfer is only characterized by the buoyancy induced flowfield, i.e. temperature fluctuations. However, in the mixed convection flow, the turbulent heat transfer characteristics not only depend upon the buoyancy induced temperature fluctuations, but also on the direction of the weakly moving ambient fluid. The direction of the ambient fluid can

be the same as the upward motion induced by buoyancy over a vertically heated flat plate (aiding flow) or in the opposite direction (opposite flow). As such, the turbulent heat transfer in the aiding and opposite flows differ significantly; it has been determined that it is suppressed in the aiding flow and augmented in the opposite flow [1].

In this thesis, we focus on strongly affected buoyancy flows in spatially developing natural- and mixed convection turbulent boundary layer flows over an isothermal heated vertical plate and mixed convection turbulent boundary layer flow over an isothermal horizontal flat plate in which the buoyancy force acts orthogonally to the forced convection. For the mixed convection turbulent boundary layer over a vertical plate, only aiding flows are considered.

1.2 Physical Mechanisms of Buoyancy Driven Flows

Let us briefly consider how the upward movement of mass flow over the heated vertical flat plate develops into a boundary layer without the inclusion of a freestream velocity. We can definitely conclude that the upward movement of mass is due to an upward force that pushes the flow in that direction. Thus, Figure1.1 depicts the force balance over a control volume within the boundary layer and in the quiescent region. Let us assume the control volumes are of identical sizes, with their volume $= \Delta x \Delta y 1$, where we have supposed $\Delta z = 1$. In the quiescent region, the weight of the fluid, $W2$, is $\rho_\infty \Delta x \Delta y 1 g$, where ρ and g represent the density and gravity force, respectively and the fluid element is in hydrostatic equilibrium, i.e. the upward pressure force balances the net downward force. Hence, the mathematical expression for the force balance in the quiescent region reads as

$$P(x) = P(x + dx) + \rho_{\infty} \Delta x g \,. \qquad (1.1)$$

From boundary layer theory, it is well known that the pressure outside the boundary layer is imposed onto the boundary layer region. Thus, the pressure forces acting upon the fluid element in the quiescent region is identical to the pressure forces within the boundary layer. However, the fluid element is not in hydrostatic equilibrium as the net downward force does not balance the upward pressure force. The weight of the fluid element within the boundary layer is $W1 = \rho \Delta x \Delta y 1 g$, where ρ is the local density. Due to the diffusion of heat caused by the heated plate, there is a density gradient within the boundary layer whereby fluid elements near the wall are less dense than those farther away from it. The imbalance of forces in the streamwise direction causes an upward acceleration of fluid elements. Thus, we can write

$$P(x) > P(x + dx) + \rho \Delta x g \,. \qquad (1.2)$$

The net upward force is typically referred to as the buoyant force. The viscous shear force *Fv* shown acting upon the fluid element within the boundary layer is a consequence of the moving fluid element in the presence of viscous shear.

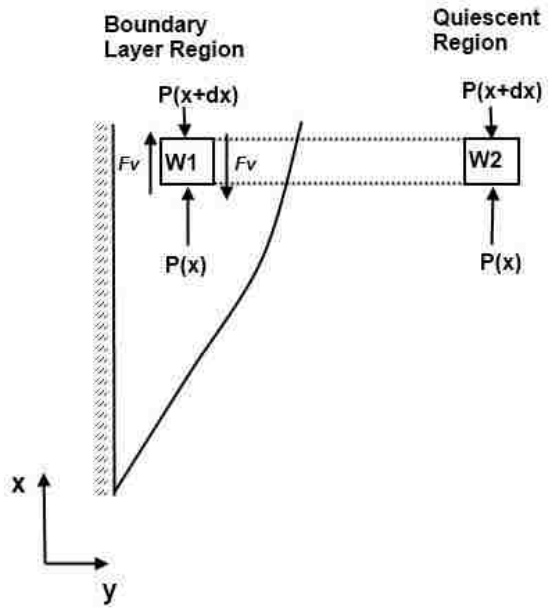

Figure 1. 1 Force balance illustration of buoyant force emergence within boundary layer.

Similarly, we can consider the presence of an isothermal hot wall in a cooler ambient without any incoming freestream, as shown in Figure1.2. As opposed to the heated vertical plate, the gravitational force is normal to the surface. Upon exposure of the hot horizontal plate to the surroundings, the temperature of the air adjacent to the surface will increase because of heat conduction. As such, the plate will be completely engulfed by a thin layer of hot air. At constant pressure, the density of air is inversely proportional to its temperature; thus, the situation arises whereby less dense air is surrounded by heavier colder air. Consequently, the lighter warm air rises due to buoyancy and the heavier unheated air nearby replaces the space vacated by the lighter air.

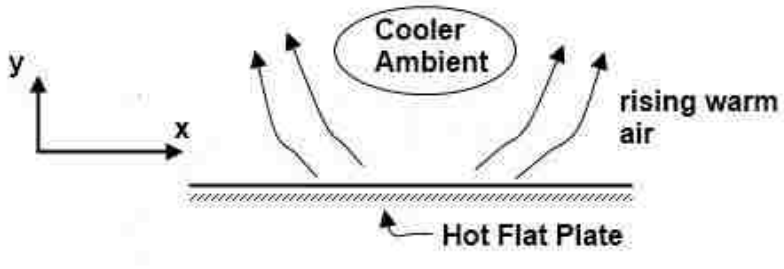

Figure 1. 2 Schematic of natural convection process over isothermal flat plate.

1.2.1 Mathematical Description of Buoyancy Affected Flows

The resulting imbalance in force causes the upward motion of fluid near the heated vertical plate and the subsequent motion becomes subjected to viscous shear forces. As such, the net force comprising pressure, gravity and viscous shear ought to balance the net flux of momentum through the control volume as dictated by the momentum conservation equation. Due to the influence of the buoyancy force in the momentum equation, there is a strong coupling between the conservation of energy and momentum equations. Essentially, the energy equation describes the temperature flowfield, which consequently affects the distribution of density. Let us quickly examine the streamwise momentum conservation equation for a two dimensional incompressible laminar boundary layer governing the flow over a vertically heated flat plate. The equation reads as

$$\mathrm{u}\frac{\partial \mathrm{u}}{\partial \mathrm{x}} + \mathrm{v}\frac{\partial \mathrm{u}}{\partial \mathrm{y}} = -\frac{1}{\rho}\frac{\partial P}{\partial \mathrm{x}} - \mathrm{g} + \nu\frac{\partial^2 \mathrm{u}}{\partial \mathrm{y}^2}, \qquad (1.3)$$

where x and y are the streamwise and wall-normal axis and u, v, ρ, g and ν are the streamwise velocity, wall-normal velocity, density, gravity and kinematic viscosity respectively.

In an effort to directly illustrate the coupling, we make mention of the Boussinesq approximation. The assumption assumes constant properties except for the density, which will be assumed to be a linear function of temperature. Thus, the pressure gradient term can be eliminated as follows:

$$\frac{\partial P}{\partial \mathrm{x}} = -\rho_\infty \mathrm{g}\,. \tag{1.4}$$

To proceed, we can write

$$-\frac{1}{\rho}\frac{\partial P}{\partial \mathrm{x}} - \mathrm{g} = \frac{\mathrm{g}}{\rho}(\rho_\infty - \rho) \tag{1.5}$$

and approximate the coefficient of volumetric thermal expansion as

$$\beta = -\frac{1}{\rho}\frac{\partial \rho}{\partial \mathrm{T}}\bigg|_{\mathrm{P}} = -\frac{1}{\rho}\left(\frac{\rho_\infty - \rho}{\mathrm{T}_\infty - \mathrm{T}}\right). \tag{1.6}$$

Thus, the streamwise momentum can be re-written using the Boussinesq assumption as

$$\mathrm{u}\frac{\partial \mathrm{u}}{\partial \mathrm{x}} + \mathrm{v}\frac{\partial \mathrm{u}}{\partial \mathrm{y}} = \mathrm{g}\beta(\mathrm{T} - \mathrm{T}_\infty) + \nu\frac{\partial^2 \mathrm{u}}{\partial \mathrm{y}^2}, \tag{1.7}$$

where the coupling between the energy and momentum equations can be clearly seen with the presence of the temperature term. A discussion pertaining to the coefficient of volumetric thermal expansion β is warranted and proceeds hereafter. As opposed to forced convection boundary layer flows where the Reynolds number, $u_\infty \mathrm{x}/\nu$, can be employed as an indication of inertia to viscous shear forces, this parameter cannot be explicitly utilized in natural convection boundary layer flows. This is due to the

absence of a freestream velocity in natural convection boundary layer flows; instead, the dimensionless parameter, Grashof number, is typically employed. The Grashof number is essentially a ratio of the buoyant force to viscous force and reads as

$$\mathrm{Gr} = \frac{\mathrm{g}\beta\Delta\mathrm{T}\mathrm{x}^3}{\nu^2}, \tag{1.8}$$

with g, x, ΔT and ν being the gravitational acceleration, characteristic length, absolute temperature difference between the wall and ambient and kinematic viscosity respectively. The parameter β, is the coefficient of volumetric thermal expansion and is defined as

$$\beta = -\frac{1}{\rho}\frac{\partial\rho}{\partial\mathrm{T}}\bigg|_{\mathrm{P}} \tag{1.9}$$

and can be further simplified if the assumption is made that the working fluid is an ideal gas:

$$\beta = -\frac{1}{\rho}\frac{\partial\rho}{\partial\mathrm{T}}\bigg|_{\mathrm{P}} = -\frac{1}{\rho}\left[\frac{\partial(\mathrm{P}/R\mathrm{T})}{\partial\mathrm{T}}\right]_{\mathrm{P}} = \frac{1}{\mathrm{T}}. \tag{1.10}$$

A dimensionless parameter employed that can be stated to be a counterpart of the Reynolds number is the Rayleigh number, which is

$$\mathrm{Ra} = \mathrm{GrPr} = \frac{\mathrm{g}\beta\Delta\mathrm{T}\mathrm{x}^3}{\nu\alpha}. \tag{1.11}$$

Just as the critical Reynolds number is usually employed in forced convection flow for the point of transition to turbulence in wall bounded turbulent flows, the critical Rayleigh number is similarly applied to free convection turbulent boundary layers. To the extent that [2] discovered that transition typically occurs when $\mathrm{Ra}\sim10^9$ for natural convection boundary layers over a vertically heated flat plate. This transition criterion was previously confirmed experimentally by [3].

In the analysis of potentially mixed convection boundary layer flows, the dimensionless parameter called the Richardson number, Ri, is employed. The Richardson number is defined as

$$\mathrm{Ri} = \frac{\mathrm{Gr}}{\mathrm{Re}^2} = \frac{g\beta\Delta \mathrm{Tx}}{\mathrm{U}_\infty^2} \qquad (1.12)$$

and is essentially a measure of the relative strength of free and forced convection. Furthermore, as illustrated by Eq.1.12, the Richardson number is a ratio of the Grashof number to the square of the Reynolds number; the parameter can be interpreted as a ratio of buoyancy to inertia forces. Thus, forced convection becomes negligible when $\mathrm{Ri} \gg 1$, natural convection effects can be ignored when $\mathrm{Ri} \ll 1$ and when $\mathrm{Ri} \approx 1$, a mixed convection flow dominates in the boundary layer.

1.3 Prior and Related Studies

The subsequent three subsections cover some of the pertinent previous theoretical, experimental and computational investigations that have been conducted on natural – and mixed convection turbulent boundary layer flows along a heated vertical plate, and mixed convection wall bounded turbulent flow over a horizontally heated plate.

1.3.1 Natural Convection along Heated Vertical Plate

Theoretical work

The pioneering work of [4] formulated the analytical equations for the streamwise velocity, temperature and heat flux over an isothermal vertical heated flat plate for the laminar free convection boundary layer. These ordinary differential equations were

developed for the laminar free convection boundary layer and are similar to its forced convection counterpart given by Blasius.

Experimental work

One of the earlier wall heat transfer measurements were made by [5] over an isothermal vertical flat plate in air. The data acquired was mentioned to be in good agreement with a heat transfer analytical correlation for the natural convection turbulent boundary layer. Meanwhile, the measurements of [6] acquired data over a vertical heated flat plate held at uniform temperature. These measurements provided the first heat transfer data in the transition and fully developed turbulent regions of the natural convection boundary layer. The local heat transfer rate data taken in the turbulent boundary layer were comparable to the power law theory of [7].

The natural convection turbulent boundary layer in water over a uniform heat flux heated vertical plate was assessed experimentally by [8]. Their measurements indicated in the fully developed turbulent region, the turbulence was profoundly affected by the buoyant production of turbulence, i.e. large temperature fluctuations dominated the generation of turbulence. The experimental work of [9] carried out measurements in a turbulent free-convection boundary layer using water and air as the medium over a vertical heated flat plate at uniform heat flux. The profound finding of their work was the observation of passing high- and low-temperature streaky structures near the wall. Their conclusion was the existence of similarity between forced- and free-convection turbulent boundary layers in possessing these streaking coherent structures near the wall. However, given their work utilized a wall

at uniform heat flux, they stated the same conclusion can be drawn for walls at a uniform temperature.

Even though measurements of turbulent quantities have been taken in the natural convection turbulent boundary layer, the fundamental understanding of the boundary layer was significantly lacking, in addition to reported discrepancies in the experimental data reported. Consequently, new sets of experiments were undertaken to comprehend the complicated near-wall turbulent field of a natural convection boundary layer. Chief among these were the ground breaking efforts of [10,11]. [10] [11]. Their measurements employed air as the working fluid and the flat plate was maintained at a uniform temperature. The experiments shed light upon the peculiar characteristics inherent to the free-convection turbulent boundary layer. Some of these peculiarities are: i) as opposed to forced-convection where velocity attains a linear profile in the viscous sub-layer up to $y^+ \leq 5$, in free-convection, this linear profile was observed to be much closer to the wall region, $y^+ \leq 1$, ii) unlike the analogy that exists between momentum and heat transport in forced-convection turbulent boundary layer flows, this cannot be stated to exist in the free-convection case; it was observed that the wall shear stress increases with increasing Grashof number and the heat transfer coefficient, i.e. heat flux remained nearly constant as Grashof number increased, iii) in forced-convection, the close relation between the Reynolds shear stress $\overline{\mathrm{u'v'}}$ and mean velocity gradient $\partial \mathrm{U}/\partial y$ exists, i.e. if $\partial \mathrm{U}/\partial y > 0$ then $\overline{\mathrm{u'v'}} < 0$, where the opposite relation holds as well. However, in free-convection, very near the wall where the condition $\partial \mathrm{U}/\partial y > 0$ holds, $\overline{\mathrm{u'v'}} \approx 0$; thus this relationship between the two quantities is lacking, and iv) in forced-convection,

the maximum of the velocity and temperature intensity fluctuations or rms values, occurs in the inner layer. For the free-convection turbulent boundary layer, the maximum of the temperature fluctuation occurs in the inner layer and the velocity fluctuation maximum was observed in the outer layer. Moreover, detailed measurements of heat transfer rates in the turbulent boundary layer were performed and correlated with an empirical formula that was employed in this thesis. In an effort to acquire further comprehension into the structure of the turbulence in the free-convection boundary layer over a heated vertical plate, measurements in air were conducted by [12]. In their experiment, it was observed that the instantaneous temperature fluctuation field was preserved in the streamwise direction. In addition, the invasion of low-temperature fluid into the near wall region was observed along with the absence of passing high- and low-temperature streaky structure near the wall as was observed in the work of [9]. The measurements also illustrated the wall-normal spatial correlation of the thermal field decreases rapidly and attain a near constant value in the outer layer independent of the wall-normal distance; whereas, the velocity field wall-normal spatial correlation continually decreased with distance from the wall.

To ascertain the effects of heated vertical flat plate at high temperatures in the free-convection turbulent boundary layer, [13] conducted experiments in air. It was determined that the temperature difference between the plate surface and ambient did not significantly affect the location of transition to turbulence and the turbulence structure in the spatially developing free-convection turbulent boundary layer.

Numerical Work

The $k-\varepsilon$ and ASM turbulence models were utilized by [14] to numerically simulate a two dimensional free-convection turbulent boundary layer over a heated vertical plate in air. Aside from the mean streamwise and temperature wall profiles that were reasonably in agreement with experimental measurements, the predicted 2^{nd} order statistics were mostly in qualitative agreement with the experiment.

In 1992, [15] performed two dimensional Reynolds Averaged Navier Stokes (RANS) computations of the turbulent boundary layer over a heated vertical surface using the Reynolds stress, Algebraic stress and k-ε turbulence models. Their numerical predictions were compared to the measurements of [10,11] [10] and [11]. In their comparisons, the Reynolds stress model was superior to the other two turbulence models employed for the study. Moreover, the comparisons with the streamwise turbulent heat flux and Reynolds shear stress very near the wall were markedly different from the experimental measurements. Significant discrepancies were observed near the wall for the computed results when compared to the experimental data. To conclude, the authors surmised that more advanced near wall models might be required for simulating natural convection turbulent boundary layer and since the inner layer is rather thin, high fidelity measurements might be a challenging task to perform.

Direct numerical simulation over a heated vertical plate was performed by [16]. Instead of solving for the spatially developing turbulent boundary layer, the authors employed time-developing conditions to significantly reduce the computational cost. To compare their numerical predictions with the measurements

of [11], their time-developing flow results were converted to space-developing flows. Moreover, the Boussinesq approximation was implemented in solving the incompressible Navier-Stokes equations. As a whole, the numerical simulations were in good quantitative agreement with the experimental data. However, similar trends in their prediction of the Reynolds shear stress and streamwise turbulent heat flux were observed as those of [15]. Negative values of these quantities very near the wall were observed and were markedly different from the measurements. The authors conjectured that perhaps the Boussinesq approximation might be inappropriate in the very near wall region.

1.3.2 Mixed Convection along Heated Vertical Flat Plate

Experimental work

The inception of experimental investigation of turbulent mixed convection boundary layer flow over a heated vertical surface was the measurement of [17]. The measurements were for an aiding flow over an isothermal flat plate and it was concluded that the turbulence was suppressed with the addition of a freestream velocity to the turbulent natural convection boundary layer. To elucidate the fundamental structure of the mixed convection turbulent boundary layer over a heated vertical flat plate, [18] conducted experiments employing water as the working fluid. The flat plate was heated by prescribing a uniform heat flux and it was observed that the Nusselt number decreased as the forced flow increased. The decrease in heat transfer was stated to be attributed to suppression of turbulence in the mixed convection turbulent boundary layer.

The experimental investigation of mixed convection turbulent boundary layer over a uniform heat flux vertical plate was undertaken by [19]. The measurements employed a freestream velocity of 5 cm/s and it was observed that imposing small forced convection effects has a stabilizing effect on the boundary layer thereby delaying the transition to turbulence. The experimental work of [20] [21] was ground-breaking in that much needed reliable data in the turbulent mixed convection boundary layer over a vertical heated plate were provided. The measurements employed air as the working fluid and the aiding freestream velocity was increased up to 1.10 m/s. In their experiment, it was determined that the cause of the turbulence suppression, which consequently reduces the heat transfer, was attributable to the stabilizing effect of the freestream on the large turbulence scales in the outer layer. It was observed that the low frequency turbulence scales, i.e. large length scales, were gradually destroyed with the addition of a freestream velocity. Similarly to the numerical observations of [22], as the freestream continually increased, the turbulent boundary layer relaminarizes and becomes a forced convection boundary layer flow.

Numerical Work

Direct numerical simulations were performed by [1] on a vertical parallel channel at two different isothermal temperatures. Aiding and opposing flows were simulated during the investigation. As it pertains to aiding flows, it was numerically observed that the Nusselt number decreased as the freestream velocity was introduced. Furthermore, it was reported that even though the skin friction coefficient increased, the turbulent fluctuations were reduced. Another approach was undertaken by [22] to comprehend the effects of gradually increasing the freestream velocity in a turbulent

natural convection boundary layer. The $k-\varepsilon$ turbulence model was utilized to simulate the spatially developing boundary layer over a heated vertical plate in air. Due to the absence of any dependable experimental data, their results were not compared with any measurements. Nonetheless, their numerical predictions were able to show that adding freestream velocity suppresses the turbulent heat transfer in the mixed convection boundary layer.

In 2010, [23] performed direct numerical simulation of a mixed convection turbulent boundary layer over a heated vertical flat plate for aiding flow. The authors employed the identical approach to the prior study of turbulent natural convection boundary layer over a flat plate as discussed in [16]. The numerical results were compared to the measurements of [24]. The results that were compared to the measurements were in quantitative agreement; however, the direct numerical simulation predictions were not compared to the streamwise turbulent heat flux measurements of [24]. The numerical simulation illustrated that increasing the freestream velocity caused the streamwise turbulent heat flux to become more negative in the near wall region. However, it seems the numerical predictions exaggerated the measurements in this region. The contours of streamwise velocity fluctuations were assessed near the wall and it was observed that as the freestream velocity increased, long-drawn high- and low-speed regions orderly appeared in the spanwise region. These high- and low-speed regions were similar to those observed in forced convection flows, although not as clearly and distinctively defined.

1.3.3 Mixed Convection along Heated Horizontal Flat Plate

Theoretical Work

A theoretical analysis based upon linear stability theory was undertaken by [25] to study the flow conditions conducive to the onset of longitudinal vortices. During the course of their study, different Prandtl number fluids were utilized and it was discovered that the $\frac{Gr_x}{Re_x^{1.5}}$ ratio was essential in correlating the relative significance of buoyancy effects (Grashof number) over forced convection (Reynolds number) effects. The ratio, $Gr_x/Re_x^{1.5}$, is essentially equal to a critical Grashof number, Gr_L^* and can be elaborated as follows:

$$Gr_L^* = \frac{Gr_x}{Re_x^{1.5}} = \frac{g\beta\Delta\mathrm{T}L^3}{\nu^2}, \qquad (1.13)$$

where $L = (\nu\mathrm{x}/u_\infty)^{0.5}$.

Linear stability analysis theory was employed by [26] to study laminar forced convection flow over a heated horizontal flat plate in the presence of appreciable buoyant force effects. In their theoretical analysis, it was noted that streamwise vortex instability can easily occur in the presence of buoyancy and the main flow becomes quite susceptible to this mode of instability as the temperature difference between the isothermally heated flat plate and freestream increases.

Experimental Work

The mixed convection boundary turbulent boundary layer flow in air over a strongly heated horizontal plate was experimentally investigated in a square duct by [27]. The measurements indicated that the temperature fluctuation intensity attained its maximum value near a region referred to as a viscous-conductive layer. Furthermore,

it was observed that the variation between the mean temperature and streamwise velocity was remarkably similar and it was concluded there was analogy between heat and momentum transfer. The measurements also illustrated the majority of the variation in mean temperature and streamwise velocity occurred within the viscous-conductive layer; the length scale of the viscous-conductive layer was also for the fully turbulent region.

The experimental measurements of [28] of a mixed convection boundary layer over an isothermally heated horizontal plate attempted to ascertain the buoyancy effects on the developing flow. As such, they were able to locate three different flow regimes present within such a flowfield. Their measurements depicted an initial region of laminar forced convection where buoyancy effects were insignificant at the leading edge of the flat plate. The second regime was termed the transition region, which is the onset and inevitable breakup of longitudinal vortices. The third regime of the developing boundary layer was called the turbulent free convection region and was labeled as such due to the constant heat transfer coefficient observed subsequent to the transition region. The constant heat transfer coefficient is usually observed in turbulent free convection boundary layer flows. To quantify the different flow regimes, empirical scaling laws were proposed along with the Nusselt number correlations when appropriate and read as follows:

$$\begin{cases} \dfrac{Gr_x}{Re_x^{1.5}} < 100 \\ Nu_x = 0.332 Pr^{1/3} Re_x^{1/2} \end{cases} (i)\,, \qquad (1.14)$$

$$100 < \frac{Gr_x}{Re_x^{1.5}} < 300 \ \ (ii), \tag{1.15}$$

$$\begin{cases} \dfrac{Gr_x}{Re_x^{1.5}} > 300 \\ Nu_x = 0.13(Gr_x Pr)^{1/3} \end{cases} (iii)\,. \tag{1.16}$$

These three regimes can be seen in Figure 1.3. The image illustrates the experimental data and empirical scaling along the horizontally heated flat plate.

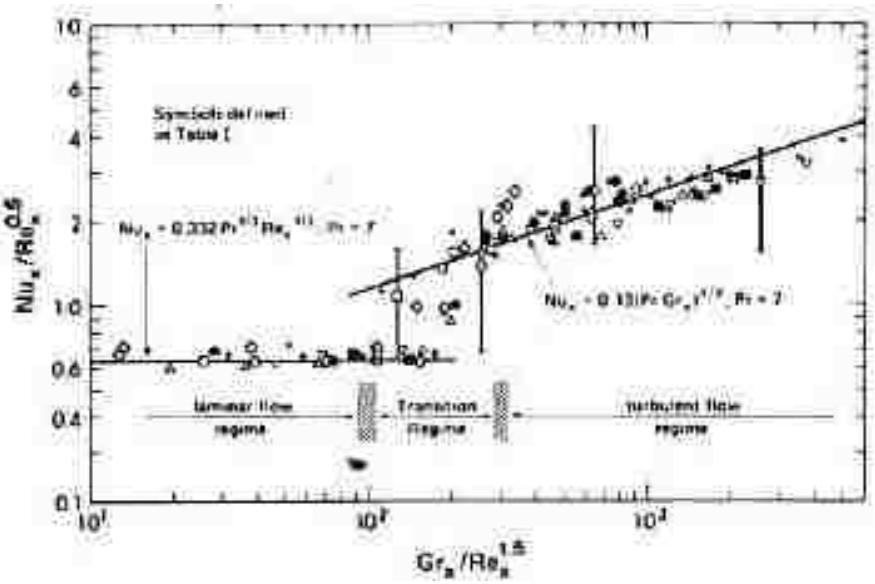

Figure 1. 3 Heat transfer scaling of thermal instability flow indicating the different flow regimes present within the flowfield. Image adopted from **[28]**.

Experimental measurements in air were taken of a mixed convection boundary layer flow over a 1.0 m heated flat plate by [29]. By varying the freestream velocity and temperature difference between the plate and fluid, it was observed that the local heat transfer coefficient was significantly dependent upon these two parameters. The

measurements indicated that the local heat transfer coefficient decreased with increasing streamwise distance as observable in laminar forced convection near the leading edge of the plate. It was also observed that further downstream, the heat transfer coefficient deviates from the laminar forced convection trend with an inflectional point and rapidly increases. Subsequently, the heat transfer coefficient remained nearly constant as observed in turbulent free convection. The author conjectured the likelihood of an instability mechanism being the cause of the inflection and abrupt increase seen in the local heat transfer coefficient.

Measurements were taken in the transition regime of a mixed convection boundary layer over an isothermal horizontal flat plate in an effort to obtain quantitative measurements of velocity and temperature distributions. The investigators, [30], established a criterion that predicted the onset of streamwise vortex instability to be

$$\frac{Gr_x}{Re_x^{1.5}} = 100\,. \qquad (1.17)$$

The onset of streamwise vortex instability was explained to be the inception of transition from two dimensional laminar flow to three dimensional vortex flow. The measurements taken illustrated that the vortex flow regime starts with ordered and stable pairs of laminar streamwise vortices in clockwise and counter-clockwise directions. The vortices grow and an unstable flow region emanates whereby the structures mix and an eventual vortex collapse occurs that forms fully developed turbulent flow.

Numerical Work

The turbulent mixed convection boundary layer over an isothermal horizontal flat plate was numerically investigated with RANS by [31]. The flowfield was resolved by solving two dimensional RANS equations and it was observed that such an approach was inherently inadequate. The inadequacies of assuming a two dimensional flowfield was attributed to its inability to reasonably capture the transition region which comprises the onset of longitudinal vortices and their eventual breakup into full turbulence.

Summary of Previous Work

Although there has been a great deal of work, both experimentally and numerically that has been put forth to the investigation of buoyancy affected turbulent natural and mixed convection boundary layer flows, most of these investigations were for vertical passages such as channels and pipes. The prior works cited in the above literature survey, primarily spatially developing natural and mixed convection turbulent boundary layers, was meant to highlight the lack of sufficient numerical studies in this area especially for Large Eddy Simulation (LES).

1.4 Motivation for Studying Buoyancy Affected Flows

As was previously mentioned, buoyancy effects can be largely a consequence of temperature gradients in the flowfield. These significant temperature gradients can be induced by a fire aboard an aerospace vehicle, such as an aircraft. Even though the risk associated with aircraft fires has been greatly reduced over the past couple of decades, the same cannot be said regarding the next generation of aircrafts. Due to the vast amount of composite materials and components utilized in the construction and manufacturing of these next generation aircrafts, the fire safety of such aerospace vehicles have not been extensively investigated. According to the Federal Aviation Administration (FAA), the primary areas of research regarding the next generation aircrafts are in-flight fires in specific zones and post-crash aircraft fires. Post-crash aircraft fires occur when the structural integrity of the aerospace vehicle has been compromised either by the forceful impact of an airborne object or with the ground and the subsequent fire is initiated by the ignition of leaking aircraft fuel. An image of a post-crash aircraft fire that occurred in 2005 can be seen Figure 1.4. The airplane was reported to catch on fire once it crashed. In Figure 1.5, a more recent post-crash aircraft fire, which occurred in July 2013, is depicted.

Figure 1. 4 Post-craft fire of Air France A340 that occurred in 2005. Image adopted from Wikipedia.

Figure 1. 5 Post-crash fire of Asiana Flight 214 that occurred at San Francisco International Airport in July 2013. Image adopted from NYDailyNews.com.

The great damages caused by the initiation of the fire and the subsequent growth of the flame can be readily seen from the Figures 1.4 and 1.5. The impact of these advanced composites on aircraft fire safety and fire growth in these aerospace

vehicles is an unanswered question that requires extensive on-going thorough research and investigation.

In-flight aircraft fires in specific zones can occur in the engine compartment and areas not easily accessible, such as the ceiling panel, ventilation ducts, just to name a few. Of these, in-flight aircraft fires on composite surfaces within and near the engine compartment is a complex aero-thermal environment that is particularly susceptible to a pool fire outbreak caused by the ignition of fuel leaking within the engine nacelle [32]. The flow encompasses partial oxygenation at higher altitudes, lower atmospheric pressure and ambient air that enters the engine compartment through vents that significantly affect the characteristics of the flame. In addition, as ambient air flows through the engine compartment, it flows through a highly cluttered and irregular environment which consequently gives rise to intricate flow irregularities. Consequently, a pool fire guarded by the cluttered environment can grow and spread within the engine nacelle and potentially result in a loss of the aircraft.

As part of a building block to eventually simulating and enhancing the comprehension of in-flight aircraft engine compartment fires inherent to next generation aircrafts, we take a step back in this thesis and perform a detailed investigation of canonical configurations in the absence of a flame. The aim will be to study buoyancy effects in a developing flow near heated walls, representative of hot plumes emerging from the flame. Furthermore, we attempt to gain a deeper understanding of the flow physics and dynamics with the utilization of Large Eddy Simulation. Moreover, since the literature is greatly lacking in numerical simulations

of buoyancy affected flows using Large Eddy Simulation, an effort will be put forth to add to enhance existing knowledge in this particularly lacking area. The subsequent subsection delves into the objectives of this thesis.

1.5 Research Objectives

The global objective of this research was the study of three flow configurations. The first two cases, which represent the bulk of this thesis, are the spatially developing natural convection (Tsuji & Nagano case) and mixed convection (Hattori case) boundary layer flow experiments over the isothermal vertical plate. As an extension of this research effort, the third case, mixed convection over the isothermal horizontal flat plate, will be studied as well in the absence of valuable experimental data. The objectives of all these cases will now be discussed.

One of the primary goals of this computational effort was to assess the predictive capabilities of Large Eddy Simulation for spatially developing natural convection turbulent boundary layers over a vertically heated flat plate at high Grashof numbers. To this end, wall-resolved LES computations will be performed and since the large eddy structure in the turbulent boundary layer are three dimensional and time-dependent, the wall resolved simulations have to be as well. This can be very computationally expensive. Consequently, in order to make the computational costs more applicable to engineering calculations, more computationally efficient means will be developed as well. Thus, the implementation and utilization of economical near-wall treatments, i.e. wall-layer modeling LES will also be undertaken.

In this thesis, an additional field of investigation was the assessment of LES in accurately reproducing the effects of weak freestream addition to a spatially developing natural convection turbulent boundary layer over a vertically heated flat plate, i.e. turbulent mixed convection boundary layer. These effects include the delayed transition to turbulence, reduction in turbulent heat transfer and suppression of the large turbulence scales. In at least that these effects will be investigated, the development and/or modification of the LES computational code (OpenFOAM®) to assess the addition of a weak freestream to the turbulent natural convection boundary layer will be required to further the codes' capability. Furthermore, economical near-wall treatments (wall-layer modeling LES) will be developed and implemented to lessen the computational cost of wall-resolved LES computations to enable an efficient means of conducting engineering simulations for the turbulent mixed convection boundary layer. Lastly, the fidelity of the LES solver in resolving the mixed convection flow over the horizontally heated flat plate will be investigated. Though this particular flow set-up may seem to be "classical" and not of a complicated nature, the contrary is actually the reality. The transition and turbulent free convection regimes are not fully understood and much research is required to shed light on the complicated physics inherent to this flow. In addition, due to the lack of ample experimental data of the turbulence quantities downstream of the transition region, the available empirical data will be employed to further the understanding of this problem numerically.

It will be worthwhile to mention as well that the implementation of high fidelity LES subgrid scale models will be compulsory to improve the computed

turbulent boundary layers. Hence, in doing so, the LES solver will be enhanced with more advanced subgrid scale models.

1.6 Outline of Thesis

Subsequent to the introductory chapter, this thesis consists of seven chapters and is sub-divided primarily into two parts based upon the subject matter. The initial part of the thesis covers the theory, derivations and computational methodology used in the course of this effort. The latter part of the thesis entails results acquired from the implementation of the theories and methodology employing the test cases. A summary of primary results along with proposal for future efforts will be included as well.

1.6.1 Theory and Methodology

In Chapter 2, the fundamental structure of wall bounded turbulent flows for forced convection is examined and reviewed using the work of prior researchers in the field of turbulence. Subsequently, Chapter 3 covers the numerical techniques employed in computing wall bounded turbulent flows. This chapter takes a brief look at a few well known methods of predicting turbulent boundary layer with the emphasis placed upon Large Eddy Simulation. The governing equations, assumptions and Sub-Grid Scale (SGS) models employed in LES are examined including an overview of models employed in this thesis. The discretization of the partial differential equations solved in the course of this research are introduced and elaborated upon in Chapter 4. In addition, the numerical schemes and solution approach are also discussed in this chapter.

1.6.2 Test Cases

Chapters 5, 6 and 7 include the numerical predictions of test cases compared with the available experimental data. To be more specific, Chapter 5 consists of wall-resolved and wall-layer modeled LES of spatially developing natural convection turbulent boundary layer over a heated vertical plate that were compared to the detailed measurements of [10]. In Chapter 6, the mixed convection measurements of [24] are employed for comparisons with wall-resolved and wall-layer modeled LES computations. Chapter 7 will cover wall-resolved LES of the mixed convection turbulent boundary layer over an isothermal horizontal heated plate and will be referred to hereafter as the thermal instability of Blasius flow to be consistent with literature. In conclusion, Chapter 8 comprises the pertinent summary of this effort in addition to potential areas of future efforts. It must be stated that the results displayed in Chapters 5 and 6 consist of the bulk of this research effort due to the availability of experimental data. After illustrating the accuracy of the computational methodology and approach, the test case of Chapter 7, due to lack of experimental measurements, is presented as an extension of this work.

1.7 Thesis Contributions

Aside from the goal of assessing the capability of Large Eddy Simulation in computing turbulent boundary layer flows affected by buoyancy in different flow configurations, several contributions were made to the compressible LES framework in the high level advance fluid dynamic solver, OpenFOAM®. In as much that these contributions significantly aided in the completion of this research effort, they also

assist the growth and advancement of the OpenFOAM® code. The primary contributions made were:

- Implementation of the wall adaptive local eddy viscosity subgrid scale model; in addition, the locally dynamic Smagorinsky subgrid scale LES model was also implemented and validated. To further the subgrid scale model's capability to combustion problems that employ eddy dissipation concept, which require a subgrid scale turbulent kinetic energy field, a hybrid means of doing as such was implemented by allowing for the locally dynamically computed subgrid viscosity to be fed to the subgrid scale turbulent kinetic energy.
- To enable computationally efficient means of resolving turbulent natural and mixed convection boundary layer flows especially for engineering calculations, two new wall layer models were implemented and validated. These wall layer models can be applied to academic and industrial turbulent boundary layers strongly affected by buoyancy effects.
- The modification of the dynamic pressure equation solved to aid in the correction of the momentum equation in mixed convection turbulent boundary layers.
- The development of a low Mach number solver within the OpenFOAM® framework, fully capable of computing turbulent natural and mixed convection boundary layer flows over isothermal vertical and horizontal flat plates.

- The demonstration of Large Eddy Simulation as a high fidelity predictor of turbulent mixed convection boundary layer flows in vertical and horizontal geometries.

Chapter 2: Turbulent Boundary Layers

2.1 Basics of Turbulent Flow

The majority of flow dynamics encountered in engineering applications and those observed in nature are turbulent. To put forth an attempt to formally and concisely define turbulence has posed to be of profound challenge. Though a succinct definition is lacking, the characteristics of turbulence are rather distinguishable. Turbulence is highly dissipative, viscous effects perform deformation work on the small length scales thereby converting turbulent kinetic energy into an increase in the flow's internal energy; turbulence comprises a wide array of spatial and time scales; it is profoundly diffusive, i.e. there is increased mixing in mass, momentum and heat; turbulent flow is not deterministic, the flow is usually characterized by rapid fluctuations in time and space; thus, statistical methods have to be employed to acquire any detailed information on the flow physics.

Generally, turbulence is only able to emerge and persist in the presence of relatively significant shear. By choosing to ignore how turbulence is generated, one can still appropriately assume that the majority of the turbulent kinetic energy is

highly concentrated around some spatial scale. As was aforementioned, turbulent flow is hugely dissipative and viscous effects convert turbulent kinetic energy into internal energy of the flow at the small turbulence scales. Moreover, it was stated above that turbulence consists of many spatial scales. Hence, there is apparently a mechanism that enables a transfer of energy from the large energy containing turbulence scales to the sufficiently small dissipative scales of turbulence. This is essentially the well-known energy cascade process of turbulence. The cascade was initially thought to be a process where small turbulence scales emerge via vortex stretching by the mean strain rate. Subsequently, smaller length scales develop containing turbulent kinetic energy as well until these spatial scales are dissipated into heat by viscous effects. However, it has been discovered that the energy cascade process proceeds in both directions [33]. There is a flow of energy from the small scales to the large length scales; this process occurs probably through vortex merging or compression. Even though the energy cascade proceeds in both directions, the net energy cascade is from the large to small turbulence scales. It must be mentioned that the energy cascade is essentially an inviscid process.

In an analysis performed by [34], it was proposed that in the case of high Reynolds number, the small dissipative scales have identical structural and statistical properties for all turbulent flows. Implicit in this notion is that the small scales are independent of the mechanisms that affect the large energy containing scales and the scale separation increases with increasing Reynolds number. Another assumption and analysis was proposed by Kolmogorov pertaining to the energy cascade process. The mathematician proposed the notion of an inertial subrange; this region of the

energy spectrum comprises wave numbers that are only dependent upon the dissipation rate. Moreover, in the inertial range of the spectrum, the premise is that energy cascades only from the large eddies to the small length scales without significant loss of turbulent kinetic energy. The length scales contained within the inertial subrange essentially transfer energy from larger to smaller scales in the absence of viscosity and were assumed to obey the decay law of [35]. The decay law is representative of a line with constant slope of $-5/3$ and is given as

$$E(k) = C_K k^{-5/3} \epsilon^{2/3}, \qquad (2.1)$$

with C_K being the Kolmogorov constant, k is wave number and ϵ is the dissipation rate of turbulent kinetic energy. Figure 2.1 illustrates the different regions of the energy spectrum that were aforementioned. These regions are, i) the large energy containing turbulence scales, i.e. low wavenumber eddies; turbulence is introduced into the system via these large eddies that extract energy from the mean flow and are greatly dependent upon the length scale of the system, ii) the second region consists of the transitive length scales in the inertial subrange; energy is transferred to smaller eddies via vortex stretching without much loss of turbulent kinetic energy; this region obeys the decay law given in Eq.2.1 and iii) the third region comprises the smallest eddies affected by viscous effects that perform deformation work by transforming turbulent kinetic energy into internal thermal energy. An additional assumption to point out shown in Figure 2.1 is the universal equilibrium range. It is merely the notion that the smaller turbulence scales have no preferred directionality and its motion is independent of the geometry. Furthermore, it is supposed that the smaller length scales instantaneously dissipate the energy transferred from the large eddies.

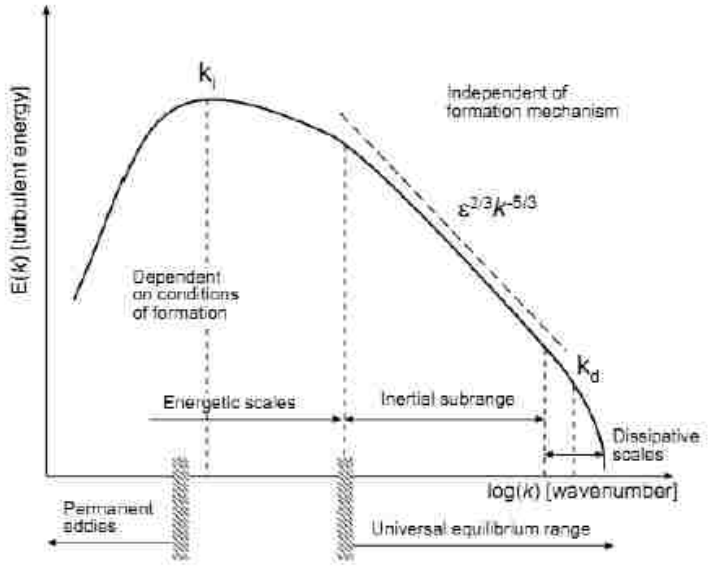

Figure 2. 1 Idealized energy spectrum of turbulence. Image adopted from [36].

The concept of the energy spectrum employed in the theory of Kolmogorov is based upon the premise that most of the turbulent kinetic energy is concentrated around large scale eddies, i.e. turbulence is introduced into the system via the integral scales. Despite its prevalence, the described energy spectrum is by far, minimally universal. In free-shear turbulent flows such as mixing layers and wakes, the most energetic containing turbulent structures are of large scales. This can be seen in Figure 2.2. Figure 2.2 depicts a mixing layer initially at two different parallel streams that has transitioned to turbulence downstream as a result of the growth of small perturbations in the unstable shear layer. This instability, known as the Kelvin-Helmholtz instability, is a typical feature of the initial stages of the mixing layer and is a profound consequence of an inflection in the velocity profile [37]. As illustrated in Figure 2.2, the wave instability continues to grow and subsequently results in the generation of large scale roller-type vortices. The mixing layer grows as these roller-

type vortices are convected downstream and vortex paring recurs. Thus, free shear flows transition to turbulence due to an inviscid instability [38]. The idealized energy spectrum applies to turbulent free shear flows where large scale eddies eventually degenerate into much smaller eddies via the Kolmogorov energy cascade.

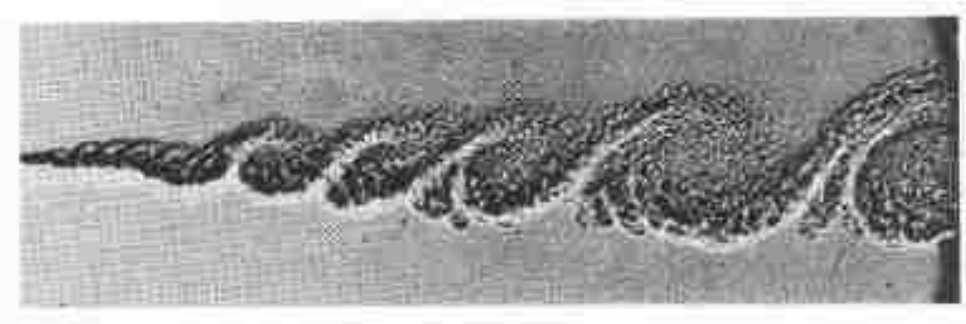

Figure 2. 2 Shadowgraph of a mixing layer between parallel streams at ~10 m/s and ~4 m/s flowing from left to right. Image from [39].

However, in wall bounded flows, solid boundaries have profound effects on the turbulence dynamics. The presence of the wall imposes a physical limit on the spatial turbulence scales near the wall to a fraction of the wall distance. Due to the high shear region near the wall, the production of turbulent kinetic energy peaks very near the wall [40]. Thus, turbulence is introduced into the system via the small scale eddies near the wall. In light of this, it is quite reasonable to wonder of the mechanism that induces turbulence transport away from the wall to the core flow in the boundary layer. To illuminate upon this issue, let us consider the equation for turbulent kinetic energy for an incompressible flow; the turbulent kinetic energy $\mathrm{K} = \frac{1}{2}\langle \mathrm{tr}(\mathbf{u}'\mathbf{u}') \rangle$ and the transport equation is given by

$$\frac{\partial \mathrm{K}}{\partial t} + \mathbf{U}.\nabla \mathrm{K} - \nabla.(\nu \nabla \mathrm{K}) + \nabla. E_{flux} = -\langle \mathbf{u}'\mathbf{u}' \rangle : \nabla \mathbf{U} - \epsilon \,, \qquad (2.2)$$

where the viscous dissipation of turbulent kinetic energy $\epsilon = \nu \langle \nabla \mathbf{u}' : \nabla \mathbf{u}' \rangle$. E_{flux} is essentially the spatial flux of turbulent kinetic energy transport due to pressure and velocity fluctuations and reads as

$$E_{flux} = \langle \mathbf{u}' \big(\mathrm{p}' + 0.5 \mathrm{tr}(\mathbf{u}'^2) \big) \rangle \,. \qquad (2.3)$$

The turbulent kinetic energy production and spatial energy flux budgets for three DNS simulations of channel flow at increasingly high Reynolds number are illustrated in Figure 2.3. Since the wall-normal component of the spatial energy flux is significant in parallel flows, only E_{flux_2} survives and thus is depicted.

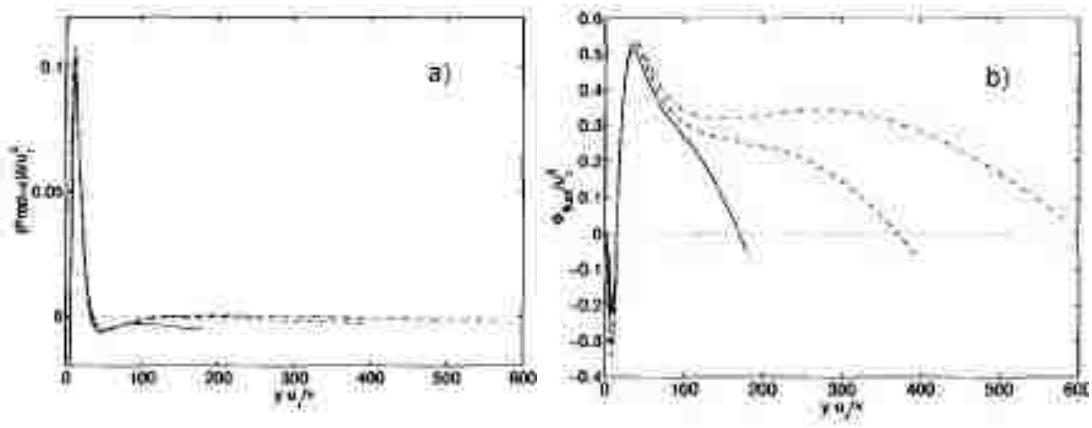

Figure 2. 3 a) Net turbulent kinetic energy production, $-\langle \mathrm{u}'\mathrm{u}' \rangle : \nabla \mathrm{U} - \epsilon$, b) turbulent energy flux $\mathrm{E}_{\mathrm{flux\_2}}$. Images adopted from [41].

Thus, it can be seen that the net turbulent kinetic energy production peaks around the buffer layer region and dissipation exceeds production of turbulence in the outer portion of the boundary layer. An inspection of the spatial energy flux budget in Figure 2.3 further expounds upon the spatial flux of energy away from the buffer region into the boundary layer. Very near the wall, the spatial energy flux is negative, indicating turbulent energy transport is leaving this region; the flux is mostly positive outside the buffer layer region, alluding to an influx of turbulent energy. Thus, it can be said that there are two turbulence cascades in wall bounded turbulent flows, namely spatial and spectral energy transfer. Some of the turbulence generated very near the wall region is dissipated as a result of high shear; however, an immense amount of the production is spatially transported via turbulent diffusion into the core region of the boundary layer as shown in Figure 2.3. This is the spatial energy cascade. The spectral energy cascade in wall bounded turbulent flows is identical to the Kolmogorov cascade; there is a flow of energy locally from the larger to smaller turbulence scales across an inertial range where neither the effects of viscosity nor the character of the largest scales affects the energy transfer [41].

2.2 Coherent Structures

The prior section elucidated the sensitivity of the outer core flow of the boundary layer to the near wall flow structures and dynamics. The converse is not so as the near wall turbulent dynamics ($y^+ < 60$) seem to recur without any need for feedback from the core flow, i.e. it operates autonomously [42]. The most prominently accepted near wall structures, namely the low-speed streaks and quasi-streamwise vortices [40], [43] and the quasi-streamwise vortices are profoundly responsible for

the increase in skin friction and heat transfer [44] in wall bounded turbulent flow. These wall structures are spatially coherent and temporally evolving vortical motions of fluid and are commonly referred to as coherent structures (CS). The incoherency in turbulence tends to decay relatively rapidly in comparison to the CS [45]; thus, the transport of fluid properties is dominated by these coherent structures and their exact nature upon the generation of turbulence will be examined further in the subsequent subsections.

2.2.1Structure of the Wall Layer

As aforementioned, the salient features in the near wall region of a turbulent boundary layer are the quasi-streamwise vortices and low-speed momentum streaks. Moreover, it was stated that these quasi-streamwise vortices were primarily responsible for the increase in skin friction and heat transfer near the wall. The ability of these primarily longitudinal vortices in enhancing mixing can be easily expounded. The vortices induce high-speed and lower temperature fluid towards the wall during the downwash motion and this motion steepens the wall velocity and thermal fields gradients [44]. Although the wall gradient is reduced during the upwash motion of the vortices, this gradient reduction is significantly smaller [44]. Thus, there is a net increase in the wall gradients.

The kinematics of the quasi-streamwise vortices and low-speed streaks was depicted by [46] as shown in figure 2.3. Figure 2.3 illustrates a pair of counter-rotating streamwise vortices with opposite signed vorticity that span roughly 1000 wall units. In their model, it was conceptualized based upon their experimental observations that these streamwise vortices pump low-speed fluid away from the wall

during the upwash motion. The low-speed fluid is essentially the low-speed streak depicted as the shaded structure between the vortices. The violent ejection and break-up of the low-speed streaks was conjectured to be the dominant cause of turbulent production [47]. This near-wall event has been referred to as the bursting phenomenon and is a quasi-cyclic process. The bursting process that contributes to the production of turbulence recurs through a process whereby the low-speed streaks gradually drift away from the wall and subsequently starts oscillating once it reaches $y^+ \approx 8 - 12$.

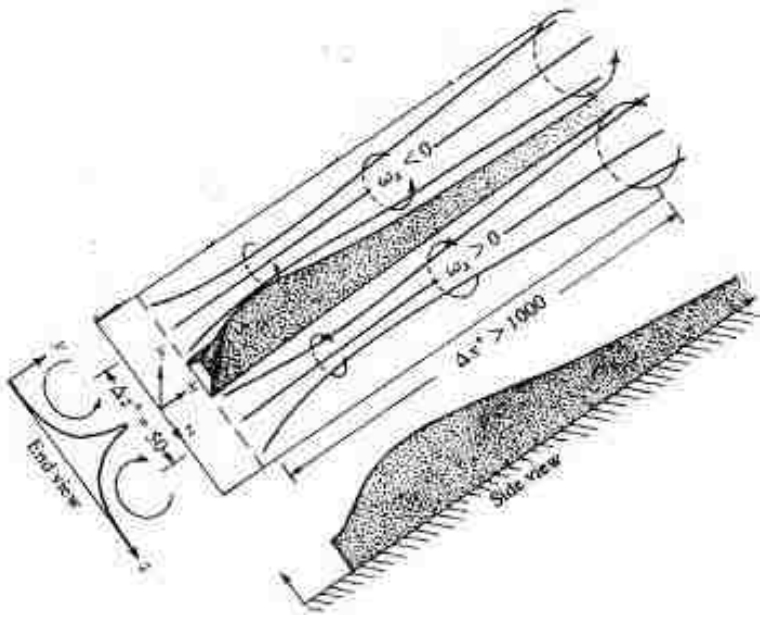

Figure 2. 4 Model of counter-rotating streamwise vortices along with low-speed streak. Images adopted from [46].

The oscillation of the low-speed streaks amplifies as it continues to move outwardly and terminates in an abrupt break-up around $10 < y^+ < 30$. Following the break-up, the streak is contorted and stretched; a depiction of this process is shown in figure 2.4 according to the observation of [40]. The eventual occurrence of the amplified

oscillation and subsequent break-up was reported to be caused by some sudden instability. This instability has been argued to be a consequence of localized shear-layer instability present in the near-wall region and has a profound impact upon the evolution of the CS near the wall [43].

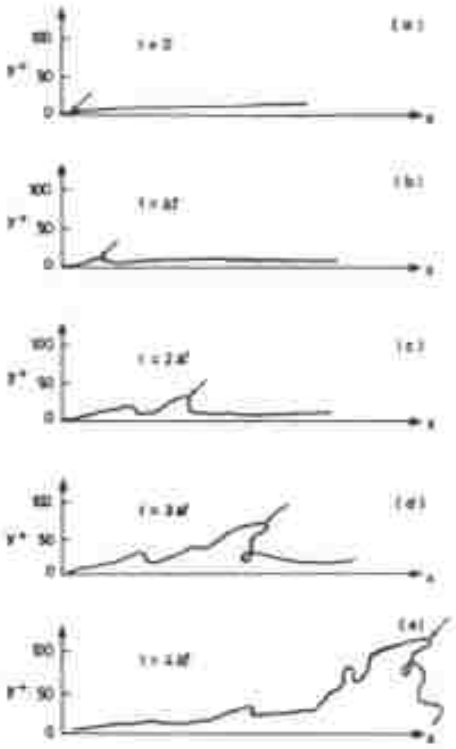

Figure 2. 5 Illustration of low-speed streak break-up process with a dye. Images adopted from [40].

A schematic of such localized shear-layer instability was illustrated by [48], refer to figure 2.5. In figure 2.5, a packet of high-speed fluid is shown penetrating the near-wall region in the midst of the low-speed streak prior to the break-up of the low-speed streak; thus, the sharp interface between the high- and low-speed fluid regions results in a localized shear-layer prone to instability due to the apparent inflection in the mean velocity profile.

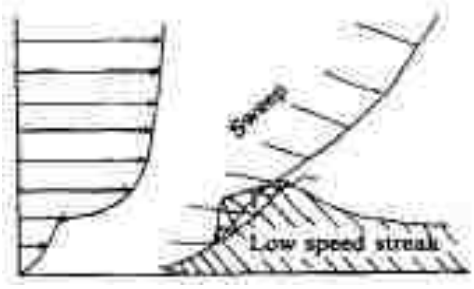

Figure 2. 6 Localized shear-layer instability between lifted low-speed streak and inrushing high-speed fluid. Images adopted from [48].

Figure 2.6 illustrates the prominent near-wall structures of a fully developed turbulent boundary layer within the buffer region $(0 < y^+ < 60)$ as computed by [42]. The base layer depicts elongated streaks of low momentum fluid that have been lifted from the edge of the viscous sublayer into the buffer region; the overlay shows quasi-streamwise vortices flanking the elongated low-speed streaks. It should be noted that further downstream, it seems the low-speed streaks are devoid of quasi-streamwise vortices. This means as the vortices are convected downstream, low-speed fluid elements are left underneath their wake; thus the streaks are elongated. As previously stated, the proximity of the low-speed streaks to the vortices is attributable to the vertical velocity induced by the vortices which lifts up the low-momentum fluid near the wall.

Figure 2. 7 Near-wall structures comprising lifted low-speed streaks (black) and quasi-streamwise vortices (grey). Images adopted from [42].

The formation mechanism of the well-accepted near-wall quasi-streamwise vortices still remains hugely uncertain; many of the mechanisms proposed are either based upon parent-offspring or instability-based mechanisms. These streamwise vortices generation mechanisms tend to widely disparate. Parent-offspring mechanisms are essentially based upon the premise that new streamwise vortices are generated by the direct induction of existing vortices. The latter, instability-based mechanisms, is based upon the presence of local instability in the base flow in the absence of parent vortices. For present purposes, a detailed comprehensive overview of quasi-streamwise vortex generation mechanisms can be seen in [49].

2.2.2 Distribution of Near-wall Coherent Structure

As opposed to the counter-rotating pairs of longitudinal vortices proposed by [46], the conceptual models of [45] and [50] proposed similar kinematics of the near-wall coherent structures that were not in pairs in the streamwise. The near-wall coherent structure model of [45] can be seen in figure 2.7. To generate the near-wall conceptual model, the instability regeneration mechanism was assumed and aided in developing the spatial relationship of the quasi-streamwise vortices. Interestingly enough, the conceptual model of [50] employed the parent-offspring regeneration mechanism and educed similar near-wall structures, see figure 2.8. Both conceptual models depict a train of alternating overlapping quasi-streamwise vortices with the downstream end of each vortex inclined away the wall. The SP and SN labels in figure 2.7 are indicative of coherent structures with $+\omega_x$ and $-\omega_x$, respectively. Similarly, the alternating signs of streamwise vorticity can be seen in figure 2.8; vortices A and C are $+\omega_x$ structures and vortex B is a $-\omega_x$ structure. In figure 2.7a, the low-speed streak is illustrated beneath the tilted quasi-streamwise vortices; the apparent tilting observable in the (x, z) plane is a consequence of mutual induction. For example, the SP structure induces motion on the SN structure whereby point A of structure C is advected in the -z direction and point B in the +z direction. Hence, mutual induction results in SN structures being convected in the clockwise direction and the SP structures in the counter-clockwise in the (x, z) plane. Quadrants Q2 and Q4 events are associated with ejection and sweep events, are shown in figure 2.7a as well. The quadrant events Q2 and Q4 are representative of $(u' < 0, v' > 0)$ and $(u' > 0, v' < 0)$, respectively. The presence of an internal shear layer with

$-\partial u'/\partial x$ located at E is indicated in figure 2.7. The internal shear layer tends to occur at sharp $+u'/-u'$ interfaces in the streamwise direction [44]. The emergence of the internal shear layer is due to the overlapping and tilting in the (x, z) plane; thus, the shear layer arises as a result of the sweep and ejection events that occur from structures C and D, respectively. These internal shear layers are quite prevalent and persistent in the near-wall region and are part of the near-wall quasi-streamwise vortices regeneration cycle [51].

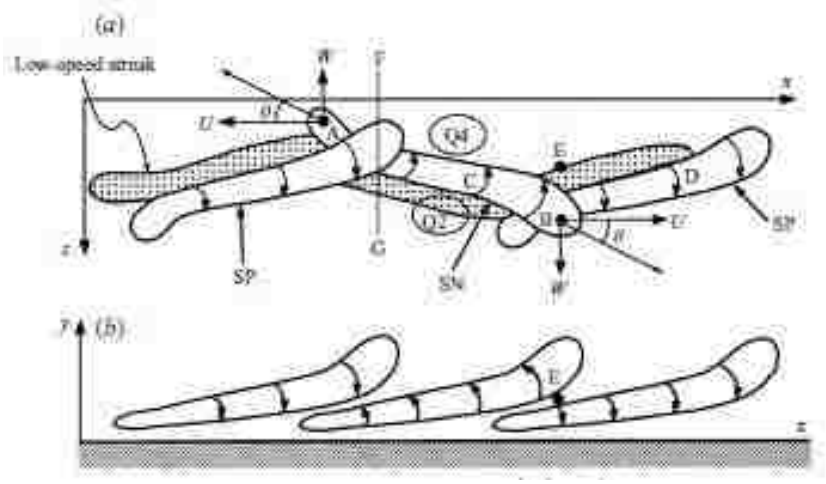

Figure 2. 8 Conceptual model of near-wall coherent structures and associated events. Images adopted from [45].

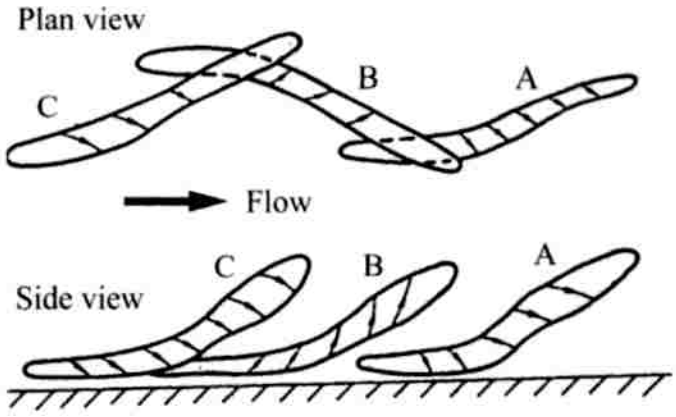

Figure 2. 9 Conceptual model of near-wall coherent structures. Images adopted from [50].

2.3 Feature Identification

Most of the features that occur in the turbulent boundary layer flow field can be defined precisely. There are other features that are not completely understood and do not lend themselves to precise definitions. One such example is the swirling feature that is of profound significance in turbulent boundary layers, i.e. the vortex, is one such feature whereby a precise definition is presently lacking. The characterization of a vortex is of a swirling fluid motion around a central region; however, a formal definition of the vortex has posed to be a formidable challenge and has been the source of many debates over the years. To overcome this challenge, [52] proposed an intuitive definition of the vortex as rotation motion of a multitude of material particles around a common center. Such an intuitive definition illustrates a vortex in terms of spiraling streamlines and such a frame of reference is only available to an observer moving with the core of the vortex. Thus, due to the vague definition proposed by [52], [43] put forth a more precise definition to identifying vortices in three dimensional flowfields and is reproduced here in brief: A vortex exists when instantaneous streamlines mapped on a plane normal to the vortex core exhibit a roughly circular or spiral pattern, when viewed from a reference frame moving with the center of the vortex core. To proceed, the debates pertaining to the many definitions of the vortex is directly irrelevant to this thesis and can be sidestepped.

2.3.1 Vortex Detection Methods

Despite the lack of a widely accepted definition for a vortex, various methods of detecting these vortices have been implemented. Some of these algorithms have been relatively able to effectively capture vortical structures in a 3D flowfield. The overview of vortical structure detection methods subsequently given is by no means comprehensive, but a few of these detection schemes will be discussed in this section.

Local Pressure Minimum

Since the vortex core tends to be a region of local pressure minimum, this criterion has been shown to effectively detect vortical structures in the turbulent boundary layer [43]. However, it was shown that it is quite challenging to adequately capture all the vortical structures by prescribing an appropriate cutoff pressure level.

Vorticity Magnitude

The vorticity magnitude, $\boldsymbol{\omega} = |\nabla \times \mathbf{U}|$, has been employed with success in free shear flows in effectively identifying vortical CS. The same approach may not suitable for wall bounded turbulent flows, especially if the background shear is comparable to the vorticity magnitude inside the vortex. Thus, such a criterion is quite problematic since the maximum of the vorticity is near the wall in turbulent boundary layers due to the high shear and it will be difficult to identify the core of the vortical structure. Hence, the vorticity magnitude may not be a suitable measure of identifying CS in wall bounded turbulent flows.

Complex Eigenvalues of $\nabla\mathbf{U}$

The eigenvalues of the velocity gradient tensor, $\nabla\mathbf{U}$, were employed by [53] to derive a general classification of varying streamline patterns that can occur in three dimensional flowfields. The classification made use of the premise that the coordinate system translates with the origin following a fluid particle and the structural features educed will be frame-independent. In order to identify a vortex core, it was proposed that such a region will be defined by possessing complex eigenvalues of $\nabla\mathbf{U}$. The implications of this definition is that the local streamlines observed will be closed or have a spiral pattern based upon the topology of the three dimensional flow pattern defined by the invariants of the eigenproblem. The corresponding eigenproblem for the 3D flowfield problem satisfies the following characteristic equation

$$\lambda^3 + \boldsymbol{P}\lambda^2 + \boldsymbol{Q}\lambda + \boldsymbol{R} = 0\,, \tag{2.4}$$

which can have: (i) distinct real roots, (ii) all real roots with at least two roots being equal, or (iii) one real root in addition to a conjugate pair of complex roots. The first invariant $\boldsymbol{P} = -\mathrm{tr}(\nabla\mathbf{U})$ and the assumption can be made that the flow is incompressible, making this term zero. The second and third invariants are $\boldsymbol{Q} = \frac{1}{2}(\|\boldsymbol{\Omega}\|^2 - \|\mathbf{S}\|^2)$ and $\boldsymbol{R} = -\det(\nabla\mathbf{U})$, respectively. The quantities, $\boldsymbol{\Omega}$ and $\mathbf{S}$ are the anti-symmetric and symmetric parts of $\nabla\mathbf{U}$ and are given as

$$\boldsymbol{\Omega} = \frac{1}{2}(\nabla\mathbf{U} - (\nabla\mathbf{U})^{\mathrm{T}})\,, \tag{2.5}$$

$$\|\boldsymbol{\Omega}\| = (\boldsymbol{\Omega}{:}\,\boldsymbol{\Omega})^{1/2}\,, \tag{2.6}$$

$$\mathbf{S} = \frac{1}{2}(\nabla \mathbf{U} + (\nabla \mathbf{U})^{\mathrm{T}}) \qquad (2.7)$$

and

$$\|\mathbf{S}\| = (\mathbf{S}:\mathbf{S})^{1/2}\,. \qquad (2.8)$$

The anti-symmetric and symmetric parts of the velocity gradient tensor are the rotation rate and strain rate tensors, respectively. Thus, to attain complex eigenvalues, the discriminant ***D*** has to be positive, i.e.

$$\boldsymbol{D} = \left(\frac{1}{3}\boldsymbol{Q}\right)^3 + \left(\frac{1}{2}\boldsymbol{R}\right)^2 > 0 \qquad (2.9)$$

and there is one real root and a conjugate pair of complex roots $(\lambda_r, \lambda_{cr} \pm \lambda_{ci})$. The physical significance of these eigenvalues are as follows: i) the inward or outward axial acceleration of the fluid particle along a vector perpendicular to the vorticity plane is given by the sign and magnitude of λ_r , ii) the fluid particle can either spiral towards or away from the center at a certain rate and the sign and magnitude of λ_{cr} dictates this event and iii) the vortical strength of the swirling fluid is given by λ_{ci} . The physical descriptions of the three eigenvalues are depicted in figure 2.9.

Figure 2. 10 Eigenvalues of $\nabla \mathbf{u}$ and physical significance, reproduced from **[54]**.

Positive Second Invariant Q

This vortex detection method, as implemented by [55], defined an eddy as a region with the second invariant of $\nabla\mathbf{U}$, $\boldsymbol{Q}$ is greater than zero. As previously given in Eq.2.*, $\boldsymbol{Q}$ is representative of the balance between the magnitude of rotation and strain rates; thus, the criterion that $\boldsymbol{Q} > 0$, means swirling motion dominates the shear strain rate. The $\boldsymbol{Q} > 0$ criterion is essentially stricter than the $\boldsymbol{D} > 0$ condition; this can be seen in figure 2.10. The figure illustrates that any region of the flowfield identified as comprising a vortex by the $\boldsymbol{Q} > 0$ detection scheme will be subsequently captured by the $\boldsymbol{D} > 0$ method. However, the converse is not so; thus, this thesis makes use of the $\boldsymbol{Q}$ criterion in the identification of coherent structures.

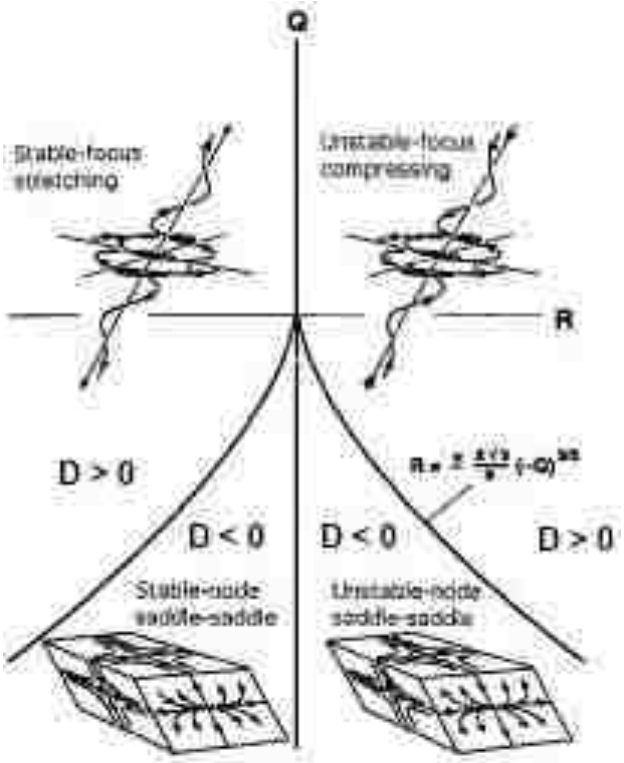

Figure 2. 11 3D flow topology for an incompressible flow, reproduced from [56].

2.4 Closing Remarks

This chapter presented an overview of the fundamental nature of turbulent flow with emphasis upon wall bounded turbulence. Although the succinct definition of turbulence is not currently available, some of its intrinsic characteristics were elucidated along with the intricacies present in the near-wall region. The most complex part of a turbulent boundary layer is the near-wall high-shear region where severe viscous effects results in turbulent processes. These turbulent processes involve the near-wall coherent structures dynamics which seemingly proceed autonomously of the outer boundary core flow. The dominance and prominence of quasi-streamwise vortices in the near-wall region is now generally accepted in the field of turbulence; there is profound disagreement regarding the mechanisms responsible for the regeneration of these flow structures.

The swirling feature of fluid motion, i.e. the vortex, has not lent itself to a precise definition due to the lack of its complete understanding. Many vortex identification schemes have been proposed based upon different definitions. Thus, the vortices (coherent structures) educed from a turbulent flowfield is greatly dependent upon how it is mathematically defined. In increasing the current understanding of the near-wall turbulent cycle, a precise definition of the vortex will be compulsory.

The features of wall-bounded turbulent flows dominated by forced-convection were introduced in this chapter. The current thesis consists of turbulent boundary layers greatly affected by buoyancy and the turbulent dynamics of such near-wall flows have not been investigated like its counterpart, forced-convection. Thus,

implicit in this chapter is that the structure of near-wall turbulence is similar to those expected in buoyancy affected turbulent boundary layers.

Chapter 3: Computing Turbulent Boundary Layers

3.1. Modeling Turbulent Flows

Advances made with computational fluid dynamics (CFD) in the modern era have enabled the ability to simulate turbulent boundary layer flows using different approaches. The simulation of turbulent boundary layers commences with the Navier-Stokes equations, which typically consists of the conservation of mass, momentum, and energy equations. The numerical approach adopted in resolving the turbulent flowfield is dictated by the form of Navier-Stokes equation solved. To date, a number of techniques are commonly utilized to compute turbulent flows; these methods include Direct Numerical Simulation (DNS), Large Eddy Simulation, Reynolds-Averaged Navier-Stokes (RANS), and hybrid LES/RANS.

Direct Numerical Simulation computes the instantaneous turbulent boundary layer without approximating or averaging the Navier-Stokes equations. As a result, turbulence modeling is not required and all the varying length and time scales have to be resolved with the spatial resolution and time advancement scheme. DNS has to resolve the largest and smallest length scales dictated by the geometry and physics of

the flow. Typically, the Kolmogorov length scale, $\eta = (\nu^3/\varepsilon)^{1/4}$, is adopted as the smallest spatial scale needed to capture in DNS, where ν and ε are the kinematic viscosity and dissipation rate of small scale turbulence. However, the DNS mesh does not have to resolve the length scale η, the grid criterion that is required to resolve the smallest scale should be $O(\eta)$ [57]. With the utilization of significantly fines meshes to resolve the small dissipative scales, DNS can be very valuable in understanding the flow physics of turbulence and gives the most accurate predictions to the Navier-Stokes equations; however, it is intrinsically computationally expensive. The number of grid points required in each spatial direction is proportional to the ratio of the largest to smallest scales which is proportional to $Re_L^{3/4}$ [58]. Re_L is the Reynolds number based upon the integral scale or domain length. In addition to the spatial resolution cost, DNS computations are also quite stiff. The stiffness is attributable to the presence of high frequency motions (smallest length scale motion) that have to be resolved and the utilization of larger time steps can introduce significant small length scale errors into the solution.

Rather than calculating the instantaneous flowfield, the statistical evolution of the boundary layer can be computed [57]. The Reynolds-Averaged Navier-Stokes equations use such an approach by averaging all of the unsteadiness in the flowfield. A specified unknown, the Reynolds stress tensor term, $\boldsymbol{\tau}_{RANS}$, emerges as a result of averaging non-linear terms in the Navier-Stokes equations. The RANS momentum equation for a flow with variable density in Favre mass averaged quantities is given as:

$$\frac{\partial \hat{\rho}\mathbf{U}}{\partial t} + \nabla.\hat{\rho}\mathbf{U}\mathbf{U} = -\nabla \mathrm{P} + \hat{\rho}\mathbf{g} + \nabla.\left(\hat{\mu}\left(\nabla\mathbf{U} + \nabla\mathbf{U}^{\mathrm{T}} - \frac{\mathbf{2}}{\mathbf{3}}\mathrm{tr}(\nabla\mathbf{U})\mathbf{I}\right)\right) + \nabla.\boldsymbol{\tau}_{RANS}\,. \tag{3.1}$$

The emergence of the Reynolds stress tensor term is known as the turbulence closure problem. In order to completely solve the averaged equations, a closure model has to be employed in conjunction with the RANS equations. Several RANS equations turbulence closure models have emerged in the past decades, such as one-equation, two-equation, algebraic, and Reynolds Stress models. It must be mentioned that a major drawback of simulating turbulence with RANS equations is the inadequacies of the closure models in resolving all the turbulence length scales. These closure models are required to capture the largest and smallest scales in the flowfield and are typically tuned for a particular flow due to the model constants. It is well known that the smallest turbulence scales are primarily a function of viscosity and can be assumed to be independent of the geometry, but the largest scales are usually a function of the geometry and boundary conditions. Hence, it can be easily deduced how ineffective a RANS closure model can be in solving different types of turbulent flow.

The simulation of turbulent boundary layer flow with LES, which is the primary subject matter of this thesis, is essentially bracketed by DNS and RANS. Large Eddy Simulation solves the spatially filtered Navier-Stokes equation by removing the high frequency motion. The filtered equations resolve the large turbulent scales and the smallest scales are modeled via sub-grid scale (SGS) terms that emerge from filtering the non-linear terms. As previously mentioned, the large turbulent scales are dependent upon the geometry and boundary condition and the

smallest scales can be assumed to be statistically and structurally universal to all turbulent flows [59]. Hence, the usage of LES to model turbulence makes it inherently more accurate than RANS, although a tad more computationally expensive. Since the smallest scales are computed with SGS models, LES is neither as computationally expensive nor possess the fidelity of DNS. The small scales effects in LES are modeled as an energy drain that occurs in turbulence from the largest to the smallest scales where viscous effects are more pronounced.

Aside from the commonly used turbulence simulation methods, the hybrid RANS-LES approach combines the two techniques in order to lessen the computational cost as opposed to performing a full LES computation. Since time-dependent turbulence simulations such as LES requires resolving small length and time scales for wall bounded turbulent flows, LES is more expensive than RANS simulations [60]. In an effort to circumvent the cost associated with full LES simulation, the hybrid RANS-LES approach employs RANS equations near the wall and LES in the outer portion of the boundary layer where the turbulence structures are larger. The coupling of RANS and LES in the boundary layer is quite challenging and still remains an open problem [61].

3.2. Principles of LES

The basic premise of Large Eddy Simulation is the application of a low-pass filter in frequency to the Navier-Stokes equation and was initially proposed by Smagorinsky for weather modeling application [62]. Once the filter is applied, a set of partial differential equations describing the large scale motion of turbulence emerges, with the smallest scales ostensibly discarded [33]. The large scales of turbulence, as

aforementioned, are profoundly dependent upon the geometry and boundary conditions of the flow set-up. Moreover, the large scales contain most of the turbulence kinetic energy and perform most of the transport of momentum and energy in the flowfield [63]. Without loss of instructional value, the effects of the smallest scales of turbulence have to be accounted for and this is usually done by SGS modeling. The modeling approach of the more "nearly isotropic length scales" is a consequence of the Kolmogorov theory of turbulence [35]. The theory presumes that small scale turbulence is statistically invariant under rotations and translations [64]. Hence, to summarize the entire concept of Large Eddy Simulation, we explicitly resolve the geometry and boundary condition dependent large energy containing turbulent scales and assume without significant loss of accuracy, the effects of the smallest turbulent scales are isotropic and modeled numerically.

3.2.1 LES Filters

To separate the large turbulent scales from the small scales, a scale separation is compulsory and is accomplished with the use of filters. The filtering process essentially "averages out" the small scale with one of the filtering properties, the spatial cutoff lengthscale or filter width, Δ.

The grid scale (GS) or resolved variable denoted by an overbar can be formally defined as

$$\bar{f}(\mathbf{x}) = \int_D G(\mathbf{x}, \mathbf{x}'; \Delta) f(\mathbf{x}') d\,\mathbf{x}' , \qquad (3.2)$$

where D is the computational domain, $\mathbf{x} \in D$, $G(\mathbf{x}, \mathbf{x}'; \Delta)$ is the convolution kernel of the characteristic filter function associated with the spatial cutoff lengthscale.

Three classical explicit convolution filters are typically utilized in Large Eddy Simulation for spatial scale separation and are characterized by a filter width: the box or top-hat filter, Gaussian filter, and spectral or sharp cut-off filter [65]. In what follows, the mathematical properties of these filters will be briefly discussed.

Top-Hat Filter

The top-hat filter is commonly employed in Finite Volume Large Eddy Simulation computations. The filter is essentially an average over some specified filter width Δ and also represents an implicit grid filter introduced by the computational mesh. Top hat filter function can be expressed in physical space as:

$$G(\mathrm{x}, \Delta) = \begin{cases} \frac{1}{\Delta}, & if \left(|\mathrm{x}| \leq \frac{\Delta}{2} \right), \\ 0, & \text{otherwise} \end{cases} \tag{3.3}$$

and the filter function in spectral space is:

$$\hat{G}(k) = \frac{\sin\left(\frac{k\Delta}{2}\right)}{\frac{k\Delta}{2}}, \tag{3.4}$$

where k is the wave number and is formally defined as:

$$k = \frac{\pi}{\Delta}. \tag{3.5}$$

Gaussian Filter

The Gaussian filter in physical space is given as:

$$G(\mathrm{x},\Delta)=\left(\frac{6}{\pi\Delta^2}\right)^{1/2}\exp\left(-6\left(\frac{\mathrm{x}}{\Delta}\right)^2\right), \tag{3.6}$$

and the corresponding filter function in spectral space is:

$$\hat{G}(k)=\exp\left(-\frac{\Delta^2k^2}{24}\right). \tag{3.7}$$

Spectral Cut-off Filter

The sharp cutoff filter is usually employed for spectral LES computations and its filter function in physical space is:

$$G(\mathrm{x},\Delta)=\frac{\sin\big(k(\mathrm{x})\big)}{k\mathrm{x}}, \tag{3.8}$$

and the filter function in spectral space is expressed as:

$$\hat{G}(k)=\begin{cases}1 & if\ |k|<\dfrac{\pi}{\Delta}\\ 0 & \text{otherwise}\end{cases} \tag{3.9}$$

To exemplify the differences between the various filters, they were applied to a test function and the energy spectra of the filtered quantities are depicted in Figure 3.1. The spectra cut-off filter only affects the spatial scales below the cutoff wavenumber; the top hat and Gaussian filters can be seen to smear spatial scales at low and high wavenumbers. The smearing behavior of the top-hat and Gaussian filters necessitates a relative increase in grid resolution to capture the high frequency eddies as their spectral cutoff counterpart. Hence, this makes spectral LES more accurate than physical space filtered LES computations.

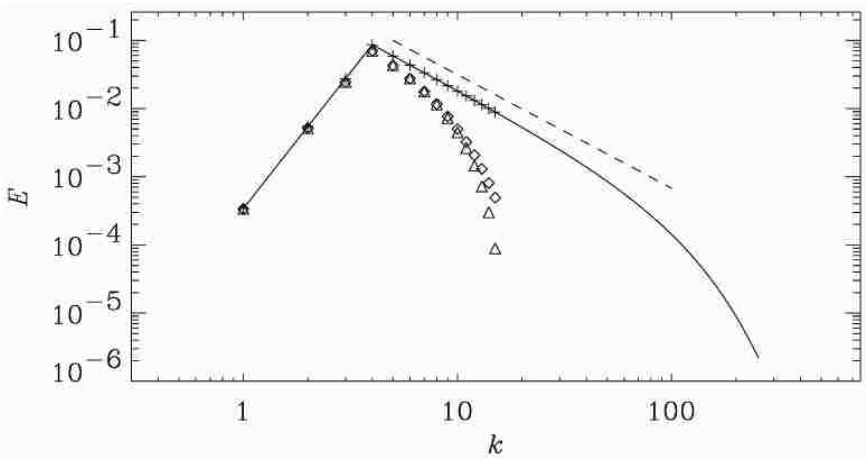

Figure 3. 1 Energy spectra of a test function, —— unfiltered, + spectra cut-off, □ Gaussian, Δ top-hat, - - - $k^{-5/3}$. Image adopted from [66].

3.2.2 Favre-Filtered Governing Equations

The fundamental equations governing the low speed motion of a single phase non-reacting flow with variable properties can be based upon the compressible Navier-Stokes system of equations and will be given in this section. These equations are the conservation laws of mass, momentum and energy.

The conservation of mass equation given in Eq.3.10, basically states that the rate of change of mass in a fluid element must be in equilibrium with the net rate of flow of mass across the fluid element.

$$\frac{\partial \rho}{\partial \mathrm{t}} + \nabla . \rho \mathbf{u} = 0, \qquad (3.10)$$

where ρ, **u** = (u, v, w), t are the density, three components of velocity and time, respectively. The conservation of momentum equation states the rate of momentum increase of a fluid element is equal to the net forces acting on it. The equation is mathematically expressed as follows:

$$\frac{\partial \rho \mathbf{u}}{\partial t} + \nabla . \rho \mathbf{u}\mathbf{u} = -\nabla \mathrm{p} + \rho \mathbf{g} + \nabla . \boldsymbol{\sigma} , \qquad (3.11)$$

where p and **g** are the pressure and gravity vector, respectively. $\boldsymbol{\sigma}$ is the viscous stress tensor and is defined as

$$\boldsymbol{\sigma} = \mu \left(2\mathbf{S} - \frac{\mathbf{2}}{\mathbf{3}} \mathrm{tr}(\nabla \mathbf{u})\mathbf{I} \right), \qquad (3.12)$$

where $\mu = \mu(\mathrm{T})$ is the dynamic viscosity term due to molecular motion and is temperature dependent quantity. The strain rate tensor, **S** is defined as

$$\mathbf{S} = \frac{1}{2}(\nabla \mathbf{u} + \nabla \mathbf{u}^{\mathrm{T}}) . \qquad (3.13)$$

The conservation of energy equation, which is essentially the first law of thermodynamics, states that the rate of change of energy of a fluid element is in equilibrium to the difference between the rate of heat added to the fluid element and work done by the fluid element. As such, the enthalpy form of the conservation law is given by:

$$\frac{\partial \rho h}{\partial t} + \nabla . \rho h \mathbf{u} = \frac{\partial \mathrm{p}}{\partial \mathrm{t}} + \mathbf{u} . \nabla \mathrm{p} + \nabla . (\kappa \nabla T) + \boldsymbol{\sigma} . \nabla \mathbf{u} , \qquad (3.14)$$

where *h* is the sensible enthalpy and is defined as

$$h = \int_{T_{ref}}^{T} C_P(T) dT . \qquad (3.15)$$

The definition of enthalpy given in Eq.3.15, which can be called the sensible enthalpy, is a function of T and C_P, the temperature and specific heat at constant pressure, respectively. In the energy equation, the term κ is the thermal conductivity and dictates a material's ability to conduct heat. The enthalpy form of the energy conservation law given in Eq.3.14 was acquired by subtracting the kinetic energy

equation from the total energy equation to get the internal energy equation. The kinetic energy equation can be derived by multiplying the momentum conservation equation by its corresponding velocity component and adding all three equations to form the resulting kinetic energy equation. Furthermore, by using the following definition for internal energy, *i*,

$$i = h - \frac{\mathrm{p}}{\rho}, \tag{3.16}$$

the substitution can be made in order to have the enthalpy form of the energy conservation equation.

To account for the unknown pressure p, the fluid was assumed to be a perfect gas enabling the following equation of state to be utilized:

$$\mathrm{p} = \frac{\rho RT}{W}, \tag{3.17}$$

where *R* and *W* are universal gas constant and molar mass of the gas, respectively.

The spatial filtering approach given in Eq.3.2 can be utilized for scale separation of the governing differential equations in addition to a change of variable technique where the filtered variables are density weighted using Favre filtering [67]. The utilization of Favre filtering disallows the presence of SGS terms in the conservation of mass equation. The Favre filtered variable $\tilde{f}$, can be defined as

$$\tilde{f} = \frac{\overline{\rho f}}{\bar{\rho}}. \tag{3.18}$$

Using the Favre filtered methodology, the governing equations of motion for flows with non-negligible density gradients [68], [69] can be expressed as:

Mass Conservation:

$$\frac{\partial \bar{\rho}}{\partial t} + \nabla . \bar{\rho}\tilde{\mathbf{u}} = 0 \tag{3.19}$$

Momentum Conservation:

$$\begin{aligned} &\frac{\partial \bar{\rho}\tilde{\mathbf{u}}}{\partial t} + \nabla . \bar{\rho}\tilde{\mathbf{u}}\tilde{\mathbf{u}} - \nabla . \tilde{\boldsymbol{\sigma}} \\ &\qquad = -\nabla \bar{\mathrm{p}} + \bar{\rho}\mathbf{g} - \nabla . \boldsymbol{\tau}_{SGS} + \nabla . (\bar{\boldsymbol{\sigma}} - \tilde{\boldsymbol{\sigma}}) , \end{aligned} \tag{3.20}$$

where

$$\tilde{\boldsymbol{\sigma}} = \tilde{\mu}\left(\nabla\tilde{\mathbf{u}} + \nabla\tilde{\mathbf{u}}^{\mathrm{T}} - \frac{\mathbf{2}}{\mathbf{3}}\mathrm{tr}(\nabla\tilde{\mathbf{u}})\mathbf{I}\right), \tag{3.21}$$

and

$$\bar{\boldsymbol{\sigma}} = \overline{\mu\left(\nabla\mathbf{u} + \nabla\mathbf{u}^{\mathrm{T}} - \frac{\mathbf{2}}{\mathbf{3}}\mathrm{tr}(\nabla\mathbf{u})\mathbf{I}\right)} . \tag{3.22}$$

The divergence of the $(\bar{\boldsymbol{\sigma}} - \tilde{\boldsymbol{\sigma}})$ term in the filtered momentum equation is a consequence of the non-linearity of the viscous stress term; it is usually considered negligible by assuming $(\bar{\boldsymbol{\sigma}} - \tilde{\boldsymbol{\sigma}}) = 0$ and its magnitude was shown to be an order of magnitude lower than $\boldsymbol{\tau}_{SGS}$ [69].

The subgrid-scale stress term,$\boldsymbol{\tau}_{SGS}$, exists as a result of applying the filtering operation to the non-linear convection term in the momentum equation. It is a consequence of $\bar{\rho}\widetilde{\mathbf{u}\mathbf{u}} \neq \bar{\rho}\tilde{\mathbf{u}}\tilde{\mathbf{u}}$ and leads to a modeling approximation to account for the difference between the two sides of the inequality. The modeling approach lends itself to the aforementioned SGS stress term:

$$\boldsymbol{\tau}_{SGS} = \bar{\rho}(\widetilde{\mathbf{u}\mathbf{u}} - \tilde{\mathbf{u}}\tilde{\mathbf{u}}) . \tag{3.23}$$

The SGS stress, $\boldsymbol{\tau}_{SGS}$ can be decomposed into three residual stresses. These residual stresses are the Leonard ($\boldsymbol{L}$), Cross ($\boldsymbol{C}$) and Reynolds ($\boldsymbol{R}$) stresses. Hence, the decomposition proceeds as follows:

$$\boldsymbol{\tau}_{SGS} = \boldsymbol{L} + \boldsymbol{C} + \boldsymbol{R} \ , \tag{3.24}$$

where

$$\boldsymbol{L} = \bar{\rho}\left(\widetilde{\tilde{\boldsymbol{u}}\tilde{\boldsymbol{u}}} - \tilde{\boldsymbol{u}}\tilde{\boldsymbol{u}}\right), \tag{3.25}$$

$$\boldsymbol{C} = \bar{\rho}\left(\widetilde{\tilde{\boldsymbol{u}}\boldsymbol{u}^{"}} + \widetilde{\boldsymbol{u}^{"}\tilde{\boldsymbol{u}}}\right), \tag{3.26}$$

and

$$\boldsymbol{R} = \bar{\rho}\widetilde{\boldsymbol{u}^{"}\boldsymbol{u}^{"}} \ . \tag{3.27}$$

It can be seen from the residual stress decomposition that $\boldsymbol{L}$, $\boldsymbol{C}$ and $\boldsymbol{R}$ represent the interaction of the resolved quantities, interaction between resolved and SGS quantities and interaction between subgrid scales, respectively. The decomposition of $\bar{\rho}\widetilde{\boldsymbol{u}\boldsymbol{u}}$ given in Eq.3.23 using $\boldsymbol{u} = \tilde{\boldsymbol{u}} + \boldsymbol{u}^{"}$, with $\tilde{\boldsymbol{u}}$ being the resolved scales and $\boldsymbol{u}^{"}$ denoting the subgrid scales, results in

$$\bar{\rho}\widetilde{\boldsymbol{u}\boldsymbol{u}} = \bar{\rho}\left(\widetilde{\tilde{\boldsymbol{u}}\tilde{\boldsymbol{u}}} + \widetilde{\tilde{\boldsymbol{u}}\boldsymbol{u}^{"}} + \widetilde{\boldsymbol{u}^{"}\tilde{\boldsymbol{u}}} + \widetilde{\boldsymbol{u}^{"}\boldsymbol{u}^{"}}\right) . \tag{3.28}$$

Thus, we can see that

$$\boldsymbol{\tau}_{SGS} = \bar{\rho}\left(\widetilde{\tilde{\boldsymbol{u}}\tilde{\boldsymbol{u}}} - \tilde{\boldsymbol{u}}\tilde{\boldsymbol{u}} + \widetilde{\tilde{\boldsymbol{u}}\boldsymbol{u}^{"}} + \widetilde{\boldsymbol{u}^{"}\tilde{\boldsymbol{u}}} + \widetilde{\boldsymbol{u}^{"}\boldsymbol{u}^{"}}\right) . \tag{3.29}$$

The Leonard stress term will be shown to be of great significance when dealing with dynamic subgrid scale LES models.

Energy/Enthalpy Conservation:

$$\frac{\partial \bar{\rho}\tilde{h}}{\partial t} + \nabla.\bar{\rho}\tilde{h}\tilde{\mathbf{u}} - \frac{\partial \bar{\mathrm{p}}}{\partial t} - \tilde{\mathbf{u}}.\nabla\bar{\mathrm{p}} - \tilde{\boldsymbol{\sigma}}:\nabla\tilde{\mathbf{u}} + \nabla.\tilde{\mathbf{q}}$$
$$= -\nabla.\left[\bar{\rho}\mathrm{C_P}\left(\widetilde{\mathrm{T}\mathbf{u}} - \tilde{\mathrm{T}}\tilde{\mathbf{u}}\right)\right] \quad (3.30)$$
$$-\nabla.\left[\overline{\mathbf{q}} - \tilde{\mathbf{q}}\right] + \left[\overline{\mathbf{u}.\nabla\mathrm{p}} - \tilde{\mathbf{u}}.\nabla\bar{\mathrm{p}}\right] + \left[\overline{\boldsymbol{\sigma}:\nabla\mathbf{u}} - \tilde{\boldsymbol{\sigma}}:\nabla\tilde{\mathbf{u}}\right]$$

The enthalpy equation apparently has four SGS terms that emanated from the filtering operation. Some assumptions that have been made to simplify the above equation will be discussed as follows:

- The term $\nabla.\left[\overline{\mathbf{q}} - \tilde{\mathbf{q}}\right]$ is a result of non-linearity inherent in the heat flux term. Proceeding in a similar fashion of the removal of the $(\overline{\boldsymbol{\sigma}} - \tilde{\boldsymbol{\sigma}})$ term in the filtered momentum equation, an identical assumption can be made to neglect its contribution [69].
- The term $\nabla.\left[\bar{\rho}\mathrm{C_P}\left(\widetilde{\mathrm{T}\mathbf{u}} - \tilde{\mathrm{T}}\tilde{\mathbf{u}}\right)\right]$ is equal to the divergence of the SGS heat flux, $\mathbf{q}_{SGS}$ [66]. The approach normally taken to modeling $\mathbf{q}_{SGS}$ is based upon the premise that the energy transfer from resolved to unresolved turbulence scales is proportional to the GS temperature, $\tilde{\mathrm{T}}$ [70] and is modeled as

  $$\mathbf{q}_{SGS} = -\bar{\rho}\alpha_{SGS}\nabla\tilde{h}\,, \quad (3.31)$$

  where α_{SGS} is the subgrid scale thermal diffusion coefficient and can be defined as

  $$\alpha_{SGS} = \frac{\nu_{SGS}}{\mathrm{Pr}_{SGS}}, \quad (3.32)$$

  where ν_{SGS} and Pr_{SGS} are the subgrid scale kinematic viscosity and Prandtl number, respectively. The modeling of ν_{SGS} is connected to $\boldsymbol{\tau}_{SGS}$ models and

will be discussed in the subsequent section. Pr_{SGS} can be acquired either dynamically or it can be set to a constant value [70]. The range of values chosen for a fixed Pr_{SGS} is [0.3,0.9] [68]. The present work utilized a fixed value of 0.9 for Pr_{SGS}.

- The velocity pressure gradient term $[\overline{\mathbf{u}.\nabla \mathrm{p}} - \tilde{\mathbf{u}}.\nabla\bar{\mathrm{p}}]$, can be decomposed into SGS pressure dilatation and temperature flux terms [66]. The mathematics is as follows and is based on the derivation in :

$$\overline{\mathbf{u}.\nabla \mathrm{p}} = \nabla.\overline{\mathrm{p}\mathbf{u}} - \overline{\mathrm{p}\nabla.\mathbf{u}} \tag{3.33}$$

$$= \nabla.\overline{\rho R T \mathbf{u}} - \overline{\mathrm{p}\nabla.\mathbf{u}} \tag{3.34}$$

$$= \nabla.\bar{\rho}R\widetilde{\mathrm{T}}\tilde{\mathbf{u}} + \nabla.\bar{\rho}R\left(\widetilde{\mathrm{T}\mathbf{u}} - \widetilde{\mathrm{T}}\tilde{\mathbf{u}}\right) - \overline{\mathrm{p}\nabla.\mathbf{u}} \tag{3.35}$$

$$= \tilde{\mathbf{u}}.\nabla\bar{\mathrm{p}} + \bar{\mathrm{p}}\nabla.\tilde{\mathbf{u}} + \nabla.\bar{\rho}R\left(\widetilde{\mathrm{T}\mathbf{u}} - \widetilde{\mathrm{T}}\tilde{\mathbf{u}}\right) - \overline{\mathrm{p}\nabla.\mathbf{u}} \tag{3.36}$$

$$[\overline{\mathbf{u}.\nabla \mathrm{p}} - \tilde{\mathbf{u}}.\nabla\bar{\mathrm{p}}]$$

$$= \nabla.\bar{\rho}R\left(\widetilde{\mathrm{T}\mathbf{u}} - \widetilde{\mathrm{T}}\tilde{\mathbf{u}}\right) - [\bar{\mathrm{p}}\nabla.\tilde{\mathbf{u}} - \overline{\mathrm{p}\nabla.\mathbf{u}}]\,. \tag{3.37}$$

The SGS temperature flux term, $\bar{\rho}R\left(\widetilde{\mathrm{T}\mathbf{u}} - \widetilde{\mathrm{T}}\tilde{\mathbf{u}}\right)$ can be combined with $\bar{\rho}\mathrm{C_P}\left(\widetilde{\mathrm{T}\mathbf{u}} - \widetilde{\mathrm{T}}\tilde{\mathbf{u}}\right)$ to model the SGS heat flux as a whole in the following manner [71]:

$$\bar{\rho}\mathrm{C_V}\left(\widetilde{\mathrm{T}\mathbf{u}} - \widetilde{\mathrm{T}}\tilde{\mathbf{u}}\right) = \bar{\rho}\mathrm{C_P}\left(\widetilde{\mathrm{T}\mathbf{u}} - \widetilde{\mathrm{T}}\tilde{\mathbf{u}}\right) - \bar{\rho}R\left(\widetilde{\mathrm{T}\mathbf{u}} - \widetilde{\mathrm{T}}\tilde{\mathbf{u}}\right), \tag{3.38}$$

where $\mathrm{C_V}$ is the specific heat at constant volume. We can define the SGS temperature flux as

$$\mathbf{Q} = \bar{\rho}\left(\widetilde{\mathrm{T}\mathbf{u}} - \tilde{\mathrm{T}}\tilde{\mathbf{u}}\right) \quad (3.39)$$

and the SGS heat flux can be expressed as

$$\mathbf{q}_{SGS} = \nabla.\mathrm{C_V}\mathbf{Q}\,. \quad (3.40)$$

The simplest approach employed to modeling $\mathbf{q}_{SGS}$ was given in Eq.3.* and that is the formulation implemented in the current work.

Pressure dilatation is largely due to compressibility effects, i.e., heating due to compression. As a result, this term can be neglected given the flow regime considered in this thesis. Moreover, previous efforts have indicated that at low Mach numbers, this term can be ignored [72] , [73].

- The fourth SGS term in the Favre-filtered enthalpy equation, $[\overline{\boldsymbol{\sigma}:\nabla\mathbf{u}} - \tilde{\boldsymbol{\sigma}}:\nabla\tilde{\mathbf{u}}]$, is subgrid scale viscous dissipation and while on this topic, it will be appropriate to discuss the resolved scale viscous dissipation term $\tilde{\boldsymbol{\sigma}}:\nabla\tilde{\mathbf{u}}$ as well. Viscous dissipation is essentially viscous heating; the kinetic energy of the flow is deformed and brought to a rest, thereby increasing the internal energy of flow. It can be safely assumed that the effects of viscous heating will be quite pronounced near solid boundaries. Furthermore, this profound heating attributed to viscous dissipation is significant in high speed compressible boundary layer flows [74], such as the re-entry of a space shuttle or rocket into the earth's atmosphere. However, viscous heating and natural convection effects are seldom of the same of order of magnitude simultaneously [75]. In the present work, an assumption was made that the viscous heating was negligible to the heat release rate of the hot wall. To that

effect, both the GS and SGS viscous dissipation terms were neglected in the current work.

To summarize, the Favre-filtered differential equations with the proposed assumptions for the conservation of momentum and energy, respectively are:

$$\frac{\partial \bar{\rho}\tilde{\mathbf{u}}}{\partial t} + \nabla.\bar{\rho}\tilde{\mathbf{u}}\tilde{\mathbf{u}} - \nabla.\tilde{\boldsymbol{\sigma}} = -\nabla\bar{\mathrm{p}} + \bar{\rho}\mathbf{g} - \nabla.\boldsymbol{\tau}_{SGS} \tag{3.41}$$

$$\frac{\partial \bar{\rho}\tilde{h}}{\partial t} + \nabla.\bar{\rho}\tilde{h}\tilde{\mathbf{u}} - \frac{\partial \bar{\mathrm{p}}}{\partial t} - \tilde{\mathbf{u}}.\nabla\bar{\mathrm{p}} + \nabla.\tilde{\mathbf{q}} = -\nabla.\mathbf{q}_{SGS}\,, \tag{3.42}$$

where further simplifications made to the filtered energy equation pertaining to the pressure terms will be discussed in the subsequent chapter.

We can re-write the filtered momentum equation by introducing an effective dynamic viscosity as $\mu_{Eff} = \mu + \mu_{SGS}$ and upon substitution into Eq.3.41

$$\frac{\partial \bar{\rho}\tilde{\mathbf{u}}}{\partial t} + \nabla.\bar{\rho}\tilde{\mathbf{u}}\tilde{\mathbf{u}} - \nabla.\mu_{Eff}\left(\nabla\tilde{\mathbf{u}} + \nabla\tilde{\mathbf{u}}^{\mathrm{T}} - \frac{2}{3}\mathrm{tr}(\nabla\tilde{\mathbf{u}})\mathbf{I}\right) = -\nabla\bar{\mathrm{p}} + \bar{\rho}\mathbf{g}\,. \tag{3.43}$$

From the filtered momentum equation given in Eq.3.43, one can see that an assumption has been made to relate the SGS stress tensor to a SGS dynamic viscosity and the resolved strain rate tensor. The reasoning behind this newly developed equation will be expounded upon in the next section.

The Favre-filtered energy equation can be re-written by expanding and combining the resolved and subgrid scale heat flux vectors as follows:

$$\tilde{\mathbf{q}} = -\bar{\rho}\frac{\nu}{\mathrm{Pr}}\nabla\tilde{h}\,. \tag{3.44}$$

Inserting Eq.3.31 and Eq.3.44 into the filtered enthalpy equation results in

$$\frac{\partial \bar{\rho}\tilde{h}}{\partial t} + \nabla.\bar{\rho}\tilde{h}\tilde{\mathbf{u}} - \frac{\partial \bar{\mathrm{p}}}{\partial t} - \tilde{\mathbf{u}}.\nabla\bar{\mathrm{p}} = \nabla.\left(\bar{\rho}\left(\frac{\nu}{\mathrm{Pr}} + \frac{\nu_{SGS}}{\mathrm{Pr}_{SGS}}\right)\nabla\tilde{h}\right). \quad (3.45)$$

3.3 Sub-Grid Scale Stress Tensor Turbulence Models

The modeling of the SGS stress tensor term, $\boldsymbol{\tau}_{SGS}$, is of the utmost importance when compared to other subgrid scale terms since it is the only quantity modeled in the filtered incompressible Navier-Stokes equations. As such, considerable effort has been put forth by different researchers to formulate high fidelity SGS models: algebraic constant coefficient models [62], [76], dynamic models [77] and [78], and one equation models [79].

The majority of SGS stress tensor models are based upon the eddy viscosity concept, wherein the subgrid scale stress is expressed linearly in terms of the resolved velocity gradient and coefficients that depend on some defined flow characteristics [80]. The SGS stress tensor is modeled with the following mathematical expression:

$$\boldsymbol{\tau}_{SGS} = \underbrace{\boldsymbol{\tau}_{SGS} - \frac{1}{3}\mathrm{tr}(\boldsymbol{\tau}_{SGS})\mathbf{I}}_{deviatoric} + \underbrace{\frac{1}{3}\mathrm{tr}(\boldsymbol{\tau}_{SGS})\mathbf{I}}_{isotropic}, \quad (3.46)$$

where the SGS tensor is split into its deviatoric and isotropic parts. The isotropic part of the SGS stress tensor, $\mathrm{tr}(\boldsymbol{\tau}_{SGS})$, can either be modeled [81] or incorporated in the filtered pressure. The deviatoric part of the SGS stress tensor employing the eddy viscosity concept assumes that it is locally aligned with the deviatoric part of the resolved strain rate tensor [82] and reads as:

$$\boldsymbol{\tau}_{SGS}^{D} = -2\bar{\rho}\nu_{SGS}\left(\tilde{\mathbf{S}} - \frac{1}{3}\mathrm{tr}(\tilde{\mathbf{S}})\right). \quad (3.47)$$

This approach is based on the premise that is analogous to how molecular motion drains energy from the flow via the molecular viscosity. Therefore, it can be

supposed that the SGS motion extracts energy from the resolved turbulence scales via a subgrid scale viscosity, ν_{SGS} to emulate the energy drain associated with the dissipation of turbulent kinetic energy. Regarding the isotropic part of the SGS stress tensor, $\frac{1}{3}\mathrm{tr}(\boldsymbol{\tau}_{SGS})\mathbf{I}$, this quantity has been shown to be insignificant for low speed turbulent boundary layers [83]. Hence, its implementation will be neglected in this thesis.

In this section, we consider four SGS stress models: the Smagorinsky model, Wall-Adapting Local Eddy Viscosity (WALE) model, turbulent kinetic energy (K) equation model and locally dynamic Smagorinsky model (LDSMG).

3.3.1 Static Sub-Grid Scale Models

In the present section, we will consider SGS models that utilize constant coefficient in computing the subgrid scale viscosity. Such models typically employ some particular flow set-up to determine the optimum value for the constant and as a result, the constant will not be well suited the varying types of flows numerically solved using LES. To proceed, a discussion of the Smagorinsky and WALE SGS models will follow.

The Smagorinsky Model

The Smagorinsky model was formulated by assuming that the small scales are in equilibrium, i.e., all the energy received by these scales are instantaneously dissipated so that production and dissipation are balanced. This model gives the subgrid scale eddy viscosity as

$$\nu_{SGS} = (\mathrm{C_S}\Delta)^2\left|\tilde{\mathbf{S}}\right|, \qquad (3.48)$$

where C_S is the Smagorinsky constant, Δ is the filter width, which is proportional to the grid size and for an anisotropic grid, is defined as

$$\Delta = \left(\Delta_x \Delta_y \Delta_z\right)^{\frac{1}{3}}, \tag{3.49}$$

and $\left|\tilde{\mathbf{S}}\right|$ is the magnitude of the strain rate tensor given

$$\left|\tilde{\mathbf{S}}\right| = \sqrt{2\tilde{\mathbf{S}}:\tilde{\mathbf{S}}}\ . \tag{3.50}$$

Different values have been suggested to prescribe the Smagorinsky constant, C_S: for example, a value of 0.1 was suggested for turbulent channel flow [84] and value of 0.2 for isotropic turbulent flow [85]. A profound drawback of the Smagorinsky model is its inherent excessive dissipative behavior in regions of large strain, thereby causing unphysical damping of large scale turbulent motion [86]. In addition, due to the presence of the viscous sublayer in the wall region where turbulence should be essentially non-existent, ν_{SGS} should tend to zero. However, the Smagorinsky model does not give this behavior in the near-wall region and a damping function is typically employed in conjunction with this model to force ν_{SGS} to zero as the wall is approached [86]. The van Driest damping function [87], which is a function of the wall-normal distance, is normally utilized by multiplying it to C_S. Consequently, this function is unable to capture the cubic rate of decay of subgrid scale eddy viscosity at the wall [36].

WALE Model

To circumvent the shortcomings of the Smagorinsky model associated with approximating the subgrid scale viscosity using only the symmetric part of the velocity gradient tensor, **S**, the WALE model employs the anti-symmetric part of the velocity gradient as well. The anti-symmetric part, the rotation rate tensor, was

included so that in the region of large strain and/or rotation rate, the LES model can sufficiently capture the turbulence structures [88]. Moreover, the SGS model was shown to produce no subgrid scale viscosity in two dimensional laminar flows. As it pertains to the cubic rate decay of the eddy viscosity, the WALE model is able to recover this behavior without a damping function or dynamically computed coefficient [88]. The expression for ν_{SGS} reads as:

$$\nu_{SGS} = (\mathrm{C_W}\Delta)^2 \frac{\left(S_{ij}^d S_{ij}^d\right)^{\frac{3}{2}}}{\left(\widetilde{S_{\iota J}}\widetilde{S_{\iota J}}\right)^{\frac{5}{2}} + \left(S_{ij}^d S_{ij}^d\right)^{\frac{5}{4}}}, \tag{3.51}$$

where $\mathrm{C_W}$ is a model constant taken to be [0.55,0.60], S_{ij}^d is given by

$$S_{ij}^d = \widetilde{S_{\iota k}}\widetilde{S_{kJ}} + \widetilde{\Omega_{\iota k}}\widetilde{\Omega_{kJ}} - \frac{1}{3}\delta_{ij}\left[\widetilde{S_{mn}}\widetilde{S_{mn}} - \widetilde{\Omega_{mn}}\widetilde{\Omega_{mn}}\right]. \tag{3.52}$$

The strain rate tensor has been defined here in tensor notation as

$$\widetilde{S_{\iota J}} = \frac{1}{2}\left(\frac{\partial \widetilde{u_\iota}}{\partial x_j} + \frac{\partial \widetilde{u_J}}{\partial x_i}\right), \tag{3.53}$$

the rotation rate tensor, $\widetilde{\Omega_{\iota J}}$ is defined as

$$\widetilde{\Omega_{\iota J}} = \frac{1}{2}\left(\frac{\partial \widetilde{u_\iota}}{\partial x_j} - \frac{\partial \widetilde{u_J}}{\partial x_i}\right), \tag{3.54}$$

and δ_{ij} is the Kronecka delta, which is equal to 1 if $i = j$ and 0 otherwise.

K-Equation Model

As opposed to the Smagorinsky model, whereby an algebraic expression is derived to obtain the velocity scale utilized to describe the eddy viscosity by assuming the production and dissipation of small scales were balanced, the subgrid scale turbulent kinetic energy equation model solves a transport equation to calculate the velocity

scale. The transport equation can be derived by adopting the approach of [79]: subtract the product of filtered velocity and filtered momentum equation from filtered product of velocity and momentum. The resulting equation can be reduced and rearranged to acquire the $\bar{\rho}\mathrm{K}_{SGS}$ transport equation. Further simplification can be made [89] to obtain the following equation:

$$\frac{\partial \bar{\rho}\mathrm{K}_{SGS}}{\partial t} + \nabla.(\bar{\rho}\tilde{\mathbf{u}}\mathrm{K}_{SGS}) = \nabla.[\bar{\rho}(\nu + \nu_{SGS})\nabla\mathrm{K}_{SGS}] - \epsilon - P\,, \qquad (3.55)$$

where the three terms on the right-hand-side of the Eq.3.55, represent, respectively, the diffusion, dissipation and production of $\bar{\rho}\mathrm{K}_{SGS}$. The dissipation of subgrid scale turbulent kinetic energy, ϵ, can be modeled as

$$\epsilon = \frac{C_\epsilon \bar{\rho}\mathrm{K}_{SGS}^{\frac{3}{2}}}{\Delta}\,, \qquad (3.56)$$

where the dissipation term model coefficient, $C_\epsilon = 1.048$. The subgrid scale viscosity for the K equation model reads as

$$\nu_{SGS} = C_k \Delta \mathrm{K}_{SGS}^{\frac{1}{2}}\,, \qquad (3.57)$$

where the $C_k = 0.094$. The production term, P, is mathematically expressed as

$$P = \boldsymbol{\tau}_{SGS} : \tilde{\mathbf{S}}\,. \qquad (3.58)$$

3.3.2 Dynamic Sub-Grid Scale Models

It would be rather challenging to effectively apply the constant coefficient SGS model to the wide range of turbulent flows. The model coefficients can be calculated as part of the turbulence simulation instead of as a priori input. Such a dynamic procedure ensures that the coefficient is directly approximated by the local transient flow conditions. Local flows condition that constant coefficient SGS model cannot capture

is the backscatter phenomenon [90] whereby the spectral energy transfer is from small to the large scales. This phenomenon will result in a local negative value for ν_{SGS} which the Smagorinsky and similar SGS models cannot compute.

To formally describe the dynamic procedure, a second, coarser spatial filter or "test filter" is applied to the filtered equations of motions. The test filter width is usually defined as $\hat{\Delta}= 2\Delta$; the caret $\left(\widehat{\ }\right)$ will henceforth denote the test filter. The subtest stress term **T** that emerges subsequent to the application of the test filter to the already filtered governing differential equations is given by

$$\mathbf{T} = \hat{\bar{\rho}}\left(\widehat{\tilde{\mathbf{u}}\tilde{\mathbf{u}}} - \hat{\tilde{\mathbf{u}}}\hat{\tilde{\mathbf{u}}}\right) \tag{3.59}$$

$$\approx \hat{\bar{\rho}}\widehat{\tilde{\mathbf{u}}\tilde{\mathbf{u}}} - \frac{\hat{\bar{\rho}}\hat{\tilde{\mathbf{u}}}\hat{\bar{\rho}}\hat{\tilde{\mathbf{u}}}}{\hat{\bar{\rho}}}. \tag{3.60}$$

Recall that the SGS stress term was given as

$$\boldsymbol{\tau}_{SGS} = \bar{\rho}(\widehat{\tilde{\mathbf{u}}\tilde{\mathbf{u}}} - \tilde{\mathbf{u}}\tilde{\mathbf{u}}) \tag{3.61}$$

$$= \bar{\rho}\widehat{\tilde{\mathbf{u}}\tilde{\mathbf{u}}} - \frac{\bar{\rho}\tilde{\mathbf{u}}\bar{\rho}\tilde{\mathbf{u}}}{\bar{\rho}} \tag{3.62}$$

and an expression for the Leonard stress, **L**, can be mathematically stated using the Germano identity [91] and adopting the approach of [92]:

$$\mathbf{L} = \mathbf{T} - \widehat{\boldsymbol{\tau}_{SGS}} \tag{3.63}$$

$$= \left(\frac{\hat{\bar{\rho}}\widehat{\tilde{\mathbf{u}}\bar{\rho}\tilde{\mathbf{u}}}}{\bar{\rho}}\right) - \frac{\hat{\bar{\rho}}\hat{\tilde{\mathbf{u}}}\hat{\bar{\rho}}\hat{\tilde{\mathbf{u}}}}{\hat{\bar{\rho}}} \tag{3.64}$$

$$= \left(\hat{\bar{\rho}}\widehat{\tilde{\mathbf{u}}\tilde{\mathbf{u}}}\right) - \frac{1}{\hat{\bar{\rho}}}\left(\hat{\bar{\rho}}\hat{\tilde{\mathbf{u}}}\hat{\bar{\rho}}\hat{\tilde{\mathbf{u}}}\right). \tag{3.65}$$

The Leonard stress defined for the dynamic procedure is basically the contribution to the Reynolds stresses by turbulence scales intermediate between the grid filter and test filter scales. To proceed, we can suppose that $\mathbf{T}$ and $\boldsymbol{\tau}_{SGS}$ can be modeled with the same constant, C_d for both filtering levels, by defining a general eddy viscosity model as follows:

$$\boldsymbol{\tau}_{SGS} = -2C_d\boldsymbol{\alpha} \tag{3.66}$$

$$\mathbf{T} = -2C_d\boldsymbol{\beta}\,, \tag{3.67}$$

where $\boldsymbol{\alpha}$ and $\boldsymbol{\beta}$ are the resolved fields at the subgrid scale and subtest filter scale, respectively. Eqs.3.66 and 3.67 can be substituted into Eq.3.63 and the following expression emerges

$$\mathbf{L} = -2C_d\mathbf{M}\,, \tag{3.68}$$

where $\mathbf{M} = \boldsymbol{\beta} - \widehat{\boldsymbol{\alpha}}$. Since Eq.3.68 is an over-determined system, i.e. more equations than unknowns, the method of least squares proposed by Lilly [77] to minimize the error $\mathbf{E}$ from the approximation of C_d can be found via

$$\mathbf{E} = \mathbf{L} + 2C_d\mathbf{M}\,. \tag{3.69}$$

The least squares approach can be formally implemented, resulting in

$$\frac{\partial\langle\mathbf{E}\colon\mathbf{E}\rangle}{\partial C_d} = 2\,\langle\mathbf{E}\colon\frac{\partial\mathbf{E}}{\partial C_d}\rangle = 0\,, \tag{3.70}$$

and substituting Eq.3.69 into Eq3.70 gives the following expression:

$$4\langle(\mathbf{L} + 2C_d\mathbf{M})\colon\mathbf{M}\rangle = 0 \tag{3.71}$$

$$C_d = -\frac{1}{2}\frac{\langle\mathbf{L}\colon\mathbf{M}\rangle}{\langle\mathbf{M}\colon\mathbf{M}\rangle} \tag{3.72}$$

where the ⟨ ⟩ denotes some ensemble average. The ensemble averaging procedure is required to avoid excessively large fluctuations of the coefficient [77] that can otherwise destabilize the numerical simulation. The averaged least squares approach of [77] has been able to improve upon earlier dynamic models that suffered from spuriously large and negative eddy viscosity. Several dynamic models have attempted to resolve this problem; one of these SGS model [86], recommended averaging the dynamic coefficient in all homogeneous directions. Such a suggested SGS model is only feasible for homogeneous turbulence flows.

To this end, it is appropriate to note that the advent of dynamic SGS models have caused marked progress in the modeling of turbulent boundary layers, especially transitional flows. Dynamic models are able to automatically reduce the coefficient in high shear and near wall regions; moreover, the eddy viscosity is "driven" to zero in the laminar flow region without the need of a damping function usually required in static SGS models.

Dynamic Smagorinsky Model

Let us introduce the dynamic procedure to the Smagorinsky model employing just the deviatoric parts of the stress tensor and recalling that

$$\boldsymbol{\tau}_{SGS} - \frac{1}{3}\mathrm{tr}(\boldsymbol{\tau}_{SGS})\mathbf{I} = -2C_d\Delta^2\bar{\rho}|\tilde{\mathbf{S}}|\left(\tilde{\mathbf{S}} - \frac{1}{3}\mathrm{tr}(\tilde{\mathbf{S}})\mathbf{I}\right) \tag{3.73}$$

We can proceed to respectively define $\boldsymbol{\alpha}$ and $\boldsymbol{\beta}$ as:

$$\boldsymbol{\alpha} = \Delta^2\bar{\rho}|\tilde{\mathbf{S}}|\left(\tilde{\mathbf{S}} - \frac{1}{3}\mathrm{tr}(\tilde{\mathbf{S}})\mathbf{I}\right) \tag{3.74}$$

$$\boldsymbol{\beta} = \widehat{\Delta^2}\hat{\bar{\rho}}\left|\widehat{\tilde{\mathbf{S}}}\right|\left(\hat{\tilde{\mathbf{S}}} - \frac{1}{3}\mathrm{tr}\left(\hat{\tilde{\mathbf{S}}}\right)\mathbf{I}\right) \tag{3.75}$$

and with quantities **L**, $\boldsymbol{\alpha}$ and $\boldsymbol{\beta}$ defined, the dynamic Smagorinsky coefficient C_d can be easily computed. In this thesis, subsequent to the computation of the dynamic coefficient, this quantity was locally averaged to smooth out the potentially large fluctuations. Following the local averaging of C_d, backscatter was enabled by allowing the SGS viscosity to acquire a minimum value of $-\nu$.

3.3.3 Choice of SGS Model

The locally dynamic Smagorinsky LES model will be primarily employed throughout this thesis. Aside from its well-known ability to accurately capture the correct near-wall behavior for the SGS viscosity, it also enables the back-scatter phenomenon that often occurs in transitional boundary layers. Hence, since all the test cases in this research effort comprises laminar to turbulent boundary layer transition, the dynamic model will be best suited to capture the expected physics with relatively high fidelity.

3.4. Wall Layer Treatment in LES

To mitigate the computational expense of resolving the viscous sublayer in an LES calculation, many different approaches are currently in use to approximate the near wall region. The discussion put forth on wall layer treatments is not meant to be exhaustive and comprehensive; the wall layer treatments discussed are those that have bearing on the current work and some of the wall models are directly relevant to the approach utilized over the course of this research. To proceed, we will consider primarily equilibrium wall models, whereby the core assumption is that the wall stress and wall heat flux are in some kind of average or instantaneous equilibrium.

Moreover, it is appropriate to note that most of the wall layer models implemented in LES are based upon Reynolds-Averaged equations. The justification is that near-wall turbulent structures go through several life cycles and the simulation time-step is typically too large to capture the transient evolution of these structures. Hence, as long as the near-wall grid size is sufficiently coarse to comprise a sufficiently large sample of near-wall turbulent structures, we can reasonably assume that only the average effect or evolution of the eddies is captured at each computational time-step.

3.4.1 Wall Layer Models (Forced Convection)

In this section, we present some of the well-known wall layer models employed in LES for momentum driven flows. These models approximate the wall stress by correcting the velocity gradient at the wall; subsequently, the corrected wall stress can be utilized to recalculate the wall heat flux for forced convection flows with heat transfer.

Standard Momentum Wall Model

The boundary layer region according to [63] can be separated into the viscous, buffer and inertial sublayers. The viscous layer being a region that turbulence fluctuations are essentially damped and the majority of the stress is attributable to viscous effects. The viscous sublayer is a very thin region next to the wall and diminishes as the Reynolds number increases. The approximate boundary condition for viscous sublayer reads as

$$U^+ = y^+, \;\; 0 < y^+ < 5 \qquad (3.76)$$

with $U^+ = \mathrm{U}/u_\tau$, $y^+ = y u_\tau/\nu$, $u_\tau = \sqrt{\tau_w/\rho}$ (friction velocity), while U is the velocity at the first grid node off the wall and $\tau_w = \mu \partial \mathrm{U}/\partial y|_w$. The buffer layer, a

region where viscous and turbulence transport are both significant, lies within $5 < y^+ < 30$ and there isn't an explicit approximated boundary condition expression for it. The inertial sublayer, also referred to as the logarithmic layer, is a region near the wall where turbulence transport dominates. The approximated boundary condition, widely known as the logarithmic law of the wall, is given by:

$$U^+ = \frac{1}{\kappa} ln(y^+) + C, \;\; 30 < y^+ < 200\,, \tag{3.77}$$

with the constants κ and C are 0.41 and 5.3, respectively. The utilization of the logarithmic law of the wall places the restriction of having the first grid node off the wall at $y^+ \geq 30$. To circumvent this restriction, a unified law of the wall which fitted the viscous, buffer and inertial sublayers into one equation iteratively solvable for the wall shear stress can be employed. The unified law, known as Spalding's law [93] is given by

$$y^+ = U^+ + \exp(-\kappa C)\left(\exp(\kappa U^+) - 1 - \kappa U^+ - \frac{(\kappa U^+)^2}{2!} - \frac{(\kappa U^+)^3}{3!}\right). \tag{3.78}$$

The unified law prevents the restriction of placing the first grid node off the wall at $y^+ \geq 30$, thus enabling the usage of the same wall function by simply refining the mesh locally in the wall-normal direction to place nodes in the buffer layer. The limitations of the approximated boundary conditions given are the absence of pressure gradient effects and the assumption that the wall stress is constant in the region adjacent to the wall.

Standard Thermal Wall Model

Approximate boundary conditions similar to those given for the standard momentum wall models can be prescribed for the thermal viscous and inertial sublayers. The streamwise momentum and energy equations governing the near-wall region for forced convection boundary layer are given in Eqs.3.79 and 3.80. Upon inspection of these two equations, it is apparent their structures are vastly similar. Hence, one can contend that if the molecular and turbulent Prandtl numbers are ≈ 1.0, i.e., momentum and heat diffuses through the fluid at the same rate, the thermal and velocity profiles near the wall will be identical. With the use of the Reynolds analogy, which attempts to draw similarities between momentum and energy transfer and supposes that the turbulent momentum diffusivity and turbulent thermal diffusivity are equal, so that the turbulent Prandtl number $Pr_t = \nu_t/\alpha_t = 1.0$.

$$0 = \frac{\partial}{\partial y}\left(\nu \frac{\partial \mathrm{U}}{\partial y} - \overline{\mathrm{u'v'}}\right), \tag{3.79}$$

$$0 = \frac{\partial}{\partial y}\left(\alpha \frac{\partial \mathrm{T}}{\partial y} - \overline{\mathrm{v't'}}\right). \tag{3.80}$$

The thermal wall model comprises a linear law where molecular transport dominates and a logarithmic law where turbulence transport dominates and has the following form:

$$\Theta^+ = \begin{cases} Pr y^+ & y^+ < y_T^+ \\ Pr_t \left[\frac{1}{\kappa} ln(E y^+) + \boldsymbol{P_J}\right] & y^+ > y_T^+ \end{cases}, \tag{3.81}$$

where E is a model constant typically equal to 9.8, $\boldsymbol{P_J}$ is the computed by using a formula acquired from pipe flow measurements [94] as:

$$\boldsymbol{P_J} = 9.24\left[\left(\frac{Pr}{Pr_t}\right)^{3/4} - 1\right]\left(1 + 0.28exp\left(\frac{-0.007Pr}{Pr_t}\right)\right) \qquad (3.82)$$

and is essentially a measure of resistance to heat transfer across the thermo-viscous sublayer [95]. The non-dimensional temperature Θ^+, is given as:

$$\Theta^+ = \frac{(T_w - T_0)\rho C_P u_\tau}{q_w}, \qquad (3.83)$$

where $T_w - T_0$ is the temperature difference between the isothermal wall and the temperature at the first computational node off the wall, C_P is the specific heat at constant pressure of the fluid, and q_w is the wall heat flux. The parameter y_T^+ is taken to be the normal distance from the wall where the values of Θ^+ predicted by the linear and log laws given in Eq.3.81 equalize.

Deardoff Wall Model

A wall model implemented for LES of wall bounded turbulent flow at infinite Reynolds number was introduced [96], by prescribing the second derivatives of the streamwise and spanwise velocities at the first grid node from the wall in addition to a zero penetration velocity as:

$$\frac{\partial^2 \tilde{u}}{\partial y^2} = -\frac{1}{\kappa y_0^2} + \frac{\partial^2 \tilde{u}}{\partial z^2}, \qquad (3.84)$$

$$\frac{\partial^2 \widetilde{w}}{\partial y^2} = \frac{\partial^2 \widetilde{w}}{\partial x^2}, \qquad (3.85)$$

with $\tilde{u}$ and $\widetilde{w}$ being the filtered streamwise and spanwise velocity components, respectively, while y_0 is the first off-wall grid node. The second derivative equation given in Eq.3.84 satisfy the logarithmic law of the wall in the mean at y_0. The wall

model was utilized to simulate infinite Reynolds number channel flow with some success; however, it is limited in that it is only applicable at infinite Reynolds number, meaning the effects of viscosity were neglected.

Schumann Wall Model

The wall model implemented by [97] assumed that the streamwise wall stress was in phase with the velocity at y_0. The boundary conditions were approximated as follows:

$$\tau_{xy,w}(x,z) = \frac{\langle \tau_w \rangle}{\langle \tilde{u}(x,y_0,z) \rangle} \tilde{u}(x,y_0,z)\,, \tag{3.86}$$

$$\tau_{zy,w}(x,z) = \nu_t \frac{\widetilde{w}(x,y_0,z)}{y_0}\,, \tag{3.87}$$

with $\tau_{xy}$and τ_{zy} being the streamwise and spanwise wall stress, respectively, while $\langle \quad \rangle$ denotes plane averaging. The plane averaged wall stress, $\langle \tau_w \rangle$, can be assigned a value equal to the prescribed pressure gradient for channel flows or calculated iteratively by imposing the constraint that $\langle \tilde{u}(x,y_0,z) \rangle$ satisfy the logarithmic law of the wall at y_0. The spanwise wall stress, τ_{yz}, was prescribed as a function of a constant turbulent viscosity, ν_t, and spanwise velocity at y_0. Since this model imposes the logarithmic law of the wall in the mean, y_0^+ has to be at least ≈ 30.

Shifted Wall Model

Schumann's wall model was modified [98] by moving the correlation point of the wall stress to instantaneous velocity downstream to account for the presence of inclined elongated turbulence structures near the wall. In addition, the spanwise wall stress was also modified to resemble that of Eq.3.87, as this boundary condition

enhanced the fidelity of the numerical predictions. The modified wall model is given by:

$$\tau_{xy,w}(x,z) = \frac{\langle \tau_w \rangle}{\langle \tilde{u}(x, y_0, z) \rangle} \tilde{u}(x + \Delta_s, y_0, z) \,, \tag{3.88}$$

$$\tau_{zy,w}(x,z) = \frac{\langle \tau_w \rangle}{\langle \tilde{u}(x, y_0, z) \rangle} \tilde{w}(x + \Delta_s, y_0, z), \tag{3.89}$$

with Δ_s being the downstream displacement and its optimum value can be acquired with experimental or DNS data [99], to be approximately $\Delta_s = (|y_0|)\cot(8^0)$ for $30 < y_0^+ < 50 - 60$ and $\Delta_s = (|y_0|)\cot(13^0)$ for $y_0^+ > 60$. It should be noted that the utilization of large near wells $(y_0^+ > 60)$ will be unable to capture the any of the near-wall turbulence structure dynamics.

3.4.2 Wall Layer Models (Natural Convection)

In contrast to forced convection wall models, the formulation of wall layer models for turbulent natural convection boundary layers is still in its developing stage. This is attributable to the different intricate physics entailed in the near-wall driven by buoyancy; as opposed to forced convection for which the constant wall stress assumption is somewhat valid near the wall; such a condition is non-existent in natural convection. Moreover, the lack of a logarithmic region for the velocity profile further complicates the development of well established natural convection wall models. We will consider some of the wall models that have been developed and established for natural convection turbulent wall flows. Hence, we are herein interested in equations of motion for turbulent natural convection flows. To proceed, we make the assumptions that all streamwise gradients are negligible; the wall normal

momentum equation is used to eliminate the pressure term in the streamwise direction and we assume constant properties with the exception of density in the buoyancy term, $\rho(\mathrm{T})$. The aforementioned assumptions reduce the equations of motion to

$$0 = \frac{\partial}{\partial y}\left(\nu\frac{\partial \mathrm{U}}{\partial y} - \overline{\mathrm{u'v'}}\right) + \mathrm{g}\beta(\mathrm{T} - \mathrm{T_{ref}}), \tag{3.90}$$

$$0 = \frac{\partial}{\partial y}\left(\alpha\frac{\partial T}{\partial y} - \overline{\mathrm{v't'}}\right). \tag{3.91}$$

George & Capp Wall Model (GC)

The wall model postulated by [100] was one of the pioneering wall functions for turbulent natural convection boundary layers on vertical surfaces. The GC model assumed the near wall region consisted of an inner layer (molecular and turbulent transport) and an outer layer where turbulent transport dominates; in addition, the GC model employed different characteristic temperature and velocity for the inner and outer layers. The inner and outer layers merge in the overlap layer; assuming that the temperature gradients from both sides are equal as they approach the overlap layer, the temperature profile in the overlap layer can be approximated as follows:

$$\Theta^{\times} = k_2 y^{\times\frac{-1}{3}} + A(Pr), \tag{3.92}$$

where $\Theta^{\times} = (T_0 - T_w)/T_I$, with T_I being the inner characteristic temperature defined as

$$T_I = \frac{\left(\frac{q_w}{\rho C_P}\right)^{3/4}}{(\mathrm{g}\beta\alpha)^{1/4}}. \tag{3.93}$$

The model constants, k_2 and A were later determined to be -4.2 and 5.0 respectively and $y^{\times} = y/\eta$, with η being the inner layer length scale and can be written as

$$\eta = \left(\frac{\mathrm{g}\beta q_w}{\rho C_P}\right)^{1/4}. \qquad (3.94)$$

Similarly, the velocity in the overlap layer can be approximated by matching the velocity gradients in the overlap layer. The approximated boundary condition yields

$$U^{\times} = k_1 y^{\times\frac{1}{3}} + B(Pr)\,, \qquad (3.95)$$

where $U^{\times} = \mathrm{U}/u_I$ and the characteristic velocity for the inner layer u_I is

$$u_I = \left(\frac{\mathrm{g}\beta\alpha\mathrm{q_w}}{\rho C_P}\right)^{1/4}. \qquad (3.96)$$

The constant k_1 was prescribed a value of 27 and B was an undetermined constant. The temperature profile in the thermo-viscous sublayer was easily attainable by integrating the near-wall region energy equation, Eq.3.91 and assuming the turbulent heat flux vanishes as the wall is approached. The resulting linear temperature profile is

$$\Theta^{\times} = -y^{\times}\,. \qquad (3.97)$$

The velocity profile in the thermo-viscous sublayer can be approximated by integrating Eq.3.90 twice and neglecting the $\overline{u'v'}$ term, the following equation is obtained:

$$U^{\times} = \frac{1}{Pr}\left[C_f y^{\times} - \frac{{C_H}^{-1}}{2} y^{\times 2} + \frac{y^{\times 3}}{6}\right], \qquad (3.98)$$

where the friction coefficient $C_f = \tau_w/\rho u_I^2$ and $C_H = T_I/(T_w - T_\infty)$.

The GC model approximate boundary conditions are able to capture the thermo-viscous sublayer with good fidelity; however, the temperature and velocity profiles were shown to deviate appreciably from experimental data at $y^{\times} > 3$. Hence, the GC model prevents the usage of larger wall-normal grid cells and this

contradictory to the essence of implementing approximate boundary conditions in wall bounded turbulent flows.

Hölling & Herwig Wall Model (BWF)

Utilizing an approach similar to the logarithmic law of the wall for forced convection, [101] formulated approximated boundary conditions for natural convection flows as $Gr \to \infty$. The temperature profile was acquired by assuming a two-layer structure in the near wall region, an inner layer where molecular and turbulent heat transport were significant and an outer layer that is dominated by turbulent heat transport. The inner and outer layers merge in an overlap layer whereby temperature gradients approaching the overlap layers from both sides should equal. To proceed, an approximate boundary condition for the temperature profile in the overlap layer is given by

$$\Theta^{\times} = Cln(y^{\times}) + D\,, \qquad 5 < y^{\times} < 200 \tag{3.99}$$

with *C* and *D* being 0.427 and 1.93, respectively. $y^{\times}$ is formally defined as

$$y^{\times} = \frac{y}{y_c}, \tag{3.100}$$

where y_c is expressed as

$$y_c = \frac{\mathrm{T}_c}{\left|\frac{\partial T}{\partial y}\right|_w}, \tag{3.101}$$

with T_c being the characteristic temperature and is thus defined as

$$T_c = \left(\frac{\alpha^2}{\mathrm{g}\beta}\left|\frac{\partial \mathrm{T}}{\partial y}\right|_w^3\right)^{1/4}, \tag{3.102}$$

where $\left|\frac{\partial T}{\partial y}\right|_w$ is the magnitude of the wall normal temperature gradient. The non-dimensional temperature, $\Theta^{\times}$ is given by

$$\Theta^{\times} = \frac{T_w - T_0}{T_c}, \tag{3.103}$$

where T_w is the wall temperature and T_0 is the temperature of the first grid node off the wall. The temperature profile in the thermo-viscous sublayer can be acquired by assuming the turbulent heat flux completely vanishes, resulting in the following equation:

$$\Theta^{\times} = y^{\times}, 0 < y^{\times} < 5. \tag{3.104}$$

The velocity profile in the viscous sublayer can be approximated by assuming velocity fluctuations are damped by the wall resulting in the non-linear boundary condition

$$U^{\times} = \frac{1}{6}y^{\times 3} - \frac{1}{2}\Theta_0^{\times}y^{\times 2} + \left.\frac{\partial U^{\times}}{\partial y^{\times}}\right|_w y^{\times}, \tag{3.105}$$

where the non-dimensional velocity $U^{\times} = \mathrm{U}/u_c$ and u_c is the characteristic velocity

$$u_c = \frac{\mathrm{g}\beta T_c^3}{\nu}\left|\frac{\partial T}{\partial y}\right|_w^{-2}. \tag{3.106}$$

The non-dimensional velocity gradient at the wall is represented by $\left.\frac{\partial U^{\times}}{\partial y^{\times}}\right|_w$ and $\Theta_0^{\times} = \left(T_w - T_{ref}\right)/T_c$, with T_{ref} taken to be the ambient temperature.

The velocity profile in the overlap layer can be acquired by neglecting viscous effects because they "fade" further away from the wall in Eq.3.90, assume an eddy viscosity closure for $-\overline{\mathrm{u}'\mathrm{v}'}$ and integrate twice to yield the following equation

$$U^{\times} = \frac{CPr}{Pr_t} y^{\times}(C[ln(y^{\times}) - 2] + D - \Theta_0^{\times}) + Eln(y^{\times}) + F\,, \qquad (3.107)$$

where E and F are assumed to be dependent upon $\left.\frac{\partial U^{\times}}{\partial y^{\times}}\right|_w$ only and are given by:

$$E = e1 \left.\frac{\partial U^{\times}}{\partial y^{\times}}\right|_w + e2 \qquad (3.108)$$

$$F = f1 \left.\frac{\partial U^{\times}}{\partial y^{\times}}\right|_w + f2. \qquad (3.109)$$

To fully determine the functions *E* and *F*, experimental velocity data was employed and *e*1, *e*2, *f*1 and *f*2 were found to be 0.49, -2.27, 1.28 and 1.28, respectively.

Kiš & Herwig Wall Model (KHWF)

Recently, results acquired from Direct Numerical Simulation were employed in formulating a new wall layer model by [102] . Outside of the thermo-viscous sublayer, an approximate boundary condition for the wall heat flux was postulated that combined a logarithmic and an error function as follows:

$$\begin{aligned} \Theta^{+} = {} & A_1 lny^{+} + \frac{A_2}{A_3}\frac{\sqrt{\pi}}{2} erf[A_3(lny^{+} - A_4)] \\ & + \Bigg[\Theta_0^{+} - A_1 lny_0^{+} \\ & - \frac{A_2}{A_3}\frac{\sqrt{\pi}}{2} erf[A_3(lny_0^{+} - A_4)] \Bigg] , y^{+} > y_0^{+} \end{aligned} \qquad (3.110)$$

where the model constants A_1, A_2, A_3 and A_4 respectively are 0.295, 0.8, 0.877 and 0.64. The edge of the thermo-viscous sublayer where the linear temperature profile

no longer holds is denoted by $y_0^+ = 0.5$ and the non-dimensional wall-normal distance y^+ is thus defined as

$$y^+ = \frac{y}{y_{co}}, \tag{3.111}$$

where y_{co} is the characteristic length for the temperature profile given by

$$y_{co} = \frac{T_c}{\left|\frac{\partial T}{\partial y}\right|_w}, \tag{3.112}$$

with T_c similarly defined as in the BWF wall model. The logarithmic and error function terms seen in Eq.3.110 is a result of $y^+ \frac{\partial \Theta^+}{\partial y^+}$ almost perfectly approaching a probability density functional form with increasing Grashof number; thus, integrating $y^+ \frac{\partial \Theta^+}{\partial y^+}$ led to the combination of the logarithmic and error functions. The KHWF model integrates the time-averaged momentum equation twice and the velocity profile outside the thermo-viscous sublayer was formulated using DNS data. The wall model for the velocity profile is thus:

$$\begin{aligned} u^\times = y^\times - \frac{1}{4} y^{\times 2} & \\ + \frac{K_g}{K_u^2} \frac{\partial \mathrm{U}}{\partial y}\bigg|_w^{-2} & \left[F(y^\times y_c) - F(y_0^+) \right. \\ \left. + \frac{1}{6} y_0^{+3} \right] & \left(K_g \left| \frac{\partial \bar{\theta}}{\partial y} \right|_w \right)^{1/4} \\ + \frac{K_g}{K_u^2} \frac{\partial \mathrm{U}}{\partial y}\bigg|_w^{-2} & \left[G(y^\times y_{cu}) - G(0) \right], \; y^+ > y_0^+ , \end{aligned} \tag{3.113}$$

with $K_g = GrPr^2$, $K_u = Pr$, $u^\times = \mathrm{U}/u_c$, while the characteristic velocity u_c is given by

$$u_c = \frac{K_u}{K_g}\left|\frac{\partial \mathrm{U}}{\partial y}\right|_w^2 u_{ref}\,, \tag{3.114}$$

$\left|\frac{\partial \mathrm{U}}{\partial y}\right|_w$ is the magnitude of the time-averaged velocity gradient at the wall, $\left|\frac{\partial \bar{\theta}}{\partial y}\right|_w$ is the time-averaged non-dimensional wall temperature gradient, with $\theta = (T - T_m)/\Delta T$, $T_m = (T_h - T_c)/2$ and $\Delta T = T_h - T_c$. T_h and T_c are usually taken to be the wall and ambient temperatures, respectively. The reference velocity $u_{ref} = \alpha/L$, where L is the plate height, the non-dimensional wall-normal distance $y^{\times} = y/y_{cu}$, while y_{cu} is the characteristic length for the velocity profile defined as

$$y_{cu} = \frac{K_u}{K_g}\left|\frac{\partial \mathrm{U}}{\partial y}\right|_w L\,. \tag{3.115}$$

The ratio of velocity and temperature profiles characteristic length, y_c given in Eq.3.*, is $y_c = y_{cu}/y_{co}$. The functions F and G in the wall function for the velocity profile are formally given in Eq.3.115 and Eq.3.116 respectively as:

$$\begin{aligned} F(y^+) = \frac{1}{2}y^{+2}\left[ln\left(\frac{y^+}{y_0^+}\right) + y_0^+ - \frac{3}{2} + \mathrm{g}(y^+) - \mathrm{g}(y_0^+)\right] \\ - exp\left(A_4 + \frac{1}{4{A_3}^2}\right)y^+\mathrm{g}\left(y^+ exp\left(-\frac{1}{2{A_3}^2}\right)\right) \\ + exp\left(2A_4 + \frac{1}{{A_3}^2}\right)\mathrm{g}\left(y^+ exp\left(-\frac{1}{{A_3}^2}\right)\right), \end{aligned} \tag{3.115}$$

$$
\begin{aligned}
G(y) \equiv \int \overline{u'v'}\, dy \\
&= \frac{1}{2} a y^2 + by \\
&+ d\left[y - (y - y_{ip}) erf\left(c(y - y_{ip}) \right) \right. \\
&\left. - \frac{1}{c\sqrt{\pi}} exp\left(-\left[c(y - y_{ip}) \right]^2 \right) \right].
\end{aligned}
\tag{3.116}
$$

The function g in Eq.3.115 is mathematically expressed as

$$
\mathrm{g}(y^+) = \frac{A_2}{A_3} \frac{\sqrt{\pi}}{2} erf[A_3(lny^+ - A_4)] \,. \tag{3.117}
$$

It should be noted that a boundary condition for the turbulent shear stress $\overline{\mathrm{u'v'}}$ was included in the velocity profile to extend the applicability of the wall model. The constants *a*, *b*, *c*, *d* and y_{ip} respectively are:

$$
a = 0.3223 \left| \frac{\partial \bar{u}}{\partial y} \right|_w^{1.27} - 307.4519 \tag{3.118}
$$

$$
b = -0.0671 \left| \frac{\partial \bar{u}}{\partial y} \right|_w^{1.11} - 200.0 \left[1 - exp\left(-4.43 \times 10^{-3} \left| \frac{\partial \bar{u}}{\partial y} \right|_w^{0.7} \right) \right] \tag{3.119}
$$

$$
c = 8.1362 \left| \frac{\partial \bar{u}}{\partial y} \right|_w^{0.2} - 26.0223 \tag{3.120}
$$

$$
d = 0.0185 \left| \frac{\partial \bar{u}}{\partial y} \right|_w^{1.18} - 497.51 \left[1 - exp\left(-1.43 \times 10^{-3} \left| \frac{\partial \bar{u}}{\partial y} \right|_w^{0.8} \right) \right] \tag{3.121}
$$

$$y_{ip} = -9.560 \times 10^{-6} \left|\frac{\partial \bar{u}}{\partial y}\right|_w^{0.6} + 0.0188 \left[1 - exp\left(-4.49 \times 10^{-6} \left|\frac{\partial \bar{u}}{\partial y}\right|_w^{1.6}\right)\right] \quad (3.122)$$

The KHWF wall model is supposed to be a more robust boundary condition in comparison to the BWF wall model due to the "improved" approximation of the wall heat flux, q_w.

3.4.3 Wall Layer Models (Mixed Convection)

Approximate boundary conditions for wall bounded mixed convection turbulent flows are nearly non-existent. Being able to formulate a wall model that equally accounts for forced convection effects and the complex near-wall nature of natural convection flows has proved to be challenging. In the discussion that follows, the proposed mixed convection wall model of [103] will be introduced.

Balaji, Hölling & Herwig Wall Model (MCWF)

The mixed convection wall model blended the standard forced and natural convection wall functions by employing a blending parameter Υ to distinguish between forced, natural and mixed convection flow regimes. The blending parameter is essentially based upon local wall conditions and is defined as

$$\Upsilon = Pr^2 \frac{u_c}{u_\tau}, \quad (3.123)$$

with the characteristic velocities u_c and u_τ respectively repeated here for convenience

$$u_c = \frac{g\beta T_c^3}{\nu} \left|\frac{\partial T}{\partial y}\right|_w^{-2} \quad (3.124)$$

$$u_\tau = \sqrt{\frac{\tau_w}{\rho}}. \tag{3.125}$$

An inspection of the blending parameter illustrates that the forced convection flows in consideration have non-zero wall stress. The blending parameter becomes zero when the flow is purely forced convection. For strictly natural convection flows, the DNS data of [104] showed that the ratio of the characteristic velocities, $u_c/u_\tau = 0.58$, assuming $Pr = 0.7,\ \Upsilon = 0.284$. Hence, by non-dimensionalizing the blending parameter so that it varies between 0 and 1, we can subsequently characterize the different regimes of flow as:

$$\begin{cases} \xi = 0: forced\ convection \\ \xi = 1: natural\ convection \\ 0 < \xi < 1: mixed\ convection \end{cases} \tag{3.125}$$

To proceed with the blending of the wall functions, temperature and velocity profiles for natural convection were transformed into the coordinates employed for forced convection profiles. Upon transforming the BWF natural convection profiles, the following temperature profile in the overlap layer was acquired:

$$\Theta^+_{nat} = \frac{1}{Pr}\frac{u_\tau}{u_c}\left[Cln(y^+) - Cln\left(\frac{1}{Pr^2}\frac{u_\tau}{u_c}\right) + D\right] \tag{3.126}$$

The temperature profile in the overlap layer for forced convection has the form

$$\Theta^+_{for} = Pr_t\left[\frac{1}{\kappa}ln(Ey^+) + \boldsymbol{P_J}\right]. \tag{3.127}$$

To blend these two approximate boundary conditions, the MCWF wall model utilized in this thesis proceeded with the following approach:

$$\Theta^+_{mixed} = \Theta^+_{for}(1-\xi) + \Theta^+_{nat}\xi\ . \tag{3.128}$$

A similar approach can be employed to derive the mixed convection velocity profile U^+_{mixed}which was not given in the proposed mixed convection wall model. We can define the following velocity profile in the overlap layer by adopting the method utilized for the temperature profiles as

$$U^+_{mixed} = U^+_{for}(1-\xi) + U^+_{nat}\xi\,, \tag{3.129}$$

where the unified law will be used to define U^+_{for} as

$$U^+_{for} = y^+ - \exp(-\kappa C)\left(\exp\left(\kappa U^+_{for}\right) - 1 - \kappa U^+_{for} - \frac{\left(\kappa U^+_{for}\right)^2}{2!} - \frac{\left(\kappa U^+_{for}\right)^3}{3!}\right). \tag{3.130}$$

To transform the natural convection velocity profile into the appropriate units, let us repeat the BWF model velocity profile here explicitly:

$$U^\times = \frac{CPr}{Pr_t} y^\times (C[ln(y^\times) - 2] + D - \Theta_0^\times) + 0.49\frac{\partial U^\times}{\partial y^\times}\bigg|_w - 2.27ln(y^\times) + 1.28\frac{\partial U^\times}{\partial y^\times}\bigg|_w + 1.28.$$

Upon transforming the Eq.3.107 into the coordinates widely employed for forced convection flows, the resulting equation emerges:

$$U_{nat}^{+} = \frac{u_c}{u_\tau}\left[\frac{CPr}{Pr_t}y^{+}Pr^2\frac{u_c}{u_\tau}\left\{C\left(ln(y^{+}) - Cln\left(\frac{1}{Pr^2}\frac{u_\tau}{u_c}\right)\right) - 2 + D - \Theta_0^{+}Pr\frac{u_c}{u_\tau}\right\}\right] + \frac{u_c}{u_\tau}\left[0.49\frac{{u_\tau}^2}{{u_c}^2Pr^2}\frac{\partial U_{nat}^{+}}{\partial y^{+}}\bigg|_w - 2.27\left(ln(y^{+}) - Cln\left(\frac{1}{Pr^2}\frac{u_\tau}{u_c}\right)\right) + 1.28\frac{{u_\tau}^2}{{u_c}^2Pr^2}\frac{\partial U_{nat}^{+}}{\partial y^{+}}\bigg|_w + 1.28\right]. \quad (3.131)$$

3.4.4 Choice of Wall Layer Treatment

The turbulent boundary layer flowfields resolved in this thesis are primarily of the natural and mixed convection type. In the case of turbulent natural convection boundary layers and wall-layer modeling, it is essential to implement approximate boundary conditions that can reasonably correct the wall heat flux. This is because the corrected wall heat flux will be employed to correct the $\frac{\partial \mathrm{u}}{\partial y}\Big|_w$. Thus, in the forthcoming wall modeling LES computations that will be covered in later chapters, the BWF and ErfWF models will be appropriately applied to the purely natural convection turbulent flow. The ErfWF model is essentially a hybrid wall layer model that corrects the wall heat flux, q_w, using combined logarithmic and error functions of Eq.3.110 and feeding the corrected q_w into Eqs.3.107-109 to correct $\frac{\partial \mathrm{u}}{\partial y}\Big|_w$. The primary reason for implementing the ErfWF was due to unfavorable near-wall behavior observed with the use of Eq.3.113 given in the KHWF model. As it pertains to the mixed convection turbulent flows, the MCWF approximate boundary condition

will be applied for the near-wall region. This wall model is supposed to account for free and forced convection effects near the wall with the utilization of a local blending parameter dependent upon the wall shear stress and near-wall buoyancy effects.

3.5. Sources of Error in LES

The fidelity of turbulence simulations profoundly depends upon the ability of the CFD practitioner to minimize and control the numerical errors intrinsic to these computations. Although all computation of turbulence (RANS, LES or DNS) does involve numerical errors, some errors are quite particular to Large Eddy Simulation and we will consider what some of these errors are in this section. These errors are discretization, modeling and filtering errors; this discussion is by no means exhaustive and is meant to only give a "feel" for some of the errors that will be encountered by an LES practitioner.

Discretization Errors

As previously mentioned, it is widely accepted that turbulence computations of RANS, DNS or LES inherently possess discretization errors to some extent. But, discretization errors pertaining to Large Eddy Simulation are unique due to the presence of the SGS term. Typically, if the mesh resolution of the computational grid is increased, it ought to increase the fidelity of a turbulence simulation; this would be the case for a RANS or DNS calculation. This is quite the contrary for an LES computation. Increasing the spatial resolution makes the discretization errors increase faster than the SGS term as long as the grid cut-off lies in the inertial sub-range [105]. This is typically the case when an implicit filter is employed and the

discretization error can be larger than the SGS term [106]. To elaborate, consider two length scales, the filter width (Δ_f) and grid width (Δ_g). The common approach is to assume $\Delta_f = \Delta_g$, which is essentially the implicit filter. Now, if we expect to sufficiently capture the smallest resolved scales down to a pre-determined Δ_f , Δ_g has to be several times smaller than Δ_f [105]. Therefore it is preferred that $\Delta_g < \Delta_f$ and assuming $\Delta_f = \Delta_g$ means that the smallest resolved scales or marginal eddies will not be adequately represented on the computational mesh. Moreover, mesh refinement will result in more near-grid scales structures being exposed to this inaccuracy as long as the grid cutoff lies in the inertial range of the energy spectrum.

Modeling Errors

Modeling errors in Large Eddy Simulation can arise due to inaccuracies in models utilized to simulate the turbulence physics and improper implementation of boundary conditions. Some of these errors can be further elaborated upon and classified as subgrid scale anisotropy, subgrid scale back-scatter, and near-wall treatment. A discussion on each of these modeling errors follows:

- **Subgrid scale anisotropy:** The whole premise of Large Eddy Simulation is based upon an assumption that the small turbulence scales can be modeled because they are largely isotropic. Such an assumption dates back to Kolmogorov's postulate of local isotropy (PLI) [35]. The postulate basically states that as the Reynolds number approaches infinity, as the energy cascade from the large energy containing scales (geometry and boundary condition dependent) which are anisotropic, to the small scales, the directional information is lost and the small scales are locally isotropic independent of

viscosity. The local isotropic behavior is assumed to occur in the inertial subrange and statistical quantities are invariant with respect to coordinate axis reflection or rotation. As such, the filter cut off is typically prescribed to be in the inertial subrange so that the assumption of local isotropy can be employed for SGS models. However, a number of works [107] & [108] have indicated that the small turbulence scales are in fact anisotropic. It has been stated that the large scale anisotropies is persistent even at the small turbulence scales and that they actually decay much more slowly [109]. Therefore, these observations can potentially have profound bearing on the underlying assumption of SGS models utilizing the local isotropy of the small scales in the inertial and dissipation ranges. Commonly used SGS models do not account for anisotropic turbulence of the small scales and its inclusion in future models can possibly increase the fidelity of LES calculations.

- **Subgrid scale back-scatter:** The role of most SGS models is to drain energy from the large energy containing eddies or resolved scales and this role is meant to be dissipative. The cascade of energy from large to small scales can be termed forward-scatter and is typically duplicated by all subgrid models, some more than others. There is also a reverse phenomenon, back-scatter, whereby subgrid turbulence scales feed energy to the large resolved turbulence scales locally and intermittently [90]. The contribution of both the back-scatter and forward-scatter to the net SGS dissipation was found to be comparable. Moreover, it was suggested that back-scatter effects on the net SGS dissipation can be profound in the case that a wall model is employed to

resolve the near wall region [110], i.e. SGS effects become more profound as the grid resolution decreases. Since the physics of back-scatter is not well understood, there are not that many SGS models that are able to account for its effect.

- **Near-wall Treatment:** High fidelity calculations can be acquired with LES if the near wall region is adequately resolved [111]. However, resolving the wall region can be prohibitively costly when the Reynolds number becomes increasingly large; as Reynolds number increases, the viscous sublayer decreases and the length scales of vortical structures in the near-wall region scale with the viscous length scale. Moreover, beyond the viscous sublayer, the near wall eddies scale with the distance from the wall [112], but their length scales is limited by the viscous scales [113]. Hence, resolving the vortical structures in the near wall region at high Reynolds number is impractical because DNS level grid resolution will be required in the wall-normal and horizontal directions [113]. To circumvent the impracticality, the use of wall layer models to approximate the near-wall flow is typically implemented. But, the addition of wall modeling to an LES calculation comes with limitations and some degree of error as well. Firstly, the implementation of the wall layer model adds empiricism to the LES. Secondly, the utilization of a coarser mesh near the wall implies that the SGS model will have to account for more anisotropic flow behavior. The contribution of these two factors can potentially lead to errors that will corrupt the LES computation.

Filtering Errors

- **Aliasing Errors:** The context of including aliasing errors in the realm of filtering errors is not to imply that the filtering procedure directly induces aliasing, but that the commonly employed implicit filter is not conducive to mitigating aliasing errors. Aliasing errors emerge when nonlinear terms are computed numerically in physical space [114]. The contribution to aliasing errors by the bilinear products of the nonlinear terms in the filtered momentum equation, $\tilde{\mathbf{u}}\tilde{\mathbf{u}}$, is profound at the highest wavenumbers [115]. The bilinear product can result in the generation of high frequencies not resolvable on the computational mesh and can "fold over" into low resolved frequencies [116]. According to [116], one of the elements in the bilinear product has to be in the upper third of the wavenumber range for the product to alias and the aliasing error can be reduced or eliminated if the energy in the high wavenumber spectrum can be damped. However, the utilization of an implicit filter does not enable the damping of the energy in the high frequency portion of the spectrum since the filter is essentially the grid size [117]. We can consider the region near the wall that typically requires high spatial resolution in LES; using an implicit filter means that the high frequencies in the wavenumber spectrum are not filtered out of the simulation and will adversely affect the solution via aliasing errors. A way of circumventing this problem is to implement an explicit filter that is larger than the nominal grid size that will consequently remove or reduce the upper portion of the wavenumber spectrum [118]. Decoupling the filter width from the local grid size means

that as we continually refine an LES mesh, our filter width can remain constant. As such, a true LES computation can be performed. However, implementing an explicit filter would require some weighted averaging over neighboring cells [119] and can easily become computationally expensive and cumbersome. Moreover, there is a lack of straightforward and robust filtering procedure that can be utilized for wall bounded turbulent flows [120].

- **Commutation Errors:** The commutation with differentiation i.e. $\frac{\overline{\partial \bar{f}}}{\partial x} = \frac{\partial \bar{f}}{\partial x}$, is only satisfied when the filter width, Δ is homogeneous. LES computations that utilize an implicit filtering typically do not employ a uniform grid over the entire computational domain, especially in wall bounded flows. Since the grid size is essentially used as a filter when the implicit filtering approach is implemented for an LES calculation, the non-commutation of the filtering introduces additional terms in the LES governing equations known as the commutation error. A fairly elementary example will be given to illustrate the concept of the commutation error by performing the filtering of a quadratic polynomial as follows:

  Let us consider the quadratic polynomial $f(x) = a_1x^2 + a_2x + a_0$, where $a_1 = -1, a_2 = 0$ and $a_0 = 1$. Therefore,

  $$f(x) = -x^2 + 1, \qquad (3.132)$$

  and we can filter this function in one spatial dimension at computational nodes P and N and assume a constant filter width of 1 for both nodes:

$$\overline{f_P} = \frac{1}{\Delta}\int_{-1}^{0} f(x)dx = \frac{2}{3} \qquad (3.133)$$

$$\overline{f_N} = \frac{1}{\Delta}\int_{0}^{1} f(x)dx = \frac{2}{3}. \qquad (3.134)$$

To proceed, the gradient of the filter, $\frac{\partial \bar{f}}{\partial x}$ at x = 0 can be calculated along with the filter of the gradient, $\frac{\overline{\partial f}}{\partial x}$ at x = 0 as well.

$$\left.\frac{\partial \bar{f}}{\partial x}\right]_0 = \frac{\overline{f_N} - \overline{f_P}}{x_N - x_P} = 0 \qquad (3.135)$$

$$\left.\frac{\overline{\partial f}}{\partial x}\right]_0 = \frac{1}{\Delta}\int_{-0.5}^{0.5} \frac{\partial f(x)}{\partial x}dx = 0\,, \qquad (3.136)$$

where $\frac{\partial f(x)}{\partial x} = -2x$. It can be readily seen that $\frac{\overline{\partial f}}{\partial x} = \frac{\partial \bar{f}}{\partial x}$ when the filter width is homogeneous and the contrary will now be proven by filtering f(x) at node M with Δ_M=0.5 as follows:

$$\overline{f_M} = \frac{1}{\Delta_M}\int_{0}^{0.5} f(x)dx = \frac{11}{12} \qquad (3.137)$$

and re-computing $\left.\frac{\partial \bar{f}}{\partial x}\right]_0$ results in

$$\left.\frac{\partial \bar{f}}{\partial x}\right]_0 = \frac{\overline{f_M} - \overline{f_P}}{x_M - x_P} = \frac{1}{3}. \qquad (3.138)$$

The utilization of different filter widths clearly proves that the filtering operation does not commute with differentiation and we can define a measure for the commutation error by

$$\left[\frac{\partial \mathrm{f}}{\partial \mathrm{x}}\right]_{error} \equiv \frac{\overline{\partial \mathrm{f}}}{\partial \mathrm{x}} - \frac{\partial \bar{\mathrm{f}}}{\partial \mathrm{x}}. \qquad (3.139)$$

Hence, abrupt mesh refinement in LES would not be appropriate as this increasingly enhances the commutation error. If grid refinement changes smoothly and gradually, the commutation error can be kept to a minimum or approach zero.

3.6 Closing Remarks

This chapter has presented the commonly employed approaches to computing turbulent boundary layers together with the governing equations of fluid motion. The filtered LES equations and SGS models were introduced along with the various assumptions made to simplify the otherwise complex filtered momentum and energy equations. Instead of fully resolving the near-wall region in an LES computation, applicable wall layer models were presented. These models were shown to be a plausible approach to greatly reduce the computational cost associated with fully resolved LES calculations. Furthermore, though the accuracy of the numerical simulation will diminish to some degree, the achievable fidelity with the implementation of wall layer models deems it an attractive option for full-scale engineering calculation. Lastly, possible sources of error in LES computations were discussed as well. This is of prime importance to the LES practitioner, as it will be profoundly beneficial to be aware of the errors that can possibly corrupt the numerical

simulation. With the awareness of these errors, it is quite possible they can be mitigated during the computational setup process.

Chapter 4: Computational Methodology

4.1 Discretization Practices

The mathematical equations given in the previous chapter cannot be readily solved as is. The governing differential equations have to be transformed into algebraic system of equations that can be solved on a computer and this is the essence of discretization practices. The discretization process, according to [121], consists of discretizing the computational domain and governing transport equations.

Careful consideration must be given to choosing a discretization method. The discretization method greatly impacts the approximated discrete algebraic equations and the discretized solution domain. Prevalently employed discretization methods include the finite difference (FD), finite volume (FV), and finite element (FE) methods.

Finite Difference Discretization

Finite difference discretization approach utilizes the differential form of the conservation equations to formulate discrete algebraic equations. The discrete algebraic equations are acquired using truncated Taylor series expansion or

polynomial fitting of the first and second derivatives of the governing differential equations at each grid point.

Finite difference methods are typically employed for structured grids and it is relatively simple to obtain higher-order schemes [122], [123] and [124] . Some of the drawbacks of finite difference methods are its difficulty of use for complex geometries and conservation laws are not necessarily guaranteed to be conserved by numerical schemes.

Finite Volume Discretization

Finite volume (FV) discretization employs the integral form of the conservation equations to develop discrete algebraic equations for each cell center, which is the computational node. The discretization method divides the computational domain into non-overlapping control volumes (CV), whereby the conservation laws are met in a discrete manner.

As previously stated, the computational node is defined as the cell center of each control volume. The mesh for the solution domain only defines the boundary of each control volume which can either be a face, i.e. it is shared with a neighboring control volume or the boundary of the domain itself.

Finite volume discretization is suitable for structured and unstructured meshes because the computational mesh does not have to be aligned with any coordinate system; hence, they can be easily implemented to complicated geometries. However, acquiring numerical schemes higher than second order is typically challenging for 3D geometries attributable to the inherent need to integrate, interpolate, and differentiate

within finite volume methods. Nonetheless, finite volume discretization is a popularly used method due to the ease of implementation.

Finite Element Discretization

The Finite Element (FE) method is quite similar to FV discretization, the computational domain is divided into non-overlapping sub-volumes or finite elements. The distinguishing feature of the FE discretization is the introduction of a weight function. Prior to the integration of the conservation equations over the solution domain, they are multiplied by the weight function. The solution within each element is assumed to be of a linear shape function and such an assumption ensures there is continuity of the solution across element boundaries, i.e. differentiability. The linear shape function is normally similar to the weight function. Similarly to the FV discretization method, the FE method can be easily applied to arbitrary geometries.

4.1.1 Finite Volume Discretization of Computational Domain

The computational domain is discretized into a collection of non-overlapping sub-volumes. These sub-volumes, also referred to as control volumes, fill the entire computational domain and are generally convex polyhedral. Figure 4.1 depicts an arbitrary control volume bounded by a set of convex flat faces *f*, where the node *P* is the centroid and *N* is the centroid of the neighboring CV. Each face *f* of the control volume *P* has an outward pointing face normal area vector **S**. As is illustrated in Figure 4.1, even though the face f is shared between control volumes *P* and *N* , this face is owned by control volume *P*.

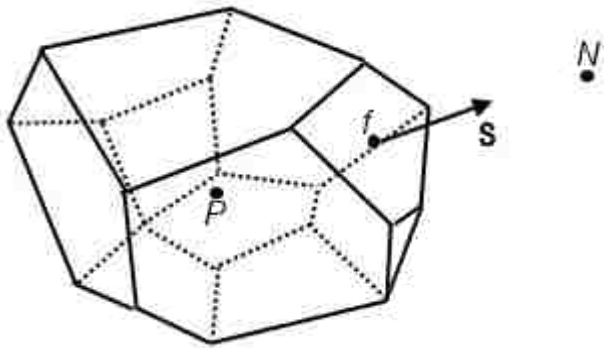

Figure 4. 1 An arbitrary control volume.

All the dependent variables of the transport equations are stored at the computational node *P* and since it was designated as the centroid of the control volume, the following equation holds:

$$\int_{V_P} (\mathbf{x} - \mathbf{x}_P)\, dV = 0\,. \tag{4.1}$$

To proceed, it will appropriate to note that the cell shapes employed in this research were primarily regular hexahedra.

4.1.2 Finite Volume Discretization of Transport Equations

The Favre-filtered equations of motion previously given will be restated here for convenience where the temporal derivative, convection and diffusion terms have been placed on the left hand side and the right hand side contains the remaining terms:

$$\frac{\partial \bar{\rho}}{\partial t} + \nabla . \bar{\rho}\tilde{\mathbf{u}} = 0\,,$$

$$\frac{\partial \bar{\rho}\tilde{\mathbf{u}}}{\partial t} + \nabla . \bar{\rho}\tilde{\mathbf{u}}\tilde{\mathbf{u}} - \nabla . \mu_{Eff}\left(\nabla\tilde{\mathbf{u}} + \nabla\tilde{\mathbf{u}}^{\mathrm{T}} - \frac{2}{3}\mathrm{tr}(\nabla\tilde{\mathbf{u}})\mathbf{I}\right) = -\nabla\bar{\mathrm{p}} + \bar{\rho}\mathbf{g}\ ,$$

$$\frac{\partial \bar{\rho}\tilde{h}}{\partial t} + \nabla.\bar{\rho}\tilde{h}\tilde{\mathbf{u}} - \nabla.\left(\bar{\rho}\left(\frac{\nu}{\mathrm{Pr}} + \frac{\nu_{SGS}}{\mathrm{Pr}_{SGS}}\right)\nabla\tilde{h}\right) = \frac{\partial \bar{\mathrm{p}}}{\partial t} + \tilde{\mathbf{u}}.\nabla\bar{\mathrm{p}} \ .$$

These equations can be put into a generic form of the conservation transport equation in differential form as:

$$\underbrace{\frac{\partial \rho\phi}{\partial t}}_{Temporal\ Derivative} + \underbrace{\nabla.(\rho\mathbf{u}\phi)}_{Convection} - \underbrace{\nabla.(\Gamma\nabla\phi)}_{Diffusion} = \underbrace{S(\phi)}_{Sources} . \qquad (4.2)$$

Before we proceed, a discussion is warranted on the treatment of the pressure term, $\bar{\mathrm{p}}$. Let us consider decomposing the pressure term by employing a similar procedure proposed by [125]; the pressure is split into a reference or ambient pressure, hydrostatic pressure and a "modified dynamic" pressure respectively, as follows:

$$\bar{\mathrm{p}} = \mathrm{p}_{ref} + \bar{\rho}\mathbf{g}.\mathbf{x} + \overline{\mathrm{p_d}} . \qquad (4.3)$$

This definition can be substituted into the pressure term in the filtered momentum equation and the resulting differential equation emerges

$$\nabla\bar{\mathrm{p}} = \nabla\mathrm{p}_{ref} + \nabla\bar{\rho}\mathbf{g}.\mathbf{x} + \nabla\overline{\mathrm{p_d}} \qquad (4.4)$$

$$\nabla\bar{\mathrm{p}} = \bar{\rho}\mathbf{g}\nabla\mathbf{x} + \mathbf{x}\nabla\bar{\rho}\mathbf{g} + \nabla\overline{\mathrm{p_d}} \qquad (4.5)$$

$$\frac{\partial \bar{\rho}\tilde{\mathbf{u}}}{\partial t} + \nabla.\bar{\rho}\tilde{\mathbf{u}}\tilde{\mathbf{u}} - \nabla.\left(\bar{\rho}(\nu + \nu_{SGS})\left(\nabla\tilde{\mathbf{u}} + \nabla\tilde{\mathbf{u}}^{\mathrm{T}} - \frac{2}{3}\mathrm{tr}(\nabla\tilde{\mathbf{u}})\mathbf{I}\right)\right) = -\mathbf{g}.\mathbf{x}\nabla\bar{\rho} - \nabla\overline{\mathrm{p_d}} . \qquad (4.6)$$

The equation employed to calculate the modified pressure $\overline{\mathrm{p_d}}$ will be discussed in a later section.

The temporal and spatial discretization of each term in the conservation transport equation requires at least a second-order accurate numerical scheme in order

to achieve acceptable accuracy in LES computations. To formulate a second-order accurate scheme in time and space, an assumption will be made that the profile of ϕ varies linearly around the computational node *P* spatially and temporally. With such an assumption, the following equations can be written for a second-order scheme:

$$\phi(\mathbf{x}) = \phi_P + (\mathbf{x} - \mathbf{x}_P).(\nabla\phi)_P \,, \tag{4.7}$$

$$\phi(t + \Delta t) = \phi^{\mathrm{t}} + \Delta \mathrm{t}\left(\frac{\partial \phi}{\partial \mathrm{t}}\right)_t \,, \tag{4.8}$$

with

$$\phi_P = \phi(\mathbf{x}_P) \,, \tag{4.9}$$

$$\phi^t = \phi(t) \,. \tag{4.10}$$

The second order accuracy of the scheme given in Eq.4.7 can be shown via a Taylor series expansion. Let us suppose that $\phi(\mathbf{x})$ is a continuously differentiable function around ϕ_P, we can subsequently express the function in the neighborhood of ϕ_P as:

$$\phi(\mathbf{x}) = \phi_P + (\mathbf{x} - \mathbf{x}_P).(\nabla\phi)_P + \frac{1}{2}(\mathbf{x} - \mathbf{x}_P)^2 : (\nabla\nabla\phi)_P + \mathrm{H} \,, \tag{4.11}$$

where it can be easily seen that the first term of the truncation error is of the order $O(|(\mathbf{x} - \mathbf{x}_P)^2|)$ and H is representative of higher order terms. The same Taylor series expansion can be performed to illustrate the second-order accuracy of the temporal scheme is of the $O(\Delta t^2)$.

Utilizing the finite volume methodology, Eq.4.2 has to be put into integral form where the integral has to be satisfied over the control volume $\mathrm{V_P}$. The integral equation written for a scalar property ϕ can be given by:

$$\int_t^{t+\Delta t}\left[\frac{\partial}{\partial t}\int_{\mathrm{V_P}}\rho\phi \mathrm{dV}+\int_{\mathrm{V_P}}\nabla.(\rho\mathbf{u}\,\phi)\mathrm{dV}-\int_{\mathrm{V_P}}\nabla.(\rho\,\Gamma\nabla\phi)\mathrm{dV}\right]dt$$
$$=\int_t^{t+\Delta t}\left(\int_{\mathrm{V_P}}S(\phi)dV\right)dt\,. \qquad (4.12)$$

In the subsequent sub-sections, the discretization of each term in Eq.4.12 will be given and discussed.

4.2 Spatial Terms Discretization

The convection, diffusion, and source terms given in Eq.4.12 have to simplified prior to their discretization. The simplification commences by utilizing the Gauss theorem to convert volume integrals to surface integrals and is as follows:

$$\int_V \nabla.\mathbf{F}\,\mathrm{dV}=\oint_{\partial V}\mathbf{F}.d\mathbf{S}\,, \qquad (4.13)$$

$$\int_V \nabla\phi\,\mathrm{dV}=\oint_{\partial V}\phi\,d\mathbf{S}\,, \qquad (4.14)$$

with V being the region in space with a bounded surface ∂V.

Using Eq.4.7, we can integrate the equation to get an approximate for volume integrals of ϕ as [126]:

$$\int_{V_P}\phi(\mathbf{x})dV=\int_{V_\mathrm{P}}[\phi_P+(\mathbf{x}-\mathbf{x}_P).(\nabla\phi)_P]dV \qquad (4.15)$$

$$=\phi_P\int_{V_P}dV+\left[\int_{V_P}(\mathbf{x}-\mathbf{x}_P)dV\right](\nabla\phi)_P \qquad (4.16)$$

$$=\phi_P V_\mathrm{P}\,, \qquad (4.17)$$

where ϕ_P is the value of ϕ at the computational node and V_P is the volume of the control volume enclosing the node *P*.

We can similarly approximate the terms under the divergence operator by taking the same approach; employing the assumption that the variables vary linearly over each face of the computational node *P* so that it can be represented by its value at the cell face center and summing over each cell face. Thus,

$$\int_{V_P} \nabla . \mathbf{a} dV = \int_f \mathbf{a} . d\mathbf{S} = \sum_f \left(\int_f \mathbf{a} . d\mathbf{S} \right) = \sum_f \mathbf{a}_f . \mathbf{S} \qquad (4.18)$$

with $\mathbf{S}$ being the outward pointing surface area vector of each face of node *P* and implicit in this approach is the assumption that $\mathbf{a}_f$ is the mean value of the surface. Such an approximation to the surface integral is of second-order accuracy and is identical to the midpoint rule. This can be further illustrated by employing the second order accuracy scheme from the Taylor series expansion of Eq.4.7 as:

$$\int_f \mathbf{a} . d\mathbf{S} = \boldsymbol{a}_f . \int_f d\mathbf{S} + \int_f (\mathbf{x} - \mathbf{x}_f) d\mathbf{S} : (\nabla \boldsymbol{a})_f = \boldsymbol{a}_f . \mathbf{S}_f \,, \qquad (4.19)$$

where a similar definition to Eq.4.** has been made for the face center:

$$\int_f (\mathbf{x} - \mathbf{x}_f) dS = 0 \,. \qquad (4.20)$$

4.2.1 Convection Term

The discretization of the convection term can be undertaken utilizing Eq.4.18 in the following manner:

$$\int_{Vp} \nabla.(\rho \mathbf{u}\phi)dV = \sum_{f} \mathbf{S}.(\rho \mathbf{u}\phi)_f \quad (4.21)$$

$$= \sum_{f} \mathbf{S}.(\rho \mathbf{u})_f \phi_f \quad (4.22)$$

$$= \sum_{f} F\phi_f \,, \quad (4.23)$$

the convection term is approximated within the control volume at point P by summing the fluxes over all the faces that share the control volume, where

$$F = \mathbf{S}.(\rho \mathbf{u})_f \quad (4.24)$$

is the mass flux through each face *f*. Since variable quantities are stored at computational nodes, ϕ_f has to be acquired with interpolation schemes and that will be the next topic of discussion.

Upwind Differencing (UDS)

In contrast to central differencing second order scheme, boundedness can be guaranteed by decreasing the order of the interpolation to the first order. Even though the nonphysical oscillatory behavior is no longer an issue, the first order scheme is numerically diffusive because the leading truncation error term resembles a diffusive flux [127]. This can be readily seen in the Taylor series expansion around computational node, P:

$$\phi_f = \phi_P + (\mathbf{x}_f - \mathbf{x}_P)\left(\frac{\partial \phi}{\partial \mathrm{x}}\right)_P + \frac{(\mathbf{x}_f - \mathbf{x}_P)^2}{2}\left(\frac{\partial^2 \phi}{\partial \mathrm{x}^2}\right)_P + H. \qquad (4.25)$$

The utilization of the upwind differencing interpolation can be mathematically expressed as follows:

$$\phi_f = \begin{cases} \phi_P \; if \; F \geq 0\,; \\ \phi_N \; if \; F < 0\,. \end{cases} \qquad (4.26)$$

The expression given in Eq.4.26 clearly illustrates that the value of ϕ at the face is approximated based on the direction of the velocity vector (upwind differencing).

Central Differencing (CDS)

The utilization of the central differencing scheme to compute the value of ϕ at the face results in a second order scheme. The value of ϕ at the face is approximated using

$$\phi_f = \phi_N f_x + \phi_P(1 - f_x)\,, \qquad (4.27)$$

where the linear interpolation factor f_x is given as:

$$f_x = \frac{fP}{NP} \qquad (4.28)$$

and is essentially a ratio of the distances as depicted in Figure 4.2.

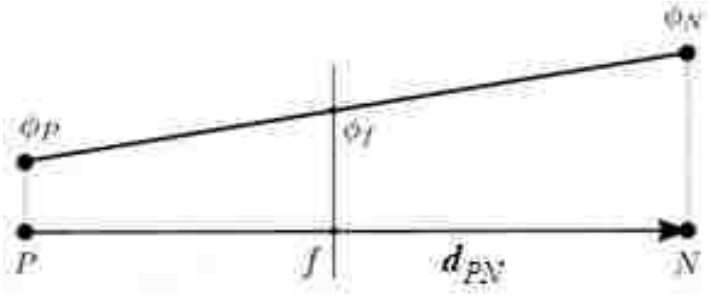

Figure 4. 2 Interpolation of face values for convection scheme.

The second order accuracy of Eq.4.27 can be shown by taking the Taylor series expansion of *N* around *P* and subsequently substituting for $\left(\frac{\partial \phi}{\partial x}\right)_P$ in Eq.4.25. The resulting Taylor series reads as:

$$\phi_f = \phi_N f_x + \phi_P(1 - f_x) - \frac{(\mathbf{x}_f - \mathbf{x}_P)(\mathbf{x}_N - \boldsymbol{x}_f)\left(\frac{\partial^2 \phi}{\partial x^2}\right)_P}{2} + H \qquad (4.29)$$

Due to the second order accuracy of this differencing scheme, it is widely known that any scheme higher than first order can potentially produce nonphysical oscillatory behavior and violate the boundedness of the solution especially in convection dominated flows. However, the flows treated in the current work are not convection dominated; it can be surmised that the usage of this scheme should not pose much problem with the boundedness of the solution.

Blending Differencing (BD)

In an attempt to merge the benefits of the two preceding interpolation schemes, i.e. maintaining the boundedness and order of accuracy, the CDS and UDS schemes can be linearly blended. A blending factor, γ, is introduced into the scheme that ranges from $0 \leq \gamma \leq 1$. Methods that have been proposed in setting the blending parameter includes prescribing a constant value of γ for all the faces [128] and making γ dependent upon the gradient at the face, $(\nabla\phi)_f$. Using the face gradients as a setting criterion stems from the logic that in the presence of sharp gradients, the blending factor will be close to 0 in order to prevent unphysical oscillations. In uniform flow regions, γ will be close to 1 where CDS can be effectively employed. The linearly blended differencing is given as:

$$\phi_f = \gamma\phi_f^{CDS} + (1-\gamma)\phi_f^{UDS} \quad (4.30)$$

The contribution of the convection term to the solution matrix is a diagonal and an off-diagonal term because the approximated face values are dependent upon computational nodes *P* and *N*. For example, if the central differencing scheme was employed to discretize the convection term, the diagonal and off-diagonal contributions, respectively are $a_P = (1-f_x)F$ and $a_N = f_x F$.

4.2.2 Diffusion Term

Let us now discretize the diffusion term using Eq.4.18 and making use of the assumption that ϕ varies linearly around the computational node, *P*. The mathematical representation is given by:

$$\int_{V_P} \nabla.(\rho\Gamma\nabla\phi)\, dV = \sum_f \mathbf{S}.(\rho\Gamma\nabla\phi)_f = \sum_f (\rho\Gamma)_f\, \mathbf{S}.(\nabla\phi)_f\,, \quad (4.31)$$

where $\mathbf{S}.(\nabla\phi)_f$ can easily be computed if the mesh is orthogonal, i.e. the vectors $\mathbf{S}$ and $\boldsymbol{d_{PN}}$ parallel (refer to Figures 4.1 and 4.2), and the dot product of the surface area vector with the face gradient can be performed with the following expression:

$$\mathbf{S}.(\nabla\phi)_f = |\mathbf{S}|\frac{\phi_N - \phi_P}{|\boldsymbol{d_{PN}}|}. \quad (4.32)$$

Similarly, the contribution of the diffusion term to the solution matrix consists of a diagonal and an off-diagonal term; thus, $a_P = |\mathbf{S}|(\rho\Gamma)_f/|\boldsymbol{d_{PN}}|$ and $a_N = |\mathbf{S}|(\rho)_f/|\boldsymbol{d_{PN}}|$. The term $(\rho\Gamma)_f$ is approximated from nodal values using an interpolation scheme. `

Source Terms

Source terms are classified as those expressions in the filtered conservation equations that cannot be written as convection, diffusion and temporal contributions to the evolution of the partial differential equations. To discretize the source terms, we assume the source at the computational node P represents the mean value over the control volume and the integration is performed by multiplying it with the cell volume. Thus,

$$\int_{V_P} S(\phi) dV \approx S\Delta V_P. \tag{4.33}$$

From the filtered momentum equation, the gradients of density and modified pressure will be discretized as source terms. Similarly, in the filtered energy equations, the two pressure terms on the right hand side of the equation will be discretized as such. Hence, the contribution to the solution matrix due to the source terms is $R_P = S\Delta V_P$.

4.2.3 Temporal Terms Discretization

Let us now consider the temporal discretization of the generic conservation equation given in Eq.4.12 which is given as follows:

$$\int_t^{t+\Delta t} \left[\frac{\partial}{\partial t} \int_{V_P} \rho\phi \mathrm{dV} + \int_{\mathrm{V_P}} \nabla.(\rho \mathbf{u}\, \phi) \mathrm{dV} - \int_{\mathrm{V_P}} \nabla.(\rho\, \Gamma \nabla\phi) \mathrm{dV} \right] dt = \int_t^{t+\Delta t} \left(\int_{V_P} S(\phi) dV \right) dt\,. \tag{4.34}$$

Employing the spatial discretization approximation for the convection, diffusion, and source terms, a semi-discrete form of the transport equation according to [121] is

$$\int_t^{t+\Delta t}\left[\left(\frac{\partial \rho\phi}{\partial t}\right)_P V_P + \sum_f F\phi_f - \sum_f (\rho\Gamma)_f \mathbf{S}.(\nabla\phi)_f\right] dt = \int_t^{t+\Delta t} (S\Delta V_P)\, dt\,. \quad (4.35)$$

Crank Nicholson Time Integration

Crank Nicholson time integration is a 2nd order scheme and requires the values at the present and previous times in order to evaluate spatial terms. Consequently, this scheme has to be implemented by solving a system of algebraic equations. But, firstly, let us consider the temporal integral and its evaluation having in mind the prescribed variation given in Eq.4.8,

$$\int_t^{t+\Delta t}\left(\frac{\partial \rho\phi}{\partial t}\right)_P dt = (\rho\phi)_P^{n+1} - (\rho\phi)_P^n\,. \quad (4.36)$$

Let us consider making a profile assumption for the time variation of the flux terms by supposing the fluxes can be interpolated between t and $t+\Delta t$ and using a constant χ between zero and one:

$$\int_t^{t+\Delta t} \phi(\mathrm{t})\mathrm{dt} = (\chi\phi^{n+1} + (1-\chi)\phi^n)\Delta t\,, \quad (4.37)$$

where χ = 0.5 is representative of the Crank-Nicholson time integration scheme. With the application of Eq.4.36 and 4.37 and dividing through by Δt, Eq. 4.35 becomes

$$\frac{(\rho\phi)_P^{n+1} - (\rho\phi)_P^n}{\Delta t} V_P + \frac{1}{2}\left[\sum_f F\phi_f - \sum_f (\rho\Gamma)_f \mathbf{S}.(\nabla\phi)_f\right]^{n+1} + \frac{1}{2}\left[\sum_f F\phi_f - \sum_f (\rho\Gamma)_f \mathbf{S}.(\nabla\phi)_f\right]^{n} = \frac{1}{2}[S\Delta V_P]^{n+1} + \frac{1}{2}[S\Delta V_P]^n . \quad (4.38)$$

The temporal derivative of the algebraic system of equations will contribute a diagonal and a source to the matrix representation and respectively are $a_P = \rho^{n+1} V_P/\Delta t$ and $R_P = (\rho\phi)_P^n V_P/\Delta t$.

4.2.5 Algebraic System of Equations

The spatial and temporal discretization of any set of differential equations results in algebraic equations. These algebraic equations can either be linear or non-linear and is determined by the parent differential equations. To this end, the discretization process of the generic transport equation gives an algebraic equation that can be written as

$$a_P\phi_P + \sum_N a_N\phi_N = R_P , \quad (4.39)$$

P denotes the cell-center of the control volume where the differential equation is approximated, the index *N* denotes the grid node of all surrounding control volumes involved in the discretization and R_P comprises all the known and right hand side terms that emerged from the discretization. With the utilization of the temporal and

spatial discretization schemes given in the prior sections, we can explicitly write the following coefficients for the previously mentioned algebraic set of equations:

$$a_P = \rho_P^{n+1}\frac{V_P}{\Delta t} + \frac{1}{2}F_P(1-f_x)^{n+1} + \frac{1}{2}\frac{|\mathbf{S}|}{|\boldsymbol{d_{PN}}|}\left(\rho_P\Gamma_P(1-f_x)\right)^{n+1}, \qquad (4.40)$$

where $F_P = \left((\rho\mathbf{u})_P.\mathbf{S}(1-f_x)\right)^{n+1}$,

$$a_N = \frac{1}{2}F_N f_x{}^{n+1} - \frac{1}{2}\frac{|\mathbf{S}|}{|\boldsymbol{d_{PN}}|}(\rho_N\Gamma_N f_x)^{n+1} \quad , \qquad (4.41)$$

where $F_N = ((\rho\mathbf{u})_N.\mathbf{S}f_x)^{n+1}$,

and

$$R_P = (\rho\phi)_P^n\frac{V_P}{\Delta t} - \frac{1}{2}F(1-f_x)\phi_P^n - \frac{1}{2}\{\rho_N\Gamma_N f_x + \rho_P\Gamma_P(1-f_x)\}^n + \frac{1}{2}S_t\,, \qquad (4.42)$$

where $F = [(\rho\mathbf{u})_P.\mathbf{S}(1-f_x) + (\rho\mathbf{u})_N.\mathbf{S}f_x]^n$ and $S_t = [S\Delta V_P]^{n+1} + [S\Delta V_P]^n$. The central differencing scheme has been utilized to approximate face quantities needed for the convective and diffusive spatial terms.

An equation of the form given in Eq. 4.39 has to be assigned for each control volume in the computational domain and can be expressed in matrix notation by

$$A\boldsymbol{\phi} = \mathbf{R}\,. \qquad (4.43)$$

$\boldsymbol{\phi}$ and $\mathbf{R}$ are both vectors; the matrix A is sparse, which is attributable to the algebraic equations that emerged from the finite volume discretization. The A matrix has diagonal coefficients a_P and off-diagonal coefficients a_N. Let us consider the methods commonly used to solve the algebraic set of equations given in Eq.4.39 namely direct and iterative methods.

Direct methods can be utilized to compute a solution to the system of equations in a finite number of arithmetic operations and are quite attractive for small linear systems. The method becomes expensive for the type of equations solved in this thesis, thereby making iterative methods more preferable. Some direct methods available in literature comprise Gaussian Elimination, LU Decomposition and Tridiagonal Matrix Algorithm (TDMA) [129].

Iterative methods initially guess a solution and utilize the system of equations to subsequently improve upon the solution until the residual criterion is met. In CFD, the errors inherent in the discretization of differential equations are larger than machine error [129]. Thus, solving the matrix exactly with direct methods is unnecessary and this makes the usage of iterative methods more economical for CFD applications.

An iterative method should to be effective and robust in solving Eq.4.39. The efficiency and robustness can be greatly enhanced with the use of preconditioning [130]. Preconditioning is essentially a methodology employed to transform Eq.4.39 into an equation with an identical solution, except this new equation ensures convergence is accelerated. In this thesis, the preconditioned biconjugate gradient iterative method was utilized. For details on such iterative solvers, see [130].

To improve upon convergence when iterative matrix solvers are employed for obtaining solutions, underrelaxation can be profoundly useful to prevent divergence of the iterative solution [131]. This is attributable to the mere fact that the inclusion of underrelaxation parameters enhances the diagonal dominance of the a_P matrix. Thus, we can show that after Eq.4.39 has been solved for the current iteration,

$$\phi_P = \frac{R_P - \sum_N a_N \phi_N}{a_P} \ . \tag{4.44}$$

The change in the solution between iterations can be defined as

$$\Delta\phi_P^* = \phi_P - \phi_P^* \tag{4.45}$$

$$= \frac{R_P - \sum_N a_N \phi_N}{a_P} - \phi_P^* . \tag{4.46}$$

Since we are want to control how much the solution changes during iterations, the change is simply multiplied by an underrelaxation parameter α_ϕ and the following equation emerges

$$\phi_P - \phi_P^* = \alpha_\phi \left(\frac{R_P - \sum_N a_N \phi_N}{a_P} - \phi_P^* \right), \tag{4.47}$$

which can be simplified to

$$\frac{a_P}{\alpha_\phi} \phi_P + \sum_N a_N \phi_N = R_P + \frac{1 - \alpha_\phi}{\alpha_\phi} a_P \phi_P^* \tag{4.48}$$

The underrelaxation parameter α_ϕ is typically between 0 and 1.

4.3 Navier-Stokes Equations Discretization

The discretized general transport equation given in Eq.4.2 resulted in algebraic set of equations and if one presumes that a_P and a_N are known, then an equation identical to that of Eq.4.39 can be employed to solve the linear system of equations. However, it ought to be stated that the flowfield cannot be known a priori. In addition, all the filtered flow variables $\left(\bar{\rho}, \bar{\rho}\tilde{\mathbf{u}}, \bar{\rho}\tilde{h}, \overline{\mathrm{p_d}}\right)$ are interdependent and the discretized governing differential equations are a tightly coupled set of nonlinear algebraic equations. These coupled set of algebraic equations can either be solved using the simultaneous or segregated approach. The simultaneous approach solves for all the

flow variables concurrently and is more suitable for linear sets of equations and small computational points. Segregated approaches assumes each equation only has one unknown and employs the most current values for the other flow variables. The equations are then sequentially solved until convergence is reached. The segregated approach was employed in this research because it was deemed more economical and computationally efficient.

Before embarking on a discussion pertaining to segregated solvers, it would be appropriate to note that there are some specific aspects of the filtered equations of motions that need further elaboration. The convection term $\nabla.\bar{\rho}\tilde{\mathbf{u}}\tilde{\mathbf{u}}$, which is basically velocity $\tilde{\mathbf{u}}$ transporting linear momentum $\bar{\rho}\tilde{\mathbf{u}}$, introduces non-linearity into the discretized solution matrix which would be quadratic in the velocity. It would be preferred to linearize this term to enable the utilization of a linear matrix solver instead of the more expensive non-linear solver.

Linearization of Convection Term

To linearize the convection term, we can employ the discretization approach given for the generic convection term and substituting the flux from the previous iteration or time-step into the equation. Thus, the velocity is lagged as follows:

$$\int_{Vp} \nabla.(\bar{\rho}\tilde{\mathbf{u}}\tilde{\mathbf{u}})dV = \int_{\partial V} (\bar{\rho}\tilde{\mathbf{u}}\tilde{\mathbf{u}}).\mathrm{d}\mathbf{S} = \sum_f \overline{\rho_f}\widetilde{\mathbf{u}_f}.\widetilde{\mathbf{u}_f}.\mathbf{S} \qquad (4.49)$$

$$\approx \sum_f \left(\overline{\rho_f}\widetilde{\mathbf{u}_f}.\mathbf{S}\right)^0.\widetilde{\mathbf{u}_f} = \sum_f F^0.\widetilde{\mathbf{u}_f}\,. \qquad (4.50)$$

The interpolation schemes given previously can be used to approximate the flux and velocity at each cell face of computational node *P*. Using any of these schemes

produces the following discretized equation for each computational node for the convection of linear momentum with $\phi_f = \widetilde{\mathbf{u}_f}$:

$$\sum_f F^0 . \widetilde{\mathbf{u}_f} = a_{cP} \widetilde{\mathbf{u}_P} + \sum_N a_{CN} \widetilde{\mathbf{u}_N} , \qquad (4.51)$$

where the coefficients a_{cP} and a_{CN} are functions of $\left(\overline{\rho_f} \widetilde{\mathbf{u}_f} . \mathbf{S}\right)^0$.

4.3.1 Segregated Solver

As aforementioned, the segregated approach solves the discretized equations sequentially as opposed to simultaneous solvers. The utilization of such solvers requires inter-coupling of the individual equations. SIMPLE (Semi-Implicit Method for Pressure-Linked Equations) [131] and PISO (Pressure Implicit with Splitting of Operators) [132] are the most popularly employed segregated solvers that uses pressure-velocity coupling for linking the equations.

PISO Approach

The PISO algorithm is particularly suited for unsteady flows, whereby it is compulsory to capture the transients inherent to the flowfield. The numerical scheme is essentially implicit; it comprises an implicit predictor step and multiple explicit corrector steps as needed. The sequence of steps as proposed by [132] will be given for incompressible flows to give a flavor of the numerical scheme before applying it to the equations used in this thesis.

Implicit momentum predictor step

To predict the velocity field $\tilde{\mathbf{u}}$ implicitly, the prevailing pressure $\bar{p}_d^n$ from the prior time-step can be employed. Thus, using a semi-discrete form of the discretized momentum equation, where $\phi_P = \widetilde{\mathbf{u}_P}$, the following emerges:

$$\widetilde{\mathbf{u}_P^*} = a_P^{-1}\mathbf{H}(\widetilde{\mathbf{u}^*}) - a_P^{-1}\nabla \bar{\mathrm{p}}_{\mathrm{d}}^{\mathrm{n}}\,, \tag{4.52}$$

where $\mathbf{H}(\widetilde{\mathbf{u}^*})$ is representative of the off-diagonal parts of the solution matrix, i.e. spatial convective and diffusive fluxes and any terms associated with the right hand side of the equation, R_P. The matrix a_P can be easily inverted since it consists of only diagonal elements.

First explicit corrector step

Using the divergence free continuity equation, $\nabla.\,\widetilde{\mathbf{u}} = 0$, the pressure can be corrected employing the predicted $\widetilde{\mathbf{u}^*}$ field as follows:

$$\nabla.\,(a_P^{-1}\nabla \bar{\mathrm{p}}_{\mathrm{d}}^*) = \nabla.\left(a_P^{-1}\mathbf{H}(\widetilde{\mathbf{u}^*})\right). \tag{4.53}$$

The face fluxes, $F = \mathbf{S}.\widetilde{\mathbf{u}_f}$, can be assembled once the pressure equation has been solved and corrected. Thus,

$$F = a_P^{-1}\mathbf{H}(\widetilde{\mathbf{u}^*}).\mathbf{S} - a_P^{-1}\nabla \bar{\mathrm{p}}_{\mathrm{d}}^*.\mathbf{S}\,, \tag{4.54}$$

which can be simplified to:

$$F = a_P^{-1}\mathbf{H}(\widetilde{\mathbf{u}^*})_f.\mathbf{S} - a_P^{-1}\frac{|\mathbf{S}|}{|\mathbf{d}|}(\bar{\mathrm{p}}_{\mathrm{d}}^*]_N - \bar{\mathrm{p}}_{\mathrm{d}}^*]_P)\,. \tag{4.55}$$

The velocity $\widetilde{\mathbf{u}}$ can be corrected utilizing the newly computed pressure as

$$\widetilde{\mathbf{u}_P^{**}} = a_P^{-1}\mathbf{H}(\widetilde{\mathbf{u}^*}) - a_P^{-1}\nabla\, \bar{\mathrm{p}}_{\mathrm{d}}^*. \tag{4.56}$$

Second explicit corrector step

A second corrector step can be implemented similarly as follows:

$$\nabla.\,(a_P^{-1}\nabla \bar{\mathrm{p}}_{\mathrm{d}}^{**}) = \nabla.\left(a_P^{-1}\mathbf{H}(\widetilde{\mathbf{u}^{**}})\right) \tag{4.57}$$

$$\widetilde{\mathbf{u}_P^{***}} = a_P^{-1}\mathbf{H}(\widetilde{\mathbf{u}^{**}}) - a_P^{-1}\nabla \bar{\mathrm{p}}_{\mathrm{d}}^{**} \tag{4.58}$$

and the face fluxes can be updated similarly to the initial corrector step employing the new pressure and velocity fields. The recommendation of [132] proposed only two corrector steps for the solution to be time-accurate; however, multiple corrector steps can be implemented until the prescribed convergence criteria is met.

SIMPLE Approach

The SIMPLE algorithm is rather similar to PISO as they are part of the pressure-velocity coupling family of algorithms. SIMPLE algorithm is suited for steady flows or when time accuracy of the solution is not required. The sequence of calculations necessary when employing the SIMPLE algorithm is essentially undertaken with the utilization of Eqs.4.52-4.56. The SIMPLE algorithm corrects the momentum and pressure only once during the iteration and underrelaxation is usually required to dampen the large oscillations in the corrected pressure and the velocity fields. Hence, to attain convergence, the underrelaxation is often utilized as suggested in [126].

Before delving into the segregated solution algorithm employed in the current work, it would be imperative to have a discussion on the derivation of the modified pressure term, $\overline{p_d}$. The subsequent subsection will also cover some assumptions made to further simplify the equations solved in this thesis.

4.3.2 Derivation of the Modified Dynamic Pressure Term

We proceed initially by discussing the original pressure equation implemented into OpenFOAM®. To derive the equation for the modified pressure term, an equation for the pressure $\overline{p_d}$ that accounts for compressibility effects will be derived following the approach of [126]. The filtered continuity equation will be employed to perform

the derivation. The time derivative term in the continuity equation will be transformed utilizing the chain rule as follows:

$$\frac{\partial \bar{\rho}}{\partial t} = \frac{\partial \bar{\rho}}{\partial \bar{\mathrm{p}}}\Big|_{\mathrm{T}} \frac{\partial \bar{\mathrm{p}}}{\partial t} + \frac{\partial \bar{\rho}}{\partial \tilde{\mathrm{T}}}\Big|_{\mathrm{P}} \frac{\partial \tilde{\mathrm{T}}}{\partial t}. \tag{4.59}$$

In order to proceed, the assumption will be made to neglect the second term on the right of Eq.4.59. The reason for such an assumption is because the pressure term, due to only fluid motion, $\overline{\mathrm{p_d}}$, is being considered here. Thus, the premise is that the density changes due to compressibility effects are only a function of the pressure term due to dynamic fluid motion. As such, the isothermal compressibility term $\psi = \frac{1}{RT} = \frac{\partial \bar{\rho}}{\partial \bar{\mathrm{p}}}\Big|_{\mathrm{T}}$ was derived using the ideal perfect gas law and the original equation given in Eq.4.59 simplifies to

$$\frac{\partial \bar{\rho}}{\partial t} = \psi \frac{\partial \bar{\mathrm{p}}}{\partial t}. \tag{4.60}$$

The velocity term in the divergence term in the continuity equation $\nabla . \bar{\rho}\tilde{\mathbf{u}}$, can be substituted by employing the semi-discrete form of the filtered momentum equation.

$$\mathrm{a}_P \widetilde{\mathbf{u}_P} = \mathbf{H}(\tilde{\mathbf{u}}) - \nabla \bar{\mathrm{p}} \tag{4.61}$$

and since a_P is a diagonal matrix and can be easily inverted, we get

$$\widetilde{\mathbf{u}_P} = \mathrm{a}_P^{-1}(\mathbf{H}(\tilde{\mathbf{u}}) - \nabla \bar{\mathrm{p}}). \tag{4.62}$$

The velocity term can be plugged into the divergence term of the continuity equation and using $\bar{\rho} = \psi \bar{\mathrm{p}}$, it reads as

$$\nabla . \bar{\rho}\tilde{\mathbf{u}} = \nabla . \bar{\rho}[\mathrm{a}_P^{-1}(\mathbf{H}(\tilde{\mathbf{u}}) - \nabla \bar{\mathrm{p}})] \tag{4.63}$$

$$= \nabla . (\bar{\rho}\mathrm{a}_P^{-1}\mathbf{H}(\tilde{\mathbf{u}}) - \bar{\rho}\mathrm{a}_P^{-1}\nabla \bar{\mathrm{p}}). \tag{4.64}$$

The pressure equation that accounts for dynamic fluid motion can be mathematically expressed as

$$\frac{\partial \psi \bar{\mathrm{p}}}{\partial t} + \nabla . \left(\bar{\rho} \mathrm{a}_P^{-1} \mathbf{H}(\mathbf{u}) \right) - \nabla . \left(\bar{\rho} \mathrm{a}_P^{-1} \nabla \bar{\mathrm{p}} \right) \tag{4.65}$$

and the pressure decomposition can be applied as follows:

$$\begin{aligned} \frac{\partial \psi \overline{\mathrm{p_d}}}{\partial t} + \mathrm{p}_{ref} \frac{\partial \psi}{\partial t} + \mathbf{g} . \mathbf{x} \frac{\partial \psi \bar{\rho}}{\partial t} + \nabla . \left(\bar{\rho} \mathrm{a}_P^{-1} \mathbf{H}(\tilde{\mathbf{u}}) \right) \\ - \nabla . \left(\bar{\rho} \mathrm{a}_P^{-1} \nabla \overline{\mathrm{p_d}} \right) - \nabla . \left(\bar{\rho} \mathrm{a}_P^{-1} \mathbf{g} . \mathbf{x} \nabla \bar{\rho} \right) . \end{aligned} \tag{4.66}$$

It is imperative to mention that over the course of this research, it was discovered that Eq.4.66, which was the originally implemented dynamic pressure implementation in OpenFOAM®, was profoundly sensitive to the initial flow conditions employed in this thesis. This sensitivity led to an inherent instability and divergence of the simulation after several time-steps; thus, to implement a new pressure equation required for the pressure-velocity coupling, it was determined to derive a pressure equation similar to that employed for incompressible flows, except with the inclusion of density gradients. The equation was derived by employing the divergence term in the continuity equation, $\nabla . \bar{\rho} \tilde{\mathbf{u}}$, and plugging the discretized momentum equation for the velocity term and decomposing the pressure accordingly. Proceeding in this manner results in the following modified pressure term:

$$\begin{aligned} \nabla . \left(\bar{\rho} \mathrm{a}_P^{-1} \nabla \overline{\mathrm{p_d}} \right) = \nabla . \left(\bar{\rho} \mathrm{a}_P^{-1} \mathbf{H}(\tilde{\mathbf{u}}) \right) - \nabla . \left(\bar{\rho} \mathrm{a}_P^{-1} \mathbf{g} . \mathbf{x} \nabla \bar{\rho} \right) \\ + \Delta V_P (\bar{\rho}^{n+1} - \bar{\rho}^n). \end{aligned} \tag{4.67}$$

Hence, the use of Eq.4.67 was deemed profoundly more appropriate for natural and mixed convection turbulent boundary layers.

4.3.3 Low Speed Flow Assumption

The fundamental equation of state given in the prior chapter can be readily applied to compressible flows where the propagation of information is dictated by the acoustic speed and speeds comparable to the flow velocity. To proceed with the equation as is will be fairly impractical for the types of flow considered in the current work. Thus, some assumptions were made to allow the solver to compute flows with negligible compressibility, such as low-Mach number flowfields. To this end, assumptions were implemented to simplify some of the equations presently examined. The purposes of the low-Mach number assumptions are twofold: (1) eliminate compressibility effects by filtering acoustic waves. Consequently, the numerical calculation will be affected and dictated only by speeds comparable to the flow velocity as opposed to the sound speed and (2) the modified equations will consist of fewer terms, thereby reducing the computational effort during the numerical simulations. Hence, the assumptions implemented for low-Mach number flows applicability are:

- Since the assumption that the coupling between pressure and density is non-existent, we can assume that temperature and density are inversely proportional in low-Mach number flows [133]. To be more specific, the pressure-density decoupling assumes the density is not dependent upon the modified pressure or "dynamic pressure" term, $\overline{p_d}$, since it is linked to the speed of the flow. Moreover, this essentially means that density is a function of the thermodynamic pressure, $\overline{p_{th}}$. Thus, we can define the equation of state as follows for low-Mach number flows:

$$\overline{\mathrm{p_{th}}} = \frac{\bar{\rho} R \tilde{T}}{W}, \qquad (4.68)$$

where $\overline{\mathrm{p_{th}}} = \mathrm{p}_{ref} + \bar{\rho}\mathbf{g}.\mathbf{x}$.

- The filtered energy equation can be simplified as well by substituting $\overline{\mathrm{p_{th}}}$ for the pressure term. As previously stated, the substitution enables the filtering of fast traveling sound waves from the solution process.

4.3.4 Segregated Solution Algorithm Approach

The segregated solution process employed in the present work was the compressible variant of the PISO algorithm. The solution process comprised one predictor step and two corrections for the momentum and modified pressure equations. The steps taken to implement the scheme are as follows:

Predictor Steps

The initial predictor step explicitly solves for the density using the conservation of mass equation:

$$\bar{\rho}_P^* = \bar{\rho}_P^n - \frac{\Delta t}{\Delta V_P} \sum_f (\bar{\rho}\tilde{\mathbf{u}}.\mathbf{S})_f^n . \qquad (4.69)$$

Subsequently, all three filtered velocity components are sequentially solved implicitly employing the momentum equation. The momentum equation is restated here for convenience and reads as:

$$\frac{\partial \bar{\rho}\tilde{\mathbf{u}}}{\partial t} + \nabla.\bar{\rho}\tilde{\mathbf{u}}\tilde{\mathbf{u}} - \nabla.\mu_{Eff}\left(\nabla\tilde{\mathbf{u}} + \nabla\tilde{\mathbf{u}}^{\mathrm{T}} - \frac{2}{3}\mathrm{tr}(\nabla\tilde{\mathbf{u}})\mathbf{I}\right) = -\mathbf{g}.\mathbf{x}\nabla\bar{\rho} - \nabla\overline{\mathrm{p_d}}$$

Let us rewrite the diffusive fluxes in a more compact form as follows:

$$\nabla.\mu_{Eff}\nabla\tilde{\mathbf{u}}_{diff} = \nabla.\mu_{Eff}\left(\nabla\tilde{\mathbf{u}} + \nabla\tilde{\mathbf{u}}^{\mathrm{T}} - \frac{2}{3}\mathrm{tr}(\nabla\tilde{\mathbf{u}})\mathbf{I}\right). \quad (4.70)$$

Thus,

$$\int_{V_P} \nabla.\left(\mu_{Eff}\nabla\tilde{\mathbf{u}}_{diff}\right) dV = \sum_f \left(\mu_{Eff}\right)_f \mathbf{S}.\left(\nabla\tilde{\mathbf{u}}_{diff}\right)_f \quad (4.71)$$

and using the discretization given in prior sections, we can write the semi-discrete form of the momentum equation as:

$$\frac{\bar{\rho}\tilde{\mathbf{u}}]^* - \bar{\rho}\tilde{\mathbf{u}}]^n}{\delta t} = -\nabla.\bar{\rho}\tilde{\mathbf{u}}]^n\widetilde{\mathbf{u}^*} + \nabla.\mu_{Eff}\nabla\tilde{\mathbf{u}}^*_{diff} - \mathbf{g}.\mathbf{x}\nabla\bar{\rho}^* - \nabla\bar{\mathrm{p}}_{\mathrm{d}}^{\mathrm{n}}. \quad (4.72)$$

The filtered momentum equation can be put into semi-discrete formulation and reads as

$$\widetilde{\mathbf{u}_P^*} = a_P^{-1}\mathbf{H}(\widetilde{\mathbf{u}^*}) - a_P^{-1}(\mathbf{g}.\mathbf{x})\nabla\bar{\rho}]^* - a_P^{-1}\nabla\bar{\mathrm{p}}_{\mathrm{d}}^{\mathrm{n}}. \quad (4.73)$$

The energy equation is subsequently solved implicitly to approximate the sensible enthalpy using the "newest" velocity and density fields:

$$\frac{\bar{\rho}^*\tilde{h}^{n+1} - \bar{\rho}^*\tilde{h}^n}{\delta t} = -\nabla.\bar{\rho}^*\tilde{\mathbf{u}}^*\tilde{h}^{n+1} + \nabla.\bar{\rho}^*\alpha_{Eff}\nabla\tilde{h}^{n+1} + \frac{\bar{\mathrm{p}}_{th}^{n+1} - \bar{\mathrm{p}}_{th}^{n}}{\delta t} + \tilde{\mathbf{u}}^*.\nabla\bar{\mathrm{p}}_{\mathrm{th}}^{\mathrm{n+1}}, \quad (4.74)$$

where $\bar{\mathrm{p}}_{th}^{n+1} = \mathrm{p}_{ref} + \bar{\rho}^*\mathbf{g}.\mathbf{x}$ and $\bar{\mathrm{p}}_{th}^{n} = \mathrm{p}_{ref} + \bar{\rho}^{\mathrm{n}}\mathbf{g}.\mathbf{x}$. The semi-discrete form of the filtered sensible enthalpy equation used is:

$$\tilde{h}_p^{n+1} = a_P^{-1}\mathbf{Y}\left(\tilde{h}^{n+1}\right) + a_P^{-1}\frac{\bar{\mathrm{p}}_{th}^{n+1} - \bar{\mathrm{p}}_{th}^{n}}{\delta t} + a_P^{-1}\tilde{\mathbf{u}}^*.\nabla\bar{\mathrm{p}}_{\mathrm{th}}^{\mathrm{n+1}}, \quad (4.75)$$

where $\mathbf{Y}(\tilde{h}^{n+1})$ consists of the off-diagonal parts of the convective and diffusive fluxes and the associated right hand side terms. Once the sensible enthalpy, $\tilde{h}^{n+1}$, is known, the filtered temperature field can be approximated utilizing $\int_{T_{ref}}^{T_1} d\tilde{h}\left(\widetilde{\mathrm{T}}\right) = \int_{T_{ref}}^{T_1} C_P\left(\widetilde{\mathrm{T}}\right) d\widetilde{\mathrm{T}}$ and the following assumption to represent the specific heat as a linear function of temperature has been made:

$$C_P \approx z_1 + z_2 \widetilde{\mathrm{T}}\,, \tag{4.76}$$

with z_1 and z_2 being the coefficients for air. To proceed, the Newton iteration root finding method was employed in order to calculate the filtered temperature $\widetilde{\mathrm{T}}$. Having computed the temperature, the equation of state was used to update the density accordingly:

$$\bar{\rho}^{n+1} = \frac{W \bar{\mathrm{p}}_{th}^{n+1}}{R \widetilde{\mathrm{T}}^{n+1}}. \tag{4.77}$$

Explicit Corrector Steps

The corrector step solves the modified pressure equation for $\overline{\mathrm{p_d}}$.

$$\begin{aligned} &\nabla.(\bar{\rho}^{n+1} \mathrm{a}_P^{-1} \nabla \bar{\mathrm{p}}_{\mathrm{d}}^{*}) \\ &\quad = \nabla.\left(\bar{\rho}^{n+1} \mathrm{a}_P^{-1} \mathbf{H}(\widetilde{\mathbf{u}^{*}})\right) - \nabla.(\bar{\rho}^{n+1} \mathrm{a}_P^{-1} \mathbf{g}.\mathbf{x} \nabla \bar{\rho}^{n+1}) \\ &\quad + \Delta V_P (\bar{\rho}^{n+1} - \bar{\rho}^{n}) \end{aligned} \tag{4.78}$$

The velocity components are corrected by solving the velocity corrector equations.

$$\widetilde{\mathbf{u}_P^{**}} = a_P^{-1} \mathbf{H}(\widetilde{\mathbf{u}^{*}}) - (\mathbf{g}.\mathbf{x}) \nabla \bar{\rho}^{n+1} - a_P^{-1} \nabla \bar{\mathrm{p}}_{\mathrm{d}}^{*} \tag{4.79}$$

The solution process utilized in the present work implemented two explicit corrector steps for the pressure and momentum equations and it was deemed adequate for the numerical simulations. Furthermore, only one implicit predictor step was

implemented during the course of this work. In an effort to ascertain the effects of increasing the outer predictor steps, two implicit predictor steps were used and its effects on the solution was completely insignificant. Hence, the utilization of an implicit predictor step sufficed and resulted in profoundly cheaper simulation costs.

4.4 Boundary Conditions

The proper implementation of boundary conditions in a complex flow field is critical in CFD. The computational mesh employed during the course of this work includes computational faces which coincide with boundaries of the domain and the equations prescribed to account for this will be elaborated. The varying boundary conditions that were utilized during the course of this research will be introduced as well.

4.4.1 Basic Boundary Conditions

Numerical boundary conditions fall into two categories: Dirichlet and Von Neumann boundary conditions. Dirichlet boundary condition prescribes a fixed value of the variable on the boundary. Von Neumann boundary condition assigns the gradient of the variable normal to the boundary. The mathematical representation of these two numerical boundaries is given below.

Fixed Value Boundary Condition

With the implementation of the fixed value boundary condition, the value of a generic variable ϕ is prescribed on the boundary face b to be ϕ_b. The discretization of the convection term as given in eq.** is

$$\int_{Vp} \nabla.(\rho \mathbf{u}\phi)dV = \sum_{f} F\phi_f.$$

The fixed value boundary condition enforces the value at the boundary face, b, to be

$$F_b \phi_b, \tag{4.80}$$

where F_b is the flux at the boundary face. The discretization of the diffusion term given by Eq.4.**

$$\int_{Vp} \nabla.(\rho\Gamma\,\nabla\phi)\mathrm{d}V = \sum_f (\rho\Gamma)_f \mathbf{S}.(\nabla\phi)_f.$$

To compute the normal gradient on the boundary face b, the subsequent equation is utilized:

$$\mathbf{S}.(\nabla\phi)_b = |\mathbf{S}|\frac{\phi_b - \phi_P}{|\mathbf{d}|}. \tag{4.81}$$

Fixed Gradient Boundary Condition

The fixed gradient boundary condition prescribes the normal gradient, $(\nabla\phi)_b$, at the face boundary and when this boundary condition is applied to the convection term, the quantity ϕ_b is computed from the cell centered value, ϕ_P and prescribed face gradient as

$$\phi_b = \phi_P + \mathbf{d}.(\nabla\phi)_b\,. \tag{4.82}$$

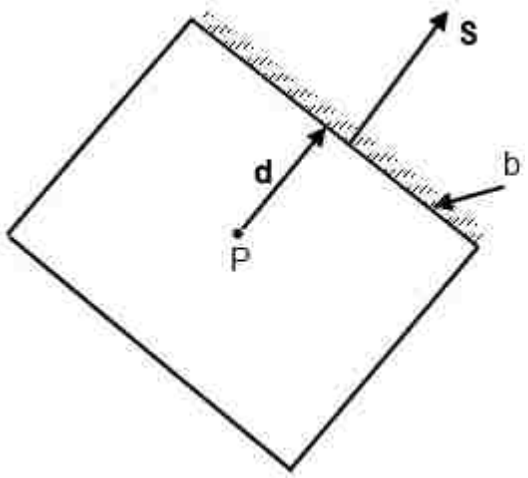

Figure 4. 3 Schematic representation of control volume with a boundary face.

A schematic of a control volume with a face that coincides with a boundary is depicted in Figure 4.3. The vector **d** is normal to the boundary face b, thus $\mathbf{S} \times \mathbf{d} = 0$ and is the normal distance from the centroid of the CV to the face of the boundary. Similarly, when the fixed gradient boundary condition is implemented for the diffusion term, the following equation emerges

$$(\rho\Gamma)_b \mathbf{S}.(\nabla\phi)_b \,. \qquad (4.83)$$

Mixed Boundary Conditions

Since the object of this thesis is computing wall bounded turbulent flows affected by buoyancy, a combination of fixed value and fixed gradient boundary conditions were compulsory at particular boundaries, especially at the inflow, outflow, and entrainment boundaries. Prescribing the appropriate boundary conditions for strongly affected buoyant flows are more challenging than momentum driven flows.

inletOutlet Boundary Condition

An inletOutlet boundary comprises the fixed value and fixed gradient boundary condition. To the fact that natural convection flows do not have a dominant

downstream convective flow, an inletOutlet boundary can be prescribed at the necessary boundaries of a computational domain. At a given time during the simulation, either a fixed value or fixed gradient is assigned on the boundary based upon the direction of the boundary normal velocity vector. If the boundary is supposed to be an outflow and the possibility of backflow exists during the simulation, a fixed value is appropriately given and is typically prescribed to diffuse any inflow that can potentially corrupt the simulation, as this is the goal of any numerical simulation performed.

pressureInletVelocity

This is typically prescribed for a boundary without the possibility of outflow during the numerical simulation. The boundary condition basically computes the velocity normal to the computational boundary from the flux acquired from the pressure condition given at that boundary. The tangential velocities at the inflow boundary are usually set to zero since the flux is only assumed to be normal to the boundary.

pressureInletOutletVelocity

This is a velocity boundary condition that's a combination of the inletOutlet and pressureInletVelocity boundaries. The boundary condition is appropriate for a boundary domain that can possibly be an outflow or inflow as the simulation progresses. At some particular time step, if the flux is into the domain, the pressureInletVelocity condition will be activated; however, if the flux is out of the domain, the velocity gradient normal to the boundary will be set to zero.

This boundary condition is employed in this research to enable the simulation to duplicate the entrainment behavior typically observed in natural convection flows.

Due to the higher temperature at the wall, and the subsequent lower density fluid adjacent to the wall, there is an accelerated upward movement of fluid and as a consequence of mass conservation; fluid from the far-field boundary is induced towards the wall. The induced mass flow is termed entrainment fluid and its effect is observed via the aforementioned boundary condition.

Periodic Boundary Condition

This type of boundary condition is usually prescribed when a particular flow direction/s can be assumed to be homogeneous. By such an assumption, a direction can be assumed to be infinite in length. Numerically, this is implemented by linking two opposite boundaries and setting the flow variables to be equal. Such an assumption is typically made in channel flows and flows over flat plates. In this research, the spanwise direction of the flowfield was assumed to be homogeneous since the flow isn't forced in that direction, thereby allowing the usage of a periodic boundary. Periodic boundaries do not require any special discretization in their implementation.

Buoyant Wall Pressure

The wall-normal pressure boundary condition employed in this research assumes

$$\frac{\partial \bar{\mathrm{p}}_{\mathrm{d}}}{\partial n} = -\frac{\partial \bar{\rho}}{\partial n} \mathrm{g\,x}\,. \qquad (4.84)$$

This boundary condition enables for a higher fidelity calculation by including the strongly buoyant flow condition near the hot wall; moreover, it allows for a more numerically stable simulation instead of assuming the wall-normal pressure gradient was zero.

Physical Boundary Conditions

Some numerical boundary conditions have to be properly specified in accordance with the actual boundaries that exist in the flow, such as no-slip condition at the wall. Let us now consider some of the boundary conditions implemented in this thesis:

- **no-slip impermeable wall** - a uniform velocity $\tilde{\mathbf{u}} = (0,0,0)$ is prescribed in order to duplicate the no-slip condition present on non-moving impermeable walls.
- **isothermal wall** - the experimental data employed to assist in this numerical effort assigned a constant uniform wall temperature and this boundary condition is implemented by prescribing a constant wall temperature over the heated flat plate.
- **inlet** – typically, a uniform velocity distribution is prescribed at this boundary if there is an incoming freestream flow.

4.5 OpenFOAM®

Before closing this chapter, it is of the utmost importance to have a brief discussion on the solver employed in this research, OpenFOAM®. OpenFOAM® (Open Field Operation And Manipulation), is a high-level object-oriented C++ open source solver released by OpenCFD Ltd. Most CFD flow solvers are written in a procedural paradigm, where the code is typically written in a top-down approach. Essentially, there is the top procedure of main, which systematically break down the CFD code into many sub-problems or sub-procedures. One of the drawbacks of procedural programming is that if any modifications are made to the main procedure, these changes can easily cascade into the sub-procedures of the flow solver. As such, the

maintenance of the software can be become challenging. As opposed to procedural programming, object-oriented programming (OOP) alleviates the problems associated with codes based upon procedures. OOP employs classes as the main module in the code and instead of modifying an already existing class to modify the code; an additional class can be created that easily inherits (inheritance) all the features and capabilities of that class. A class is essentially consists of various objects and the object is an instance of a class. Without getting into all the intricacies inherent to the OpenFOAM® solver, an attempt will be made to illustrate an example of the coding methodology utilized. To proceed, we make mention of the implicit and explicit FV discretization in three dimensional space using the finite volume calculus (fvc) and finite volume method (fvm) operators. The fvc operator calculates the partial derivatives explicitly and returns a field; the fvm operator is an implicit approach and converts the appropriate terns into the matrix equation and return matrix coefficients. Thus, let us take the following standard momentum equation:

$$\frac{\partial \rho \mathbf{u}}{\partial t} + \nabla . \rho \mathbf{u}\mathbf{u} - \nabla . (\mu \nabla \mathbf{u}) = -\nabla \mathrm{p} \, ,$$

and represent it in OpenFOAM® language as:

```
solve
(
fvm::ddt(rho, U)
+ fvm::div(phi, U)
- fvm::laplacian(mu, U)
==
- fvc::grad(p)
);
```

with $\mathrm{fvm::ddt} = \frac{\partial}{\partial t}$, $\mathrm{fvm::div} = \sum_i \frac{\partial}{\partial x_i}$ and $\mathrm{fvm::laplacian} = \sum_i \frac{\partial^2}{\partial x_i^2}$. In this formulation, fvm and fvc are classes with the following static functions, ddt( ), div( ), laplacian( ) and grad( ), among others not listed here. The flow variables, rho, phi (ρu), mu and p are objects of a class that fvm and fvc can "work" on. Clearly, it can be seen that an OpenFOAM® programmer has to think quite differently when approaching a solver based solely upon objects and classes. This brief introduction in the OpenFOAM® flow solver was not meant to be comprehensive; the reader can consult the doxygen and source-code, available at www.openfoam.com , for further inquiries.

4.6 Closing Remarks

In this chapter, the fundamental concepts of the finite volume methodology applied to the filtered governing partial differential equations were introduced. Using the finite volume method, the discretized equations, which resulted in algebraic set of equations, were discussed as well. The assumptions made to enable the discretization of the integral equations were elaborated; these assumptions entailed integration, differentiation and interpolation approximations required to arrive at reasonably developed algebraic equations that can be implemented on computers. Furthermore, the numerical scheme employed to couple the non-linear and inter-dependent algebraic equations were discussed to the effect of their computational efficiency when compared to simultaneous algorithms. The modification of the filtered pressure into several decomposed quantities and the re-definition of the ideal gas equation that is more computationally efficient for low-Mach number flows were discussed in detail in this chapter. In what follows, the theory and computational methodology

covered in this chapter will be basis of all the numerical predictions that will be presented in the subsequent chapters.

Chapter 5: Tsuji & Nangano Test Case

5.1 Test Case Description

This test case entails the experimental measurements of [10] over a vertically heated isothermal flat plate. The heated flat plate was 4 m high, 1 m wide and 2 mm thick and was held at a constant wall temperature of 333 Kelvin. The ambient temperature was roughly 289 Kelvin. The physical properties of the flow were assessed at the film temperature defined to be $T_f = (T_w + T_\infty)/2$, except for the thermal expansion coefficient, β, was defined as $1/T_\infty$. Stainless steel strips heaters were employed to heat the flat plate and were horizontally implemented at the rear of the plate at some determined length intervals. To attain a two dimensional turbulent natural convection boundary layer in the mean, side boards were positioned appropriately to prevent the span-wise entrainment of mass flow towards the center of the plate. Tungsten hot and cold wires were employed to measure the fluid velocity and temperature. In addition, platinum thermocouples were utilized to measure the fluid temperature as well. A schematic of the geometry employed for the experimental measurements is illustrated in Figure 5.1.

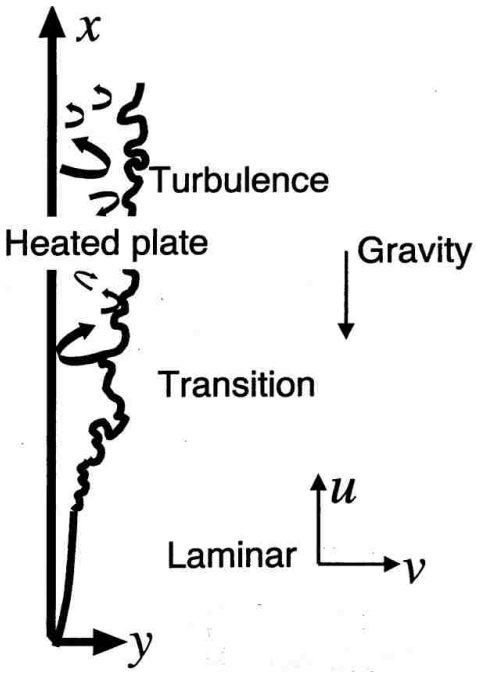

Figure 5. 1 Schematic of geometry and coordinate system utilized for experimental measurement, from [24].

5.2 Computational Setup

The numerical simulation domain and prescribed boundary conditions are graphically represented in Figure 5.2. The length, width and thickness of the computational domain were 5 m, 2 m and 0.3 m respectively. Due to the presence of a non-existent velocity in the freestream and at the inflow boundary, it was ascertained that it was not problematic for the boundary layer to commence at the edge of the flat plate. Thus, an entrance length was not implemented in the numerical setup. The far-field boundary, which is the entrainment boundary, was positioned 2 m away from the wall region to completely mitigate any potential disturbance that can possibly corrupt the simulation. The thickness of the computational domain, i.e. the span-wise length, is

0.3 m, it was selected via an iterative process which will be discussed in a subsequent section.

The entrainment boundary condition was prescribed for the far-field to enable an inflow of mass towards the wall as buoyancy effects induce upward flow acceleration near the wall in the streamwise direction, i.e. conservation of mass effect. Since the boundary layer flow over the heated plate is not forced by any mechanism in the span-wise direction, we can assume that the flow is homogeneous in the spanwise; thus, cyclic or periodic boundaries were implemented for this reason.

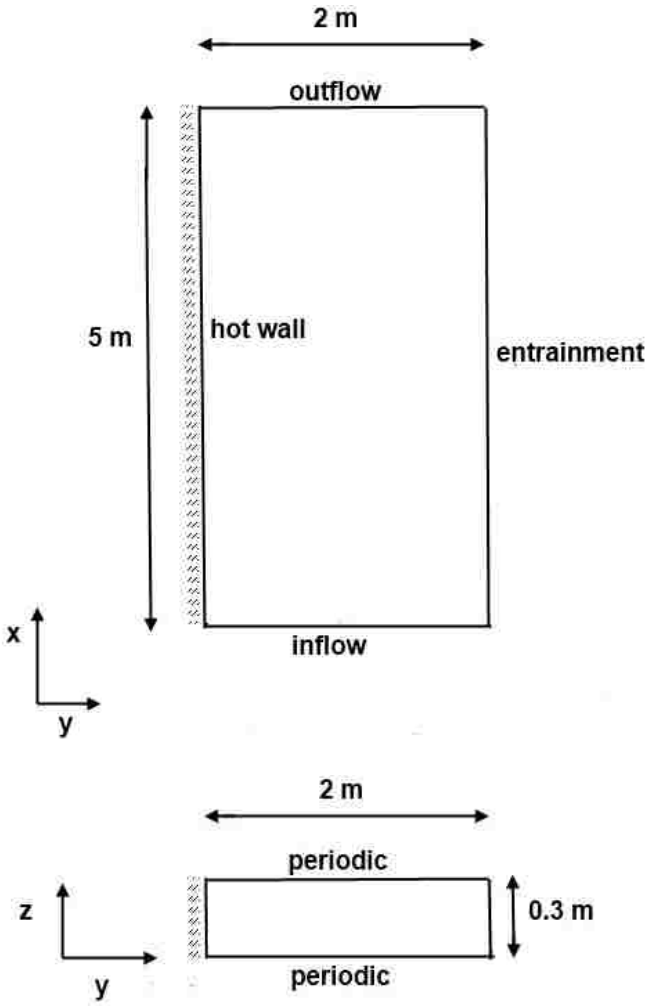

Figure 5. 2 Computational domain and boundary conditions for Tsuji & Nagano test case.

5.2.1 Computational Grid

The grid generation process for the Tsuji & Nagano test case was significantly affected by the necessity for the numerical grid to capture the laminar to turbulent boundary layer transition. Therefore, this posed to be a profound challenge due to the necessity to resolve the transition region and concurrently generate a mesh that will not drastically increase the computational cost of the simulation. Thus, to reasonably resolve the non-linear transition waves and subsequent discrete turbulent spots prior to a fully developed turbulent boundary layer without excessive damping that can be caused by a coarse mesh, the grid resolution in the laminar-transition is more demanding than the fully developed turbulent wall bounded flow. To account for the physics inherent to laminar-turbulent transition region, the streamwise grid resolution was $\Delta x = 7$ mm in the laminar region of the boundary layer. Over the course of this research, it was discovered that the streamwise resolution needed to be refined near the inception of transition to turbulent location. Hence, a refinement of $\Delta x = 2$ mm was implemented and maintained within the transition region. Subsequently, the grid was gradually stretched to $\Delta x = 30$ mm once a fully developed turbulent boundary layer was achieved. The mesh resolution in the streamwise direction was maintained at $\Delta x = 30$ mm in the fully turbulent portion of the flowfield. In order to keep the grid as simple as possible without excessive stretching, the span-wise grid resolution was uniform and kept at $\Delta z = 5$ mm. In the wall-normal direction, the grid spacing at the wall was $\Delta y \approx 1$ mm. At the edge of the boundary layer, at $y \sim 0.30$ m, the grid spacing was $\Delta y \approx 6$ mm; this resulted in approximately 120 grid cells within the turbulent boundary layer. A coarse mesh version of the grid is illustrated in Figure

5.3. The majority of grid cells were concentrated in the boundary layer region and coarser grid cells were employed away from any region of interest. Starting at a wall-normal distance of $y = 0.6\,\text{m}$ to $2.0\,\text{m}$, the grid cells were $\Delta x = 60\,\text{mm}$ and $\Delta z = 8\,\text{mm}$ in the streamwise and spanwise directions in the fully developed turbulent region. The wall-normal grid spacing in this region ranged from $\Delta y \approx 20\,\text{mm}$ to $70\,\text{mm}$.

The grid generation process just elaborated was utilized for the wall-resolved simulations performed in this research. A similar numerical grid was employed for the wall-modeled simulations, except the wall-normal spacing in the fully turbulent boundary layer region was coarsened for the utilization of wall layer boundary conditions. This was enabled by having a separate block of mesh in the fully developed turbulent region.

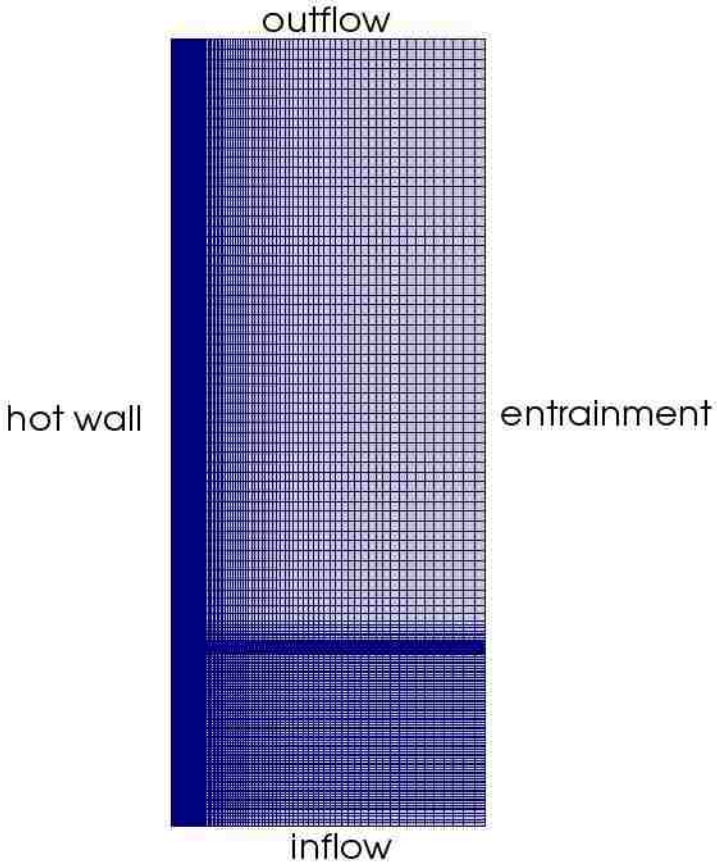

Figure 5. 3 Coarse mesh version for Tsuji & Nagano test case.

5.2.2 Simulation Details

The numerical simulations were initialized with a time-step of $\Delta t = 1 \times 10^{-4} s$ and the time-step was adjusted accordingly by the evolving flowfield as the solution process progressed using the Courant number (CFL) criterion, $\Delta t \sum_i u_i / \Delta x_i \leq \mathrm{CFL}$, with u_i and Δx_i being the filtered flow velocity and grid spacing, respectively and the subscript i denotes the dimensions of the computational mesh. The Courant number was fixed to a value of 0.5 for the entire duration of the numerical simulations. The simulations were conducted by allowing for at least 40 flow-through times and the solution was time-averaged after the initial transients were flushed through the computational domain which was roughly after 5 flow-through times. Subsequent to

the completion of the simulations, the results that will be presented in the following sections were also spatially averaged in the homogeneous span-wise direction.

5.3 Wall-Resolved Simulations

5.3.4 Spanwise Domain Convergence

It was previously mentioned that the width of the heated flat plate was iteratively chosen to be 0.3 m in the homogeneous direction. Moreover, it was stated that the assumption of a homogeneous direction was due to the absence of any forcing mechanism in the span-wise direction. To this end, we can suppose that the turbulent boundary layer will be homogeneous in the spanwise for the mean flow and consequently statistically 2D. Thus, to safely assume that the flow is statistically 2D in the mean, the span-wise width has to be sufficiently wide to contain ample turbulent structures. For this purpose, three grids with varying spanwise lengths were employed to ascertain which mesh can be used to acquire high fidelity results while still keeping the computational cost at a minimum. The characteristics of the grids are summarized in Table 5.1. All the grids had identical grid spacing and in the fully developed turbulent region, they were $\Delta x = 30\text{mm}$, $\Delta y \sim 1\text{mm}$ and $\Delta z = 5\text{mm}$ in the streamwise, wall-normal and spanwise directions, respectively. It should be noted that the spanwise widths given in Table 5.1 correspond to 1δ, 1.5δ and 2δ, respectively, with δ being the thickness of the turbulent boundary layer or integral length scale at a streamwise location of ~ 3.6 m.

Grid No.	Spanwise (cm)
One	30
Two	45
Three	60

Table 5. 1 Computational domain spanwise length characteristics.

Heat transfer rate

The wall heat transfer rates as a function of Rayleigh number, $Gr_X Pr$, are illustrated in Figure 5.4. The empirical equations formulated by [10] for the laminar and turbulent portions of the natural convection boundary layer over a heated vertical flat plate are shown in Figure 5.4 as well. The laminar and turbulent heat transfer rate equations, respectively read as

$$Nu_{\mathrm{x}} = 0.387(Gr_{\mathrm{x}} Pr)^{1/4} \quad (5.1)$$

and

$$Nu_{\mathrm{x}} = 0.120(Gr_{\mathrm{x}} Pr)^{1/3}\,. \quad (5.2)$$

The calculation of the wall heat transfer rates from the LES results was acquired via the following equation

$$Nu_{\mathrm{x}} = \frac{\mathrm{x}\dfrac{(\alpha_{SGS}+\alpha)}{\alpha}\dfrac{\partial \mathrm{T}}{\partial y}\Big|_w}{\Delta \mathrm{T}}, \quad (5.3)$$

with ΔT and $\frac{\partial \mathrm{T}}{\partial y}\Big|_w$ being the difference between the wall and ambient temperatures and wall-normal mean temperature gradient at the wall, respectively. Furthermore,

α_{SGS} is the thermal diffusivity due to the small dissipative SGS motion and α is the thermal diffusivity of laminar and large scale turbulent motions.

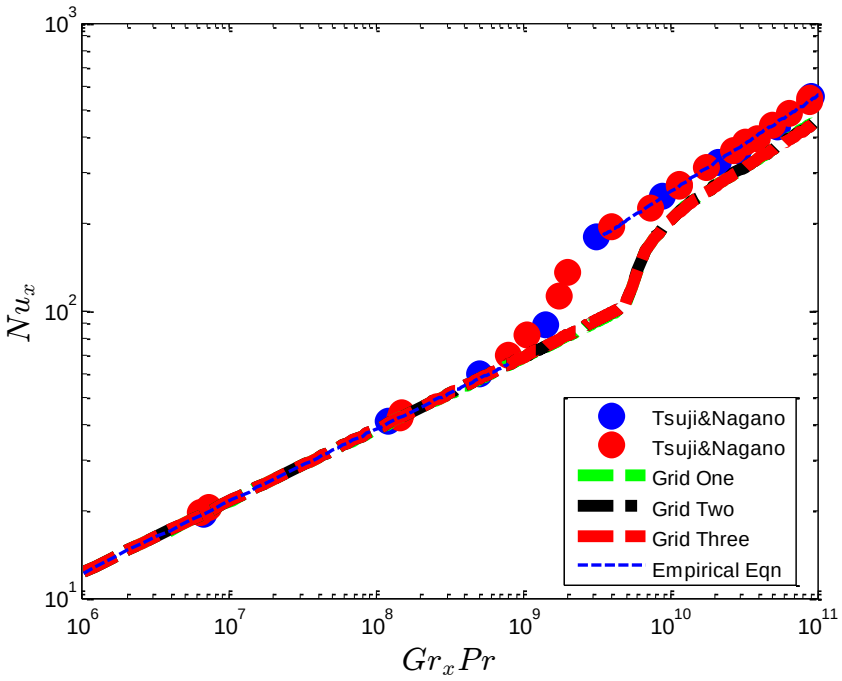

Figure 5. 4 Heat transfer rates of experiment, LDSMG and empirical equation.

Upon examination of the heat transfer rates, all the LES results were able to accurately capture the turbulent wall heat transfer. However, it is apparent from Figure 5.4 that the LES calculation predicted a delayed transition from laminar to turbulent boundary layer. In fact, according to the experiments, boundary layer transition commenced at a streamwise location of roughly 0.80 m; the CFD results computed a transition location that started at 1.20 m. Furthermore, it ought to be mentioned that the boundary layer transition was not "forced" either by tripping the flow or feeding turbulent fluctuations at the inflow region of the computational domain. Thus, even though the transition process was briefly delayed in the

numerical simulations, it was considered a success given the immense challenge posed by capturing natural turbulent boundary layer transition. This challenge is a result of the development of small disturbance waves in the laminar portion of the boundary layer that needs to be resolved numerically that subsequently grow into turbulent spots and finally into fully developed turbulence further downstream. The experimental results that will be shown were measured at x = 3.244 m; however, due to the delayed transition calculated by the LES, numerical data will be assessed at x ~ 3.6 m, which corresponds to $Gr_x \sim 1.8E+11$. This decision was made in order to match the length of fully developed turbulence of the experiment.

Mean velocity and temperature profiles

The mean streamwise velocity profiles at $Gr_x \sim 1.8E+11$ are shown in Figure 5.5. The semi-logarithmic scale plots were appended in order to assess the near wall region clearly. All the LES calculations accurately captured the near-wall region and the peak of the mean velocity profile. Moreover, the outer layer was also resolved with high fidelity. In moving forward and keeping with the terminology commonly employed for natural convection turbulent boundary layers, we define the inner-layer as the region from the wall to the maximum velocity and the outer-layer as the region from the maximum velocity to the edge of the boundary layer. It is apparent that the velocity peak occurs near the wall region. This is attributable to the density gradient across the boundary layer caused by the diffusion of heat from the heated flat plate. Thus, the air near the plate is less dense and the resulting buoyancy force is able to accelerate the fluid pockets further than air in the outer parts of the boundary layer.

The distribution of mean temperature within the turbulent boundary layer at the same streamwise location is shown in Figure 5.6. As is apparent from the temperature profiles, the LES results are in very good agreement with the measurements in the inner- and outer layers of the boundary layer.

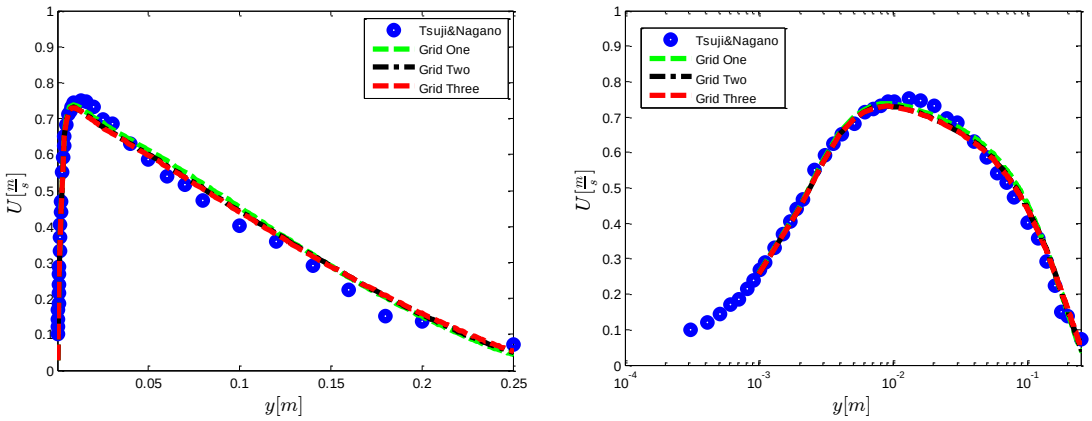

Figure 5. 5 Mean streamwise velocity profiles at $Gr_x \sim 1.8E+11$.

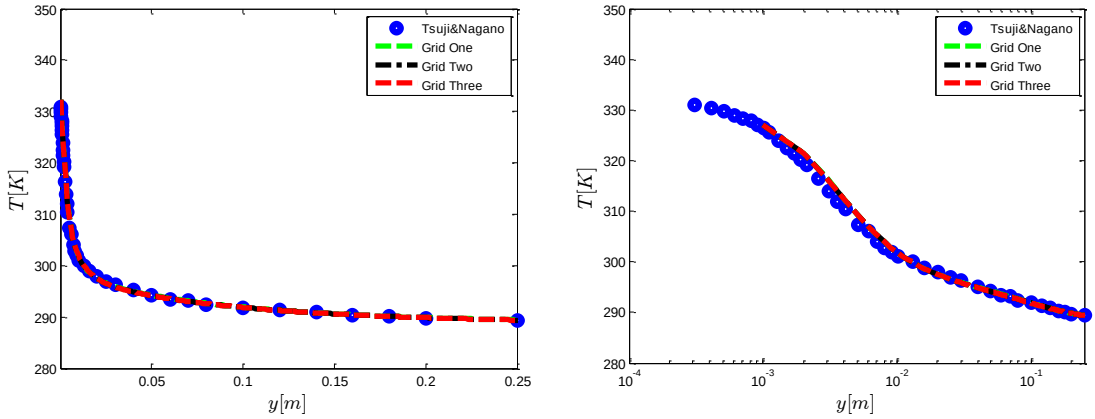

Figure 5. 6 Mean temperature profiles at $Gr_x \sim 1.8E+11$.

Intensities of temperature and velocity fluctuations profiles

The intensity of temperature turbulent fluctuation is shown in Figure 5.7. The LES predictions are in very good agreement with the experimental data in the entire boundary layer. The peak of the temperature fluctuation, which occurs in the inner layer, was accurately captured by the three LES computations. Figure 5.8 illustrates the streamwise velocity fluctuation intensity; excellent agreement between the measurements and numerical predictions are apparent throughout the boundary layer. It can be seen that the experimental data depicts the maximum streamwise velocity fluctuation intensity occurs in the outer-layer of the boundary layer. However, the numerical results predicted the maximum velocity fluctuation within the inner-layer.

The wall-normal velocity fluctuation intensity can be seen in Figure. 5.9. The agreement between the measurement and LES predictions is excellent in the outer-layer of the boundary layer. Within the inner layer, it can be seen from Figures 5.14 that the wall-normal velocity fluctuation was under-estimated numerically. It seems the LES computations clearly dampen or diffuse the wall-normal velocity turbulent fluctuations in the inner-layer and this damping becomes non-existent as the outer-layer is approached.

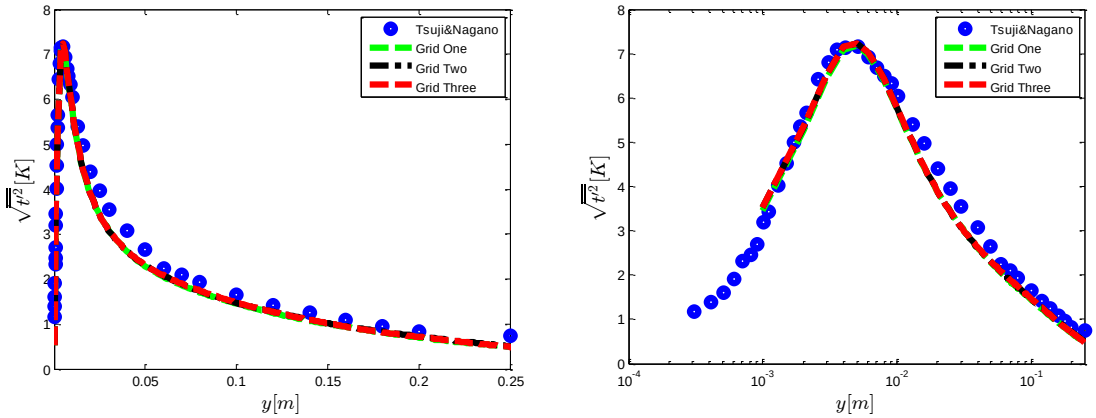

Figure 5. 7 Intensity of temperature fluctuation profiles at $Gr_x \sim 1.8E+11$.

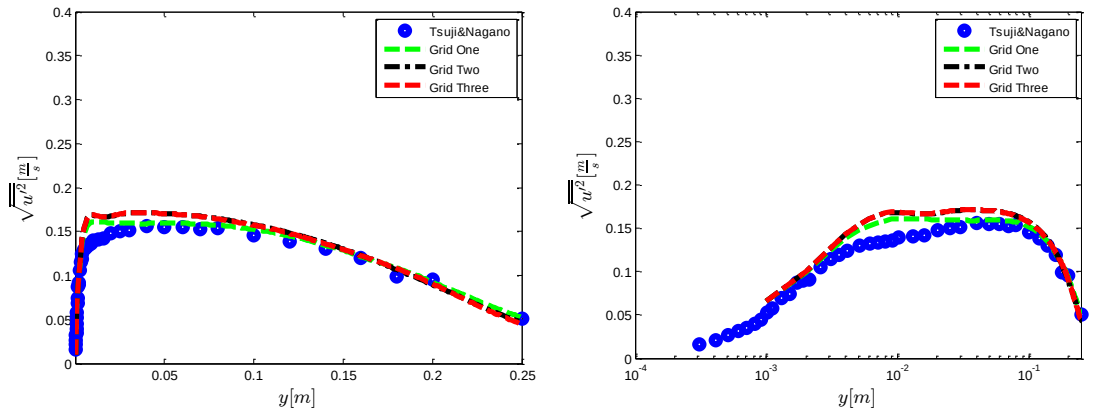

Figure 5. 8 Intensity of streamwise velocity fluctuation profiles at $Gr_x \sim 1.8E+11$.

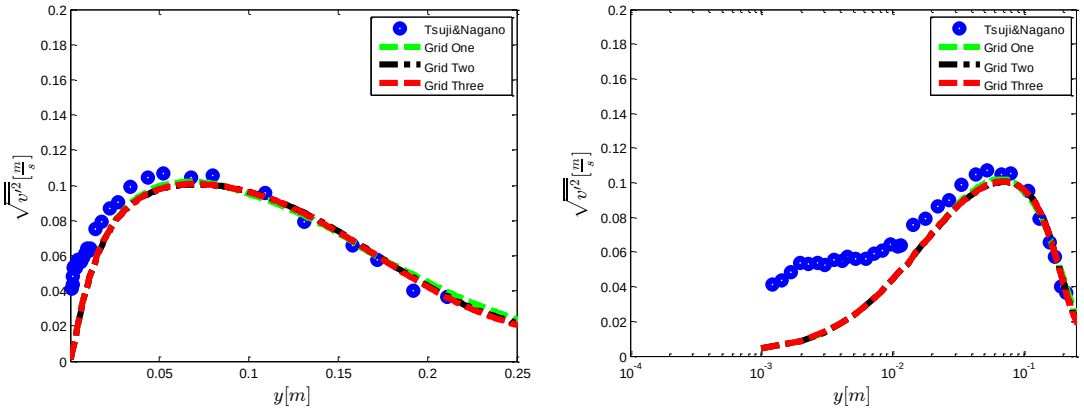

Figure 5. 9 Intensity of wall-normal velocity fluctuation profiles at Gr_x ~ 1.8E+11.

Reynolds shear stress

The Reynolds shear stress distribution in the boundary layer is shown in Figure 5.10. Again, the LES results are in excellent agreement with the experimental data in the inner- and outer layers. The Reynolds shear stress peaks in the outer layer and the numerical predictions accurately captured that feature. The interesting aspect of the Reynolds stress distribution occurs within the inner layer, in the near-wall region. Both the measurement and LES results seem to illustrate that $\overline{u'v'}$ is approximately ~ 0 over most of the inner layer region. If we re-examine Figure 5.5, one would see that $\partial U/\partial y$ in that region is greater than 0. Thus, in the presence of a positive mean velocity gradient, the Reynolds shear stress is close to 0. This may be indicative of the fact that the turbulence generation in the inner-layer might not be driven by the deformation of mean motion. In light of this, one may proceed to conclude that the eddy viscosity assumption typically employed for forced convection turbulent boundary layer flows

$$-\overline{u'v'} = \nu_t \, \partial U/\partial y \,, \qquad (5.4)$$

with ν_t being the turbulent eddy viscosity, cannot be applied to the inner-layer of the natural convection turbulent boundary layer. The generation of turbulent kinetic energy in the inner and outer layers of the turbulent natural convection boundary layer will be examined in a later section.

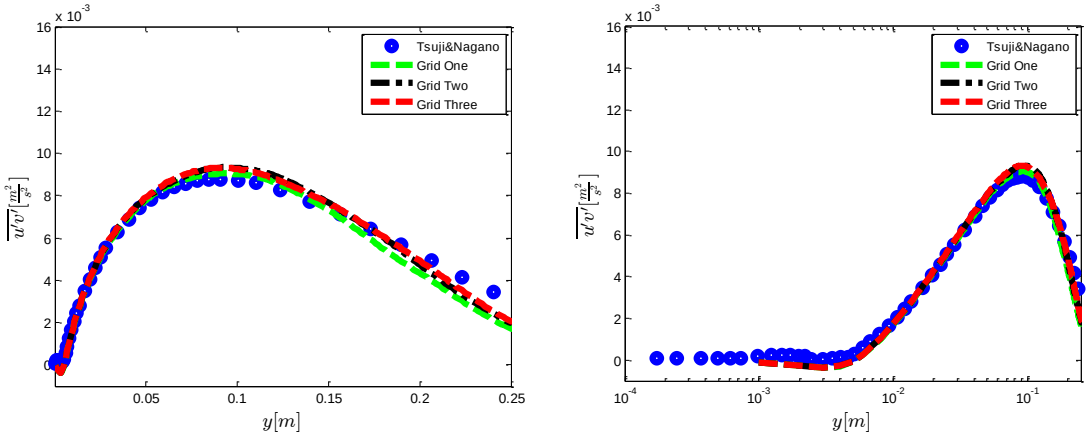

Figure 5. 10 Reynolds shear stress profiles at Gr_x ~ 1.8E+11.

Summary of spanwise domain study

In performing this study, it was concluded that the spanwise width of 30 cm would suffice for the computational domain. The first and second order statistics acquired from LES computations using the three different meshes were indistinguishable; thus conveying the fact that a domain of size δ can resolve enough turbulent structures to represent a statistically 2D turbulent boundary layer flow.

5.3.5 Mesh Resolution

The effects of coarsening the baseline mesh on 1st and 2nd order turbulent statistics were investigated in this section. The characteristics of the mesh employed in this study are described in Table 5.2. The Fine Mesh in Table 5.2 will be referred to as the baseline mesh and its resolution was decreased by a factor of two (Coarse Mesh). The grid labeled Grid One was included in this study to compare its results to the baseline mesh because the computational cost of the Fine Mesh was excessively expensive. Thus, the only difference between the two grids is the spanwise spatial resolution and one can anticipate insignificant differences between their predicted results since Grid One is already a wall-resolved LES mesh.

Case	Δx	Δy	Δz
Grid One	30 mm	~1 mm	5 mm
Coarse Mesh	60 mm	~2 mm	6 mm
Fine Mesh	30 mm	~1 mm	3 mm

Table 5. 2 Wall spatial resolution densities.

Heat transfer rate

The effects of spatial resolution on the wall heat transfer rates can be seen in Figure 5.11. The heat transfer rate predicted by the baseline mesh is seemingly identical to those acquired with the Grid One mesh, as expected. The Coarse Mesh is able to capture the heat transfer rate and is very comparable to the baseline mesh.

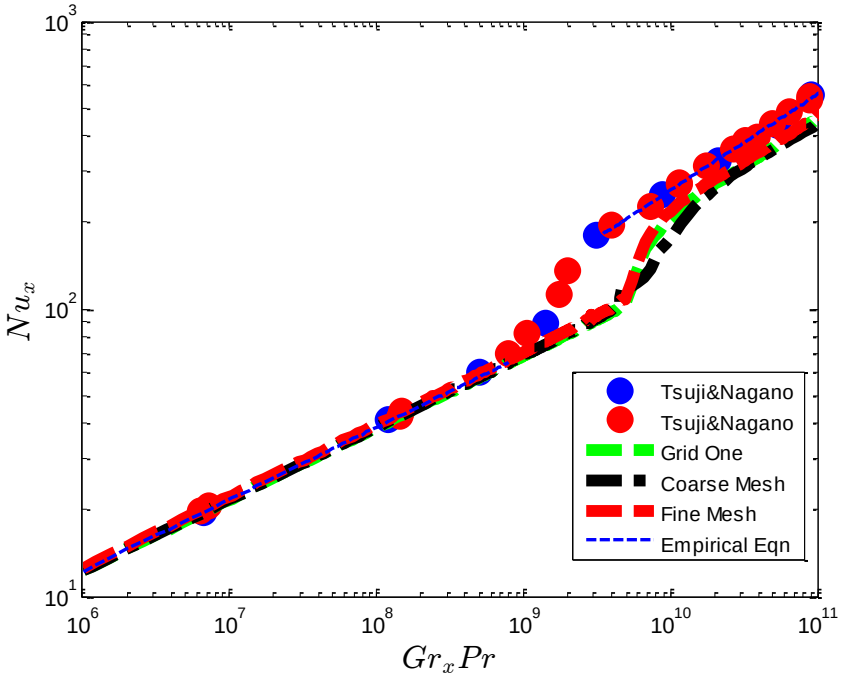

Figure 5. 11 Effects of spatial resolution on heat transfer rate.

Mean velocity and temperature profiles

The mean streamwise velocity wall profiles can be seen in Figure 5.12. The velocity distribution in the inner- and outer layers are identical for the Grid One and Fine Mesh cases. The Coarse Mesh underestimates the velocity maximum at the edge of the inner layer, but only slightly. In the outer layer of the boundary layer, the coarser mesh under-estimates the streamwise velocity and subsequently overestimates the inertia of the flow at the edge of the boundary layer. The effects of grid resolution on the mean temperature wall profile can be seen in Figure 5.13. All the grids employed were able to accurately capture the diffusion of heat in the inner- and outer layers of the turbulent boundary layer.

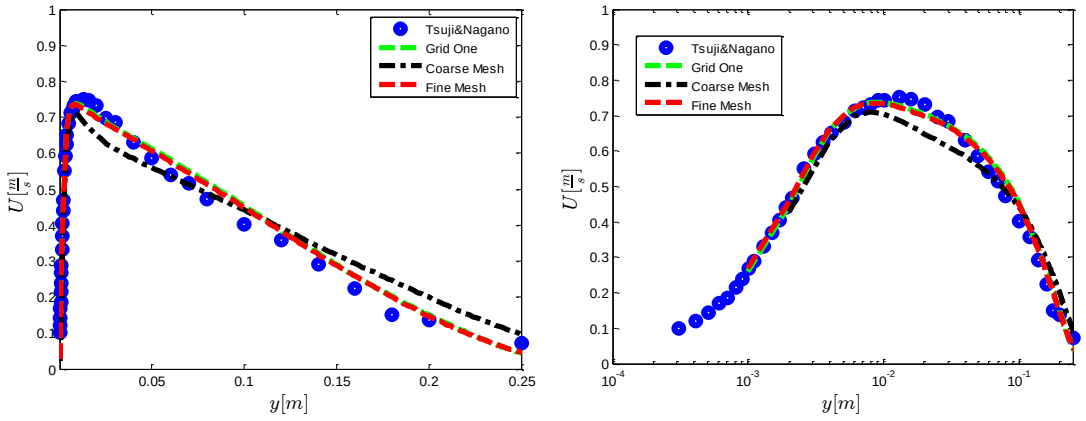

Figure 5. 12 Effects of spatial resolution on mean streamwise velocity.

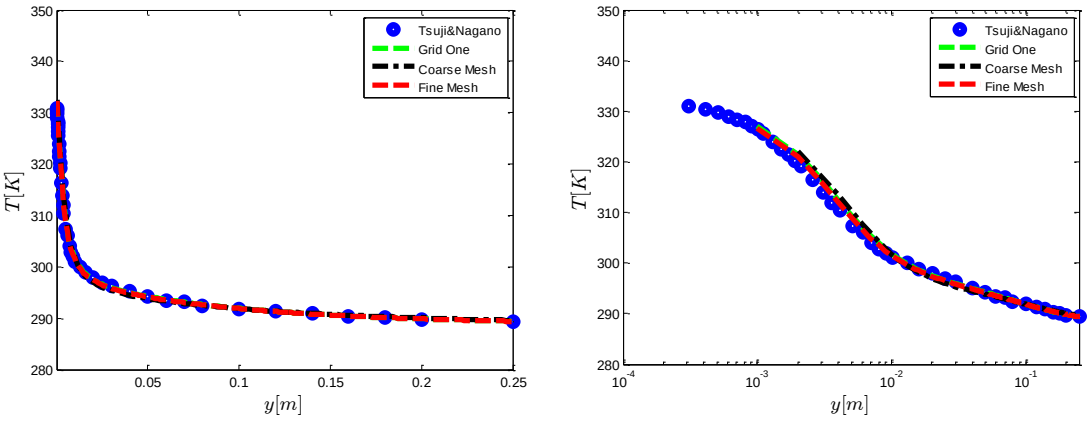

Figure 5. 13 Effects of spatial resolution on mean temperature.

Intensities of temperature and velocity fluctuations

Figure 5.14 illustrates the spatial resolution effects on temperature fluctuation intensity. The temperature fluctuation distributions in the outer layer are essentially identical for all the meshes. However, in the inner layer, the Coarse Mesh underpredicted the temperature fluctuation intensity peak in the inner layer. The streamwise velocity fluctuation intensity is shown in Figure 5.15 and it can be seen that the Coarse Mesh exaggerates the velocity fluctuation intensity in the inner- and outer layers of the boundary layer. The velocity fluctuation of the baseline and Grid One cases are fairly identical throughout the boundary layer region. The wall-normal velocity fluctuation intensity can be seen in Figure 5.16; the inner layer comparisons for the three grids are very comparable with hardly any differences. In the outer layer, the Coarse Mesh overestimates the velocity fluctuation intensity as the edge of the boundary layer is approached.

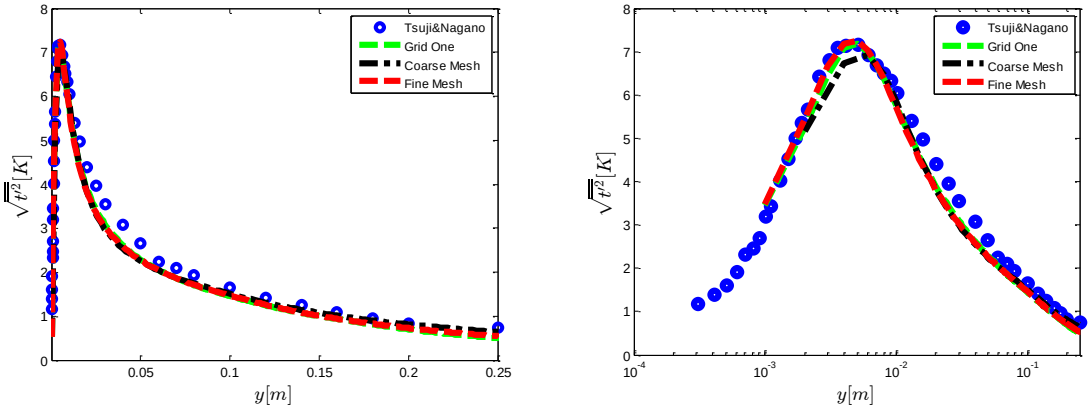

Figure 5. 14 Effects of spatial resolution on intensity of temperature fluctuation.

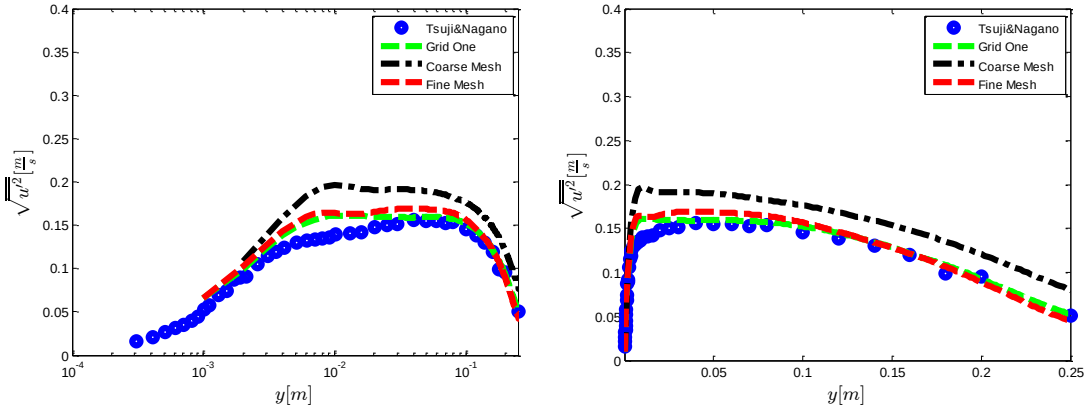

Figure 5. 15 Effects of spatial resolution on intensity of streamwise velocity fluctuation.

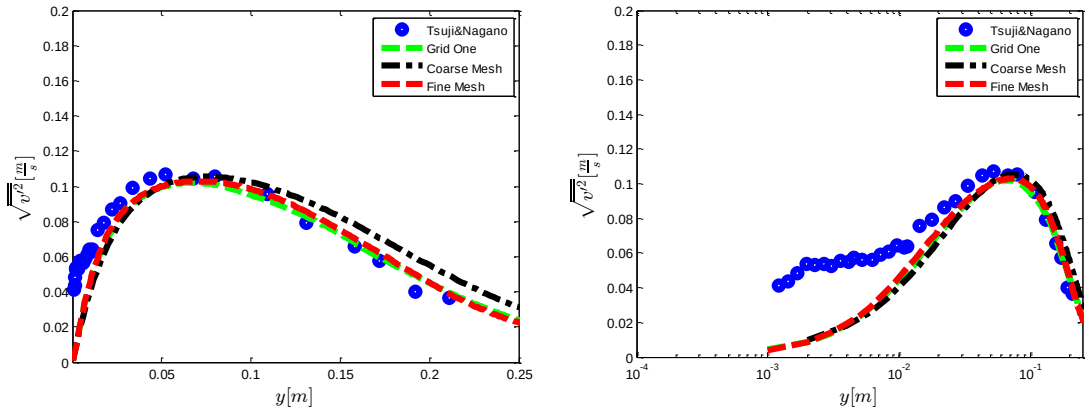

Figure 5. 16 Effects of spatial resolution on intensity of wall-normal velocity fluctuation.

Reynolds shear stress

Spatial resolution effects on the Reynolds shear stress wall profiles are shown in Figure 5.17. The turbulent shear stress distribution is very comparable for all the LES cases in the inner layer. Further out in the outer layer of the boundary layer, the Coarse Mesh overestimates the Reynolds stress slightly in comparison to the experimental data.

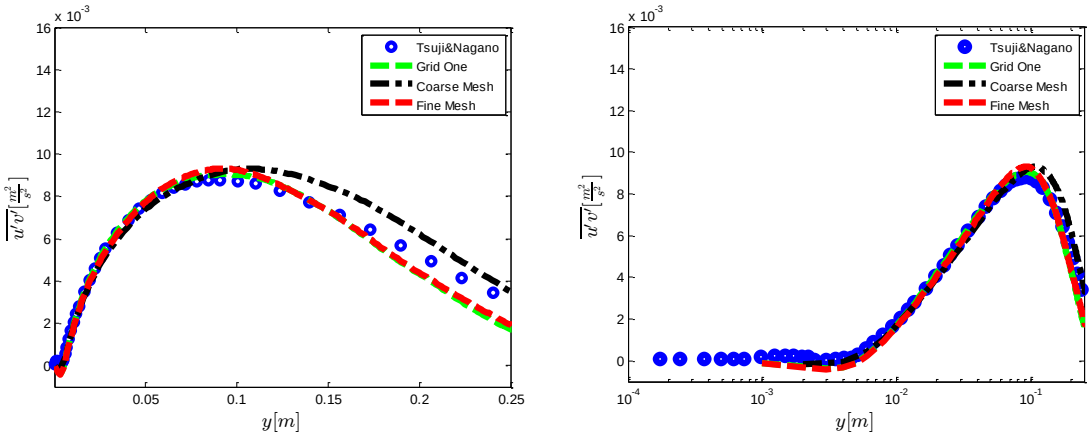

Figure 5. 17 Effects of spatial resolution on Reynolds shear stress.

Summary of Spatial Resolution Study

Due to the inherent nature of LES, the basic concept of grid convergence in physical space, to some degree, is inapplicable. To avoid employing finer and more expensive meshes in order to assess their resolution in wave number space, LES results acquired from the baseline mesh were compared to the Coarse Mesh and the comparisons were very acceptable. Although the Coarse Mesh is only able to resolve larger turbulent structures in the flow, it was concluded that appreciable turbulent structures were captured even with the coarsened mesh solution. Thus, the spatial resolution of Grid

One will be employed for the rest of this study regarding wall-resolved LES calculations.

5.3.6 Effects of Boundary Layer Trip

Thus far, the LES results that have been presented were shifted approximately $\sim$40 cm downstream to compare with the experimental data. This was required due to the delayed transition captured by the numerical simulation; the delayed transition occurred 40 cm beyond the location measured in the experiment.

The transition process computed was strictly numerical, i.e. initial errors (disturbance) intrinsic to the simulation were amplified as the computation progressed and finally allowed for the flow to transition. In the present section, an effort will be facilitated to implement some physical disturbance within the spatially developing flowfield to induce an earlier onset of transition to match the measurement, which will result in a direct comparison at the same streamwise location with the experiment. To achieve this, it was determined after attempting different methods to implement a three dimensional surface block upstream, at $x = 20$ cm, to perturb the flowfield. The boundary layer trip was 30 mm, 6 mm and 300 mm in the streamwise, wall-normal and spanwise directions, respectively. In the wall-normal direction, it was ensured that the trip was less than the boundary layer thickness and blockage was avoided. Table 5.3 lists the characteristics of the computational mesh employed in the present study. In Figure 5.18, a magnified view of the mesh near the placement of the tripping device can be seen. The subsequent results acquired from the boundary layer trip simulation will be referred to hereafter as LDSMG-Trip.

Case	SGS model	Δx	Δy	Δz	Transition
LDSMG	LDSMG	30 mm	~1 mm	5 mm	Numerical
LDSMG_BLTrip	LDSMG	30 mm	~1 mm	5 mm	Surface trip

Table 5. 3 Computational domain characteristics employed for boundary layer transition study.

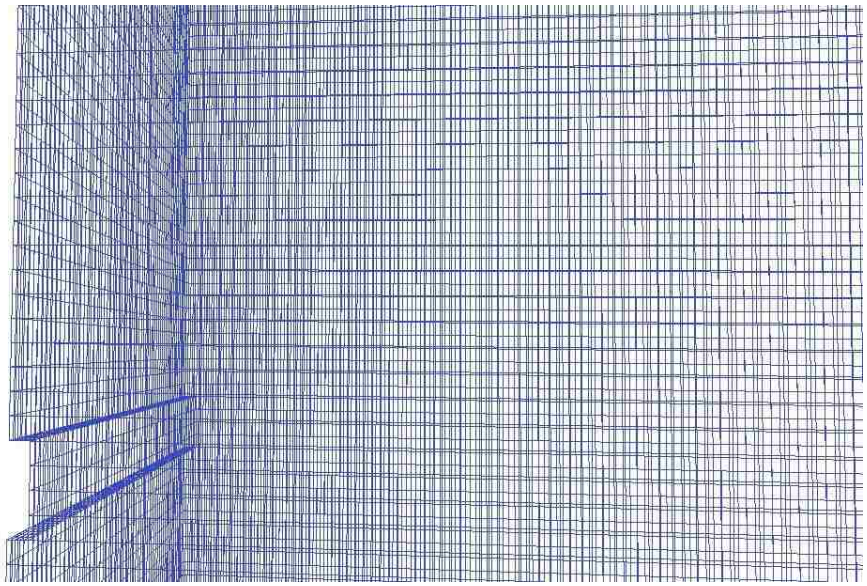

Figure 5. 18 Magnified view of computational mesh employed for boundary layer tripping simulation.

Heat transfer rate

The heat transfer rates illustrating the effects of tripping the boundary layer can be seen in Figure 5.19, along with the measurements and empirical data. In the upstream region, the placement of the tripping device caused a disturbance resembling a localized rapid fluctuation. The fluctuation, however, is not localized; disturbances in the form of vortices are shed at the trailing edge of the trip at a particular frequency

and convected downstream. The onset of boundary layer transition was matched with the experiment, meaning the convected disturbances were not dissipated by the freestream. The LDSMG-BLTrip solution transitions in a manner similar to the experiment. Once full turbulence has commenced, the magnitude of turbulent wall heat transfer predicted by the boundary layer tripped LES matches the experimental and empirical data. However, it should be noted that the wall heat transfer gradients of the tripped and untripped LES are essentially identical.

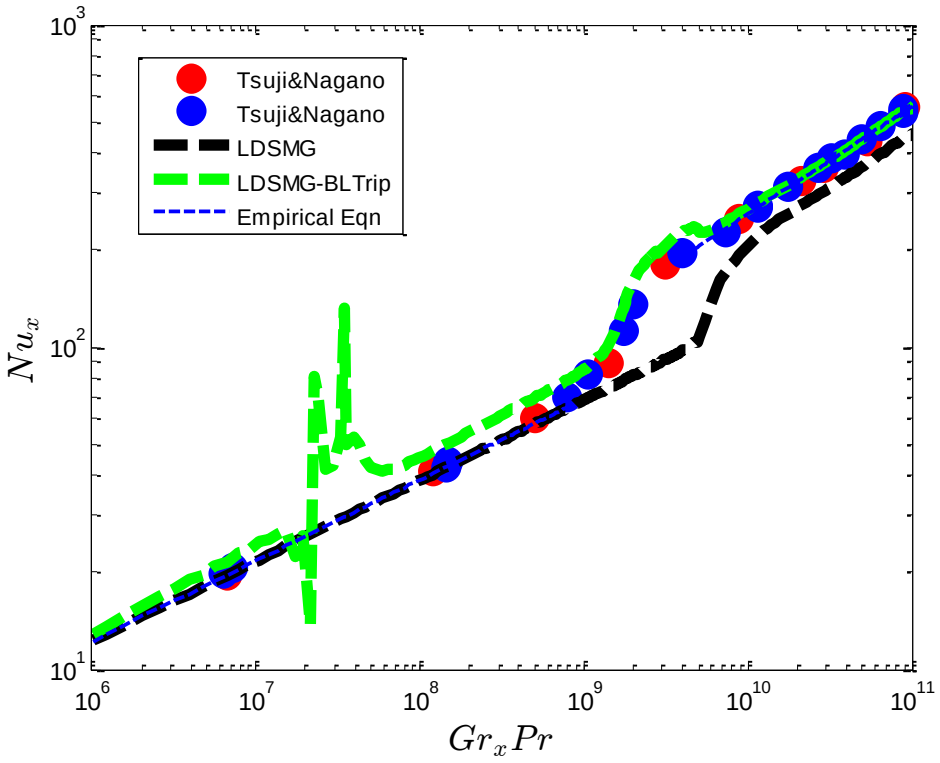

Figure 5.19 Local heat transfer rates showing effects of tripping boundary layer.

Mean velocity and temperature profiles

The wall mean profiles of streamwise velocity and temperature can be seen in Figures 5.20 and 5.21. In Figure 5.20, the comparison between the LDSMG and LDSMG-BLTrip is nearly indistinguishable in the inner and outer layers of the boundary layer. Furthermore, it is apparent that the two LES computations approximate the boundary layer thickness identically. This clearly illustrates that the growth of the turbulent boundary layer thickness, δ, beyond the transition region is a reasonable measure to consider when performing comparisons with experiments that entail a laminar-turbulent transition. The mean temperature profiles seen in Figure 5.21 similarly show the comparison is exact between the LES computations.

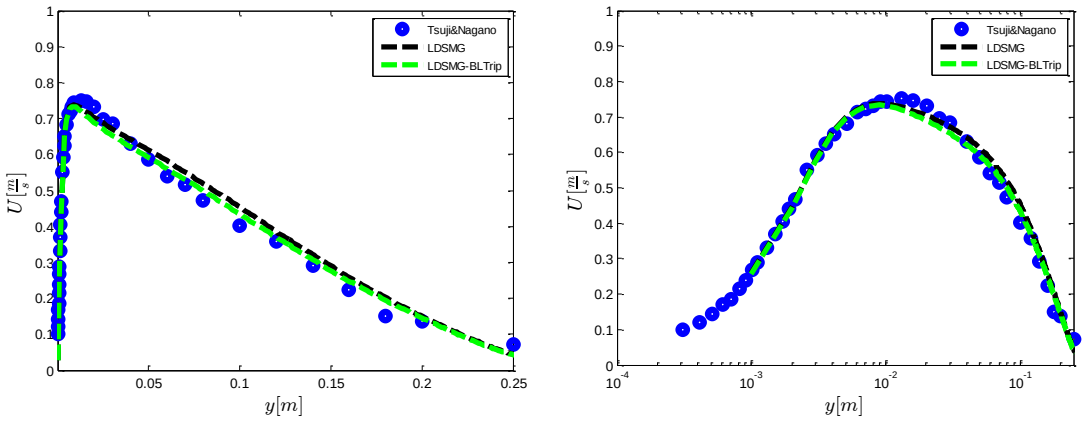

Figure 5. 20 Mean streamwise velocity profiles comparing wall profiles of numerical and tripped boundary layer transition LES.

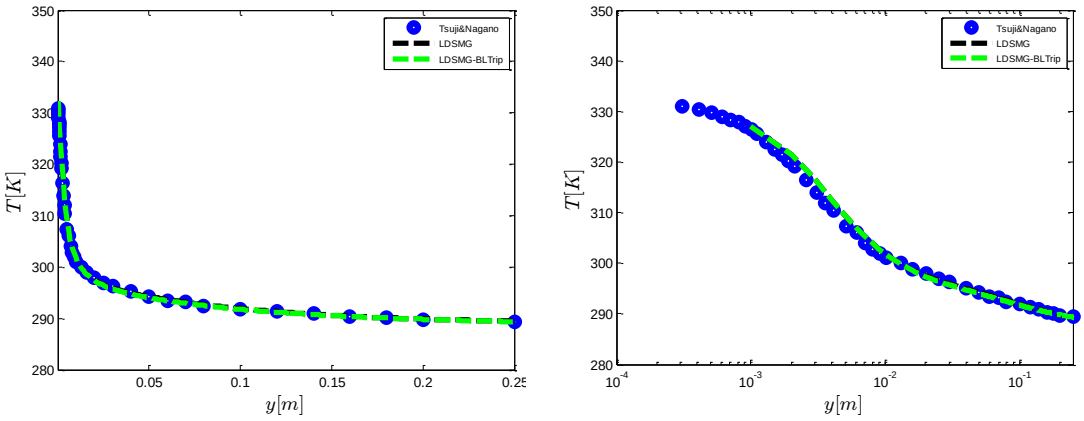

Figure 5. 21 Mean temperature profiles comparing wall profiles of numerical and tripped boundary layer transition LES.

Intensities of temperature and velocity fluctuations

The intensity of temperature fluctuation intensity can be seen in Figure 5.22; the comparison between the numerical simulations is exact in the inner and outer layers of the turbulent boundary layer. In Figures 5.23 and 5.24, the streamwise and wall-normal velocity fluctuation intensities are shown and the comparisons are nearly exact. Both figures do illustrate really small differences between the LES results in the outer layer. Nonetheless, the numerical predictions of the numerical and forced transition results are in excellent agreement.

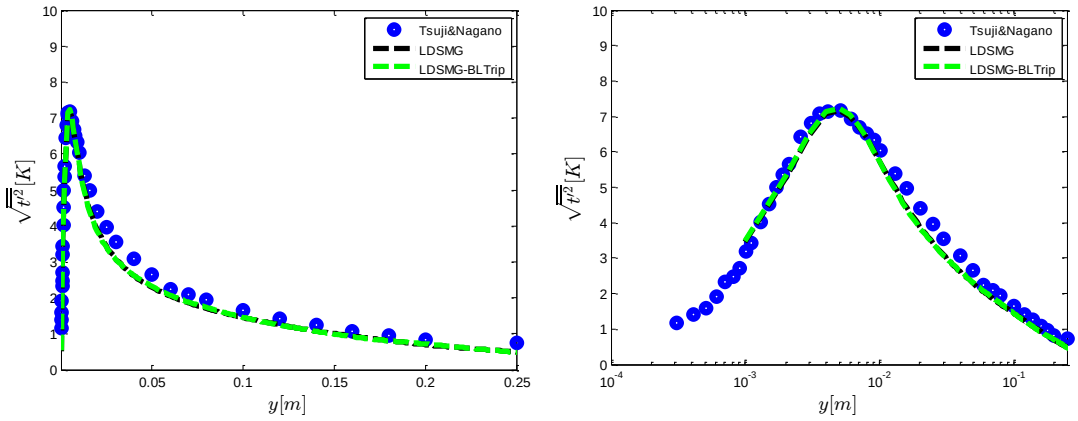

Figure 5.22 Intensity of temperature fluctuation profiles comparing wall profiles of numerical and tripped boundary layer transition LES.

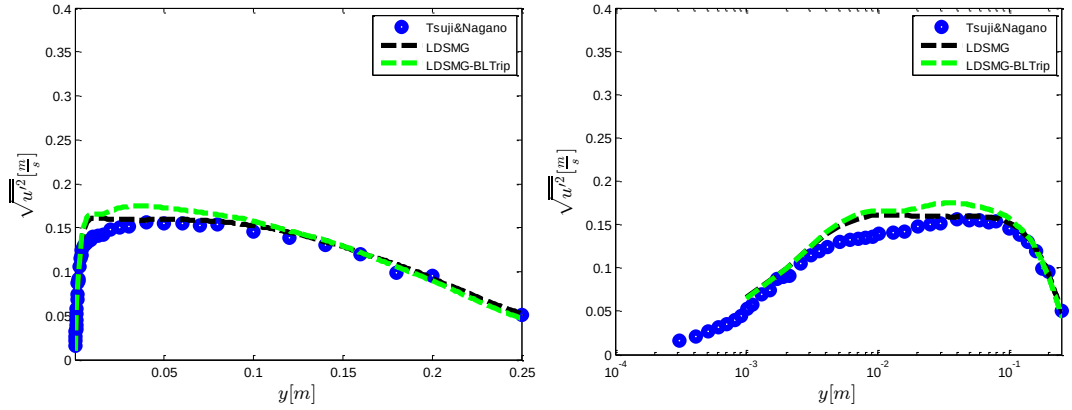

Figure 5. 23 Intensity of streamwise velocity fluctuation profiles comparing wall profiles of numerical and tripped boundary layer transition LES.

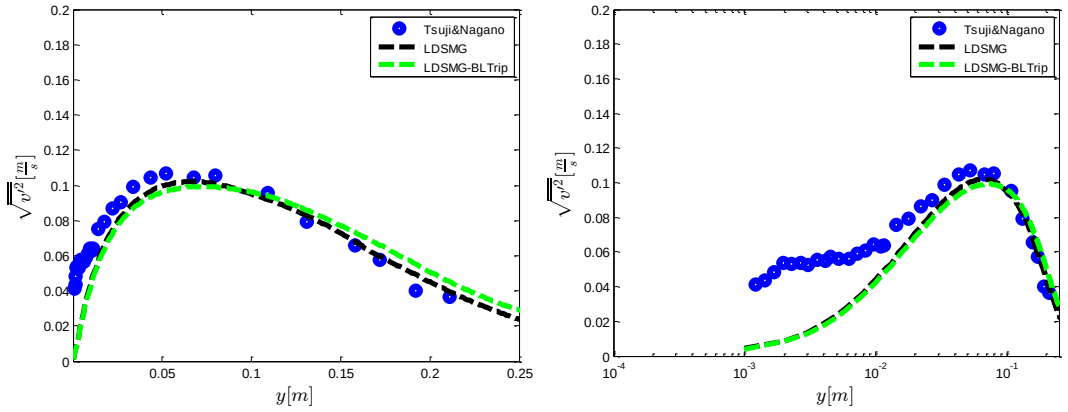

Figure 5. 24 Intensity of wall-normal fluctuation profiles comparing wall profiles of numerical and tripped boundary layer transition LES.

Reynolds shear stress and Turbulent heat fluxes

The Reynolds shear stress profiles are depicted in Figure 5.25 and excellent agreement between the two LES computations is apparent. The predictions in the inner and outer layers can be seen to be indistinguishable. Figures 5.26 and 5.27 show the streamwise and wall-normal turbulent heat fluxes; the comparison is exact in the inner layer for both components of the turbulent heat fluxes. Even though small differences between the LDSMG and LDSMG-BLTrip results can be seen in the outer layer, they are apparently insignificant.

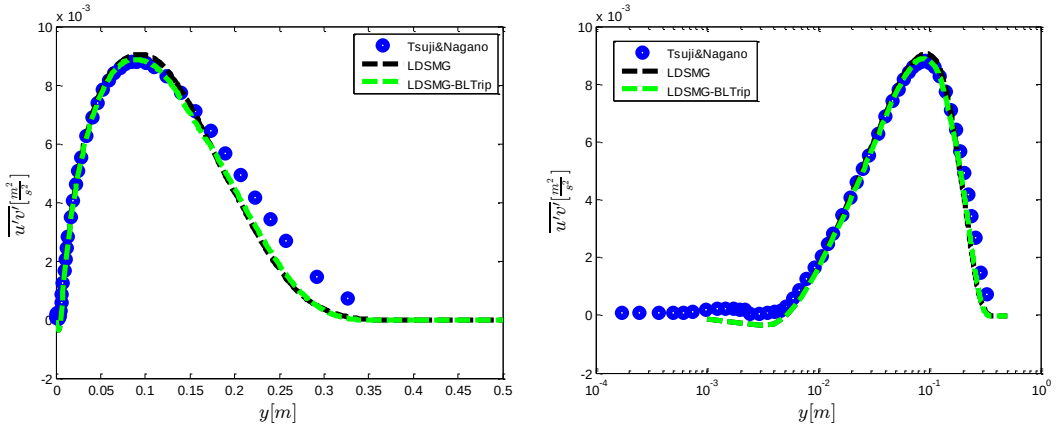

Figure 5. 25 Reynolds shear stress profiles comparing wall profiles of numerical and tripped boundary layer transition LES.

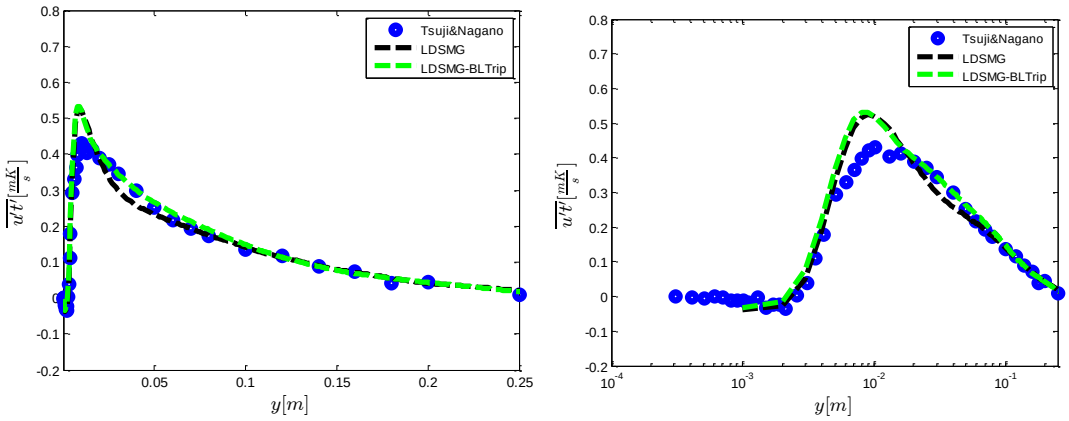

Figure 5. 26 Streamwise turbulent heat flux profiles comparing wall profiles of numerical and tripped boundary layer transition LES.

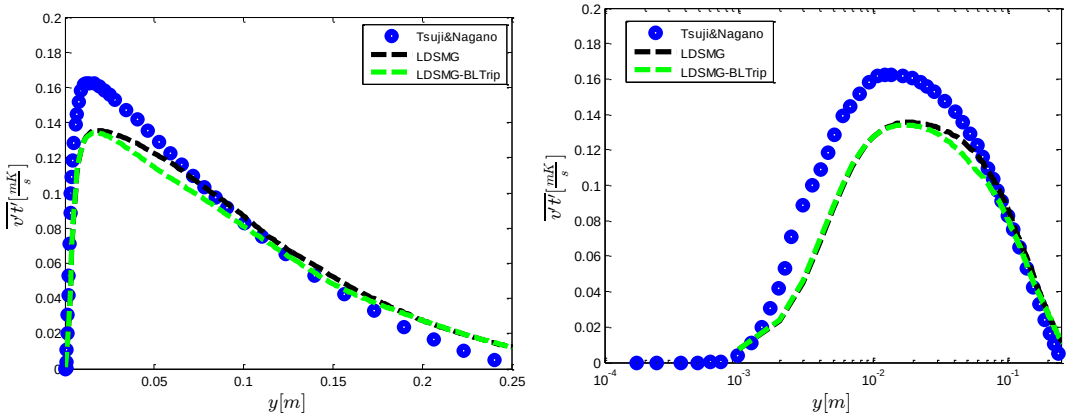

Figure 5. 27 Wall-normal turbulent heat flux profiles comparing wall profiles of numerical and tripped boundary layer transition LES.

Summary of boundary layer trip study

The boundary layer trip study illustrated that the exact location of the transition to turbulence does not have to be captured numerically in order to attain reasonably accurate first and second order statistics. Upon the commencement of full turbulence in the spatially developing boundary layer, the growth of the turbulent boundary layer thickness, δ, is function of streamwise distance. Thus, the present study showed that shifting the location of comparison downstream by the distance the flow "spends" in the fully turbulent boundary layer, is a reasonable physical assumption that lends itself to acquiring high fidelity comparisons with the experimental measurements.

5.4 Wall-Modeled Simulations

The effects of progressively coarser grids on turbulent statistics and eddy structures over the isothermally heated vertical flat plate will be investigated in this section. Aside from the wall resolved computational grid employed in the previous section, which will be referred to here as RLES, the successive levels of coarse grids were employed in conjunction with the wall layer models described in Chapter 4. The results of the under-resolved computational grids will be useful to determine the limit of resolution requirements necessary to produce reasonable LES computations of the natural convection turbulent boundary layers at high Grashof numbers. For this purpose, different grids were constructed for the computational domain described in Figure 5.2. Of these meshes, three were using to gauge the limits of the necessary grid resolution across the boundary layer thickness and the characteristics of these grids are summarized in Table 5.4, with emphasis placed upon the sixth column. For the cases that employed wall modeling, it should be noted that the wall-normal coarsened mesh was only applied downstream of the transition to turbulence region, around $Gr_x = 10^{10}$, at x = 1.5 m.

Prior to discussing the wall-modeled LES results, it would be wise to state that with the utilization of wall-models, numerical errors will be inherently introduced near the wall as the grid is progressively coarsened. This is due to the input-output nature of the LES wall model [134]. Essentially, the implemented wall model will take some instantaneous data/information from the LES at some computational node above the wall at each time-step. Subsequently, the wall model takes this data and uses it to calculate the wall heat flux and wall shear stress. These quantities are then

fed into an equation to approximate the SGS thermal diffusivity and eddy viscosity at the wall. Thus, the problem lies in the fact that, as the mesh is progressively coarsened, the data given to the wall model will be erroneous unresolved data.

Case no.	Wall-Model	Δx (mm)	Δy (mm)	Δz (mm)	**# Cells in boundary layer**
1	RLES	30	1	5	**120**
2	ErfWF	30	5	5	**35**
3	BWF	30	5	5	**35**
4	ErfWF	30	10	5	**15**
5	BWF	30	10	5	**15**
6	ErfWF	30	15	5	**10**
7	BWF	30	15	5	**10**

Table 5. 4 Mesh densities, varying wall-normal grid spacings in fully developed turbulent flow region of boundary layer.

Local heat transfer rates

The heat transfer rate along the heated flat plate of all the cases given in Table 5.4 can be seen in Figure5.28 along with the experimental data. The transition location is identical for all these cases solely because the mesh and computational set-up were the same up to $Gr_x = 10^{10}$. Beyond $Gr_x = 10^{10}$, we can see that the LES wall models predicted higher heat transfer than the resolved LES solution. The equation given previously to compute the wall heat transfer rate is a function of the molecular and SGS thermal diffusivities and will be repeated here for convenience:

$$Nu_{\mathrm{x}} = \frac{\mathrm{x}\dfrac{(\alpha_{SGS}+\alpha)}{\alpha}\dfrac{\partial \overline{\mathrm{T}}}{\partial y}\Big|_{w}}{\Delta \mathrm{T}}$$

Thus, the higher heat transfer given by coarser meshes can be attributed to the increase in the near wall SGS thermal diffusivity as the mesh is progressively coarsened. Essentially, as the grid is coarsened, increasingly larger eddies that are unresolvable on the LES mesh has to be accounted for by the SGS turbulence model. Hence, instead of resolving "mostly" dissipative small turbulence scales, the subgrid scale model is also resolving large energy containing eddies near the wall region.

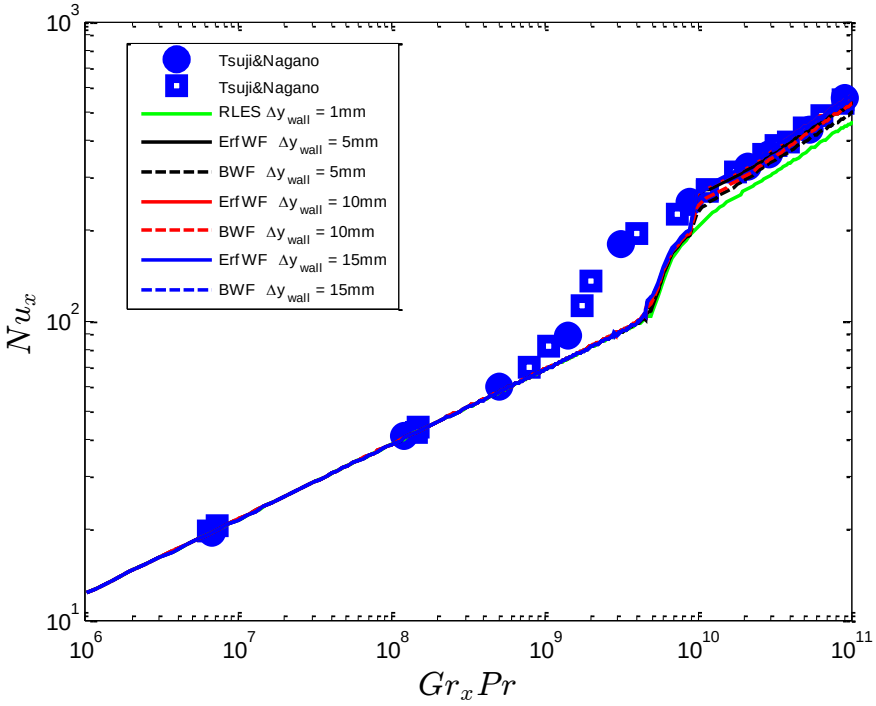

Figure 5. 28 Local heat transfer rates comparison.

Mean velocity and temperature profiles

Profiles of the mean streamwise velocity can be seen in Figure 5.29. It is apparent that results acquired from the ErfWF and BWF are quite similar, with hardly any

profound differences. The agreement between the wall-modeled and resolved LES is certainly acceptable. It should be noted that the first grid point off the wall for the two coarsest meshes lies within the outer layer of the boundary layer. The wall-modeled predictions are in good agreement with the experimental data, although the two coarsest grids fractionally underpredicted the streamwise velocity in the outer layer. The mean temperature profiles can be seen in Figure 5.30; the predictions of the wall-modeled LES computations are in good agreement with the experiment in the inner and outer layer of the boundary layer. Again, the differences between the ErfWF and BWF results are quite marginal.

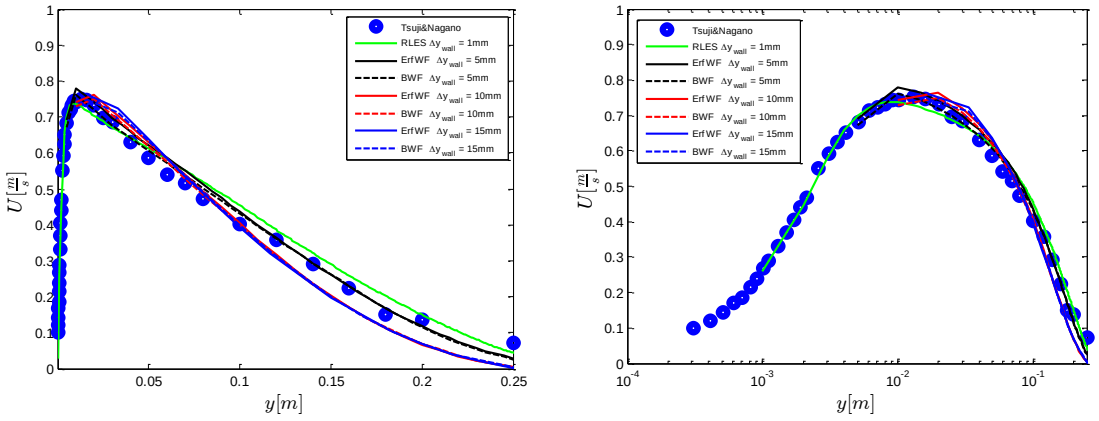

Figure 5. 29 Mean streamwise velocity profiles at $Gr_x \sim 1.8E+11$ for various near-wall turbulence treatments.

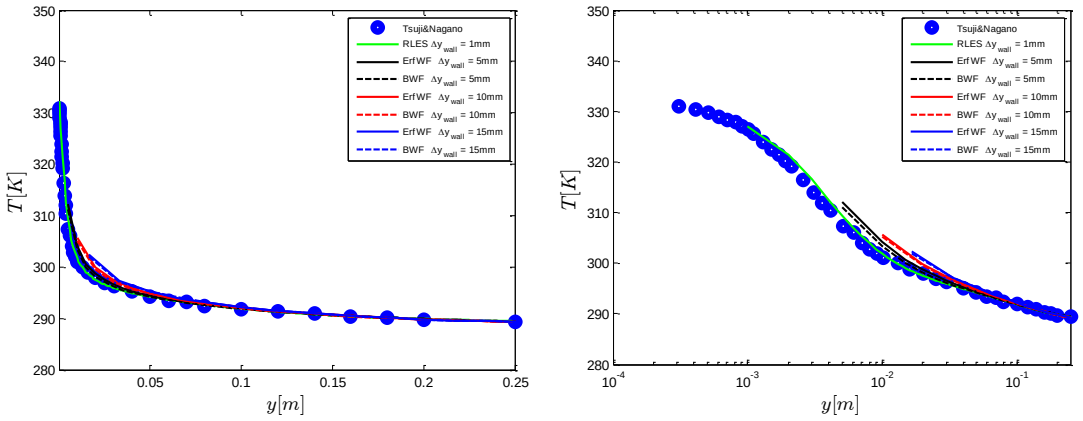

Figure 5. 30 Mean temperature profiles at $Gr_x \sim 1.8E+11$ for various near-wall turbulence treatments.

Intensities of temperature and velocity fluctuations

The temperature fluctuation intensity profiles are illustrated in Figure 5.31. The second order turbulent statistics predictions of both wall models are in good agreement with the experiment. For the $\Delta y_{wall} = 5mm$ wall case, the inner layer region was underpredicted by both wall models. However, in the outer layer, all the wall modeled LES results were quite comparable to the measurements. Figure 5.32 depicts the streamwise velocity fluctuation intensity profile and it readily apparent that the wall modeled LES results overpredicted $\sqrt{\overline{u'^2}}$ in the outer layer region. The inner layer was similarly overpredicted by the $y_{wall} = 5$mm mesh; this behavior is well known to be a symptom of under-resolved LES computations [135]. It is essentially caused by the inability of the coarse LES grid to capture the fine near-wall turbulence producing dynamics. The near-wall profiles of wall-normal velocity fluctuation intensity, $\sqrt{\overline{v'^2}}$, are shown in Figure 5.33. We can see that by successively coarsening the grid, $\sqrt{\overline{v'^2}}$ is further underpredicted in the outer layer.

An interesting phenomenon intrinsic to coarse LES computations can be observed by carefully assessing the normal stresses, namely $\sqrt{\overline{u'^2}}$ and $\sqrt{\overline{v'^2}}$ depicted in Figures 5.32 and 5.33. These two figures clearly show that as the mesh resolution is coarsened, $\sqrt{\overline{u'^2}}$ increases and $\sqrt{\overline{v'^2}}$ decreases, especially near the wall. In order to explain this, it should be noted that turbulence is typically introduced into the flowfield in the dominant fluctuating flow component, which is the streamwise direction. Subsequently, the turbulent energy is transferred to the other fluctuating components (inter-component transfer of turbulent energy) [136]. In light of this, one can surmise that mean flow energy is transferred to the fluctuating component in the streamwise direction, $\sqrt{\overline{u'^2}}$ and the turbulent energy is then distributed to the other components, $\sqrt{\overline{v'^2}}$ and $\sqrt{\overline{w'^2}}$. However, in LES, as the mesh is progressively coarsened, the mechanism of distributing turbulent energy from $\sqrt{\overline{u'^2}}$ to $\sqrt{\overline{v'^2}}$ and $\sqrt{\overline{w'^2}}$ is poorly resolved [137]. As a result, $\sqrt{\overline{u'^2}}$ becomes increasingly overestimated and $\sqrt{\overline{v'^2}}$ is further underpredicted, as can be seen Figures 5.32 and 5.33. As a whole, there is good agreement between the LES wall model results and the experimental data. Thus, all the cases illustrated good agreement of temperature and velocity fluctuation intensity when compared to the experiment.

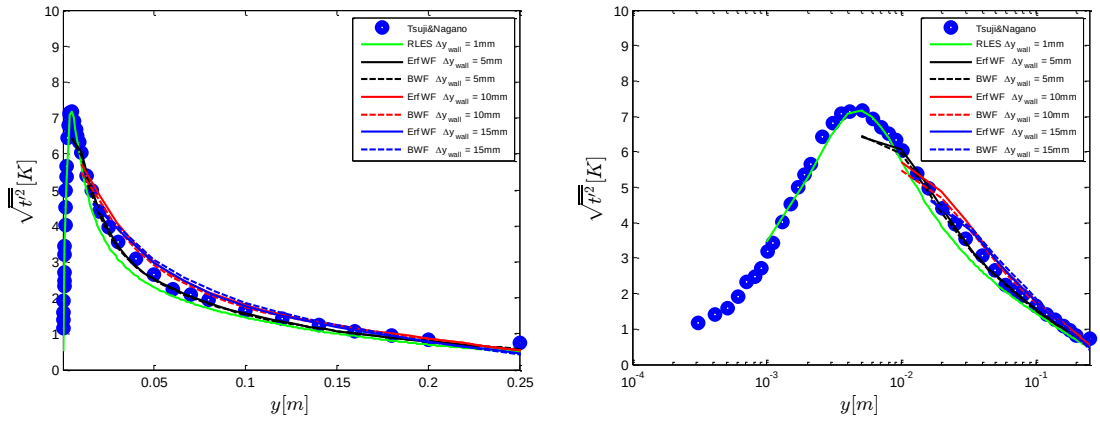

Figure 5. 31 Intensity of temperature fluctuation profiles at Gr_x ~ 1.8E+11 for various near-wall turbulence treatments.

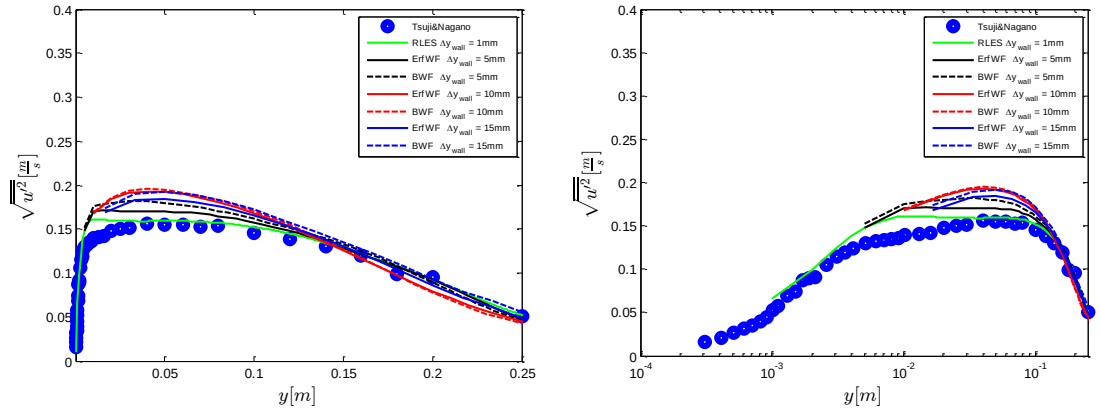

Figure 5. 32 Intensity of streamwise velocity fluctuation profiles at Gr_x ~ 1.8E+11 for various near-wall turbulence treatments.

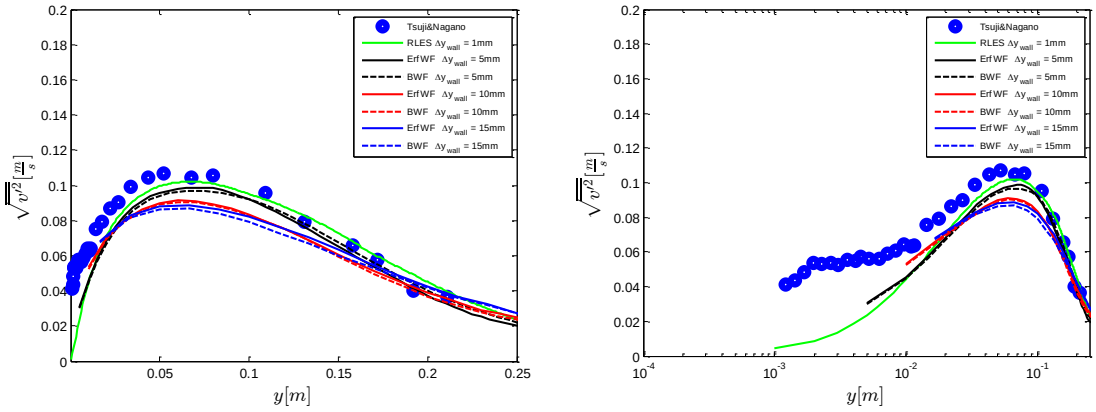

Figure 5. 33 Intensity of wall-normal velocity fluctuation profiles at $Gr_x \sim 1.8E+11$ for various near-wall turbulence treatments.

Reynolds shear stress and Turbulent heat fluxes

Figure 5.34 shows the Reynolds shear stress profiles of the experimental data, resolved LES and coarse grid wall-modeled LES results. For this turbulent quantity, apparent differences between the wall models are quite distinct in the outer layer region. Along with the resolved LES results, all the coarse LES computations slightly underpredicted the Reynolds shear stress in the outer layer. The wall-modeled results are also reasonably in good agreement with the measurements.

Figures 5.35 and 5.36 depict the streamwise turbulent and wall-normal heat fluxes. The two coarsest meshes overpredicted $\overline{u't'}$ in the outer layer of the boundary layer. The predictions of all of the LES wall models are in good agreement with the experimental data. Especially for the two coarsest meshes, the ability to reasonably capture the complex dynamics of the correlation between u' and t' with only a few points within the boundary speaks to the validity of the wall models. Similarly, in Figure 5.36, the predictions of $\overline{v't'}$ made by the coarse LES wall models are in good agreement with the measurements.

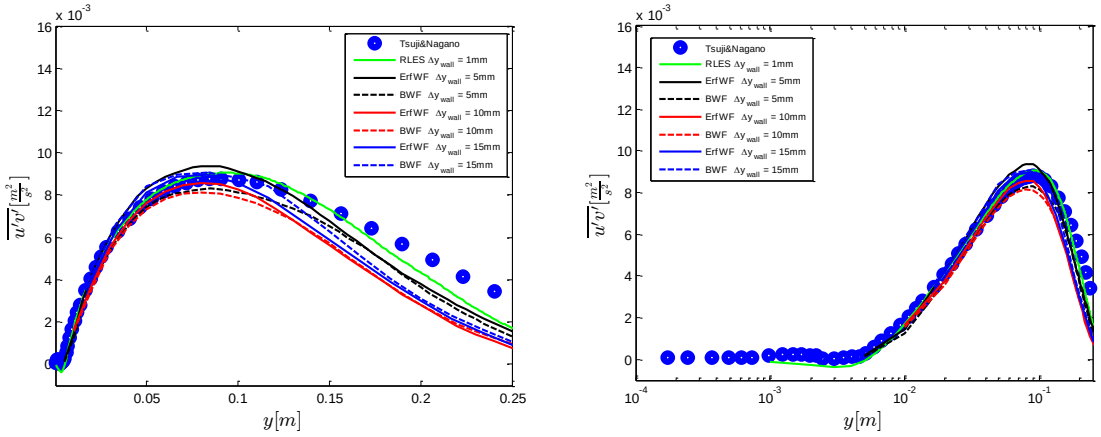

Figure 5. 34 Reynolds shear stress profiles at Gr_x ~ 1.8E+11 for various near-wall turbulence treatments.

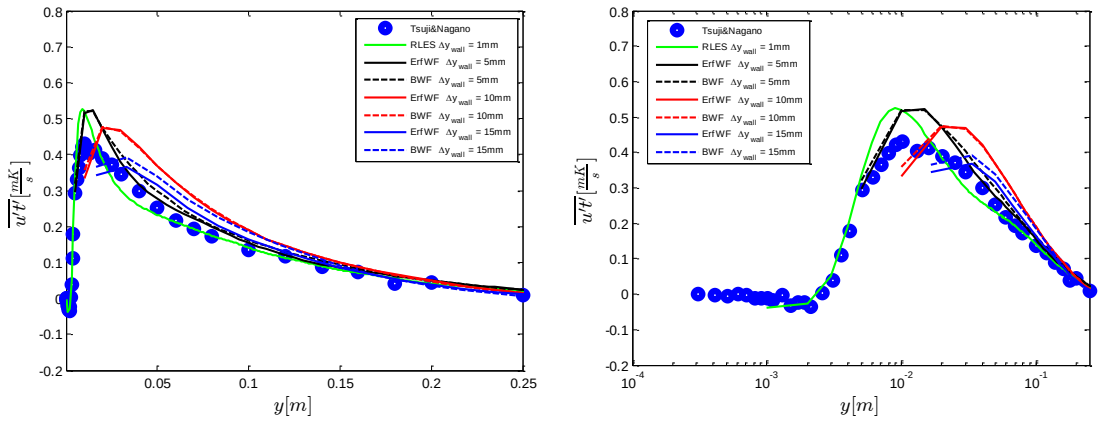

Figure 5. 35 Streamwise turbulent heat flux profiles at Gr_x ~ 1.8E+11 for various near-wall turbulence treatments.

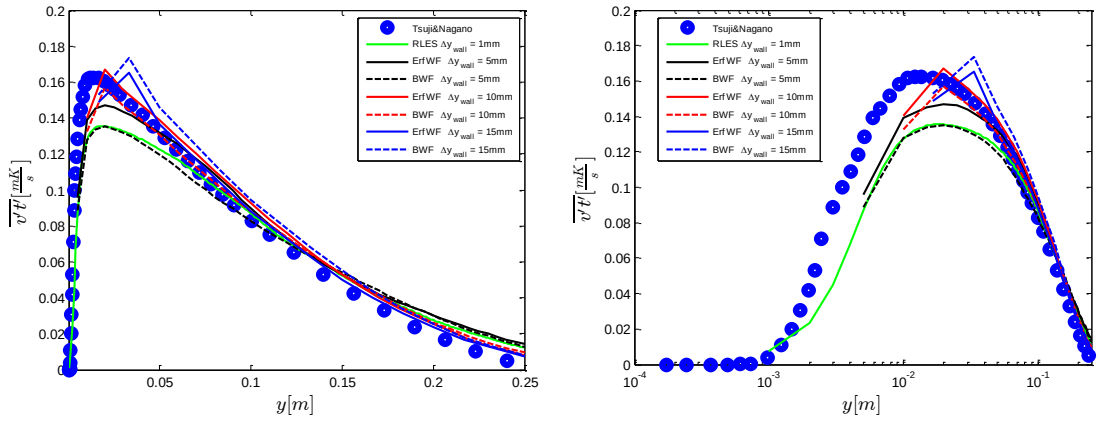

Figure 5. 36 Wall-normal turbulent heat flux profiles at $Gr_x \sim 1.8E+11$ for various near-wall turbulence treatments.

Near- Wall Turbulent Structures

The effects of grid resolution on the instantaneous near-wall turbulent structures are illustrated in Figures 5.37 and 5.38. To perform this analysis, the ErfWF wall model was employed along with the resolved LES computation. On the finest mesh, RLES $\Delta y_{wall} = 1$ mm, long strands of vortical structures can be seen oriented predominantly in the streamwise direction. These structures, educed from the $Q > 0$ criterion, do not seem to have the similar formation as those observed near the wall in forced convection turbulent boundary layer. Overlapping and tilted coherent structures are not apparent in the near-wall topology of the natural convection turbulent boundary layer. Furthermore, a densely packed set of near-wall structures are observable on the finest mesh. On the second finest mesh, ErfWF $\Delta y_{wall} = 5$ mm, we easily see a less dense near-wall coherent structure field. The near-wall turbulent structures can be seen to be relatively oriented predominantly in the streamwise direction. Another observation is the appearance of larger near-wall structures with this coarsened mesh simulation. In Figure 5.38, isosurfaces of the

$Q > 0$ criterion near the wall for the two coarsest meshes are depicted. For the ErfWF $\Delta y_{wall} = 10$ mm case, a progressively enlargement of the near-wall structures can be seen. In addition, turbulent structures seem to be absent near the wall and the streamwise orientation of the structures is non-existent. At the coarsest mesh, ErfWF $\Delta y_{wall} = 15$ mm , the near-wall structures are more enlarged and no preferred direction of the coherent structures can be ascertained. These near-wall vortex structures seem to lack any coherence and it is apparent that this computational mesh may be too coarse to capture any physical turbulent dynamics near the wall. The enlargement of the near-wall turbulent structures with progressively coarser grids is caused by an over-compensation for their lack of resolution due the excess energy contained in the large scales. Thus, larger pseudo-turbulent near-wall structures are created. Moreover, this phenomenon is indicative of insufficient turbulent dissipation and the subsequent inaccurate SGS turbulent viscosity predictions of coarse mesh LES computations.

Figure 5. 37 Instantaneous isosurface of the second invariant of the velocity gradient tensor, $Q > 0$, (left) RLES $\Delta y_{wall} = 1$ mm, (right) ErfWF $\Delta y_{wall} = 5$ mm at $y^{\times} \approx 10$.

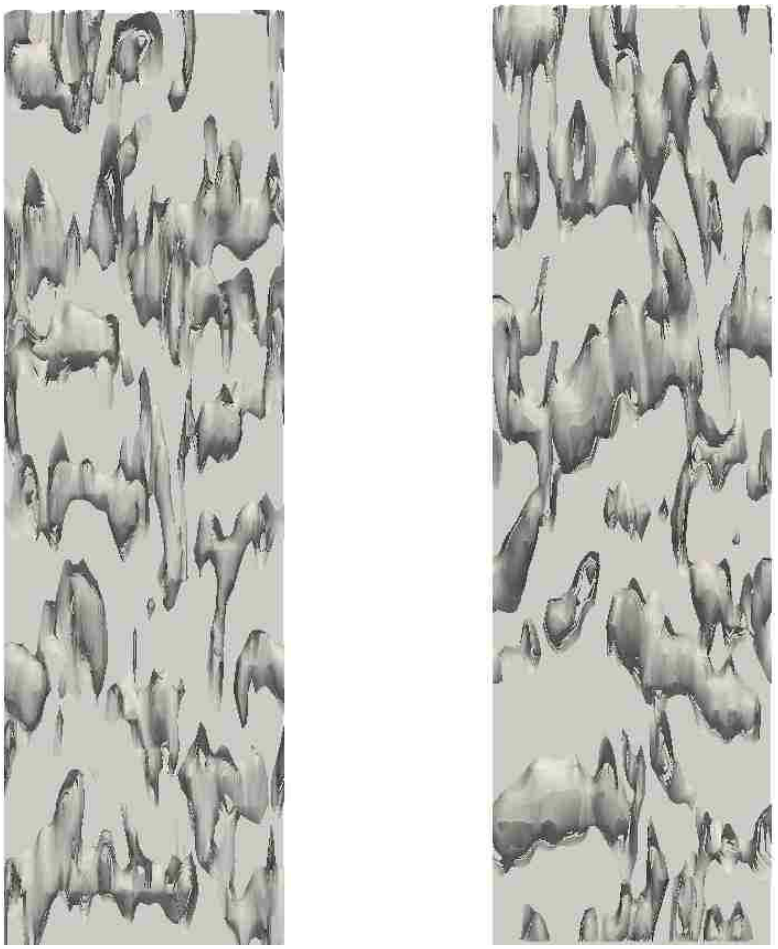

Figure 5. 38 Instantaneous isosurface of the second invariant of the velocity gradient tensor, Q > 0, (left) ErfWF $\Delta y_{wall} = 10$ mm, (right) ErfWF $\Delta y_{wall} = 15$ mm at $y^{\times} \approx 10$.

We can take a look at the turbulent energy spectrum of the resolved streamwise velocity fluctuations shown in Figure 5.38 to further illustrate effects of coarsened mesh on the LES calculations. The aforementioned plot is of one-dimensional spectra representation of the turbulent kinetic energy at $y^{\times} = 5$, which corresponds to $y = 5$ mm.. It is obvious from Figure5.38 that dissipation of turbulent eddies takes place at higher wavenumbers for the resolved LES result, shown in the red colored line. In addition, at lower wavenumbers, the energy content of the

resolved LES computation is lower than all the LES wall-modeled simulations. A close examination of Figure 5.39 indicate that dissipation of turbulent eddies occurs at slightly larger wavenumbers with successively coarsened grids. Furthermore, it can be seen that the coarse wall-modeled LES computations have significantly excess energy at the lower wavenumbers, i.e. large scale eddies. This observation is consistent with the coherent vortex structure visualizations of Figures 5.37 and 5.38.

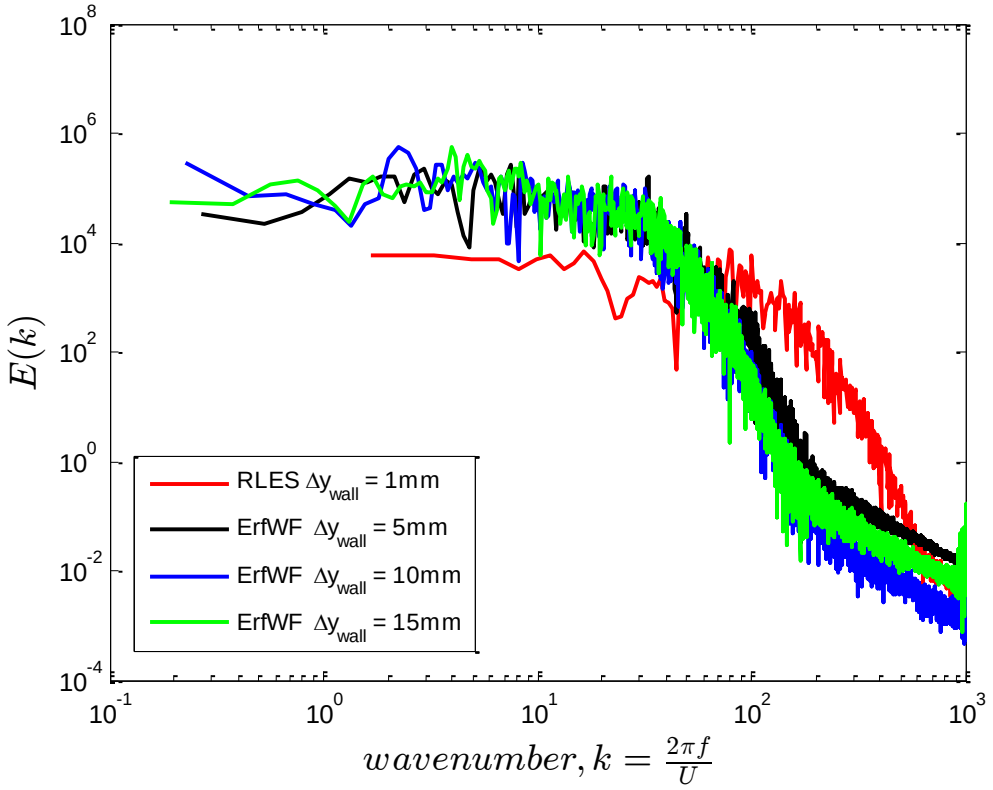

Figure 5. 39 One dimensional energy spectrum of resolved streamwise velocity fluctuations at $\mathbf{y}^{\times} = \mathbf{5}$.

5.5 Waveforms for Thermal Fields

Waveforms of the temperature fluctuation field starting at $Gr_x = 8.3 \times 10^{10}$, x = 2.4 m, are depicted in Figure 5.40. The computational probes were implemented at the streamwise locations listed in the aforementioned figure at the center of the heated flat plate, i.e. $z = 0.15$ m and a wall-normal distance of 1.7 mm. From Figure 5.40, it is apparent that a well preserved thermal turbulent field exists in the streamwise direction spanning nearly 10 cm. In Figure 5.41, a plot identical to Figure 5.40 is shown, except the instantaneous temperature is depicted with identical turbulent fluctuations.

Waveforms of the temperature fluctuation in the wall-normal direction at $Gr_x = 8.3 \times 10^{10}$ can be seen in Figure 5.42. The waveforms illustrate that high $(t' > 0)$ and low $(t' < 0)$ temperature fluid encompass the near wall boundary layer region. Up to 4.4 mm, it is apparent that low temperature fluids frequently invade the near wall region. Farther away from the wall, low temperature fluid signals become nearly non-existent. As opposed to the low temperature fluid, high temperature fluid can be seen near the wall and also farther away from the wall. However, the amplitude of high temperature fluid signal diminishes as the wall normal distance increases. Identical waveforms of instantaneous temperature can be seen in Figure 5.43. In addition to the temperature fluctuations, these waveforms include the average temperature at the probed location and are shown to only illustrate the magnitude of temperature at the various locations.

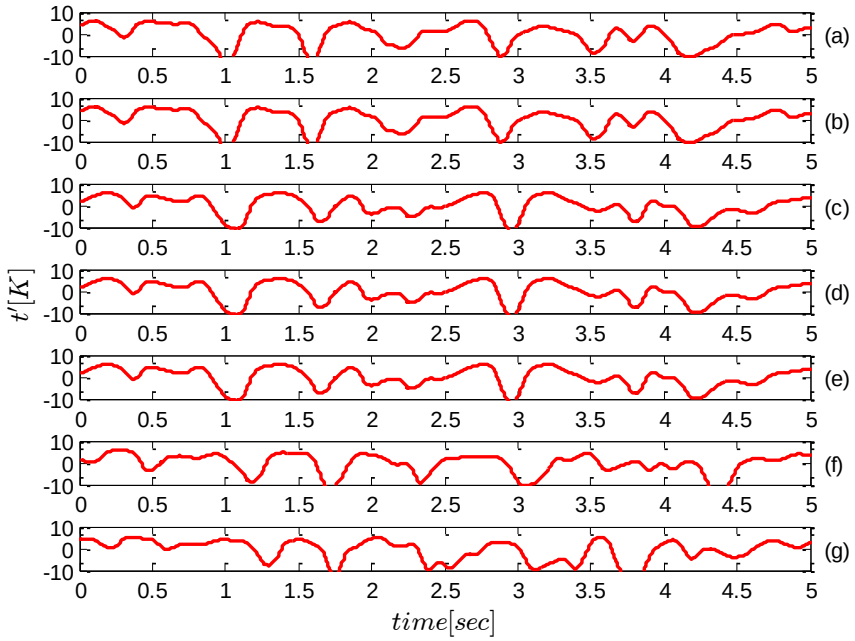

Figure 5. 40 Waveforms of temperature fluctuations in the streamwise direction; locations are :(a) = 2.4 m, (b) = 2.4012 m, (c) = 2.4039 m, (d) = 2.4068 m, (e) = 2.411 m, (f) = 2.438 m, (g) = 2.486 m.

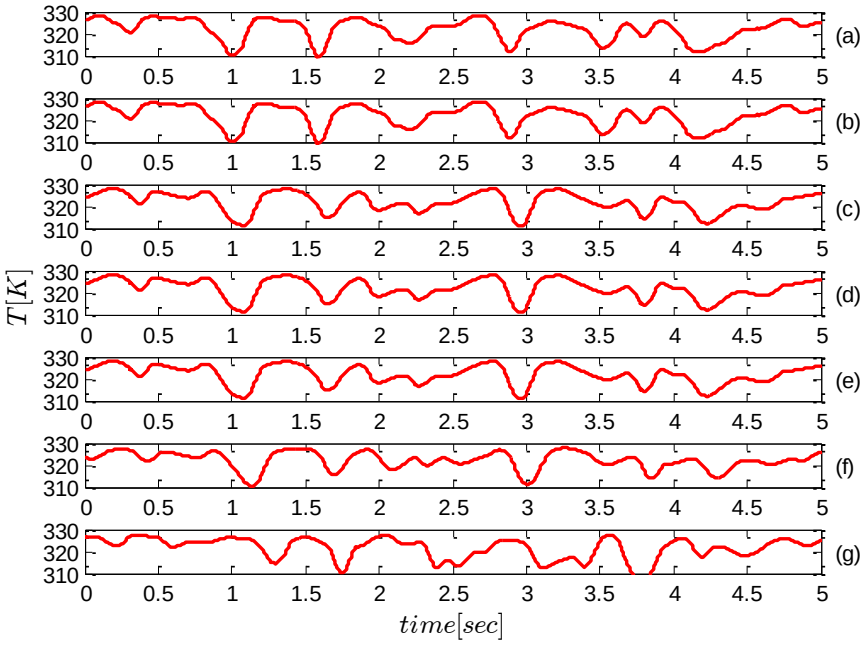

Figure 5. 41 Waveforms of instantaneous temperature in the streamwise direction; locations are :(a) = 2.4 m, (b) = 2.4012 m, (c) = 2.4039 m, (d) = 2.4068 m, (e) = 2.411 m, (f) = 2.438 m, (g) = 2.486 m.

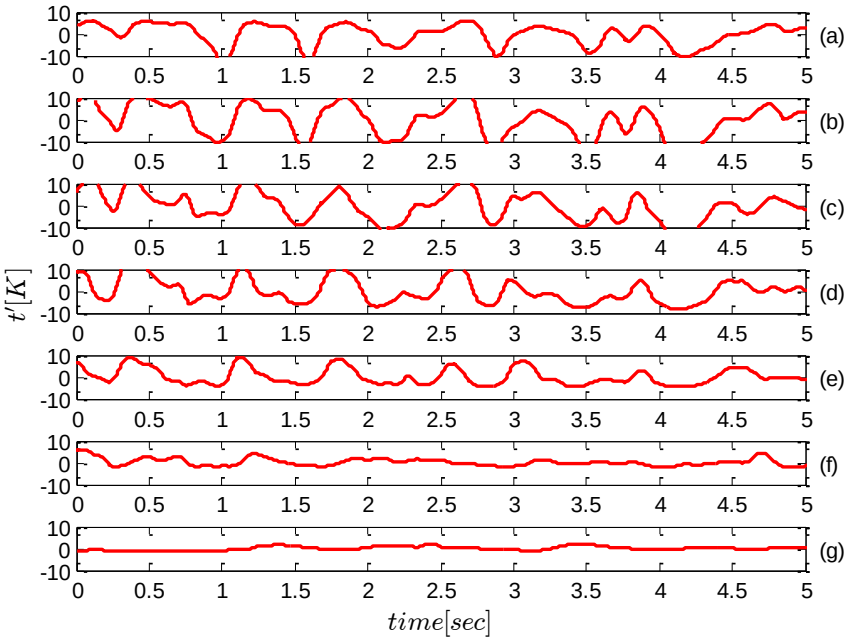

Figure 5. 42 Waveforms of temperature fluctuations in the normal direction at $\mathbf{Gr_x = 8.3 \times 10^{10}}$; wall-normal locations are :(a) = 0.4 mm, (b) = 1.7 mm, (c) = 4.4 mm, (d) = 7 mm, (e) = 12 mm, (f) = 38 mm, (g) = 86 mm.

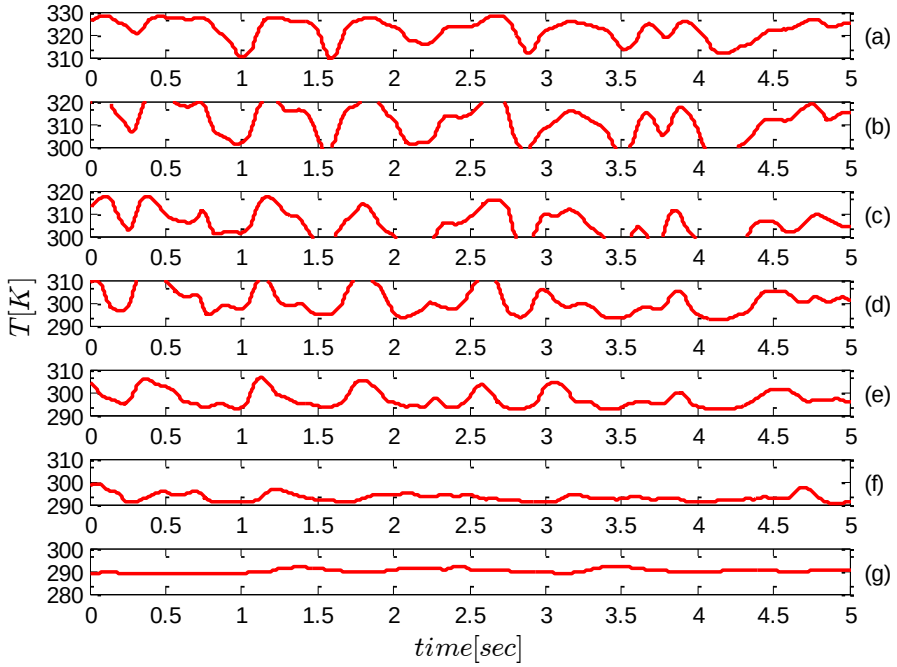

Figure 5. 43 Waveforms of instantaneous temperature in the normal direction at $\boldsymbol{Gr_x = 8.3 \times 10^{10}}$; wall-normal locations are :(a) = 0.4 mm, (b) = 1.7 mm, (c) = 4.4 mm, (d) = 7 mm, (e) = 12 mm, (f) = 38 mm, (g) = 86 mm.

5.6 Turbulent Kinetic Energy

Before closing the discussion on the results acquired in this chapter, a discussion is profoundly warranted on the turbulent kinetic energy intrinsic to buoyancy affected spatially developing turbulent boundary layer. In light of this, the turbulent kinetic energy was numerically computed and the LES results, along with the experimental data are presented in Figures 5.44 and 5.45 at a streamwise location of $Gr_x = 8.9 \times 10^{10}$, i.e. x = 2.53 m. The comparison between the LES and measurements is very good in the inner and outer layers. It is apparent that turbulent kinetic energy peaks in the outer layer of the boundary, as opposed to forced convection turbulent boundary layers. It was aforementioned and illustrated in Chapter 2 that the turbulent kinetic energy peaks in the near-wall region due to the presence of high shear and such a profile is not evident in the natural convection turbulent boundary layer. In order to elucidate upon the mechanisms and physics of the turbulent energy production pertaining to turbulent natural convection boundary layers, we can refer Figure 5.46. Figure 5.46 shows the buoyant and shear productions of turbulent kinetic energy comparison between the measurements and Large Eddy Simulation at $Gr_x = 8.9 \times 10^{10}$. We can see that the buoyant production of turbulence peaks near the edge of the inner layer. In this region, $\frac{\partial \mathrm{U}}{\partial y} = 0$, alluding to the absence of shear production, as can be seen in Figure 5.45. In the outer layer, there is buoyant and shear production of turbulence, although shear production is dominant. The shear production predicted by the LES computation is in excellent agreement with the experimental data. In the outer layer of the boundary layer, there is relatively high shear, $\frac{\partial \mathrm{U}}{\partial y} < 0$, and this shear layer region is a source of turbulent kinetic energy. Also

apparent in Figure 5.46 is the discrepancy between the measured and LES shear production in the inner layer of the boundary layer. The measurement illustrate there is a loss to turbulent kinetic energy production due to shear near the wall. In fact, it was stated by [138], that the velocity-pressure gradient term, $.\nabla p$, found in the components of the turbulent kinetic energy equation, was responsible for the majority of the production near the wall. To clarify, the velocity-pressure gradient term is known to be the cause of inter-component transfer of turbulent kinetic energy and it does not create nor destroy turbulent energy [136]. In the turbulent boundary layer considered in this work, turbulent kinetic energy is produced primarily in the dominant direction of the flow, i.e. streamwise; turbulence enters the system via the shear production term, $-\overline{u'v'}\,\partial U/\partial y$, and buoyant production term, $g\beta\overline{u't'}$, which are the production terms pertaining to the streamwise turbulent kinetic energy equation. Thus, it is the velocity-pressure gradient terms that act to exchange turbulent energy between the three components of turbulent kinetic energy. In the inner layer, Figure 5.46 illustrates that the profile of shear production predicted by the LES is a gain for the turbulent energy. It is obvious that the shear production in the outer layer is larger in magnitude than the inner layer shear production. Even though there are shear layers in the inner and outer layers of the flowfield, the shear production of turbulence near the wall is impeded due the presence of the wall. As opposed to the shear production in the inner layer, large scale eddies are dominant in the outer layer, similar to those observed in free-shear layer turbulent flows. These large scale eddies produce most of the turbulent kinetic energy in the boundary layer.

For comparison, Figure 5.47 depicts shear and buoyant productions of turbulent kinetic energy in a turbulent natural convection boundary layer acquired from the DNS results of [139]. The edge of the inner layer was mentioned to be located at $\frac{y}{\delta} = 10^{-1}$, where $\frac{\partial U}{\partial y} = 0$. The DNS results show there is not any buoyant production of turbulence in the outer layer. In addition, the shear production show two peaks, indicative of the two shear layers within the boundary layer. The profile is quite similar to LES result shown in Figure 5.46. However, in the DNS predictions, the shear production of turbulence in the inner layer is shown to be larger than the outer layer. As was previously discussed, this should not be the case given the presence of the wall in destroying some of the turbulence generated by the deformation of mean motion by the Reynolds stress.

To further shed light upon the apparent discrepancy in the shear production of turbulence between the experimental data and LES, Figure 5.48 shows the Reynolds shear stress wall profiles at $Gr_x = 8.9 \times 10^{10}$. Excellent agreement between the measurement and LES can be seen in the inner and outer layers. The discrepancy lies in the differences between the experiment and LES very near the wall, refer to Figure 5.49. In the near-wall region, the LES computes $\overline{u'v'}$ that is slightly less than zero, whereas the measurement gives $\overline{u'v'}$ higher than zero. Hence, it can be conjectured that since the inner layer is profoundly thin, the accuracy of the measurements near the wall might be questionable to some degree.

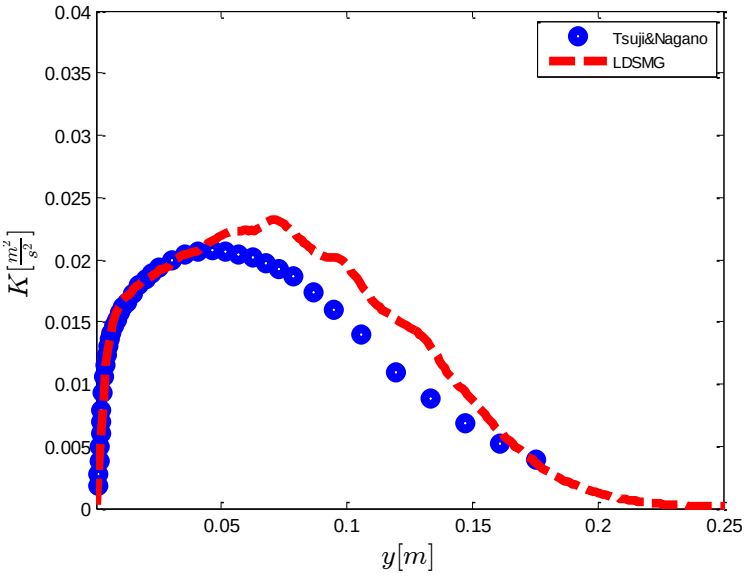

Figure 5. 44 Mean turbulent kinetic energy comparison between measurements and LDSMG in linear scale at $\mathrm{Gr_x} = 8.9 \times 10^{10}$.

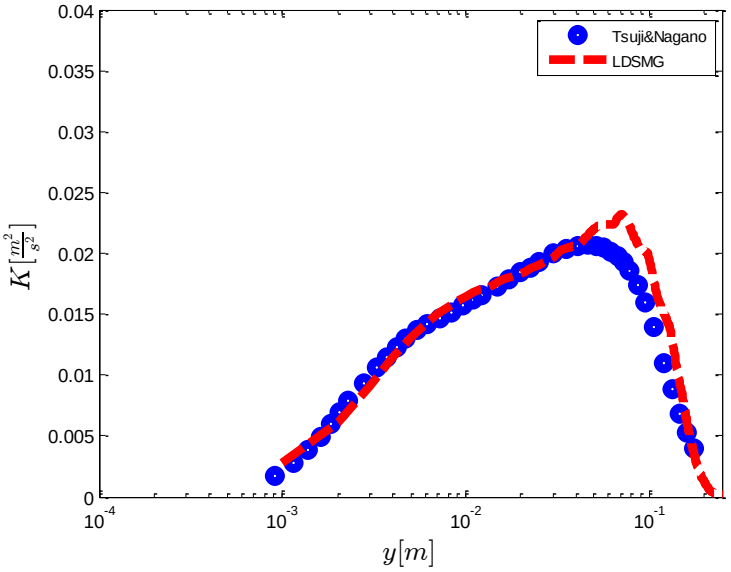

Figure 5. 45 Mean turbulent kinetic energy comparison between measurements and LDSMG in semi-log scale at $\mathrm{Gr_x} = 8.9 \times 10^{10}$.

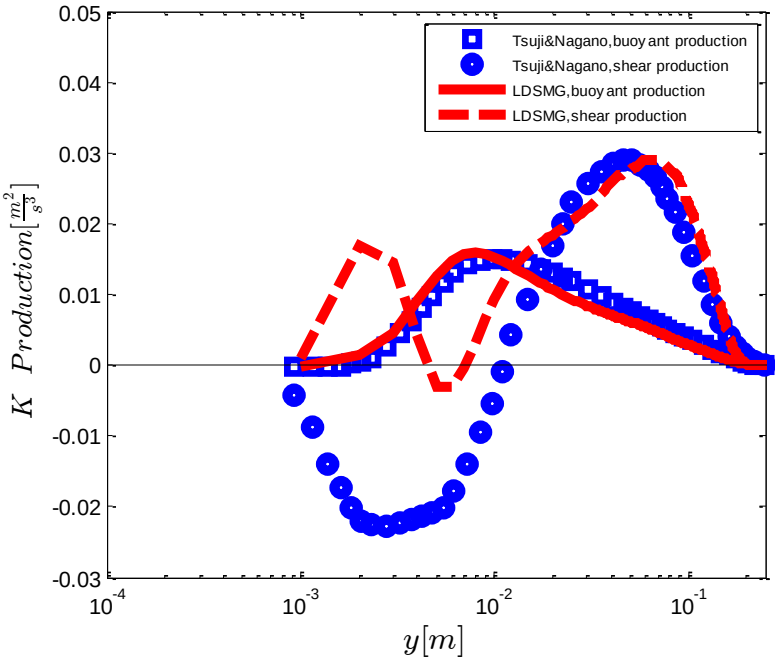

Figure 5. 46 Turbulent kinetic energy production comparisons of measurements and LDSMG at $\mathrm{Gr_x} = 8.9 \times 10^{10}$.

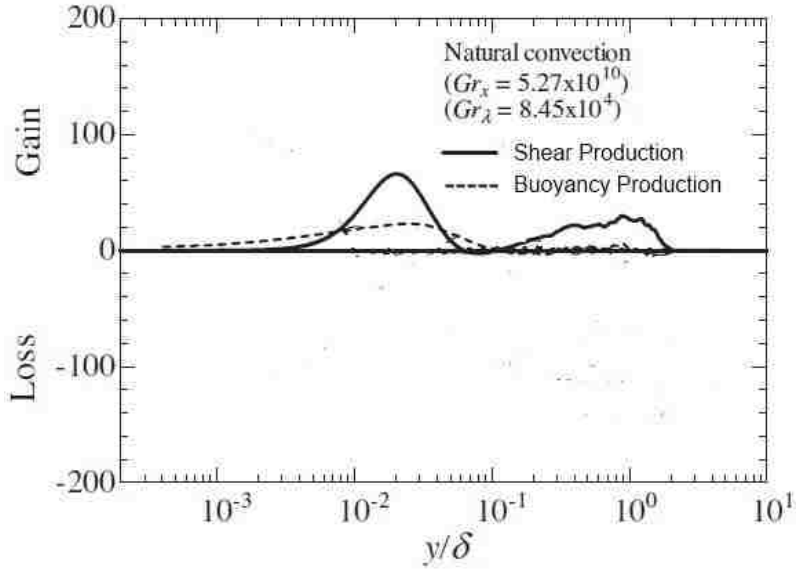

Figure 5. 47 Turbulent kinetic energy productions of shear and buoyancy mechanisms acquired from DNS computations of [139].

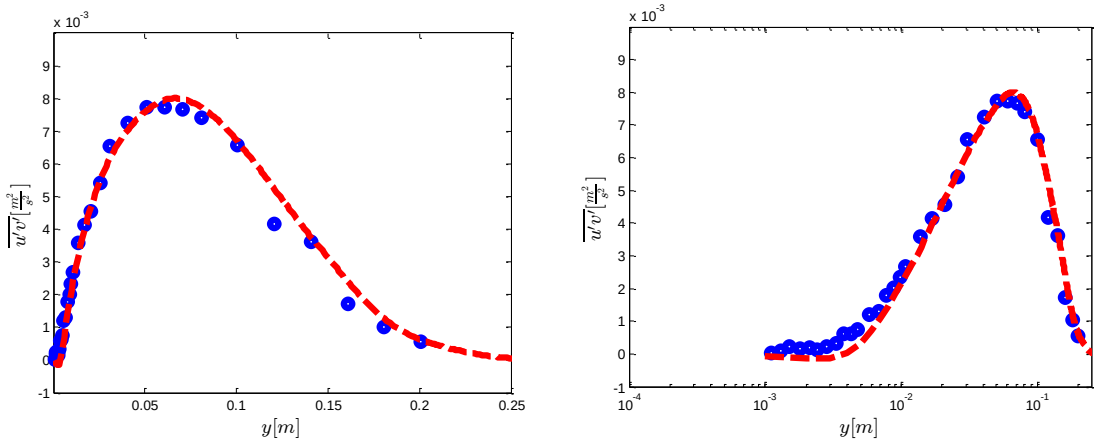

Figure 5. 48 Reynolds shear stress profiles at $\mathrm{Gr_x} = 8.9 \times 10^{10}$.

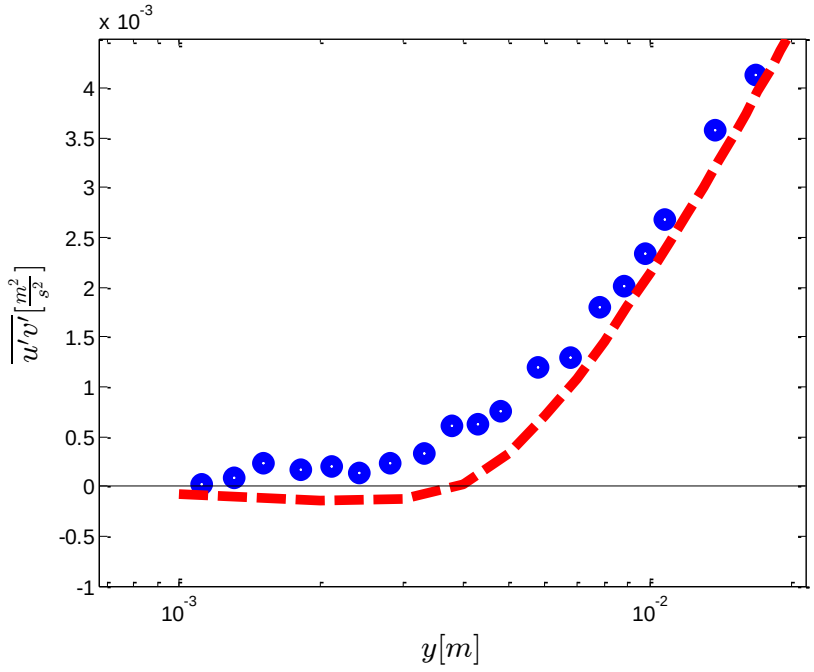

Figure 5. 49 Magnified near-wall view of Reynolds shear stress at $\mathrm{Gr_x} = 8.9 \times 10^{10}$.

5.7 Closing Remarks

The Large Eddy Simulation of the turbulent natural convection over the isothermal vertically heated flat plate has led to some conclusions and the highlights will be discussed in this section.

- A spanwise domain study was undertaken in order to ascertain the width required to capture sufficient turbulent structures in the spanwise direction and to assume a statistically two dimensional flowfield. By comparing 1st and 2nd order turbulent statistics, the study revealed that the spanwise width of $O(\delta)$ resolved adequate spanwise structures in the boundary layer.
- The utilization of wall-layer modeling was necessitated by the need to relax the wall-normal grid spacing subsequent to the commencement of full turbulence; the coarse wall-layer modeling simulations indicated that placing the first off the wall computational grid at the edge of the inner layer produced relatively accurate results. In this particular mesh construction, only ~10 grid cells were prescribed across the boundary layer thickness.
- The near-wall flow topology of coherent structures educed using the $Q > 0$ criterion illustrated the structures observed in the turbulent natural convection boundary layer were dissimilar to those observed in forced convection turbulent boundary layer flows. Even though predominantly streamwise vortices were seen near the wall, the overlapping and spanwise tilting orientation noticeable in forced convection, was absent in this flow configuration.

- Well preserved thermal turbulent field spanning $10\,\mathrm{cm}$ in the streamwise direction was observed in the near-wall region. In addition, high temperature, $t' > 0$, and low temperature, $t' < 0$, encompass the near-wall turbulent boundary layer region.
- The peak of the turbulent kinetic energy occurred in the outer layer of the boundary layer. In addition, shear and buoyant production of turbulent energy were observed to be of the same order of magnitude. Furthermore, discrepancy between the LES and experimental data of the shear production was observed very near the wall. This discrepancy stemmed from the near-wall profiles of the Reynolds shear stress, $\overline{u'v'}$. The near-wall inner layer is extremely thin and it is reasonable to question the fidelity of the experimental data in this particular region. Furthermore, the assistance of a detailed non-Boussinesq Direct Numerical Simulation would be of profound help in shedding some light on the near-wall flow region of this turbulent boundary layer.

Chapter 6: Hattori Test Case

6.1 Test Case Description

This test case entails the experimental measurements of [24] over a vertically isothermal heated flat plate implemented inside a low-speed vertical wind tunnel. The dimensions of the heated plate were 4 m high, 0.8 m wide and 0.02 m thick. The plate was mounted vertically on the back wall of the vertical wind tunnel. The temperature of the plate was kept uniform at 369 Kelvin via electric heaters implemented at the rear of the plate. The ambient temperature was maintained at approximately 298 Kelvin. Temperature and velocity data in the mixed convection turbulent boundary layer were measured with tungsten hot wire and cold wire measurements using a sampling frequency of 500 Hz. To observe the instantaneous velocity field, particle image velocimetry (PIV) were employed by injecting 30 micrometer plastic microspheres tracer particles into the boundary layer. A schematic of the coordinate system adopted for the experiment is depicted in Figure 6.1. In Figure 6.2, an image of the vertical wind tunnel utilized to carry out the measurements can be seen. The wind tunnel comprises a blower which can force mass into the test section at a maximum freestream speed of 10 m/s equivalent to a

local Reynolds number of 1.9×10^6 at x~3.765 m . Downstream of the blower resides a diffuser with a relatively large cone angle that can possibly slow down the flow enough to induce flow separation. Thus, three safety screens were positioned in the diffuser to smooth out variations in the velocity field and maintain a satisfactory flow. To dampen freestream disturbance or turbulence, four fine mesh damping screens along with a honeycomb were placed in the settling chamber.

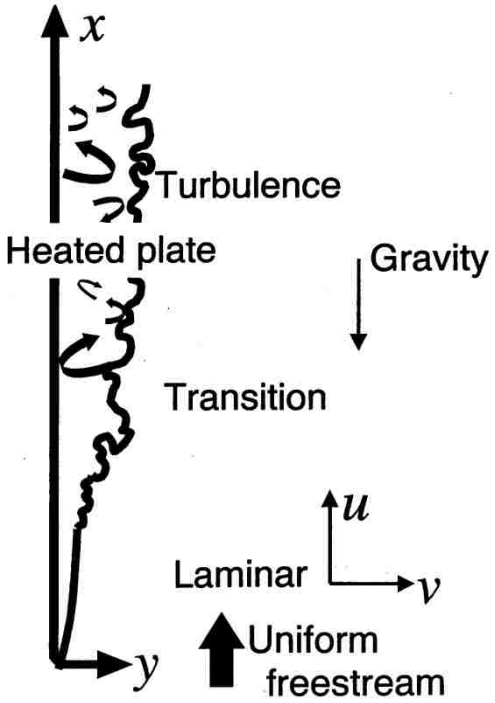

Figure 6. 1 Schematic of geometry and coordinate system utilized for experimental measurement, from [24].

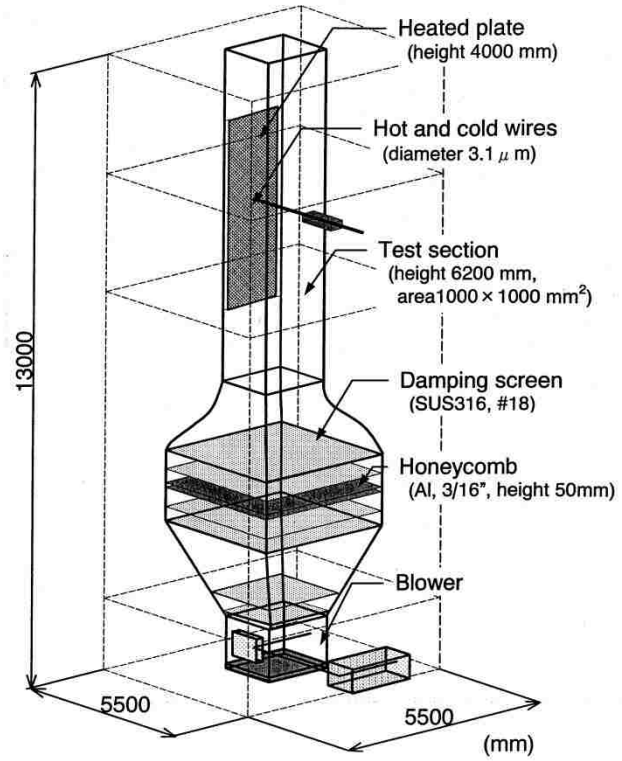

Figure 6. 2 Schematic of experimental apparatus, from [24].

6.2 Computational Setup

The numerical simulation domain and prescribed boundary conditions are graphically represented in Figure 6.3. As can be seen from the figure, uniform freestream values, U_∞ and T_∞ , were prescribed at the inflow accordingly to match those employed for the experiments. Just downstream of the inflow region is a 0.1 m long entrance domain implemented particularly to prevent an abrupt start of the boundary layer since a non-zero inflow velocity was prescribed. The length of the plate was chosen to be 5 m to enable the numerical simulation to capture the delayed transitioning turbulent boundary layer as the freestream velocity is increased; moreover, a 5 m plate was utilized to disallow potentially corrupted solution that can develop near the outflow to affect the region of interest. The spanwise width of the computational

domain was selected based upon the integral length scale, δ, of the boundary layer and will be described in the subsequent subsection. The wall-normal simulation domains spans 2 m. The far-field boundary was purposely implemented to be far away from the wall region because the spatially growing turbulent boundary layer will accelerate the prescribed non-zero freestream velocity and its effects can be mitigated by positioning the boundary far from the plate. Similarly to the Tsuji & Nagano test case, the entrainment and cyclic boundary conditions were prescribed for the far-field and homogeneous boundaries respectively.

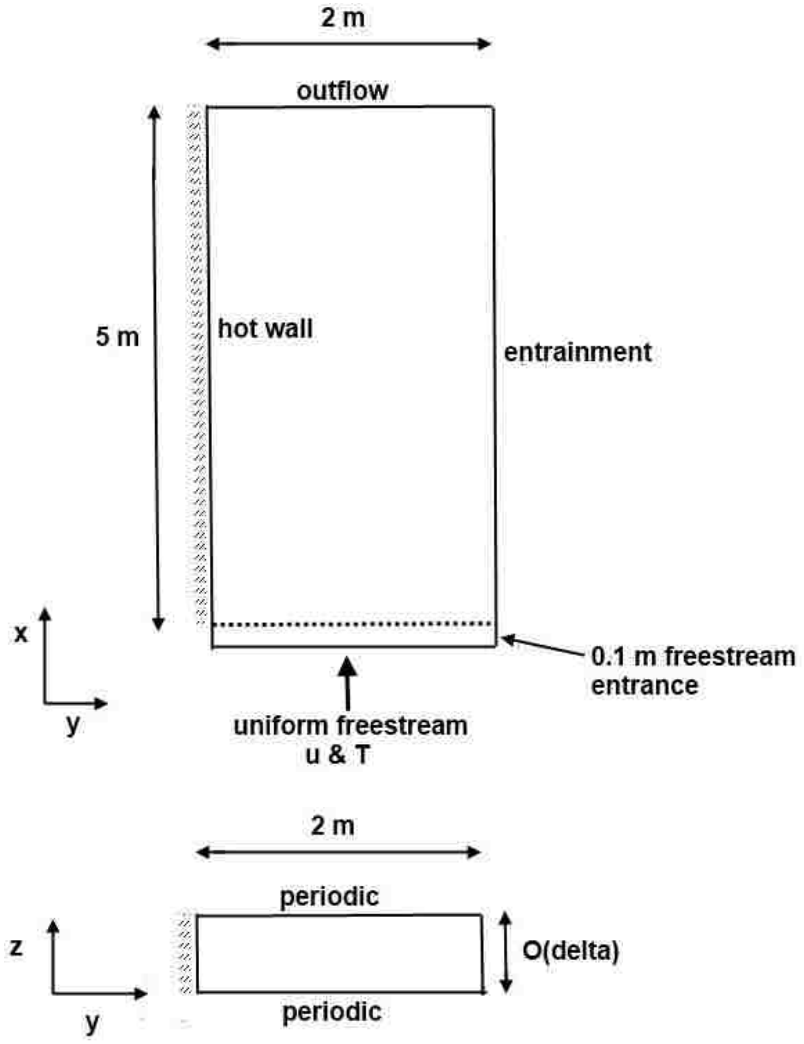

Figure 6. 3 Computational domain and boundary conditions for Hattori test case.

The Hattori experiments simulated in this current numerical effort are described in Table 6.1, below. In total, three cases were chosen and their corresponding freestream velocity and wall to freestream temperature difference can be seen in columns two and three, respectively. The fourth column consists of streamwise location ratios where the measurements were taken; this downstream location was around x = 3.7 m.

Case	U_∞ m/s	ΔT Kelvin	Gr_x/Re_x^3
HT01	0.0	~70	∞
HT02	0.53	~70	4.68×10^{-4}
HT03	0.80	~70	1.05×10^{-4}

Table 6. 1 Quantities employed for Hattori experimental test cases.

6.2.1 Computational Grid

The numerical grid utilized for the three Hattori test cases were similar to the mesh employed for the Tsuji & Nagano test case, except for the presence of the entrance length required for the prescribed velocity and temperature freestream quantities at the inflow region. The computational grid wall spacing employed in the fully developed turbulent region are described in Table 6.2; it is apparent that successively finer grid resolutions are employed with increasing freestream velocity for reasons that will be elucidated later. For each Hattori case simulated, the spanwise width of the computational domain was specified to be $\sim\delta$, where δ was taken to be the wall-

normal length from the wall to the point the mean streamwise velocity attains its freestream value. The approximate value of δ was chosen from the available experimental data of [24].

Case	Δx mm	Δy mm	Δz mm	δ (mm)
HT01	25	0.53	3.6	500
HT02	25	0.30	2.0	150
HT03	7	0.14	0.6	50

Table 6. 2 Grid wall spacing in dimensional units utilized for Hattori simulations along with the computational widths.

6.2.2 Simulation Details

The numerical simulations employed were somewhat similar to those implemented for the Tsuji & Nagano test case. For all the simulations, velocity and temperature freestream values used for the experiment were prescribed for the internal flowfield and inflow at the start of the simulation. In addition, in the process of achieving reasonably accurate results, it was determined to run the simulations initially on coarser grids and to map the coarse mesh solution onto successively finer grids until the second order turbulent statistics were deemed acceptable when compared to experimental data.

6.3 Wall-Resolved Simulations

Mean velocity and temperature profiles

The mean streamwise velocity acquired from the experiments and LES are illustrated in Figures 6.4-6.6. As a whole, there is excellent agreement between the measurements and LDSMG results in the inner and outer layers. It can be seen that the maximum mean streamwise velocity increases with the introduction of a low freestream. This is because forced convection effects are augmenting the streamwise velocity in a non-linear manner. Furthermore, it is quite evident that the boundary layer progressively becomes thinner as the freestream velocity is increased. In Figures 6.7-6.9, the mean temperature wall profiles of the measurements and LES are depicted and the agreement between the results is quite impressive. The mean temperature profiles also indicate that as the freestream velocity is slightly increased, there seems to be mechanism that is causing the diffusive action of the large turbulent scales to be restricted. An interesting thing to note is the increase in wall shear, i.e. $\partial U/\partial y_w$, as the freestream is added to the turbulent boundary layer. Usually, turbulence is known to emerge as a result of increasing shear and the subsequent boundary layer becomes successively more diffusive as the wall shear increases. However, we can see from Figure 6.10 that in the presence of increasingly wall shear stress, the mixed convection boundary layer thickness diminishes. Furthermore, the wall heat transfer decreases as the freestream velocity increases, refer to Figure 6.11. Thus, it is apparent that the nature of the turbulence generated, either by shear production or buoyant production is being suppressed by some mechanism with the addition of a freestream flow.

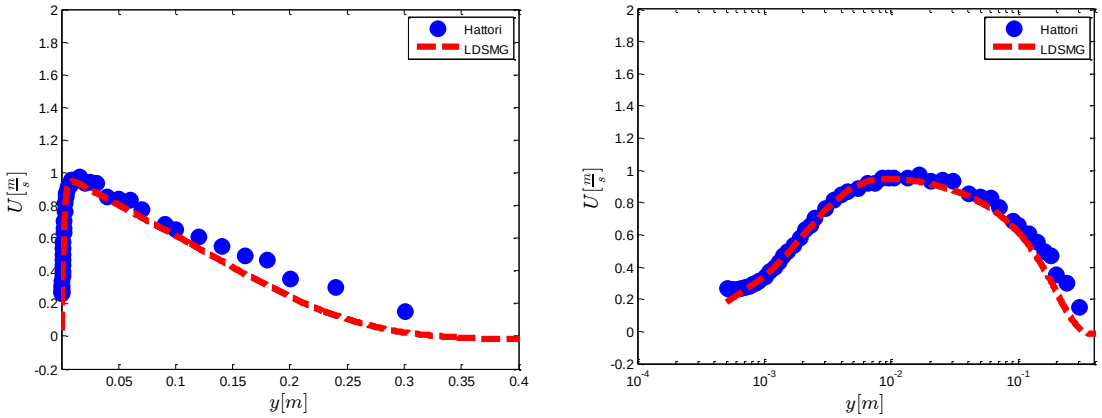

Figure 6. 4 Mean streamwise velocity profile at $Gr_x \sim 3.40E{+}11$ for $Gr_x/Re_x^3 = \infty$.

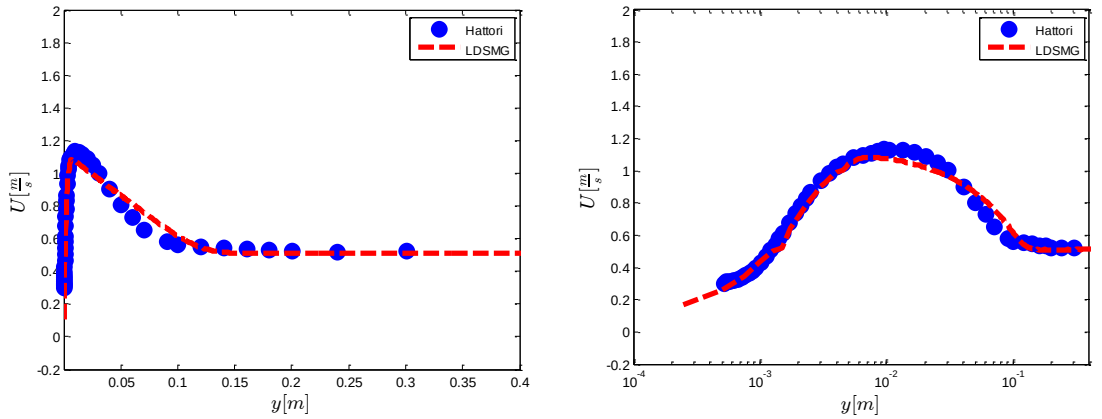

Figure 6. 5 Mean streamwise velocity profile at $Gr_x \sim 3.40E{+}11$ for $Gr_x/Re_x^3 = 4.68 \times 10^{-4}$.

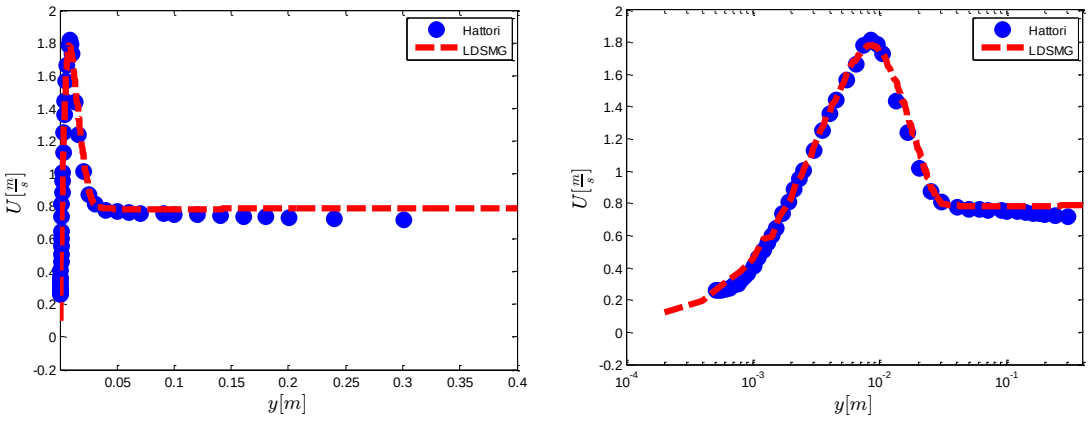

Figure 6. 6 Mean streamwise velocity profile at $Gr_x \sim$ 3.40E+11 for $Gr_x/Re_x^3 = 1.05 \times 10^{-4}$.

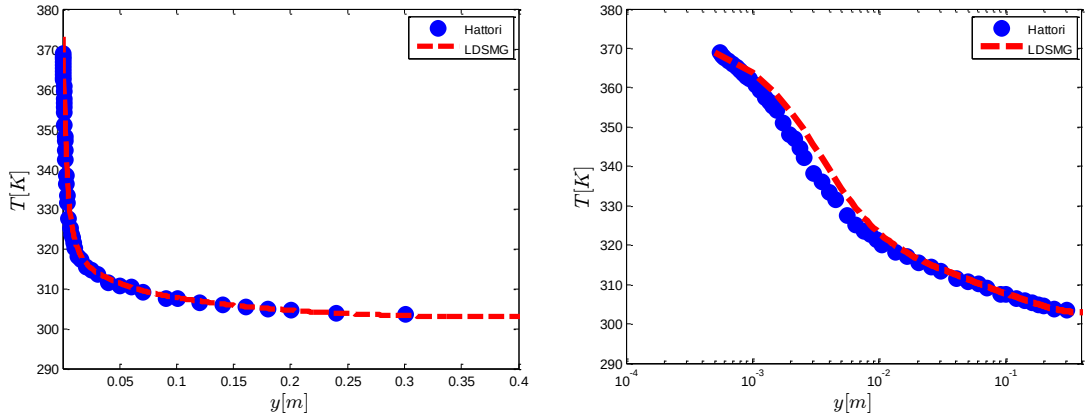

Figure 6. 7 Mean temperature profile at $Gr_x \sim$ 3.40E+11 for $Gr_x/Re_x^3 = \infty$.

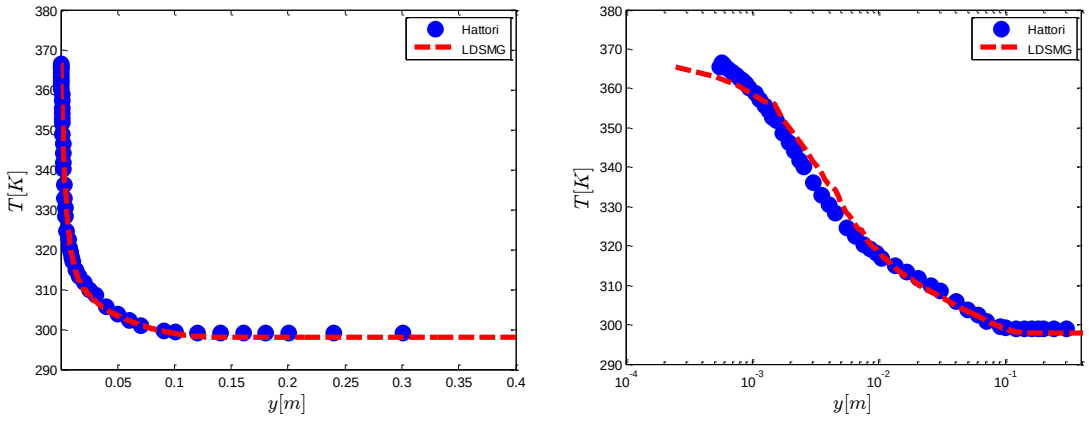

Figure 6. 8 Mean temperature profile at $Gr_x \sim$ 3.40E+11 for $Gr_x/Re_x^3 = 4.68 \times 10^{-4}$.

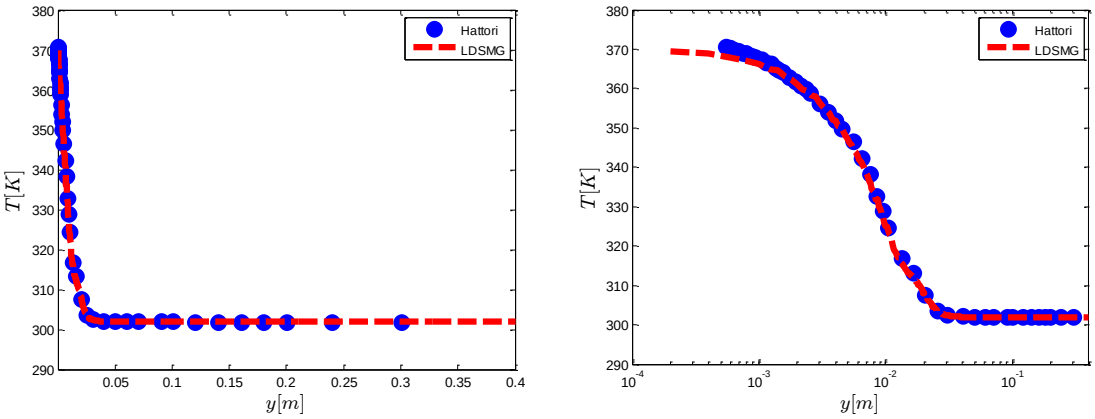

Figure 6. 9 Mean temperature profile at $Gr_x \sim$ 3.40E+11 for $Gr_x/Re_x^3 = 1.05 \times 10^{-4}$.

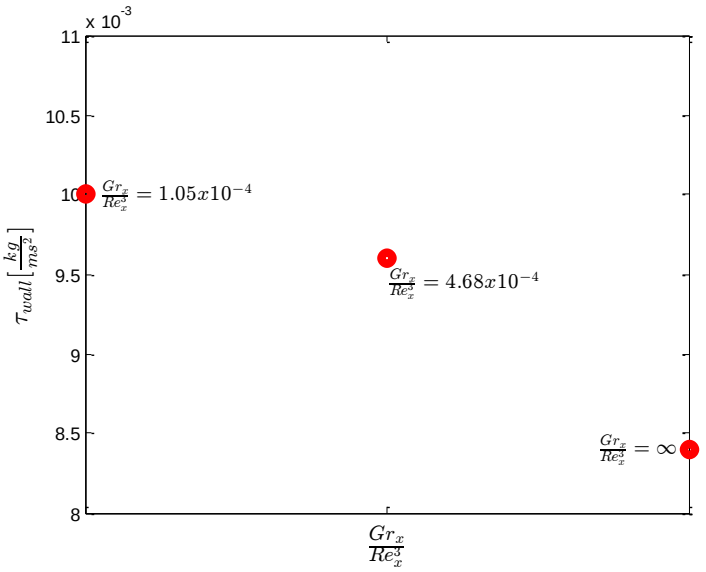

Figure 6. 10 Effects of freestream on wall shear stress of natural and mixed convection boundary layer using LDSMG.

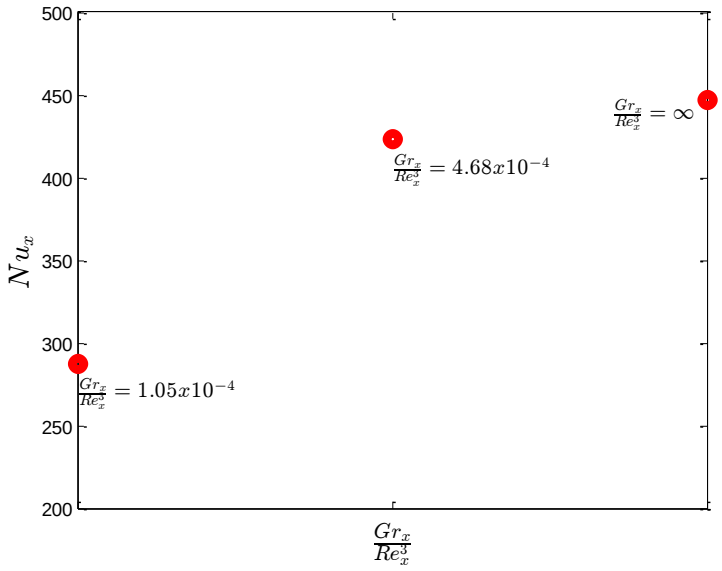

Figure 6. 11 Effects of freestream on local heat transfer rates of natural and mixed convection boundary layer using LDSMG.

Intensities of velocity and temperature fluctuations

The intensity of streamwise velocity fluctuations are depicted in Figures 6.12-6.14 for the measurements and LDSMG. The agreement between the experimental data and LES predictions are remarkable in the inner- and outer layers of the boundary layer. With a slight addition of freestream velocity, at $Gr_x/Re_x^3 = 4.68 \times 10^{-4}$, the magnitude of the streamwise velocity fluctuation intensity attains a value less than the $Gr_x/Re_x^3 = \infty$ case. Furthermore, as was observed with the mean velocity and temperature profiles, the intensity of the velocity fluctuation has diminished in the entire boundary layer region and is confined to a lower wall-normal region. Figures 6.15-6.16 illustrates the temperature fluctuation intensities at $Gr_x/Re_x^3 = \infty$ and 4.68×10^{-4}. The effects of freestream addition can be clearly seen by the reduction of temperature fluctuation in the whole boundary layer region. By further increasing the freestream velocity, Figures 6.14 and 6.17 reveals an increasingly diminishing velocity and temperature fluctuation intensities globally. However, in Figure 6.14, very near the wall, the experimental data show a higher peak of $\sqrt{\overline{u^{2\prime}}}$ when compared to that of $Gr_x/Re_x^3 = 4.68 \times 10^{-4}$. As opposed to predicting this subtle trend, the LES computed $\sqrt{\overline{u^{2\prime}}}$ values approximately of the same magnitude in the near-wall region, see Figures 6.13 and 6.14. Nonetheless, along with an apparent decrease in turbulence in the entire boundary layer, a peculiar double-peak can be seen in the measurement of velocity fluctuation intensity. The LDSMG prediction was able to capture this behavior in the velocity fluctuation intensity wall profile, although the initial peak was underpredicted. The appearance of the double peak in the velocity fluctuation intensity profile was described to be indicative of a beginning

transition to turbulence of a mixed convection boundary layer [140], [19]. Thus, it can be concluded that at $Gr_x/Re_x^3 = 1.05 \times 10^{-4}$, the mixed convection boundary layer did not attain a fully developed turbulence state and is a direct consequence of the increased forced flow. It should be noted as well that the relative difference in magnitude of velocity and temperature intensity fluctuations is profoundly pronounced for the variation in temperature fluctuations, see Figures 6.15 and 6.17. The magnitude of the temperature intensity fluctuation at $Gr_x/Re_x^3 = 1.05 \times 10^{-4}$ is nearly 50% of the pure natural convection turbulent boundary layer. Therefore, it may be conjectured that in this range of mixed convection regime, buoyant production of turbulence might be dominant over shear production. It is apparent that increasing the forced flow suppresses these temperature fluctuations, thereby reducing the overall turbulence of the flow. Another interesting observation from Figure 6.17 is the appearance of a double peak in the experimental temperature fluctuation intensity. The LES prediction was unable to capture this transitioning phenomenon; similarly, the DNS result of [23] was unable to replicate this behavior in their simulations.

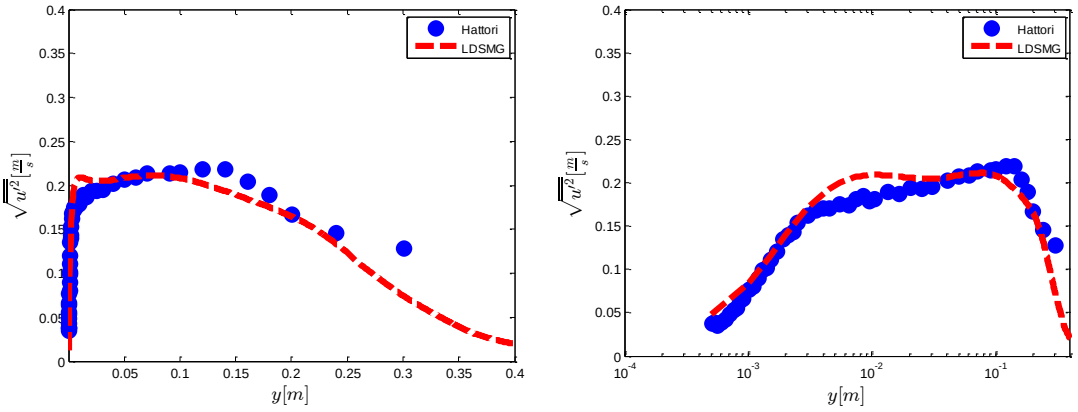

Figure 6. 12 Intensity of streamwise velocity fluctuation intensity profile at $Gr_x \sim$ 3.40E+11 for $Gr_x/Re_x^3 = \infty$.

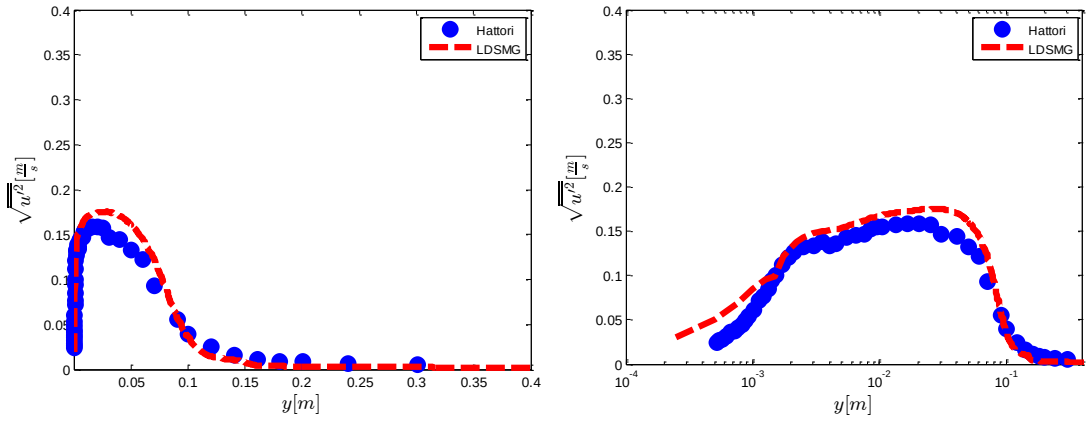

Figure 6. 13 Intensity of streamwise velocity fluctuation intensity profile at $Gr_x \sim$ 3.40E+11 for $Gr_x/Re_x^3 = 4.68 \times 10^{-4}$.

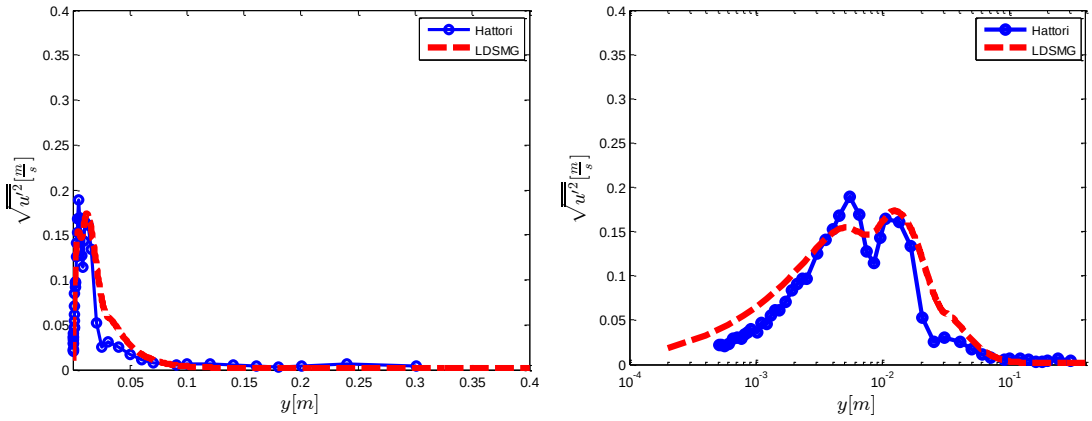

Figure 6. 14 Intensity of streamwise velocity fluctuation intensity profile at $Gr_x \sim$ 3.40E+11 for $Gr_x/Re_x^3 = 1.05 \times 10^{-4}$.

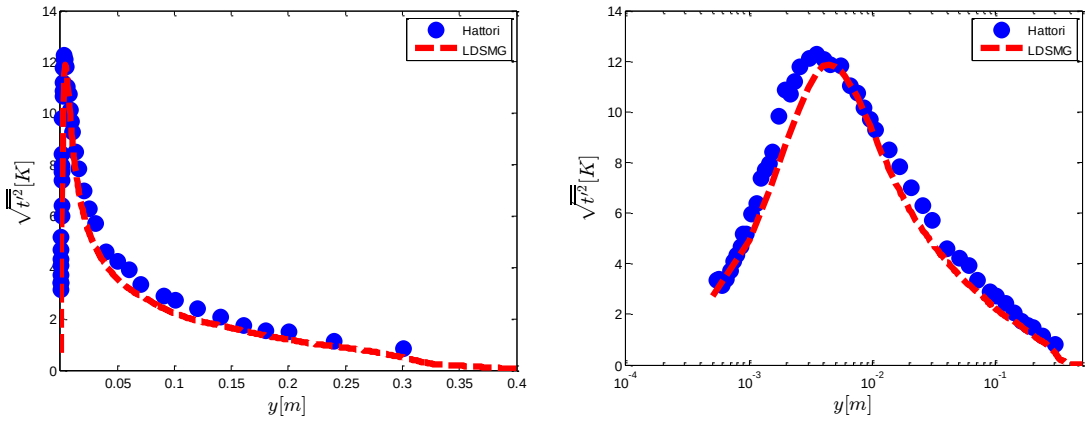

Figure 6. 15 Intensity of temperature fluctuation intensity profile at $Gr_x \sim$ 3.40E+11 for $Gr_x/Re_x^3 = \infty$.

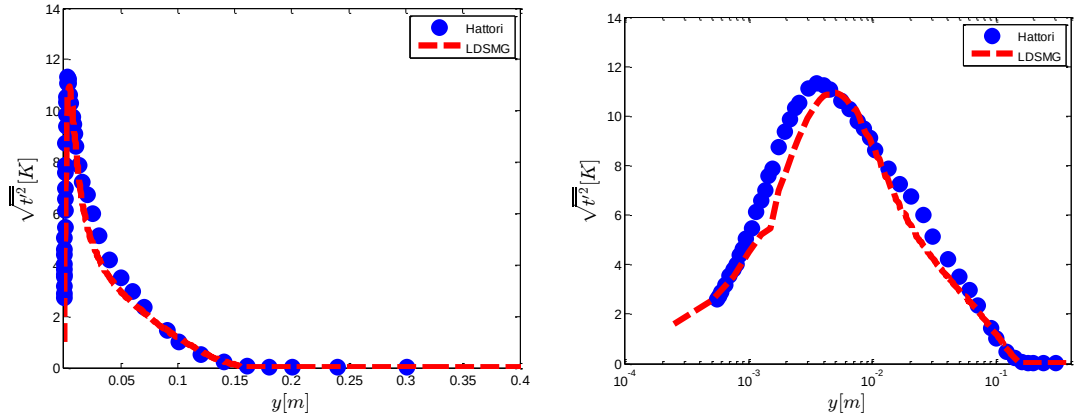

Figure 6. 16 Intensity of temperature fluctuation intensity profile at $Gr_x \sim 3.40E+11$ for $Gr_x/Re_x^3 = 4.68 \times 10^{-4}$.

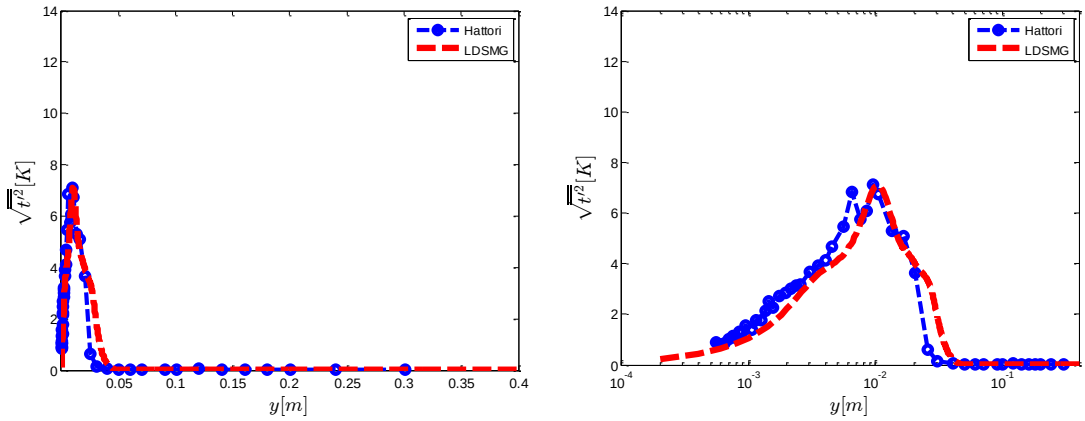

Figure 6. 17 Intensity of temperature fluctuation intensity profile at $Gr_x \sim 3.40E+11$ for $Gr_x/Re_x^3 = 1.05 \times 10^{-4}$.

Streamwise Turbulent Heat Flux

Wall profiles of the streamwise turbulent heat flux, $\overline{u't'}$, are depicted in Figures 6.18-6.20. The streamwise turbulent heat flux is essentially a measure of the correlation between u' and t' and is a fairly challenging quantity to numerically capture with high fidelity. At $Gr_x/Re_x^3 = \infty$ and 4.68×10^{-4}, there is good agreement between the experimental data and LES predictions, both in the inner and outer layers of the turbulent boundary layer. Although at the edge of the inner and outer layers, the turbulent heat flux was minimally over-estimated. In Figure 6.20, at $Gr_x/Re_x^3 = 1.05 \times 10^{-4}$, the LES prediction was unable to accurately resolve the turbulent heat flux in the transitioning boundary layer, particularly near the wall. The LDSMG result was able to approximately resolve the streamwise turbulent heat flux in the outer layer. However, the inner layer behavior was unsatisfactory. The reason for this discrepancy was attributed to the lack of sufficient grid cells within the incredibly thin transitioning boundary layer to resolve the intricate flow dynamics.

An interesting phenomenon is the increasingly negative value of $\overline{u't'}$ in the very near wall region of the inner layer. It can be seen from the measurements that this trend becomes more pronounced with the addition of forced flow; the LES results were able to duplicate this behavior at $Gr_x/Re_x^3 = \infty$ and 4.68×10^{-4}. This occurrence near the wall can be due to an invasion of either low speed fluid, $u' < 0$ or low temperature fluid, $t' < 0$. Figures 6.21 and 6.22 depict the probability density functions (PDF) of temperature and velocity fluctuations near the wall, respectively. The PDF of t' is largely skewed towards negative and it can be qualitatively concluded that it is indeed low temperature fluid that invades the near-wall region.

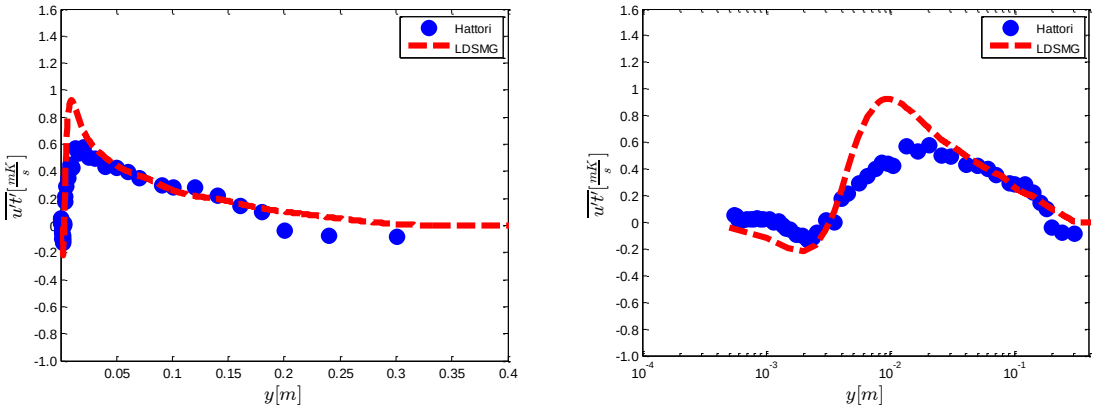

Figure 6. 18 Streamwise turbulent heat flux profile at $Gr_x \sim 3.40E+11$ for $Gr_x/Re_x^3 = \infty$.

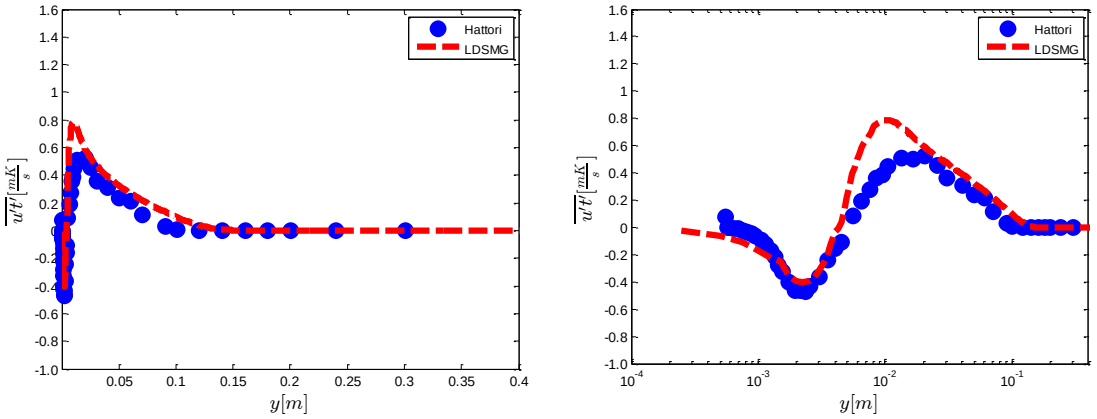

Figure 6. 19 Streamwise turbulent heat flux profile at $Gr_x \sim 3.40E+11$ for $Gr_x/Re_x^3 = 4.68 \times 10^{-4}$.

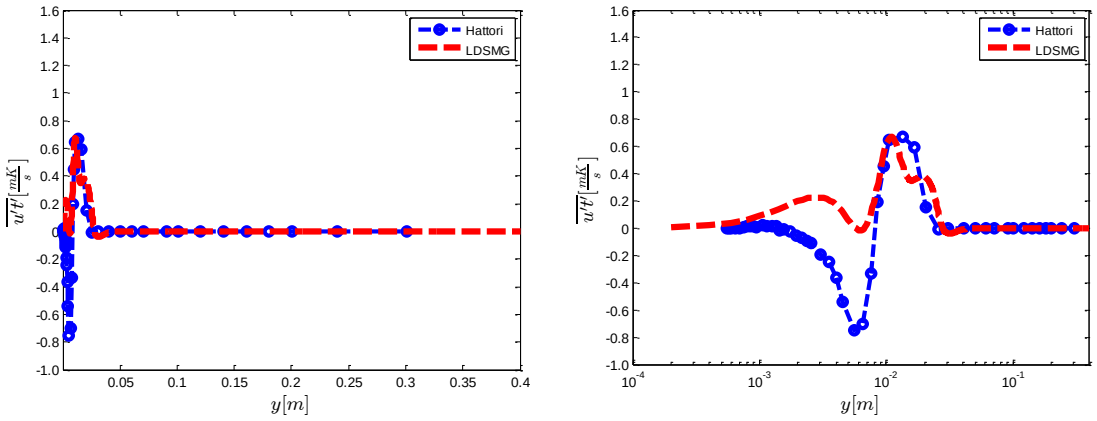

Figure 6. 20 Streamwise turbulent heat flux profile at $Gr_x \sim$ 3.40E+11 for $Gr_x/Re_x^3 = 1.05 \times 10^{-4}$.

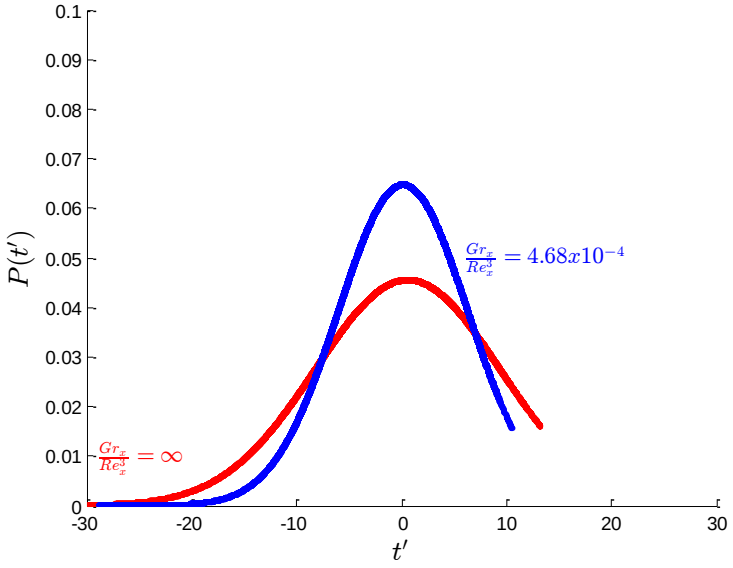

Figure 6. 21 Probability density function of temperature fluctuation in the near wall region.

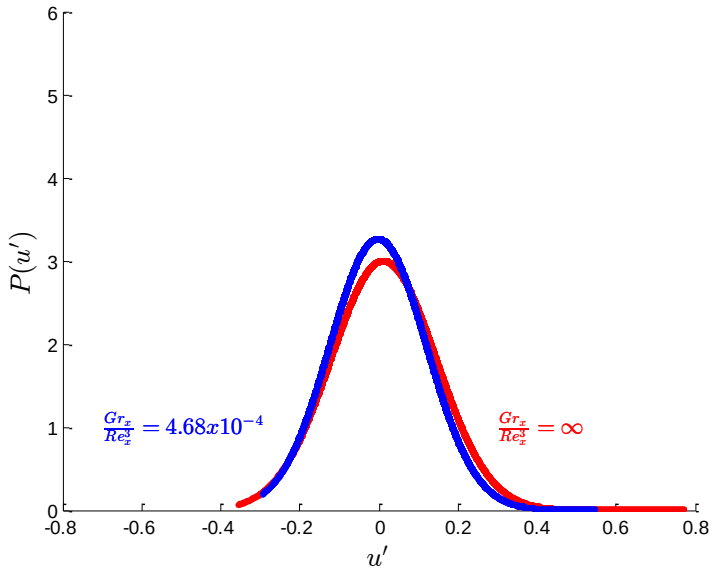

Figure 6. 22 Probability density function of velocity fluctuation in the near wall region.

6.4 Waveforms and Spectra of Velocity and Temperature Fluctuations

Waveforms of temperature and velocity fluctuations are illustrated in Figures 6.23 and 6.24. In order to capture the temperature and velocity time-series data, computational probes were implemented at a streamwise location of x~3.70 m, the center of the simulation domain in the spanwise direction and two locations in the wall-normal direction. These locations correspond to the near-wall region (inner layer), where the mean streamwise velocity is half of the maximum mean velocity and in the outer layer, where the mean velocity acquires an intermediate value between the maximum and freestream velocity values. In what follows, it must be mentioned that these fluctuation waveforms are only meant to emphasize the frequencies of turbulent motion active at the probed locations.

In Figure 6.23, the waveforms in the inner-layer clearly show that for $Gr_x/Re_x^3 = \infty$ and 4.68×10^{-4}, high and low frequency random fluid motion are

dominant near the wall. With a slight increase in freestream velocity, at $Gr_x/Re_x^3 = 1.05 \times 10^{-4}$, the random fluid motion seem to have been completely destroyed. Even though turbulent fluctuations still exist, harmonic fluid motions of a specific frequency have become dominant near the wall. The waveforms given in Figure 6.24 illustrate that large scale fluid motion, indicative of the long period waves, dominate in the outer layer for $Gr_x/Re_x^3 = \infty$. However, by adding a low freestream flow, at $Gr_x/Re_x^3 = 4.68 \times 10^{-4}$, large scale eddies of higher frequencies now dominate the outer layer. Furthermore, by increasing the freestream flow to $Gr_x/Re_x^3 = 1.05 \times 10^{-4}$, harmonic fluid motion at a single frequency is dominant in the outer layer.

To further assess the phenomenon observed in Figures 6.23 and 6.24, the frequency spectra of temperature and velocity fluctuations in the outer layer acquired from the experiments and LES computations are illustrated in Figure 6.25.

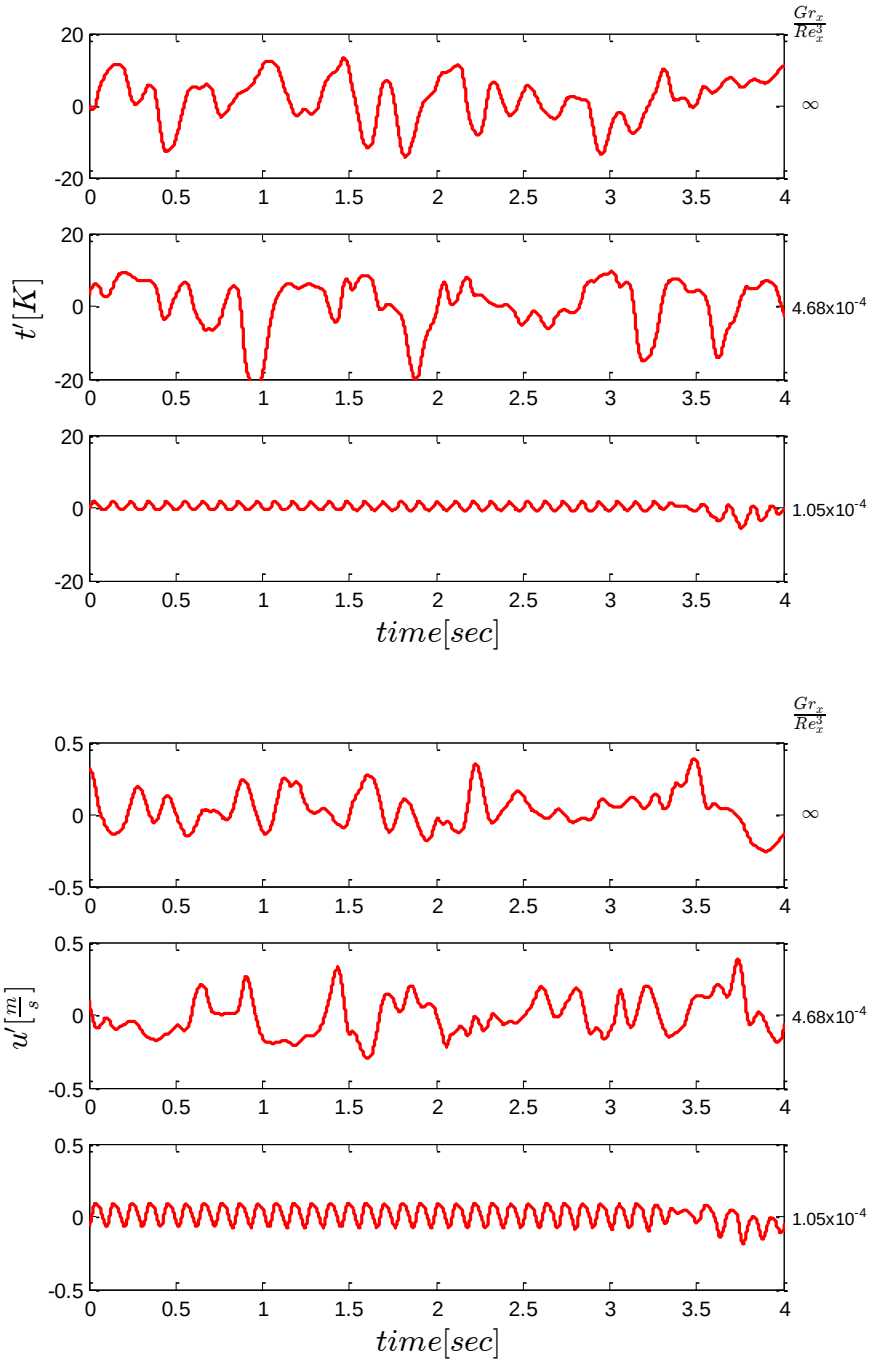

Figure 6. 23 Waveforms of temperature and velocity fluctuations in the inner layer region.

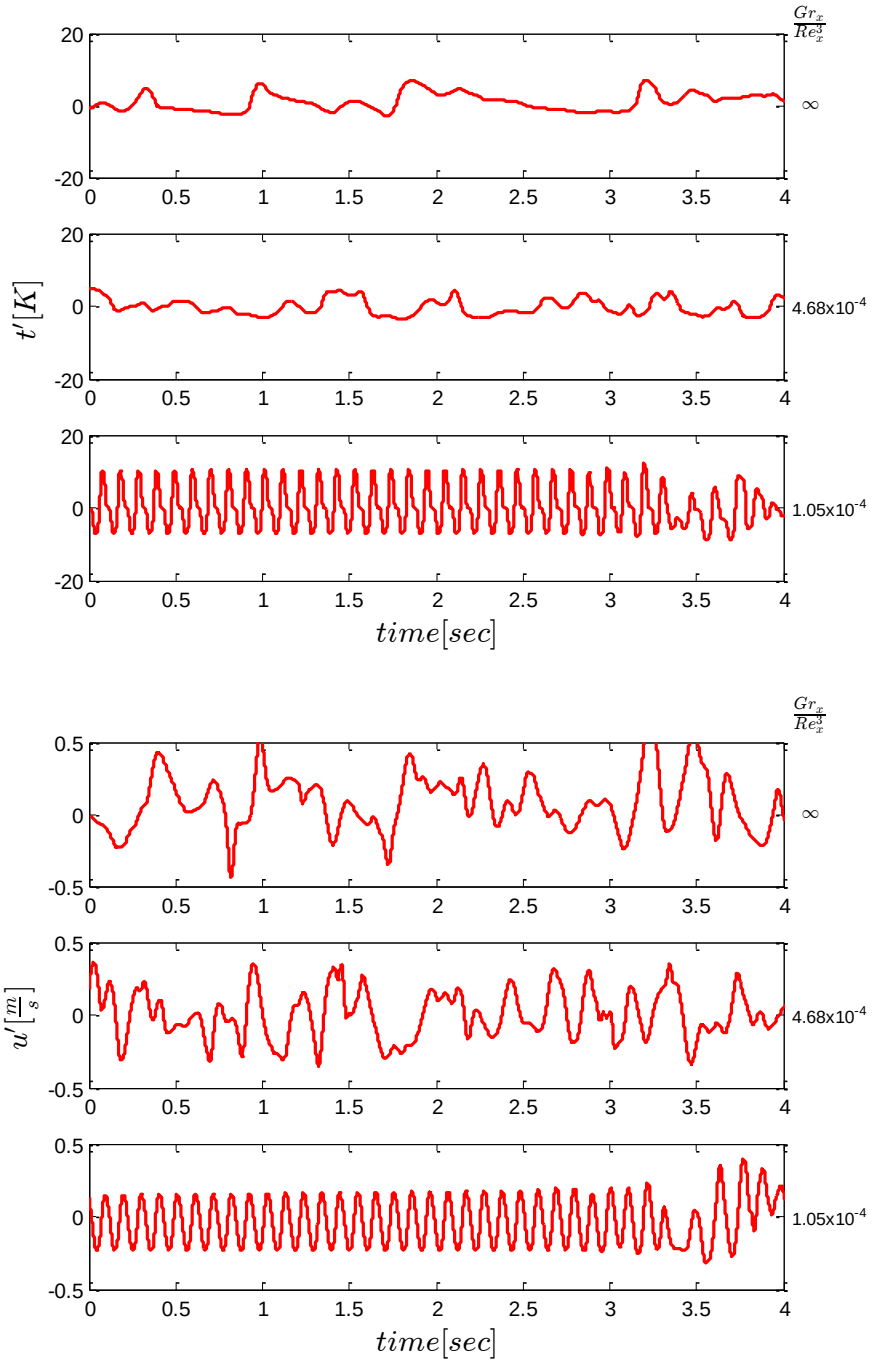

Figure 6. 24 Waveforms of temperature and velocity fluctuations in the outer layer region.

For the pure natural convection turbulent boundary layer without any freestream flow, i.e. $Gr_x/Re_x^3 = \infty$, the measurements and LDSMG both predicted large scale eddies of approximately 0.8 Hz are the most energetic fluid motion present in the outer layer. Moreover, it is also apparent that eddies of lower and higher frequencies than 1 Hz are also in motion in this region. At $Gr_x/Re_x^3 = 4.68 \times 10^{-4}$, eddies of varying frequencies are present in the outer layer region; however, the dominant frequency is higher than 0.8 Hz and is around 3 Hz. Thus, it is apparent that with the addition of a slight freestream flow, the larger scale eddies in the outer layer responsible for the most of momentum and heat transfer are being destroyed. This is further evident by examining the frequency spectra in the outer layer at $Gr_x/Re_x^3 = 1.05 \times 10^{-4}$. From Figure 6.24, it was seen that the random fluid motion was markedly nonexistent and harmonic fluid motion was dominant at a specific fundamental frequency. We can see from Figure 6.25 that this fundamental frequency is around 11 Hz. It can be surmised that turbulent fluid motions are less dominant at $Gr_x/Re_x^3 = 1.05 \times 10^{-4}$.

.

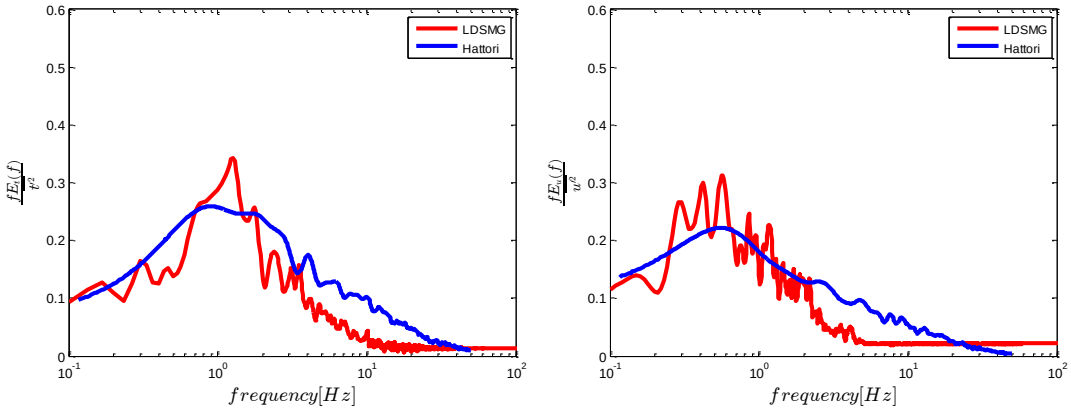

$$Gr_x/Re_x^3 = \infty$$

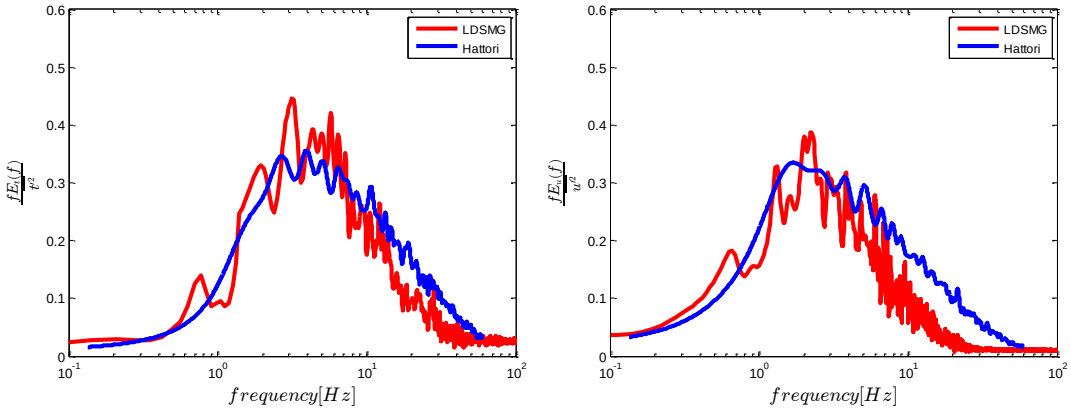

$$Gr_x/Re_x^3 \approx 4.68 \times 10^{-4}$$

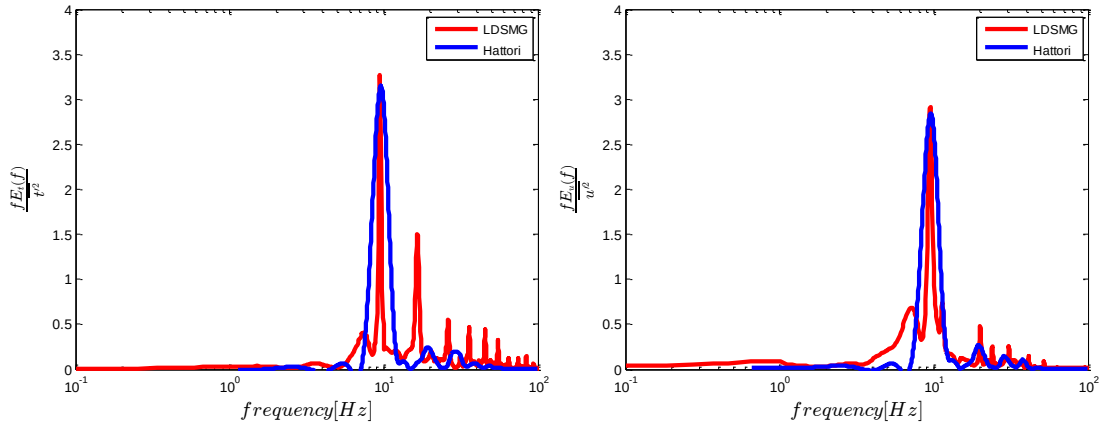

$$Gr_x/Re_x^3 \approx 1.05 \times 10^{-4}$$

Figure 6. 25 Frequency spectra of temperature and velocity fluctuation in outer layer region.

6.5 Structural Characteristics of Velocity Field

The inner and outer layer characteristics of the mixed convection turbulent boundary layer will be assessed subsequently. Figure 6.26 depicts the mean streamwise velocity at $Gr_x/Re_x^3 = 4.68 \times 10^{-4}$ with the regions pertaining to the inner and outer layers. The streamwise and wall-normal velocity fluctuation intensities at $Gr_x/Re_x^3 = 4.68 \times 10^{-4}$ can be seen in Figures 6.27 and 6.28; it is apparent that the maximum fluctuation intensity occurs in the outer layer for both turbulence quantities. In Figure 6.29, the Reynolds shear stress profile can be seen to attain its maximum value in the outer layer as well. It is interesting to note that in the inner layer, especially near the wall, $\overline{u'v'}$ is essentially zero, although it attains a slightly negative value near the edge of the inner layer. This is further exemplified with the time series signals of u', v' and $u'v'$ given in Figure 6.30. Clearly, from Figure 6.26, the mean streamwise velocity gradient is greater than 0. Thus, in the presence of substantial shear, the Reynolds shear stress near the wall is zero in a mixed convection turbulent boundary layer. As it was previously noted in an earlier chapter, the production of turbulent kinetic energy near the wall is dominated by sweeps, $u' > 0, v' < 0$, in wall bounded forced convection turbulent flow. These sweeps are a profound contributor to Reynolds shear stress producing events and it can be readily concluded from the above discussion such localized turbulence producing events are not found in the near wall region of a mixed convection turbulent boundary layer. Hence, we may conclude that the generation of turbulence in the inner layer is primarily driven by buoyant turbulent production.

At the wall-normal location where the mean streamwise velocity reaches its maximum value, i.e. $\partial U/\partial y = 0$, $\overline{u'v'}$ is greater than 0. This behavior is depicted in Figure 6.29. Furthermore, Figure 6.31 illustrated the time series signals at the identical location and the dominance of positive amplitude fluctuations of $u'v'$ can be observed in the absence of significant shear. Thus, the production of Reynolds shear stress in this region can be ascribed to the temperature fluctuations (buoyant production) in the boundary layer. In the outer layer of the boundary layer, we can see that the Reynolds shear stress continues to increase and acquires its highest value in that region, see Figure 6.29. In addition, from Figure 6.26, $\partial U/\partial y$ becomes progressively less than zero and the $u'v'$ signals in that region can be seen to have frequent higher amplitude fluctuations, see Figure 6.32. As such, the conclusion can be drawn that the presence of substantial shear in the outer layer contributes to the production of Reynolds shear stress, in addition to buoyant turbulent production. Therefore, in the outer layer of the mixed convection turbulent boundary layer, a behavior similar to that of the forced convection turbulent boundary layer exists, i.e., $\overline{u'v'} > 0$ when $\partial U/\partial y < 0$.

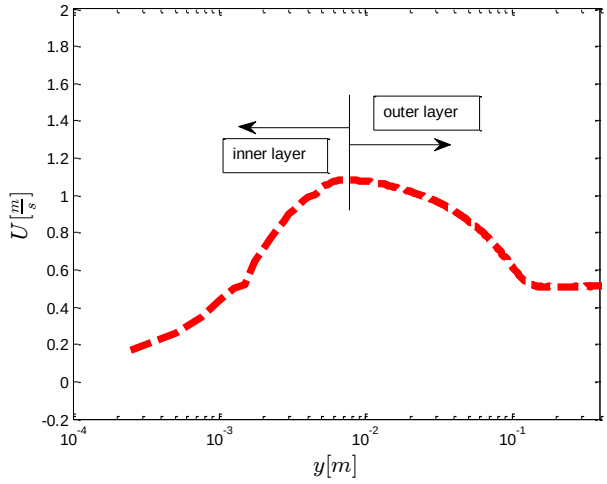

Figure 6. 26 Streamwise velocity profile at $\mathrm{Gr_x}/\mathrm{Re_x^3} = 4.68 \times 10^{-4}$ illustrating the inner and outer layers of the mixed convection turbulent boundary layer.

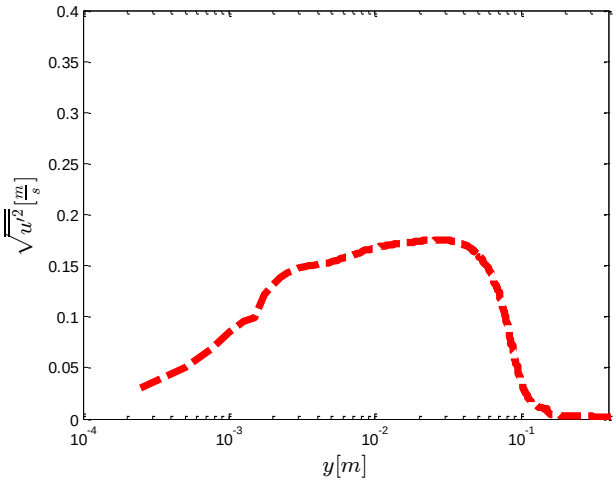

Figure 6. 27 Streamwise velocity fluctuation intensity profile at $\mathrm{Gr_x}/\mathrm{Re_x^3} = 4.68 \times 10^{-4}$.

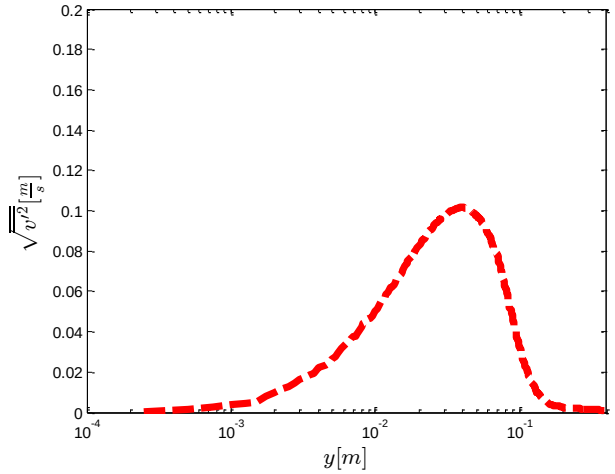

Figure 6. 28 Wall-normal velocity fluctuation intensity profile at $\mathrm{Gr_x/Re_x^3} = 4.68 \times 10^{-4}$.

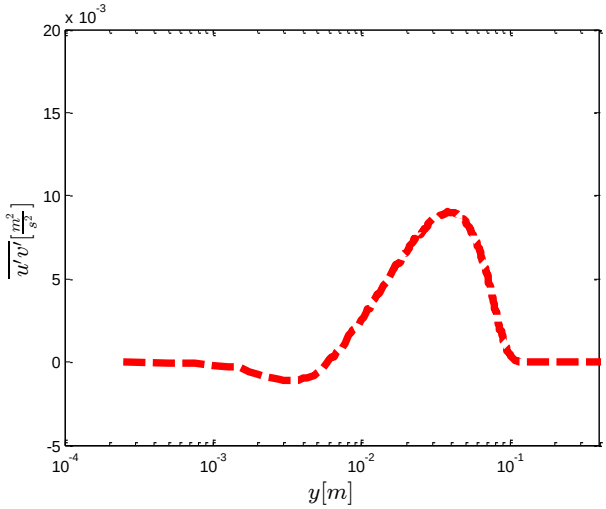

Figure 6. 29 Reynolds shear stress profile at $\mathrm{Gr_x/Re_x^3} = 4.68 \times 10^{-4}$.

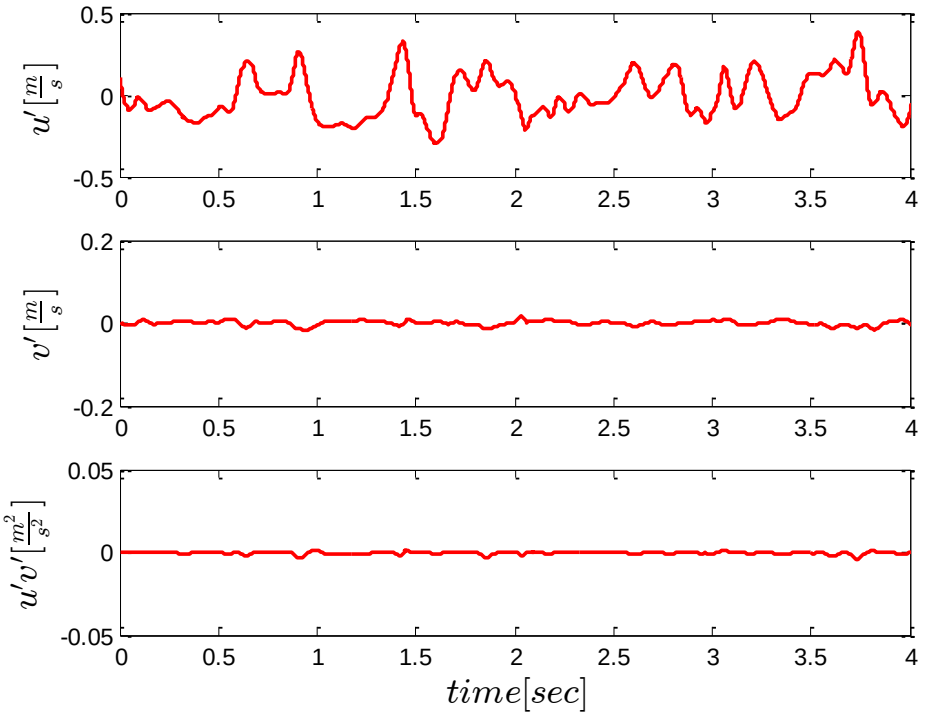

Figure 6. 30 Time series signals of velocity fluctuations, u', v' and $u'v'$ near the wall in the inner layer of the boundary layer.

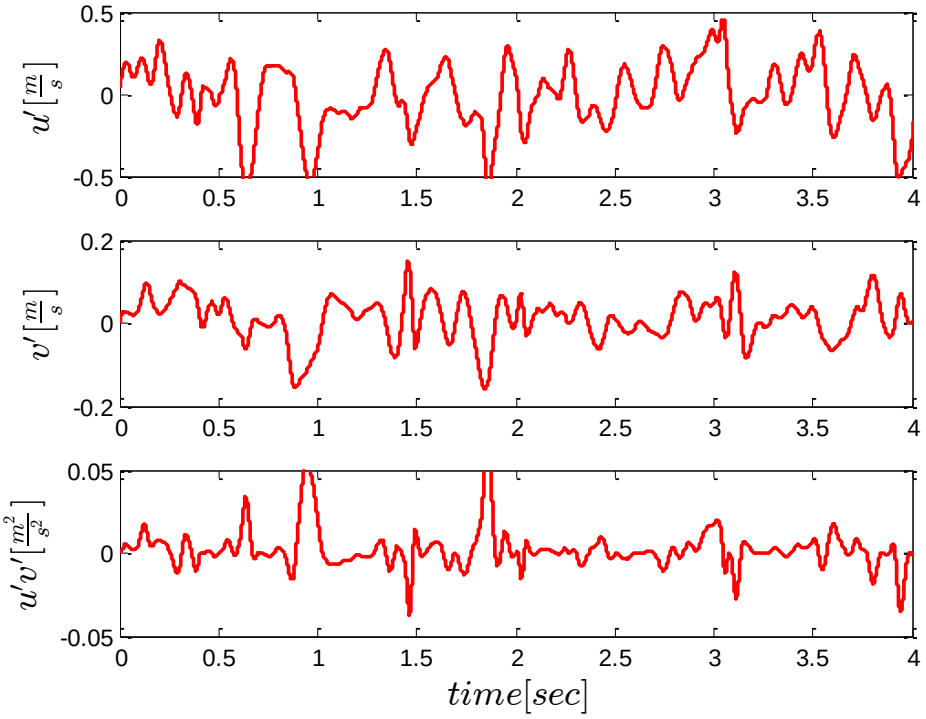

Figure 6. 31 Time series signals of velocity fluctuations, u′, v′ and u′v′ at the edge of the inner and outer layers.

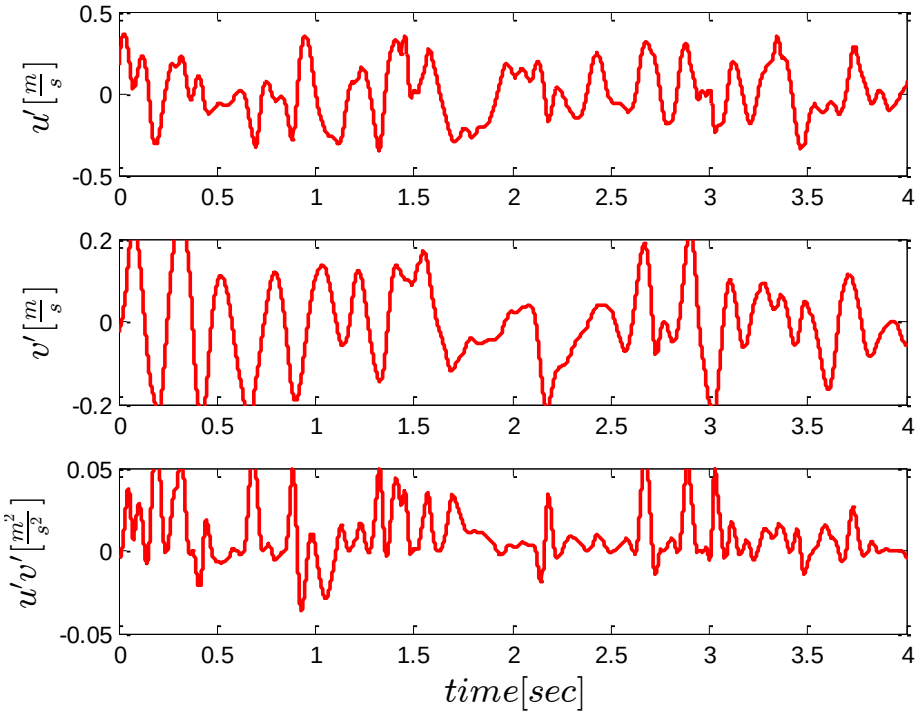

Figure 6. 32 Time series signals of velocity fluctuations, u′, v′ and u′v′ in the outer layer.

6.6 Wall-Modeled Simulations

In this section, the goal will be to apply the proposed mixed convection wall function of Chapter 3 to the Hattori case, HT02. It was previously shown that this case falls into the mixed convection regime and the flow configuration does transition to a fully developed mixed convection turbulent boundary layer. By assessing the turbulent flowfield, it was ascertained that transition to turbulence in the mixed convection boundary layer commences just upstream of x ~ 2.5 m. Figure 6.33 depicts the wall heat transfer as a function of streamwise location and the region of transition to turbulence can be seen. Thus, the mixed convection wall function will be implemented in the fully developed turbulent region, i.e. at x > 2.5 m, to assess the

effects of successively coarsened meshes in the wall-normal direction in the mixed convection turbulent boundary layer. The cost-savings computationally lies in the ability to prescribe significantly less grid cells across the boundary layer with the use of wall layer modeling. This is due to the correction made to the wall heat flux and wall shear stress with approximate boundary conditions; the correction is usually applied to the wall-normal gradients of the temperature and velocity.

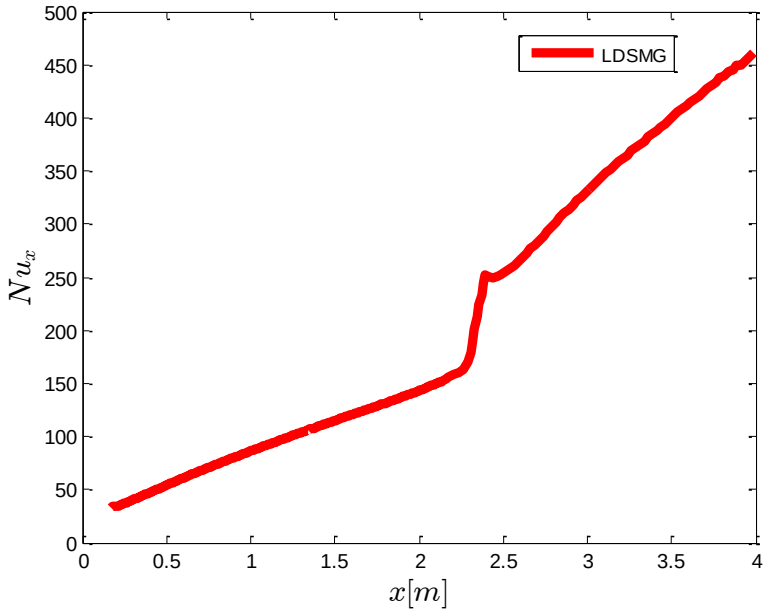

Figure 6. 33 Wall heat transfer along heated vertical flat plate for $U_\infty = 0.53$ m/s and $\Delta T = 69$ Kelvin.

The characteristics of the meshes employed are summarized in Table 6.3 and the significant decrease in grid cells across the boundary layer are tabulated as well. The results of the wall-resolved LES computations will be included to properly investigate and quantify the numerical errors attributable to the utilization of relatively coarse grids in resolving the boundary layer.

Due to the extremely high cost of simulating this turbulent flowfield, which is due to the fact that over half of the flat plate pertains to the laminar-to-turbulent transition, only two cases of wall-normal coarsened grids were selected to test the mixed convection wall function. Furthermore, the limiting condition for this flow set-up is the requirement to capture the transition region, whereby the grid resolution needed in the spanwise direction is profoundly high. Although the mesh could have been stretched fairly gradually in the spanwise once a fully turbulent boundary layer commences, this would have required a fairly complicated mesh. In addition, since transition occurs so far downstream, it was desired to have a fairly uniform mesh upstream of the region of interest in order to not corrupt the turbulent structures traveling in the streamwise direction.

Case no.	Wall-Model	Δx (mm)	Δy (mm)	Δz (mm)	# Cells across boundary layer
1	RLES	25	0.3	2	130
2	MCWF	25	4	2	23
3	MCWF	25	8	2	11

Table 6. 3 Mesh densities, varying wall-normal grid spacings employed in fully developed mixed convection turbulence region of boundary layer.

Mean velocity and temperature profiles

Figures 6.33 and 6.34 show the profiles of mean velocity and temperature, from which we can see the predicted wall-layer model results are in good agreement with the experimental data, even though the inner layer of the turbulent boundary layer is

not resolved. In Figure 6.33, it is obvious from the green curve, $\Delta y_{wall} = 8$ mm, has the first computational node off wall at the edge of the inner layer. It is apparent with this type of implemented mesh that a lot of near-wall physics and structures will be completely unresolved; however, the expectation is that the prescribed wall function will correct for some of the missing near-wall dynamics.

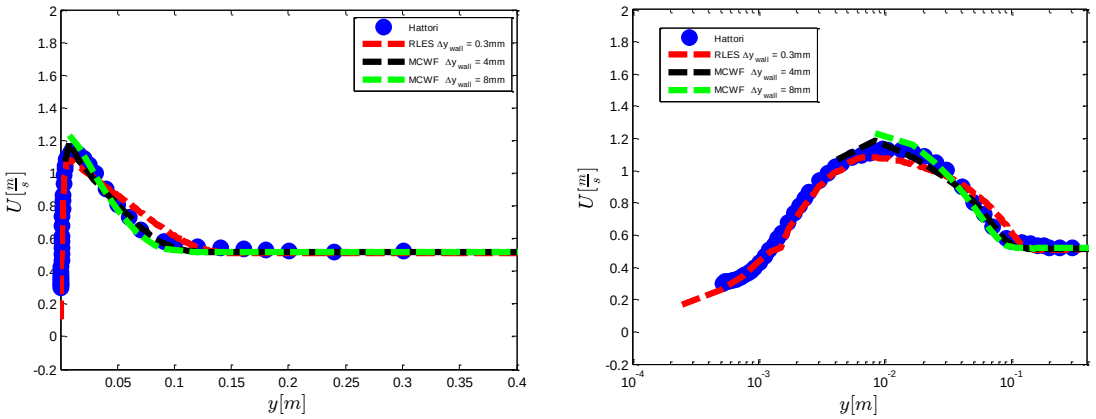

Figure 6. 34 Mean streamwise velocity profile at $\mathrm{Gr_x}/\mathrm{Re_x^3} = 4.68 \times 10^{-4}$ of resolved and wall-layer model results.

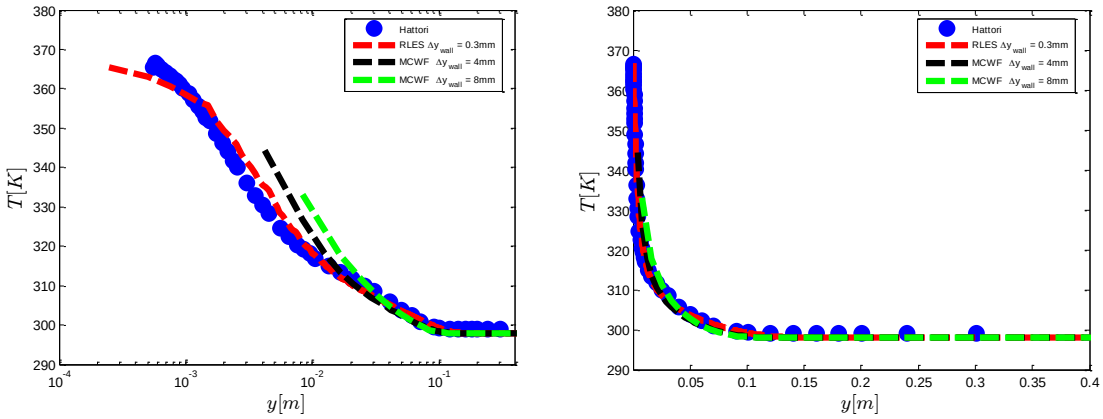

Figure 6. 35 Mean temperature profile at $\mathrm{Gr_x}/\mathrm{Re_x^3} = 4.68 \times 10^{-4}$ of resolved and wall-layer model results.

Intensities of velocity and temperature fluctuations

The streamwise velocity fluctuation intensity can be seen in Figure 6.35. The usual effects of coarse grid LES computations can be seen with the apparent overprediction of $\sqrt{\overline{u'}}$. In the outer layer of the boundary layer, the agreement between the experiment and wall layer model results is good. Figure 6.36 illustrate the profiles of temperature fluctuation intensity and we can see that $\sqrt{\overline{t'}}$ is fairly overestimated by coarsest mesh, $\Delta y_{wall} = 8$ mm. However, the agreement in the outer layer of mixed convection turbulent boundary layer was deemed acceptable.

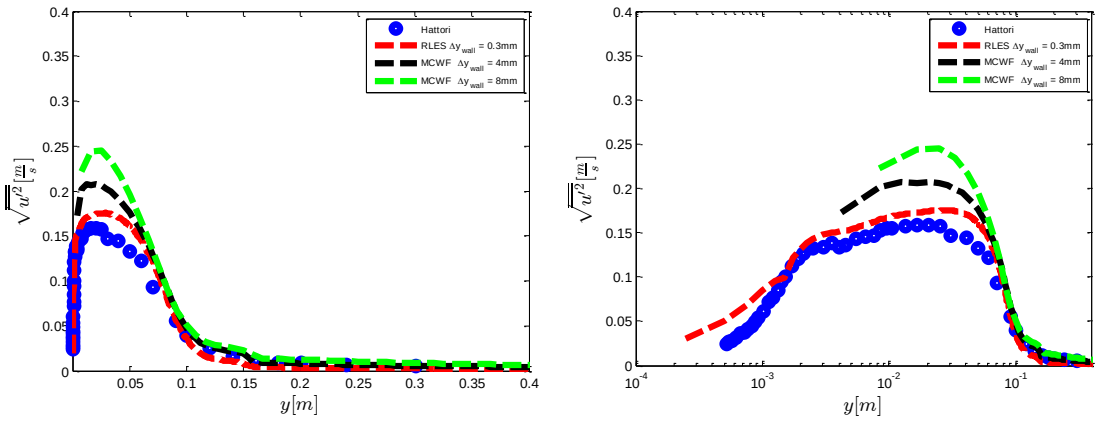

Figure 6. 36 Intensity of streamwise velocity fluctuation profiles at $\mathrm{Gr_x}/\mathrm{Re_x^3} = 4.68 \times 10^{-4}$ of resolved and wall-layer model results.

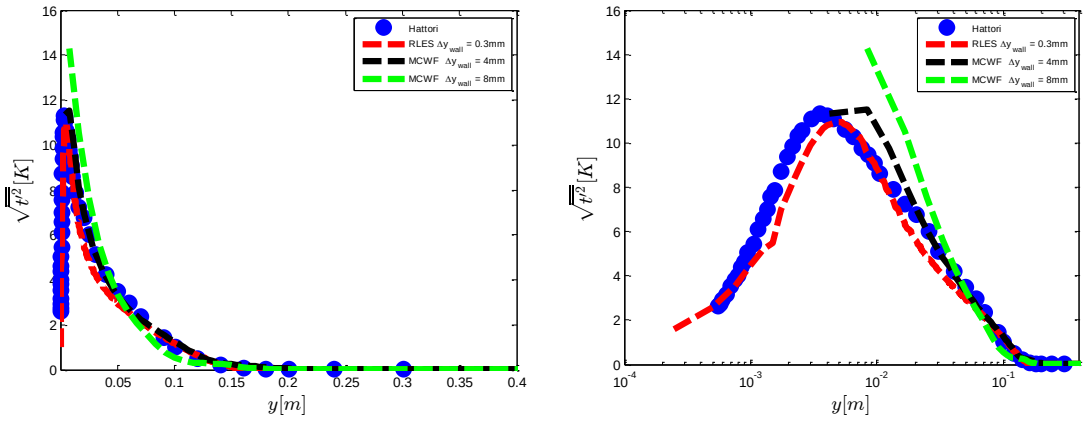

Figure 6. 37 Intensity of temperature fluctuation profiles at $\mathrm{Gr_x}/\mathrm{Re_x^3} = 4.68 \times 10^{-4}$ of resolved and wall-layer model results.

Streamwise turbulent heat flux

Profiles of the correlation between u′ and t′, $\overline{u't'}$, are shown in Figure 6.37. As was previously mentioned, capturing this correlation with high fidelity is quite challenging numerically; the predicted values of streamwise turbulent heat flux by the wall model in the outer layer is in good agreement with the experiment and resolved LES. We can see as well that $\overline{u't'}$ was overpredicted by the wall model near the edge of the inner layer. This overprediction can be due to several reasons, one of which could be the inter-component transfer of turbulent energy previously mentioned. There are also non-linear effects and errors introduced with the utilization of such wall-normal coarse grids to resolve the boundary layer flow; perhaps, excess energy within the large turbulent scales due to incorrect amount of dissipation can also be a cause of the overestimation. In addition, it should be noted that the mixed convection wall model employed was a blend of natural and forced convection approximate boundary conditions, whereby the forced convection aspect is typically applicable to high Reynolds number flows. Hence, this can also be another source of

error contributing to the overestimation of the turbulent quantities. With all that said, the wall-layer model predictions as whole were satisfactory.

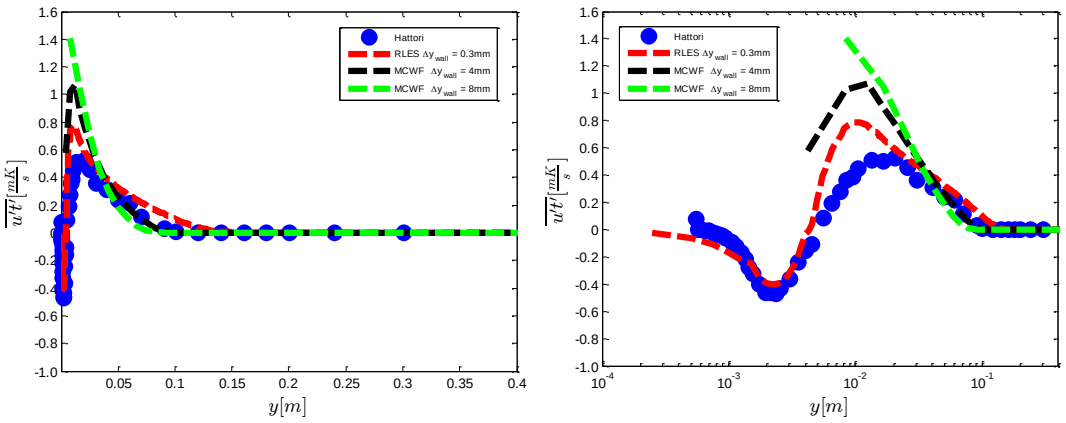

Figure 6. 38 Streamwise turbulent heat flux profiles at $\mathrm{Gr_x/Re_x^3} = 4.68 \times 10^{-4}$ of resolved and wall-layer model results.

Resolved normal stresses

Up till now, we have mad mentioned of the inter-component turbulent kinetic energy transfer and how it pertains to the overprediction of $\sqrt{\overline{u'^2}}$ with the utilization of coarser meshes in LES. The conjecture was made that the cause of overpredicting the streamwise velocity fluctuation intensity was due to the inability of the coarse mesh to adequately transfer energy to the other two components of the flow, $\sqrt{\overline{v'^2}}$ and $\sqrt{\overline{w'^2}}$. Consequently, if we were to compare the result of a resolved LES simulation to a relatively coarse, the other two components ought to be successively underpredicted due to the mechanism transferring turbulent energy from the dominant streamwise direction to the spanwise and wall-normal directions. The

intercomponent energy transfer mechanism is said to be due to the velocity-pressure gradient term found in the all the components for the turbulent kinetic energy. As to intricacies of how the mechanism transfers energy between components, it is said to be not fully understood [141]. Nevertheless, the exact nature of this mechanism is beyond the scope of the current effort. To proceed, Figures 6.38-6.40 show the resolved normal stresses in the streamwise, wall-normal and spanwise directions, respectively. In order to facilitate this illustration more clearly, it was decided to compare the results of the resolved and $\Delta y_{wall} = 8$ mm coarse LES results. As was shown before, Figure 6.38 depicts the overprediction of the streamwise velocity fluctuation intensity by the coarse mesh. In Figures 6.39-40, we can see that the wall-normal and spanwise turbulent intensities were underpredicted, as expected. It was aforementioned that this behavior is a well-known coarse grid LES symptom. From this analysis, it can be concluded that the same intercomponent turbulent energy transfer mechanism, quite possibly, exists for buoyancy affected turbulent boundary layer flows as well.

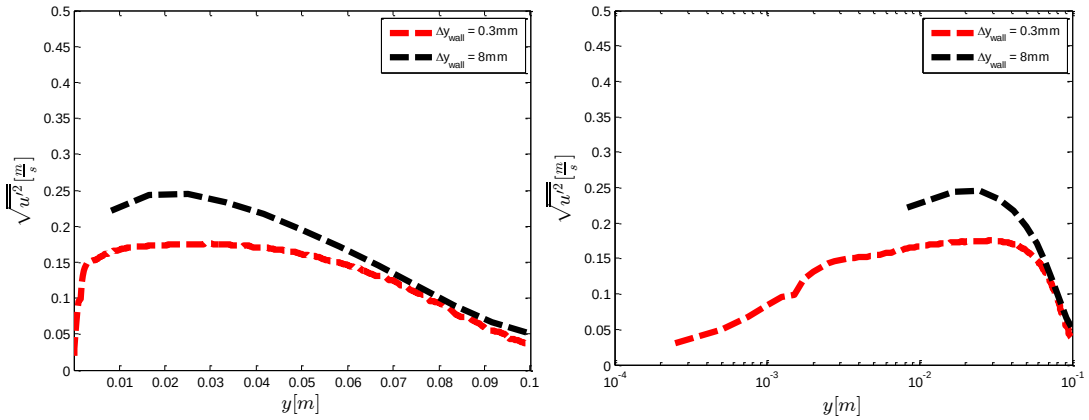

Figure 6. 39 Normal stresses in streamwise direction illustrating effects of under-resolving the boundary layer.

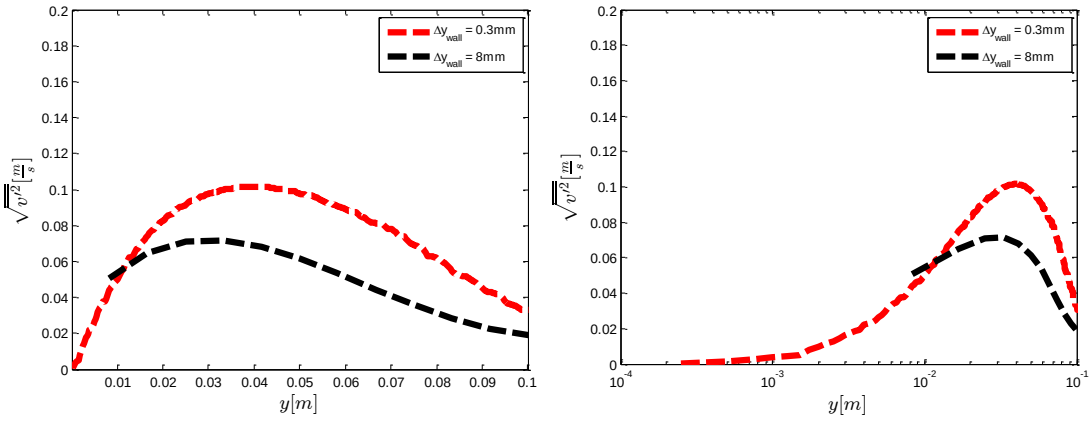

Figure 6. 40 Normal stresses in wall-normal direction illustrating effects of under-resolving the boundary layer.

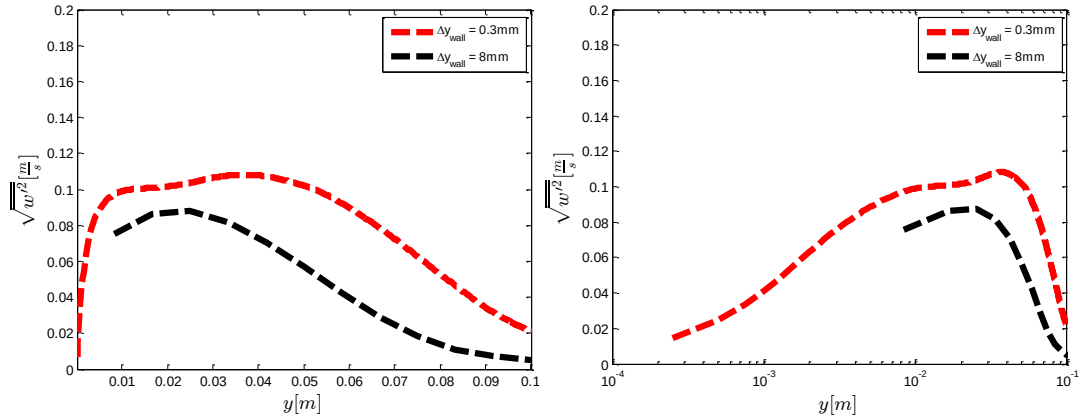

Figure 6. 41 Normal stresses in spanwise direction illustrating effects of under-resolving the boundary layer.

6.6 Closing Remarks

The LES of mixed convection turbulent boundary layer flow over an isothermal vertical flat plate has led to some pertinent conclusions that will be subsequently summarized:

- Imposing and increasing the freestream velocity onto a turbulent natural convection boundary layer causes the boundary layer thickness to diminish despite an increase in wall shear stress. In addition, as the wall shear stress increased, the wall heat transfer decreased.
- As the freestream flow increased, the peak of $\sqrt{\overline{u'^2}}$ near the wall remained near constant; however, the value of $\sqrt{\overline{u'^2}}$ in the outer layer is drastically suppressed. Moreover, $\sqrt{\overline{t'^2}}$ was also suppressed significantly in the outer layer.
- As the freestream velocity was increased to $0.8\ \mathrm{m/s}$, the mixed convection boundary layer did not transition to full turbulence within the computational domain and in the experiment. Double peaks seen in $\sqrt{\overline{u'^2}}$ and $\sqrt{\overline{t'^2}}$ were stated to be indicative of a transitioning flow.
- Negative values of $u't'$ were observed very near the wall; the PDF of u' and t' indicated that low speed fluid and high temperature fluid invaded the near-wall region.
- Waveforms of streamwise velocity and temperature fluctuations illustrated high and low frequency motion encompass the near-wall region at $Gr_x/Re_x^3 = \infty$ and 4.68×10^{-4}. At $Gr_x/Re_x^3 = 1.05 \times 10^{-4}$, turbulent

motions of different lengthscales were absent and harmonic fluid motion of a specific frequency seems to be dominant near the wall. In the outer layer, large scale eddies were dominant at $Gr_x/Re_x^3 = \infty$. However, increasing the forced flow caused high frequency eddies to dominate the outer layer.

- Frequency spectra of u' and t' in the outer layer showed that the most energetic lengthscale was at 0.8 Hz at $Gr_x/Re_x^3 = \infty$. At $Gr_x/Re_x^3 = 4.68 \times 10^{-4}$ and 1.05×10^{-4}, the most energetic fluid motion in the outer layer were 3 Hz and 11 Hz, respectively.
- The production of turbulent kinetic energy dominated by sweeps in wall bounded forced convection turbulence was absent in the near wall region of the turbulent mixed convection boundary layer. In the outer layer, it seems buoyant production and shear production contribute to the generation of Reynolds shear stress.
- The implementation of a mixed-convection wall function predicted acceptable first and second order turbulent statistics by prescribing the first grid node off the wall at the edge of the inner layer.
- Although the results were not illustrated in this chapter, discrepancies with the computed heat flux acquired from the mixed-convection wall model were observed. Since the wall model corrects the SGS thermal diffusivity at the wall, which is employed in computing the wall heat flux, it seems there might be issues with using a high Reynolds number wall model in a low Reynolds number flow. This further elucidates the lack of available wall models specifically for mixed convection turbulent wall flows.

- Coarse grid LES results were compared to resolved LES showed that as the grid was coarsened, $\sqrt{\overline{u'^2}}$ was overpredicted and and $\sqrt{\overline{w'^2}}$ were underestimated. Typically, this phenomenon is a well-known symptom of LES of forced convection turbulent flows and it can be assumed to be caused by the poorly resolved intercomponent turbulent energy transfer. Hence, this occurrence is present with buoyancy affected turbulent boundary layers as well.

Chapter 7: Thermal Instability of Blasius Flow Test Case

7.1 Test Case Description

The thermal instability of Blasius flow test case is based partly upon the experimental measurements of [28] over an isothermally heated horizontal flat plate. This experiment was undertaken in a water tunnel to measure data in the developing mixed convection turbulent boundary layer flow. However, the current effort makes use of air exclusively as the working fluid. Thus, in the absence of any readily available experimental data to make direct comparisons to, it was determined to formulate a case comparable to those employed for the water tunnel experiments. This case comprises a Reynolds number that disallows for the onset of hydrodynamic instability, i.e. $Re_x < 5.0 \times 10^5$. An illustration of the hydrodynamic instability known to occur in a forced convection boundary layer transition can be seen in Figure 7.1. Following the stable laminar flow near the leading edge of the plate, unstable Tollmien-Schlicting wave emerge, which form into lambda vortices that eventually break-up into full turbulence downstream.

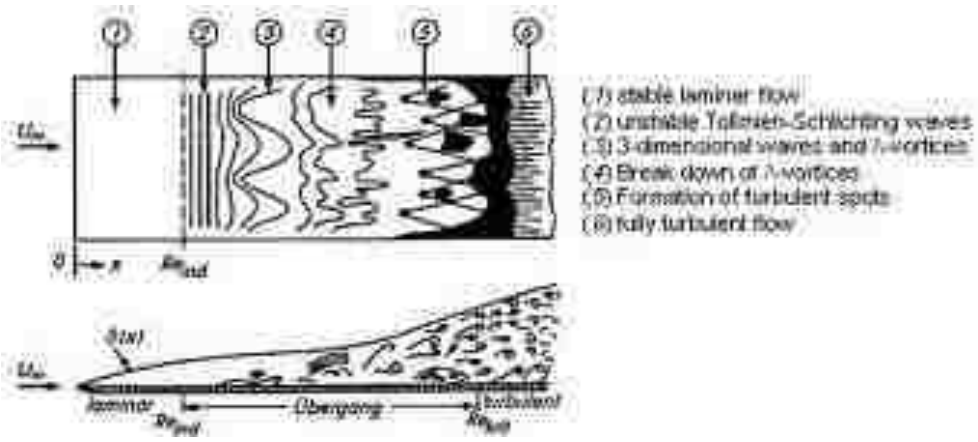

Figure 7. 1 Schematic of Tollmien-Schlicting wave mode instability in forced convection boundary layer flow from [142].

The isothermally heated plate was 1.5 m and 0.3 m in the streamwise and spanwise directions, respectively. The freestream velocity prescribed was 0.84 m/s, which correspond to $Re_x = 8.4 \times 10^4$ at the downstream end of the flat plate. The freestream temperature was 298 Kelvin and a wall temperature of 394.4 Kelvin was used to produce sufficient buoyancy force conducive to the generation of longitudinal vortices. This buoyancy force, similarly to the centrifugal force responsible for the emergence of vortex rolls (Görtler vortices) aligned in the streamwise direction over a concave wall [143], is the primary cause of the longitudinal vortices in a Blasius flow over a heated plate. As aforementioned, the physics behind this phenomenon lies in the fact that whenever there is a force normal to the streamwise direction in a laminar boundary layer at a sufficiently low Reynolds number, initial counter-rotating vortex rolls situated in the primary flow direction are manifested. In regards to Görtler vortices, Figure 7.2 shows the velocity profile over a concave surface where the center of curvature is at a radial location of $\mathrm{r} = 0$. From Figure 7.2, it is apparent that at $\mathrm{r} = 0$, $\mathrm{ru}_\infty = 0$ and at the wall, $\mathrm{r}_w\mathrm{u} = 0$. Therefore, along the radial direction

and away from the center where $u = u_\infty$, $\frac{\partial(ru)}{\partial r} > 0$ and a maximum value of ru will be attained. Furthermore, a minimum value of ru occurs at $r_w u$. Thus, there is must exist a region along the radial direction where $\frac{\partial(ru)}{\partial r} < 0$. As such, with the utilization of disturbance equations, Görtler was able show that the solution resulted in the form of streamwise counter-rotating vortices [144]. These counter-rotating streamwise vortices can be seen in Figure 7.3.

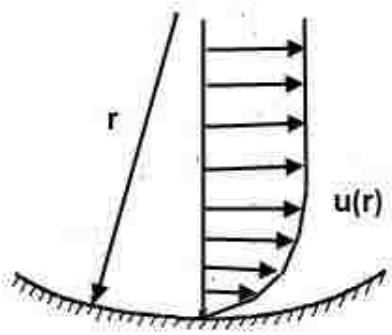

Figure 7. 2 Depiction of streamwise velocity distribution along concave wall surface. Image adopted from [144]

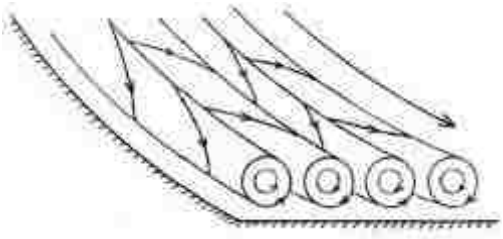

Figure 7. 3 Schematic of streamwise oriented counter-rotating vortices formed above concave wall from [144].

As it pertains to the current work, the manifestation of the streamwise vortices is only realized when the Grashof number excels a critical value for the thermal instability Blasius flow. Figure 7.4 shows a schematic interpretation of a typical thermal boundary layer at low Reynolds number.

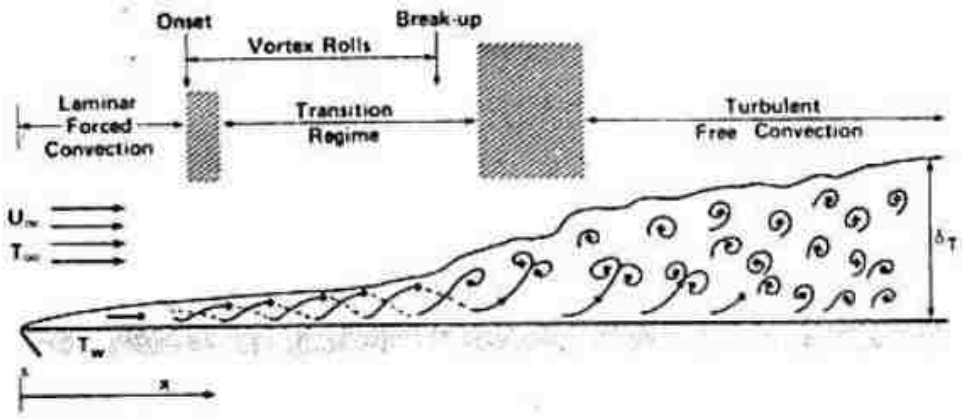

Figure 7. 4 Schematic of flow regimes over isothermally heated flat plate experiment, from [28].

7.2 Computational Setup

A schematic of the computational domain along with the boundary conditions are illustrated in Figure 7.5. As it can be seen from the figure, uniform freestream values for the velocity and temperature were prescribed at the inflow boundary. Immediately ahead of the freestream boundary, there is a 0.1 m entrance length appropriately implemented to avert a sudden start of the boundary layer. The isothermally heated plate length was 1.8 m and the simulation domain spanned 0.30 m in the spanwise direction. In the wall-normal direction, the computational domain was 1.0 m. The spanwise and wall-normal computational domain lengths corresponds to $\sim 4\delta$ and $\sim 8\delta$, respectively. The size of the simulation domain was

iteratively selected by examining the thickness of the thermal boundary layer. Similarly to the two prior test cases, the spanwise direction was treated as a homogenous boundary.

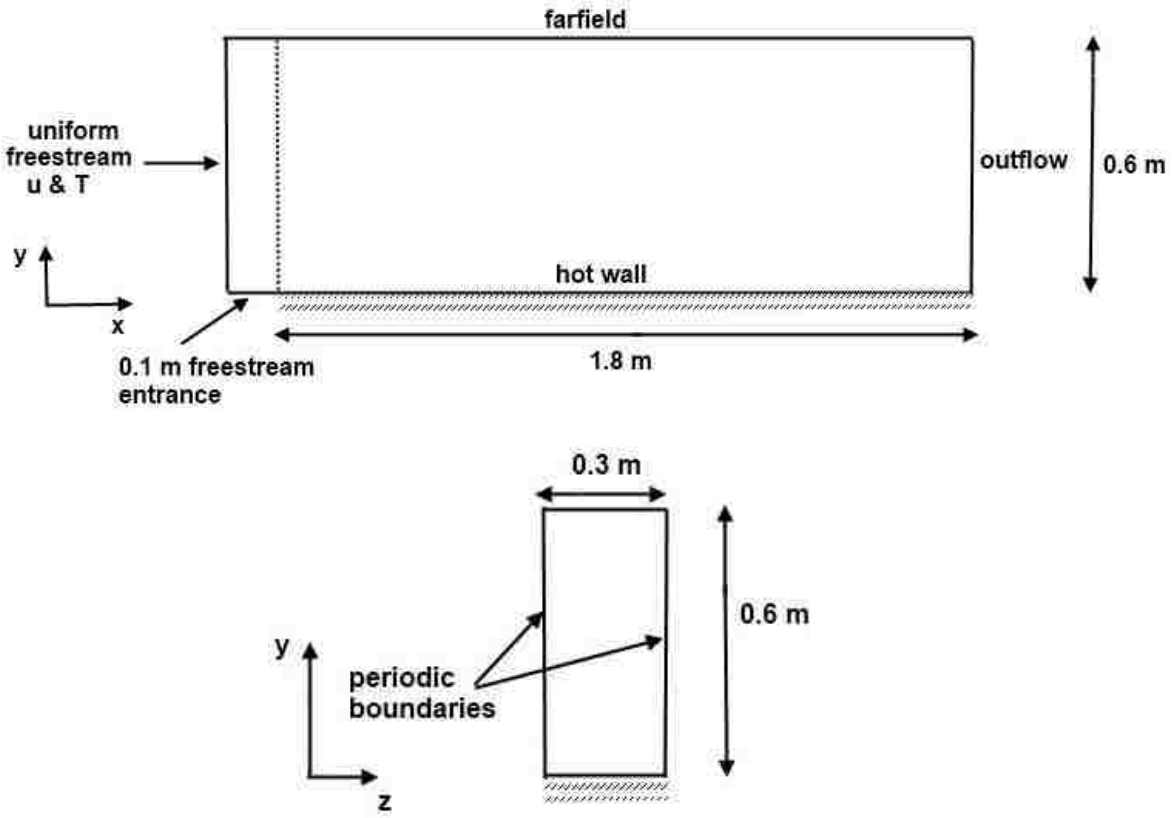

Figure 7. 5 Computational domain and boundary conditions for vortex instability test case.

7.2.1 Computational Grid

Building upon the previous experiences acquired from the other test cases and the relatively small size of the simulation domain needed to capture the growth and subsequent breakup of streamwise vortices, the grid generation process was fairly straightforward. In the freestream entrance region, $\Delta x = 10$ mm was employed and a uniform grid spacing of $\Delta x = 5$ mm was prescribed along the heated flat plate. The spanwise grid resolution was maintained at $\Delta z = 5$ mm and the wall-normal grid spacing was $\Delta y \approx 0.5$ mm. An illustration of the computational mesh can be seen in Figure 7.6.

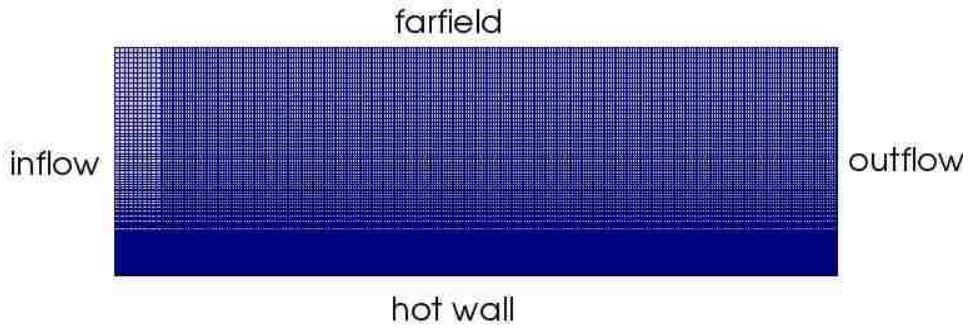

Figure 7. 6 Computational mesh illustration employed for thermal instability of Blasius flow test case.

7.2.2 Simulation Details

The numerical simulation details utilized for the vortex instability case is identical to those implemented for the Tsuji & Nagano test case. In this test case, however, appropriate freestream values for temperature and velocity were implemented at the inflow and the internal domain of the simulation field.

7.3 Wall-Resolved Simulations

As opposed to the exhaustive and extensive efforts that have been put forth to experimentally and numerically investigate the hydrodynamic instability of a Blasius flow, the vortex instability of the Blasius flow is incredibly lacking in research efforts. To the author's knowledge, these LES results are the only relatively extensive predictions to date. Thus, this numerical effort hopes to shed some light upon the empirical and experimental results available in current literature. In moving forward, wall resolved LES results will be presented in the subsequent subsections.

Heat Transfer Correlations

Figure 7.7 depicts the heat transfer coefficient in the Blasius flow heated from below. Up to a downstream distance of approximately 0.5 m, it is apparent the boundary layer is dominated by laminar forced convection dynamics. Thus, we see the correlation between laminar flow theory and the LES prediction. In this region, the effects of the buoyancy are negligible compared to the momentum of the incoming freestream flow. And without any significant free convection effects, the wall heat transfer progressively decreases with increasing streamwise distance, x. Subsequently, around the streamwise distance of ~ 0.5 m, an abrupt increase in wall heat transfer is observed. This rapid increase in heat transfer, as will be illustrated later, is ascribed to the onset of longitudinal vortices. These streamwise vortex rolls create a secondary finite amplitude flow that enhances the wall heat transfer especially during the downwash motion of the vortices as they bring colder higher momentum fluid towards the wall. Eventually, these ordered counter-rotating streamwise vortex rolls become increasingly unstable as they travel downstream and

break-up into fully developed turbulence. The onset and break-up of these vortices spans roughly ~0.3 m and a fully developed turbulent boundary layer commences around ~0.8 m, see Figure 7.7. In the fully turbulence region, a relatively constant heat transfer coefficient seems to prevail along the heated flat plate. In contrast to a decreasing heat transfer coefficient with increasing x for a fully developed forced convection turbulent boundary layer, the constant heat transfer coefficient is typical of turbulent free convection boundary layer flow. In Figure 7.8, wall heat transfer rates correlated with $Gr_X/Re_X^{1.5}$ and $Nu_X/Re_X^{0.5}$ are shown in the laminar forced convection, transition and turbulent free convection regimes. The most profound takeaway from Figure7.5 is the ability of the LES to accurately validate the criteria of regimes given by [28]. Those criteria indicating the different regimes will be repeated here for convenience and are:

$$\begin{cases} \dfrac{Gr_{xc}}{Re_{xc}^{1.5}} < 100 \\ Nu_x = 0.332 Pr^{1/3} Re_x^{1/2} \end{cases} \quad laminar\ forced\ flow\ ,$$

$$100 < \frac{Gr_{xc}}{Re_{xc}^{1.5}} < 300 \quad transition\ ,$$

and

$$\begin{cases} \dfrac{Gr_{xc}}{Re_{xc}^{1.5}} > 300 \\ Nu_x = 0.14 (Gr_x Pr)^{1/3} \end{cases} \quad turbulent\ free\ convection\ .$$

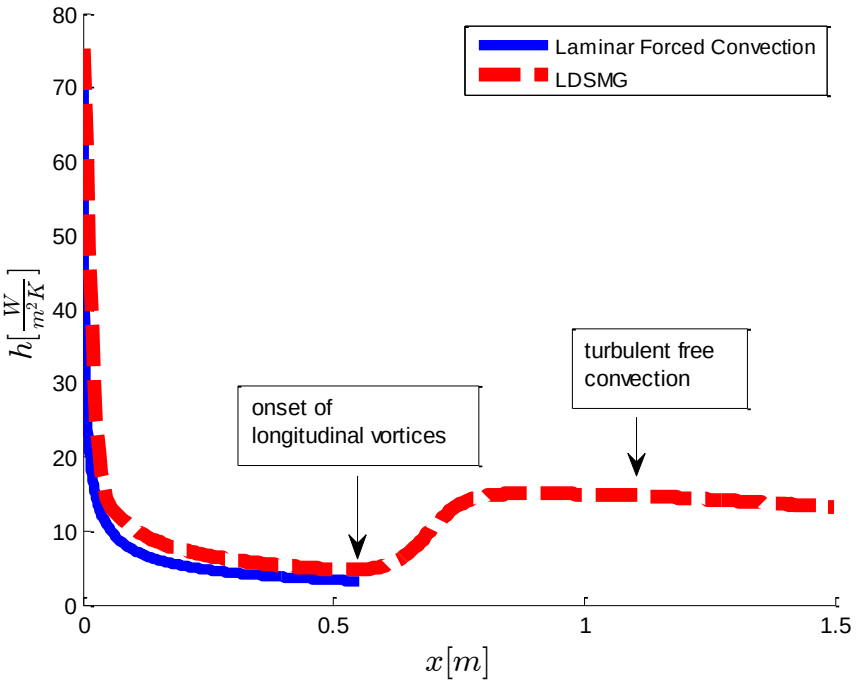

Figure 7. 7 Variation of heat transfer coefficient along heated flat plate illustrating different flow regimes.

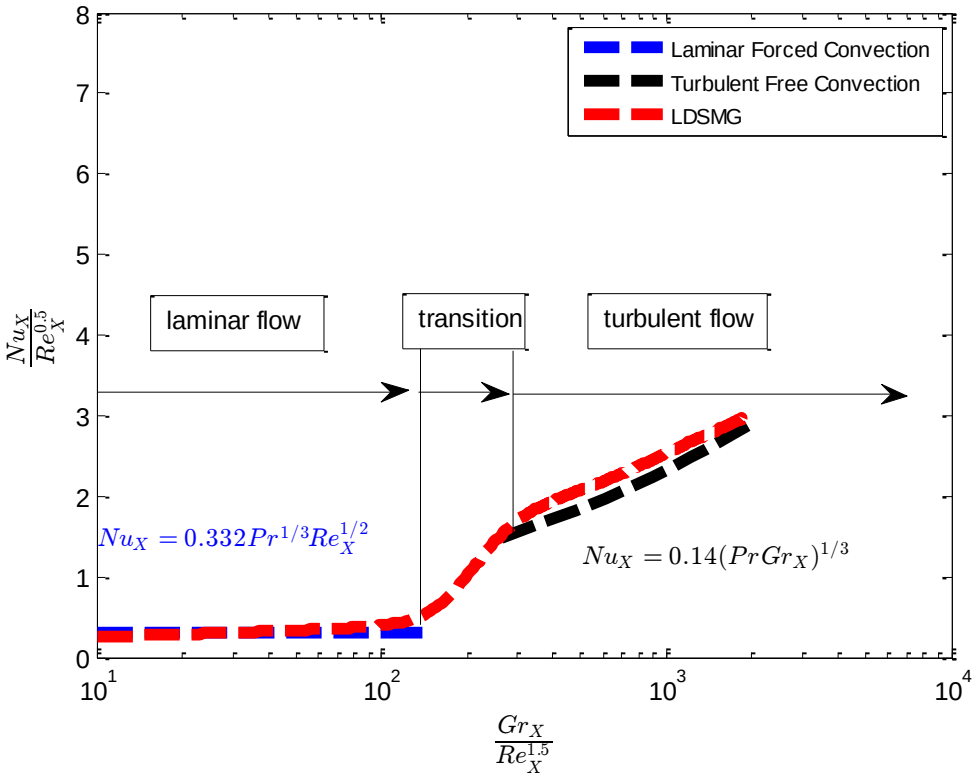

Figure 7. 8 Heat transfer rates correlated with $Gr_X/Re_X^{1.5}$ and $Nu_X/Re_X^{0.5}$.

From Figure 7.8, it can be seen that laminar forced convection flow is the mode of dominance for $Gr_X/Re_X^{1.5} < 100$ and the LES prediction was able to replicate that behavior. In the transition range, $100 < Gr_X/Re_X^{1.5} < 300$, which marks the onset and break-up of the longitudinal vortices, the LES result successfully captured this phenomenon. It is obvious from Figures 7.7 and 7.8 that up to $Gr_X/Re_X^{1.5} \approx 300$, the wall heat transfer is affected by forced convection effects, although the effects become increasingly enfeebled as $Gr_X/Re_X^{1.5}$ increases. In the transition region, it can be assumed that inertia and buoyancy effects are both important. However, the buoyancy effects become more dominant once the longitudinal vortices break-up into full turbulence. This is quite evident from Figure 7.4; the heat transfer coefficient is nearly independent of the Reynolds number. The Reynolds number independence is characteristic of the wall heat transfer behavior observed in fully developed natural convection turbulence over a horizontal heated flat plate without any freestream flow [28]. The Reynolds number independence can also be seen in Figure 7.8 as the wall heat transfer increases as a function of $PrGr_X$.

Near-Wall Boundary Layer Structure

Figure 7.9 depict the growth of the instantaneous streamwise velocity and thermal boundary layer on the Blasius flow heated from below. It is interesting to note that from Figure 7.7, the onset of longitudinal vortices was observed to occur around a streamwise location of x~0.5 m; from Figures 7.9, the boundary layer does not markedly increase in the presence of the streamwise vortices. However, it can be seen that the boundary layer thickness immediately increases at the inception of full turbulence, around streamwise distance of x~0.8 m.

The isosurface of $Q > 0$ criterion, which essentially illustrates the presence of coherent structures in the near-wall layer, can be seen in Figure 7.10. Figure 7.10 show the absence of streamwise structures near the leading edge of the heated flat plate, in what seems to be "quiescent region". Further downstream, we can see that strands of streamwise oriented structures exist around x~0.45 m. These streamwise structures, i.e. longitudinal vortices, seem to be profoundly coherent up to x~0.6 m. Thereafter, counter-rotating streamwise vortices can still be seen, except they seem to be gradually merging with increasing streamwise distance. Moreover, instances of spanwise meandering of the vortices is apparent as well. Such a behavior classifies the transition region. Eventually, around to x~0.8 m, the longitudinal vortices have apparently disintegrated into full scale turbulence. A magnified view of the coherent structures in the fully developed turbulent boundary layer flow region can be seen in Figure 7.11. It is apparent that the existence of clearly defined quasi-streamwise vortices is absent in the near-wall flow topology. A combination of streamwise and spanwise situated structures can be seen near the wall without a dominant directional orientation. These near-wall structures profoundly differ from those typically seen in forced convection turbulent boundary layers. The tilting of structures in the spanwise direction, caused by mutual induction, cannot be seen near the wall for this flow configuration.

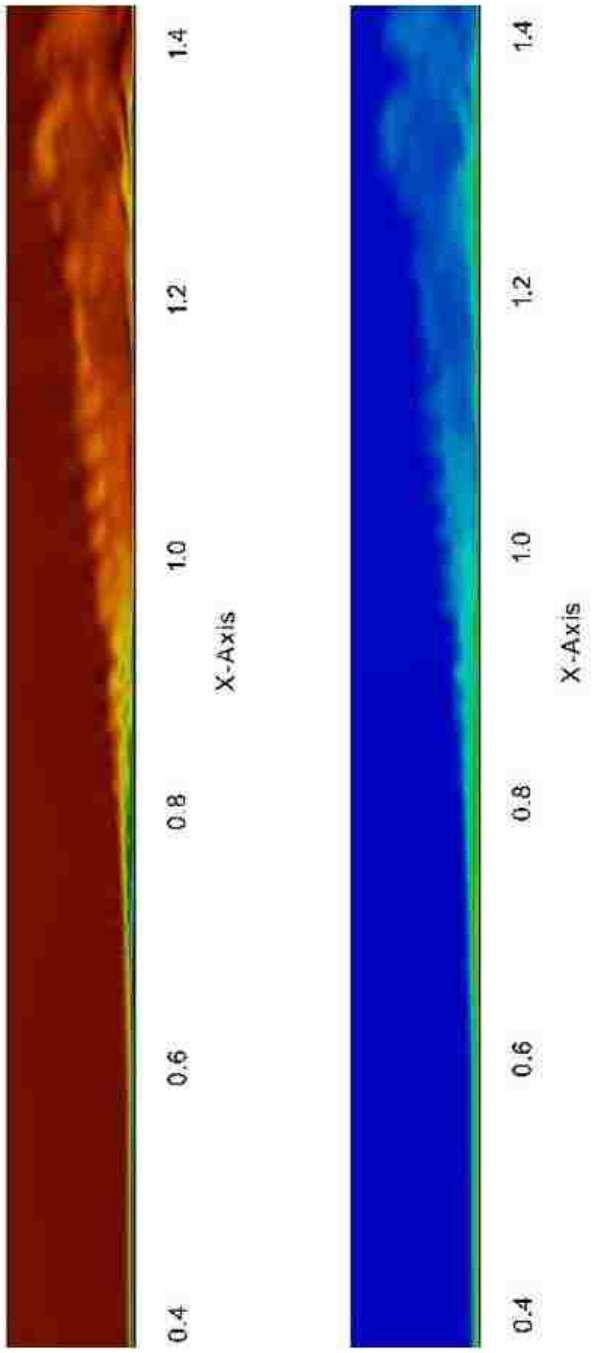

Figure 7. 9 Evolution of instantaneous streamwise velocity (left) and instantaneous temperature along heated flat plate.

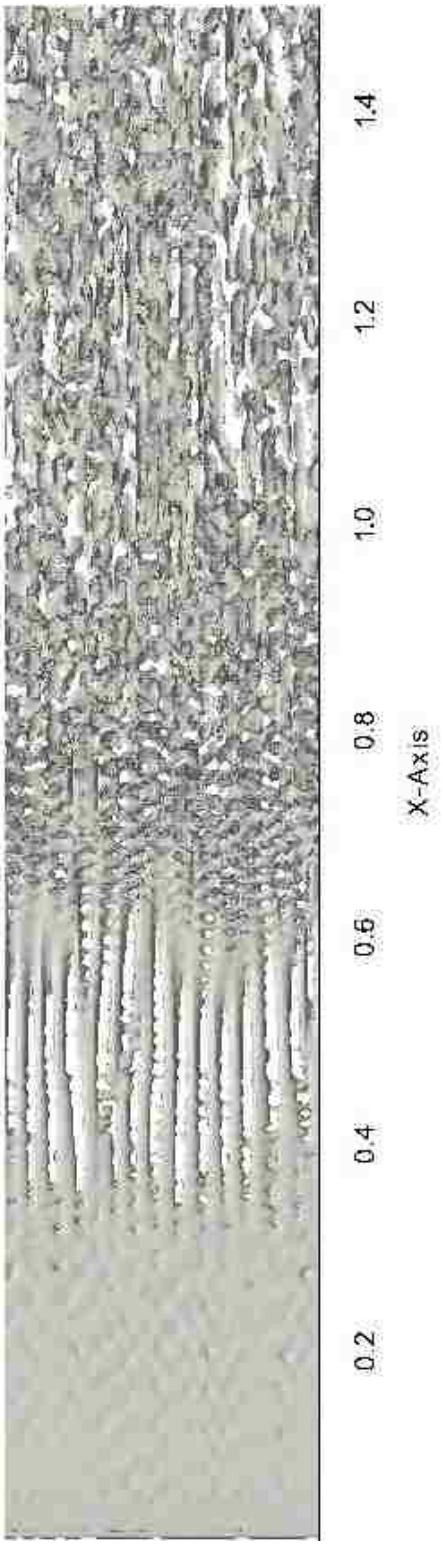

Figure 7. 10 Isosurface of $Q > 0$ criterion illustrating formation and eventual break-up of longitudinal vortices.

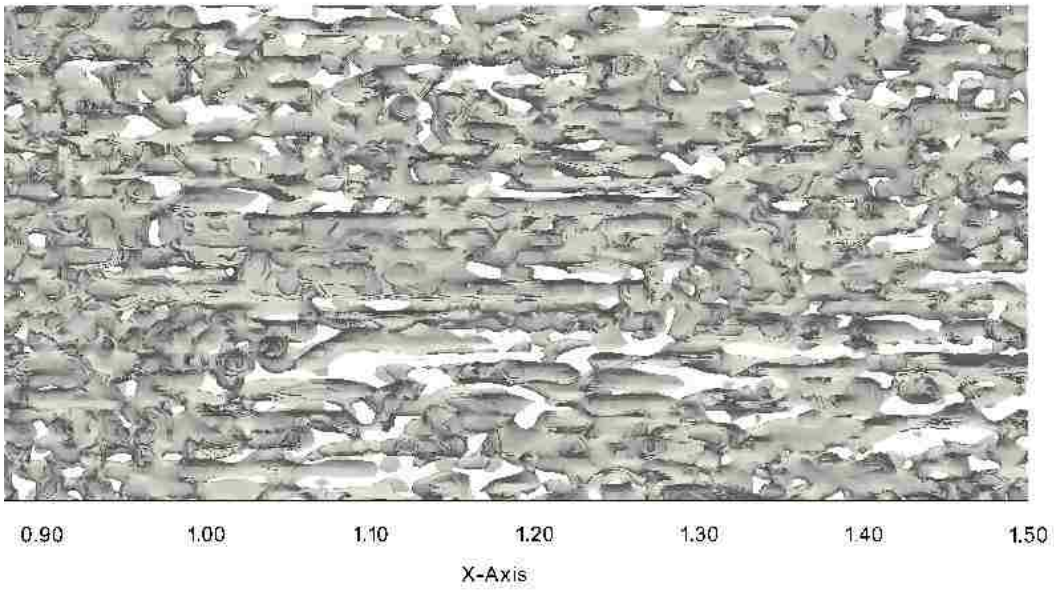

Figure 7. 11 Isosurface of $Q > 0$ criterion in fully developed turbulent flow region of Blasius flow heated from below.

Mean and fluctuation intensity profiles of Temperature

To proceed with the analysis of the flowfield following the breakup of the longitudinal vortices into full turbulence, it would necessary to do so with the utilization of available turbulent free convection flow experiments.

Figure 7.12 show a near-wall blown-up view of the mean temperature profile at the streamwise location of $x = 1.2$ m. Following in the footsteps of [145], [146], [147], we define the thermal layer thickness, δ_{th}, as the wall-normal location where the extrapolation of the linear part of the mean temperature profile near the wall intersects with the line of constant ambient temperature, T_∞. Doing as such, δ_{th} was approximated to be 3 mm. In Figure 7.13, the temperature fluctuation intensity is shown with a blue line to depict the edge of the thermal layer. The peak of the

temperature fluctuation intensity occurs near the edge of the thermal layer and in order to explain the peak, we can take a look at Figure 7.14. The mean temperature profile along the normalized wall-normal distance $\frac{y}{\delta_{th}}$, is shown in Figure 7.14. Also depicted in aforementioned figure are the conduction layer, conduction and convection layer, and convection layer [148]. The conduction layer is essentially the region next to wall where heat transfer is by diffusion only. In the conduction and convection layer, heat transfer occurs via diffusion and rapid mixing (buoyancy induced convection) away from the wall. The convection layer is a region where diffusion of heat is absent and convection is dominant. In the current flow configuration, the convection layer commences around $\frac{y}{\delta_{th}} \sim 20$; the work of [147], [148] reported the convection layer began at approximately $\frac{y}{\delta_{th}} > 10$. We can proceed to explain the peak of temperature fluctuation intensity near the edge of the thermal layer. The conduction layer near the wall grows by diffusion and gradually becomes unstable. As a result of the instability within the conduction layer, the layer erupts and releases hot blobs of turbulent fluid (thermal). As such, these recurring intermittent events inside the conduction layer is the reason for the temperature fluctuation peak near the edge of the thermal layer.

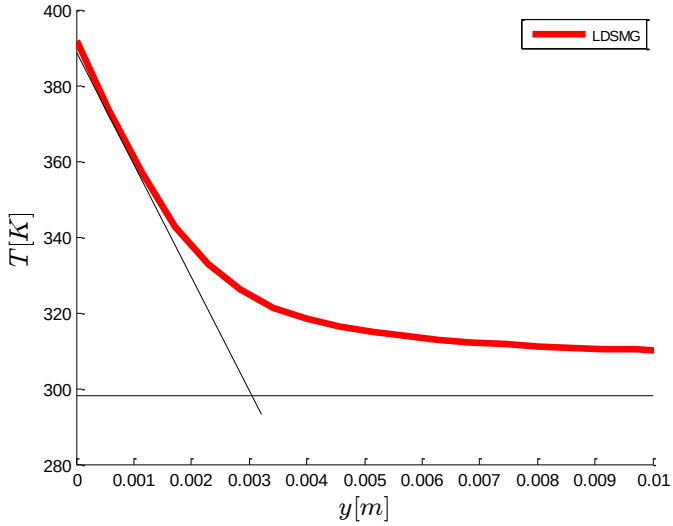

Figure 7. 12 Magnified illustration of mean temperature wall profile at x = 1.2 m indicating approximation of thermal layer thickness.

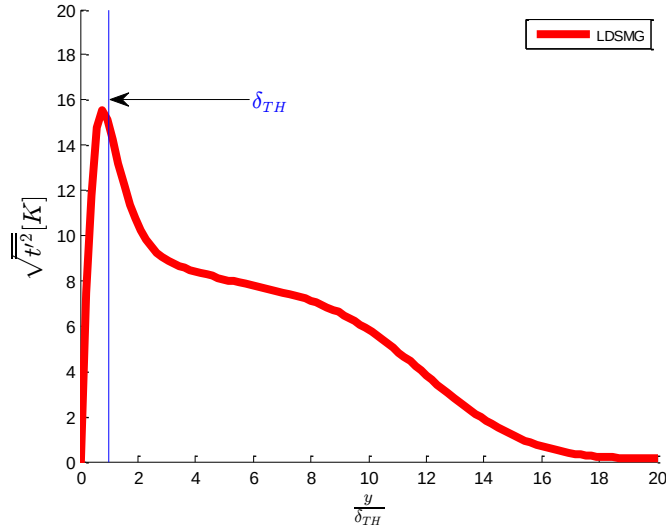

Figure 7. 13 Temperature fluctuation intensity at x = 1.2 m with blue line depicting edge of thermal layer thickness.

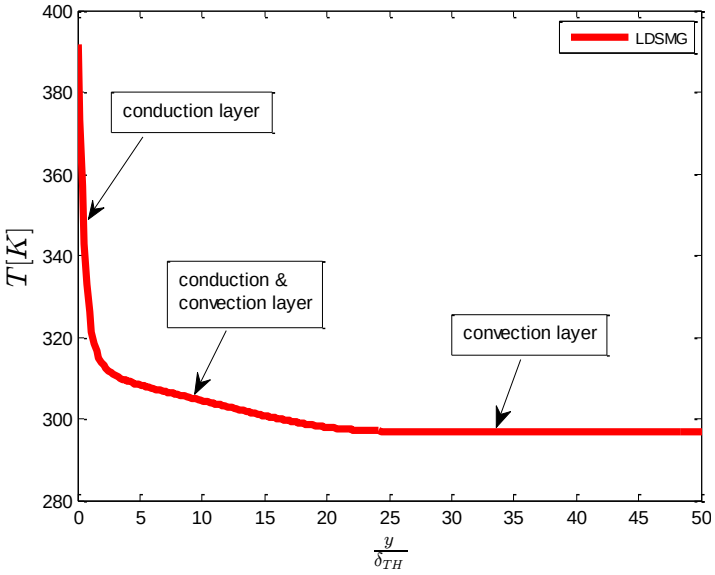

Figure 7. 14 Mean temperature profile at x = 1.2 m indicating the three regions in the wall-normal direction.

Flow Visualization

It was previously mentioned that the reason for the temperature fluctuation intensity peak near the edge of the thermal layer was due to the unstable growth of the conduction layer. The conduction layer subsequently erupts and releases hot turbulent buoyant fluid. In order to illustrate the characteristics of these structures near the wall, successive flow grayscale visualization at $\frac{1}{20}$ secs intervals at a streamwise location of x = 1.2 m can be seen in Figure 7.16. It can be seen from Figure 7.16 that the characteristic orientation of the structures is in the vertical direction, even though some meandering in the spanwise can be seen as the thermals get further away from the wall. As these structures get further away from the wall, they become weaker as they interact with colder turbulent fluid. Consequently, these thermal plumes loose heat to their surroundings and erode as they rise. Observable mushroom type elliptical structures can be seen in some of the structures presented in

Figure 7.15 and is indicative of the front of the thermals. In addition, some of these structures are seen to merge as they rise prior to erosion.

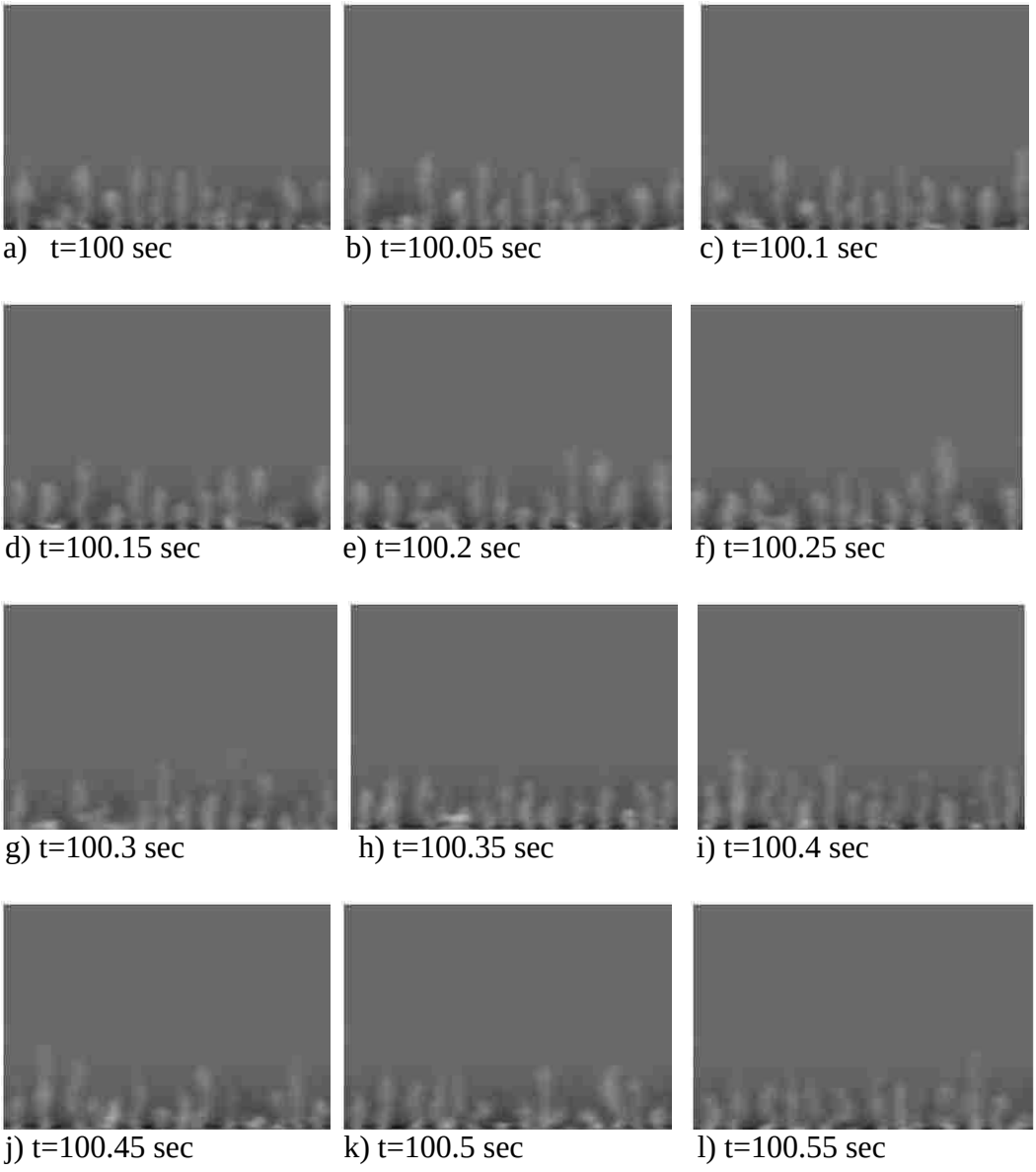

Figure 7. 15 Successive flow visualization of temperature fluctuations in y-z plane illustrating bursting thermals pattern over heated flat plate at streamwise location $x = 1.2$ m.

It would be expected to see the thermal plumes shown in Figure 7.15 develop along the streamwise direction in the fully turbulent flow region. With this notion in mind, Figure 7.16 illustrates the $Q > 0$ isosurface in the x-y plane. The isosurfaces depicts the orientation of the structures in the fully turbulent region of the flowfield and it can be seen that these structures are inclined forward, while some seem to be in a relatively vertical position. These structures are due to the thermal plumes bursting from the unstable conduction layer. As they travel away from the near-wall region, the streamwise global motion slowly sweeps them horizontally causing the apparent forward inclination.

Figure 7. 16 Isosurface of $Q > 0$ in the x-y plane depicting inclined oriented structures due to attenuated thermal plumes.

7.4 Closing Remarks

The thermal instability of the Blasius flow was examined using LES and the numerical data was only validated with engineering and empirical solutions due to the extensive lack of experimental data. Nonetheless, the following conclusions were drawn and are summarized below:

- The three flow regimes, laminar forced convection, transition and turbulent free convection, were validated with the empirical criteria of [28].
- The formation and eventual break-up of the streamwise vortices was numerically validated employing the Q criterion feature identification scheme. The break-up of the vortices was seen to occur as they meandered in the spanwise direction and merge as they traveled in the streamwise direction.
- The near-wall flow topology observed in the turbulent free convection regime did not have a dominant direction and lacked the orientation seen in forced convection turbulent wall flows.
- Bursts of turbulent hot fluid were numerically illustrated to be the dominant mechanism for turbulent in the downstream region. These thermals emerged as a result of the unstable growth of the conduction layer near the wall. In addition, the temperature fluctuation intensity attained its maximum value near the edge of the conduction layer.

Chapter 8: Conclusions and Future Efforts

The primary goal of this thesis was to assess the predictability, practicality and applicability of the LES methodology to various wall bounded turbulent flows strongly affected by the presence of the gravitational buoyancy force in the absence and presence of a forced flow. Through a variety of numerical experiments and validations, it was determined that the Large Eddy Simulation approach can definitely be of profound use for these types of flow configuration.

8.1 Summary of Key Observations

8.1.1 Tsuji & Nagano Test Case

The wall-resolved and wall-layer modeled LES of natural convection turbulent boundary layer over an isothermal vertical plate was performed; based upon the acquired results and analysis, the following conclusions were drawn:

- Excellent agreement was achieved with the experimental data for the first and second order turbulent statistics.
- The study undertaken to ascertain the required width of the simulation domain in the spanwise direction needed to sufficiently capture turbulent structures revealed δ, the thickness of the turbulent boundary layer, can be

used. This enabled a cost-effective computed turbulent flowfield that resulted in high fidelity results.

- It was discovered that the exact location of transition to turbulent does not have to match the experiment. The important parameter following the start of a fully turbulent boundary layer is the growth of the boundary layer thickness, δ. The numerical study of forcing the boundary layer transition to match those of the experiment illustrated that it is the "time-spent" in full turbulence by the flowfield that ought to match the experiment in order to make a fair comparison between the LES and measured data.
- Wall-layer modeling LES results showed that prescribing approximately 10 grid cells across the boundary layer thickness can give reasonably accurate first and second order statistics, in addition to highly accurate reconstruction of the wall heat flux. The utilization of 10 grid cells across the boundary layer resulted in the first computational node off the wall being placed in the outer layer of the turbulent boundary layer. This realization resulted in a much cheaper simulation easily applicable to engineering calculations.
- The production of turbulent kinetic energy was observed to be nearly equally impacted by shear and buoyant productions. The shear production was dominant near the wall and in the outer edge of the turbulent boundary layer. In the middle of the boundary layer, buoyant production of turbulence was dominant.

8.1.2 Hattori Test Case

The Hattori test case comprised the wall-resolved and wall-layer modeled LES of mixed convection turbulent boundary layer over an isothermal vertical flat plate. For this case,

- Excellent agreement was achieved with experimental measurements for the first and second order turbulent statistics. The only discrepancy in the results was due to the near-wall behavior of the streamwise turbulent heat flux computed by the LES as the freestream velocity was increased to $0.8\,\mathrm{m/s}$. This discrepancy was attributed to the inadequate grid resolution required to resolve the extremely thin near-wall flowfield.
- Despite an increase in wall shear stress as the freestream velocity was increased, the boundary layer thickness diminished due the suppression of the large length scales in the outer layer. Since larger eddies are mostly responsible for the majority of mixing in turbulent boundary layers, it was determined that the decrease in wall heat transfer was a consequence of the suppression of the outer layer large length scales. Furthermore, increasing the freestream resulted in dominance of higher frequency eddies in the outer layer. The frequency of the most dominant eddies ranged from ~ 1Hz to 11 Hz as the freestream velocity increased.
- It was observed during this research that the wall-layer modeling of turbulent mixed convection computed acceptable first and second order turbulent statistics that were comparable to the experimental data. However, discrepancies in the wall heat flux acquired from the wall model were noted

when compared to the wall-resolved wall heat flux. It can be understood that the cause of this discrepancy can be due to the blending of the asymptotic wall functions for high Grashof and Reynolds numbers. For this particular flow configuration, a low forced flow was applied resulting in a significantly low Reynolds number flow. Hence, given the non-existence of any suitable mixed-convection law of the wall, on-going efforts to derive and implement an appropriate wall model will be required to accurately reconstruct the wal heat flux.

8.1.3 Thermal Instability of Blasius Flow Test Case

Having tested and validated the fidelity of the approach and flow solver employed in the current work, it was decided to compute the thermal instability over an isothermal horizontal flat plate. The conclusions drawn are as follows:

- The three flow regimes, laminar forced convection, mixed convection transition to turbulence and turbulent free convection were numerically validated with LES.
- The formation and eventual break-up of the longitudinal vortices were qualitatively validated using the Q criterion vortex feature identification scheme.
- The near-wall flow topology in the turbulent free convection regime did not have a dominant direction and lacked the orientation seen in forced convection turbulent wall flows.
- Bursts of turbulent hot fluid were numerically illustrated to be the dominant turbulent mechanism in the downstream region. The blobs of hot turbulent

fluid, i.e. thermals, emerged as a consequence of the intermittent nature of the conduction layer near the wall.

8.2 Recommendations for Future Efforts and Suggestions

An essential outcome of this research was the insight acquired into the limitations posed by the utilized approach and how they could be possibly improved upon. Some of these improvements pertain to the LES methodology as a whole, while some are pertinent to the on-going improvement and enhancement of the OpenFOAM® solver. These suggestions will be subsequently touched upon and elaborated as follows:

- The issue of turbulent inlets in LES is a fairly well known problem, to date. Even though there are some available methodologies that can be employed to prescribe some turbulence at the inlet of a simulation domain, some of these methods fail to accurately represent realistic spatial scales between the grid spacing and integral length scales of the particular flow topology. The ability of a turbulent methodology to reproduce reasonably accurate turbulent and mean statistics of the flow at the inlet is challenging for spatially developing turbulent boundary layer flow. A possible approach will be the implementation of the turbulent synthesis inlet method. Such a methodology essentially imposes some random noise over the mean inlet profile by artificially reconstructing the turbulent structures with the appropriate scales and spacing. With the implementation of turbulent inlet in the OpenFOAM® library of codes, the computational cost of the simulations undertaken in this thesis will be profoundly reduced. Furthermore, such an enhancement will

make the code more applicable to engineering calculations that typically require fast and efficient numerical simulations.

- SGS modeling in LES is a crucial aspect of acquiring accurate results. The improvement of SGS models will be required in order to increase the utilization and acceptance of LES as the main tool in numerically simulating turbulence. In the aspect of buoyancy affected turbulent boundary layer flows, mostly all the SGS models are based upon the premise that production of turbulent kinetic energy is attributable to shear. The inclusion of buoyant production in SGS models can possibly have profound effects upon the accuracy of results for turbulent flowfields affected by buoyancy. Another issue of SGS models observed in the current effort is the effects of intercomponent turbulent energy transfer. In order to fully enable engineering calculations, coarser LES grids will be required; thus, further effort may be required to comprehend the phenomenon of intercomponent turbulent energy transfer and SGS modeling. In addition, employing coarser LES grids means larger anisotropic length scales will be modeled by the SGS model. In light of this, the utilization and further study of the full Reynolds stress closure of the SGS stresses will be necessary. This essentially removes the SGS isotropy assumption and quite possibly, allow for the use of much coarser meshes in LES computation. It should be noted that such an approach require the calculation of 6 additional transport Reynolds stress equations, 3 equations for the Reynolds normal stresses and 3 equations for the Reynolds shear stresses. The question will be if the accuracy gained with

the utilization of such SGS model is worth the additional computational cost; this is yet to be determined.

- A profound limitation encountered in the current work was the extensive computational time required to perform the required simulations. On average, approximately 27,000 grid cells were prescribed to each core of the computational hardware employed in this research; the number of cores used ranged from 32 to 256, depending upon the computational requirements of the numerical simulation. It was observed that more efficient parallel algorithms would potentially drastically reduce the time needed in simulating wall turbulent flows. Some of the simulations in this thesis took nearly 2 months to complete and further optimization of parallel algorithms can help to reduce the simulation time.
- In gaining further comprehension of the current work, a detailed DNS study of the natural convection turbulent boundary layer without the use of the Boussinesq approximation will be profoundly helpful. To be more specific, the near-wall turbulent structures and flow-dynamics needs to be further understood. Acquiring such knowledge may potentially be helpful in developing SGS models for buoyancy affected turbulent wall flows.
- Since this research effort was part of a building block to enable the computation of in-flight next-generation aircraft engines pool fires using LES, an extension of the current code will be required to enable flame spread simulations in such an environment. This environment may very well consist of a turbulent freestream entering the engine compartment. In light

of this, given the myriad of complexities inherent to such a flow, a reasonable path forward would be the initial calculation and understanding of ground-test aircraft engine compartment fires.

8.3 Closing Comments

This thesis illustrated the impressive accuracy that can be achieved with LES in resolving buoyancy affected turbulent boundary layer flows. Presently, the utilization of LES as a practical engineering tool in simulating turbulence is somewhat over-shadowed by RANS. In order to take LES to a profound level whereby its computational cost will be comparable to that of RANS, a decent amount of future work and improvements will have to be made to the SGS models currently being used. Nonetheless, it does seem that LES will be the go-to tool in simulating turbulence in the coming years. Simply put, LES has the ability to surpass RANS and DNS as the primary turbulence simulating tool and these capabilities seem to become promising with time.

Bibliography

[1] N. Kasagi and M. Nishimura, "Direct numerical simulation of combined forced and natural turbulent convection in a vertical plane channel," *International Journal of Heat and Fluid Flow,* vol. 18, pp. 88-99, 1997.

[2] I. F.P. and D. DeWitt, Fundamentals of Heat and Mass Transfer 4th Edition, New York: Wiley, 1990, pp. 490-491.

[3] R. Godaux and B. Gebhart, "An experimental study of the transition of natural convection adjacent to a vertical surface," *International Journal of Heat and Mass Transfer,* vol. 17, pp. 93-107, 1974.

[4] S. Ostrach, "An analysis of laminar free-convection flow and heat transfer about a flat plate parallel to the direction of the generating body force," NACA TN 2635 Report 1111, 1952.

[5] C. Y. Warner and V. S. Arpaci, "An experimental investigation of turbulent natural convection in air at low pressure along a vertical heated flat plate," *International of Heat and Mass Transfer,* vol. 11, pp. 397-406, 1967.

[6] R. Cheesewright, "Turbulente Natural Convection From A Vertical Plane Surface," The University of Michigan Laboratory for Fluid Flow and Heat Transport Phenomena, 1967.

[7] F. Bayley, "An analysis of turbulent free-convection heat transfer," *Proc. Instn Mech. Engrs,* vol. 169, no. 20, pp. 361-, 1955.

[8] R. Bill and B. Gebhart, "The development of turbulent transport in a vertical natural convection boundary layer," *International Journal of Heat and Mass Transfer,* vol. 22, pp. 267-277, 1979.

[9] K. Kitamura, M. Koike, I. Fukuoka and T. Saito, "Large eddy structure and heat transfer of turbulent natural convection along a vertical flatl plate," *International of Heat and Mass Transfer,* vol. 28, no. 4, pp. 837-850, 1985.

[10] T. Tsuji and Y. Nagano, "Characteristics of a turbulent natural convection boundary layer along a vertical flat plate," *International Journal of Heat and Mass Transfer,* vol. 31, no. 8, pp. 1723-1734, 1988.

[11] T. Tsuji and Y. Nagano, "Turbulence Measurements in a natural convection boundary layer along a vertical flat plate," *International Journal of Heat and Mass Transfer,* vol. 31, pp. 2101-2111, 1988.

[12] T. Tsuji, Y. Nagano and M. Tagawa, "Experiment on Spatio-Temporal Turbulent Structures of a Natural Convection Boundary Layer," *Journal of Heat Transfer,* vol. 114, pp. 901-908, 1992.

[13] Y. Hattori, T. Tsuji, Y. Nagano and N. Tanaka, "Turbulence characteristics of natural-convection boundary layer in air along a vertical plate heated at high temperatures," *International Journal of Heat and Fluid Flow,* vol. 27, pp. 445-455, 2006.

[14] W. To and J. Humphrey, "Numerical simulation of buoyant, turbulent flow-I. Free convection along a heated, vertical, flat plate," *International Journal of Heat and Mass Transfer,* vol. 29, no. 4, pp. 573-592, 1986.

[15] T. Peeters and R. Henkes, "The Reynolds-stress model of turbulence applied to the natural-convection boundary layer along a heated vertical plate," *International Journal of Heat and Mass Transfer,* vol. 35, no. 2, pp. 403-420, 1992.

[16] M. Z. Adedin, T. Tsuji and Y. Hattori, "Direct numerical simulation for a time-developing natural convection boundary layer along a vertical flat plate," *International Journal of Heat and Mass Transfer,* vol. 52, pp. 4525-4534, 2009.

[17] W. Hall and P. Price, "Mixed forced and free convection form a vertical head plate to air," *Proceedings of the Fourth International Heat Transfer Conference,* vol. 4, no. NC 3.3, 1970.

[18] K. Kitamura and T. Inagaki, "Turbulent heat and momentum transfer of combined forced and natural convection along a vertical flat plate-aidng flow," *International Journal of Heat and Mass Transfer,* vol. 30, no. 1, pp. 23-41, 1987.

[19] R. Krishamurthy and B. Gebhart, "An Experimental Study of Transition to Turbulence in Vertical Mixed Convection Flows," *Journal of Heat Transfer,* vol. 111, pp. 121-130, 1989.

[20] Y. Hattori, T. Tsuji, Y. Nagano and N. Tanaka, "Characteristics of turbulent combined-convection boundary layer along a vertical heated plate," *International Journal of Heat and Fluid Flow,* vol. 21, pp. 520-525, 2000.

[21] Y. Hattori, T. Tsuji, Y. Nagano and N. Tanaka, "Effects of freestream on turbulent combined-convection boundary layer along a vertical heated plate," *International Journal of Heat and Fluid Flow,* vol. 22, pp. 315-322, 2001.

[22] K. Patel, B. Armaly and T. Chen, "Transition From Turbulent Natural To Turbulenlt Forced Convection," *Journal of Heat Transfer,* vol. 120, no. 4, pp. 1086-1089, 1998.

[23] M. Z. Abedin, T. Tsuji and Y. Hattori, "Direct numerical simulation for a time-developing combined-convection boundary layer along a vertical flat plate," *International Journal of Heat and Mass Transfer,* vol. 53, pp. 2113-2122, 2010.

[24] Y. Hattori, "Turbulent Characteristics and transition behavior of combined-convection boundary layer along a vertical heated plate," Nagoya Institute of Technology, 2001.

[25] R.-S. Wu and K. Cheng, "Thermal Instability of Blasius Flow Along Horizontal Plates," *International Journal of Heat and Mass Transfer,* vol. 19, pp. 907-913, 1978.

[26] A. Moutsoglou, T. Chen and K. Cheng, "Vortex Instability of Mixed Convection FLow over a Horizontal Flat Plate," *Journal of Heat Transfer,* vol. 103, pp. 257-261, 1981.

[27] A. Townsend, "Mixed Convection over a heated horizontal plane," *Journal of Fluid Mechanics,* vol. 55, no. part 2, pp. 209-227, 1972.

[28] H. Imura, R. Gilpin and K. Cheng, "An Experimental Investigation of Heat Transfer and Buoyancy Induced Transition from Laminar Forced Convection to Turbulent Free Convection over a Horizontal Isothermally Heated Plate,"

Journal of Heat Transfer, vol. 100, pp. 429-434, 1978.

[29] X. Wang, "An Experimental Study of Mixed, Forced, and Free Convection Heat Transfer From a Horizontal Flat Plate to Air," *Journal of Heat Transfer,* vol. 104, pp. 139-144, 1982.

[30] S. Moharreri, B. Armaly and T. Chen, "Measurements in the Transition Vortex Flow Regime of Mixed Convection Above a Horizontal Heated Plate," *Journal of Heat Transfer,* vol. 110, pp. 358-365, 1988.

[31] N. Ramachandran, B. Armaly and T. Chen, "Turbulent Mixed Convection Over an Isothermal Horizontal Flat Plate," *Journal of Heat Transfer,* vol. 112, pp. 124-129, 1990.

[32] R. G. Gann, "Advanced Fire Suppression Technology For Aircraft: Findings of The Next Generation Fire Suppression Technology Program," National Institute of Standards and Technology, Gaithersburg, 2011.

[33] P. S. Bernard and J. M. Wallace, Turbulent Flow: Analysis, Measurement, and Prediction, Hoboken: John Wiley and Sons, 2002.

[34] A. Kolmogorov, "Dissipation of Energy in the Locally Isotropic Turbulence," *Proceedings: Mathematical and Physical Sciences,* vol. 434, no. 1890, pp. 15-17, 1991.

[35] A. Kolmogorov, "The local structure of turbulence in incompressible viscous fluids for very large Reynolds numbers," *Dokl. Akad. Nauk SSSR,* vol. 30, pp. 301-305, 1941.

[36] J. Hinze, Turbulence, McGraw-Hill, 1975.

[37] P. Kundu, I. M. Cohen and D. R. Dowling, Fluid Mechanics, Elsevier, 2012, p. 512.

[38] B. J. Bayly and S. A. Orszag, "Instability mechansims in shear-flow transition," *Annual Review of Fluid Mechanics,* vol. 20, pp. 359-391, 1988.

[39] G. Brown and A. Roshko, "On density effects and large structure in turbulent mixing layers," *Journal of Fluid Mechanics,* vol. 64, pp. 775-816, 1974.

[40] S. Kline, W. Reynolds, F. Schraub and P. Runstadler, "The structure of turbulent boundary layers," *Journal of Fluid Mechanics,* vol. 30, no. 4, pp. 741-773, 1967.

[41] J. Jimenez, "The Physics of wall Turbulence," *Physica A,* vol. 263, pp. 252-262, 1999.

[42] W. Schoppa and F. Hussain, "Coherent structure generation in near-wall turbulence," *Journal of Fluid Mechanics,* vol. 453, pp. 57-108, 2002.

[43] S. Robinson, "Coherent motions in the turbulent boundary layer," *Annual Review of Fluid Mechanics,* vol. 23, pp. 601-639, 1991.

[44] W. Schoppa and F. Hussain, "Coherent structure dynamics in near-wall turbulence," *Fluid Dynamics Research,* vol. 26, pp. 119-139, 2000.

[45] J. Jeong, F. Hussain, W. Schoppa and J. Kim, "Coherent structures near the wall in turbulent channel flow," *Journal of Fluid Mechanics,* vol. 332, pp. 185-214, 1997.

[46] R. F. Blackwelder and H. Eckelmann, "Streamwise vortices associated with the bursting phenomenon," *Journal of Fluid Mechanics,* vol. 94, no. 3, pp. 577-594, 1979.

[47] C. Smith and S. Metzler, "The characteristics of low-speed streaks in the near-wall region of a turbulent boundar layer," *Journal of Fluid Mechanics,* vol. 129, pp. 27-54, 1983.

[48] B. J. Cantwell, "Organized Motion in Turbulent Flow," *Annual Review of Fluid Mechanics,* vol. 13, pp. 457-515, 1981.

[49] R. L. Panton, "Overview of the self-sustaining mechanisms of wall turbulence," *Progress in Aerospace Sciences,* vol. 37, pp. 341-383, 2001.

[50] Y. Miyake, R. Ushiro and T. Morikawa, "The regeneration of quasi-streamwise vortices in the near-wall region," *JSME international journal. Series B, fluids and thermal engineering,* vol. 40, no. 2, pp. 257-264, 1997.

[51] A. V. Johansson, P. H. Alfredsson and J. Kim, "Evolution and dynamics of shear-layer structures in near-wall turbulence," *Journal of Fluid Mechanics,* vol. 224, pp. 579-599, 1991.

[52] H. Lugt, Vortex Flow in Nature and Technology, Wiley, 1972.

[53] M. Chong, A. Perry and B. Cantwell, "A general classification of three dimensional flow fields," *Physics of Fluids,* vol. 2, no. 5, pp. 765-777, 1990.

[54] S. J. Kamkar, "Mesh Adaption Strategies for Vortex-Dominated Flows," PhD Thesis, Stanford University , 2011.

[55] J. Hunt, A. Wray and P. Moin, "Eddies, stream, and convergence zones in turbulent flows," Center for Turbulence Research Report CTR-S88, 1988.

[56] J. Soria, R. Sondergaard, B. Cantwell, M. Chong and A. Perry, "A study of the fine-scale motions of incompressible time-developing mixing layers," *Physics of Fluids,* vol. 6, pp. 871-884, 1994.

[57] P. Moin and K. Mahesh, "DIRECT NUMERICAL SIMULATION: A Tool in Turbulence Research," *Annu. Rev. Fluid Mech.,* vol. 30, pp. 539-578, 1998.

[58] U. Piomelli and E. Balaras, "Wall-Layer Models For Large-Eddy Simulations," *Annu. Rev. Fluid Mech.,* vol. 34, pp. 349-374, 2002.

[59] C.-J. Chen and S.-Y. Jaw, Fundamentals of Turbulence Modeling, New York: Taylor & Francis, 1998.

[60] J. Schluter, "Toward the prediction of turbulent boundary layers using a coupled RANS-LES method," Center for Turbulence Researrch Proceedings of the Summer Program , Stanford, 2006.

[61] J. Frolich and D. Von Terzi, "Hybrid LES/RANS methods for the simulation of turbulent flows," *Progress of Aerospace Sciences,* vol. 44, pp. 349-377, 2008.

[62] J. Smagorinsky, "General Circulation Experiments with the Primitive Equations," *Monthly Weather Review,* vol. 91, no. 3, pp. 99-164, March 1963.

[63] H. Tennekes and J. Lumley, A First Course in Turbulence, Cambridge: The MIT Press, 1972.

[64] M. Lesieur, O. Metais and P. Comte, Large-Eddy Simulations of Turbulence,

New York: Cambridge University Press, 2005.

[65] P. Sagaut, Large eddy simulation for incompressible flows, New York: Springer, 2001.

[66] U. Piomelli, "Large-eddy simulation: achievements and challenges," *Progress in Aerospace Sciences,* pp. 335-362, 1999.

[67] A. Favre, "Turbulence: Space-time statistical properties and behavior in supersonic flows," *Physics of Fluids,* pp. 2851-2863, 1983.

[68] E. Garnier, N. Adams and P. Sagaut, Large Eddy Simulation for Compressible Flows, Springer, 2009.

[69] B. Vreman, B. Geurts and H. Kuerten, "A priori tests of large eddy simulation of the compressible plane mixing layer," *Journal of Engineering Mathematics,* pp. 299-327, 1995.

[70] M. P. Martin, U. Piomelli and G. V. Candler, "Subgrid-Scale Models for Compressible Large-Eddy Simulations," *Theoretical and Computational Fluid Dynamics,* pp. 361-376, 2000.

[71] E. Lenormand, P. Sagaut, L. T. Phuoc and P. Comte, "Subgrid-Scale Model for Large-Eddy Simulations of Compressible Wall Bounded Flows," *AIAA Journal,* vol. 38, pp. 1340-1350, 2000.

[72] X. Xu, J. S. Lee and R. H. Pletcher, "A compressible finite volume formulation for large eddy simulation of turbulent pipe flows at low Mach number in Cartesian coordinates," *Journal of Computational Physics,* pp. 22-48, 2005.

[73] B. Vreman, B. Geurts and H. Kuerten, "Subgrid-Modelling in LES of Compressible Flow," *Applied Scientific Research,* vol. 54, pp. 191-203, 1995.

[74] P. Martin, "Direct numerical simulation of hypersonic turbulent boundary layers. Part 1. Initialization and comparison with experiments," *Journal of Fluid Mechanics,* pp. 347-364, 2007.

[75] R. Bird, W. E. Stewart and E. N. Lightfoot, Transport Phenomena, New York: John Wiley & Sons, 2007.

[76] F. Ducros, F. Nicoud and T. Poinsot, "Wall-adapting local eddy-viscosity models for simulations in complex geometries," in *6th ICFD Conference on numerical methods for fluid dynamics*, 1998.

[77] D. Lilly, "A proposed modification of the Germano subgrid-scale closure method," *Physics of Fluids A,* vol. 4, no. 3, pp. 633-635, 1992.

[78] U. Piomelli and J. Liu, "Large-eddy simulation of rotating channel flows using a localized dynamic model," *Physics of Fluids,* vol. 7, no. 4, pp. 839-848, 1995.

[79] X. Chai and K. Mahesh, "Dynamic k-Equation Model for Large Eddy Simulation of Compressible Flows," in *40th Fluid Dynamics Conference and Exhibit*, Chicago, 2010.

[80] J. Piquet, Turbulent Flows: Models and Physics, New York: Springer, 2003.

[81] A. Yoshizawa, "Statistical theory for compressible turbulent shear flows with the application to subgrid modeling," *Physics of Fluids,* vol. 29, pp. 2152-2164, 1986.

[82] C. Fureby, C. Tabor, H. G. Weller and A. D. Gosman, "A comparative study of subgrid scale models in homogeneous isotropic turbulence," *Physics of Fluids,* vol. 9, pp. 1416-1429, 1997.

[83] G. Erlebacher, M. Hussaini, C. Speziale and T. Zang, "Toward the Large-Eddy Simulation of Compressible Turbulent Flows," *Journal of Fluid Mechanics,* vol. 238, pp. 155-185, 1992.

[84] J. Deardoff, "A numerical study of three-dimensional turbulent channel flow at large Reynolds numbers," *Journal of Fluid Mechanics,* vol. 41, pp. 453-480, 1970.

[85] J. Deardoff, "On the magnitude of the subgrid scale eddy viscosity coefficient," *Journal of Computational Physics,* vol. 7, pp. 120-133, 1971.

[86] M. Germano, U. Piomelli, P. Moin and W. H. Cabot, "A dynamic subgrid-scale eddy viscosity model," *Physics of Fluids A,* vol. 3, no. 7, pp. 1760-1765, 1991.

[87] E. vanDriest, "On The Turbulent Flow Near a Wall," *Journal of Aeronautical Sciences,* vol. 23, no. 11, pp. 1007-1011, 1956.

[88] F. Nicoud and F. Ducros, "Subgrid-scale stress modelling based on the square of the velocity gradient tensor," *Flow Turbulence and Combustion,* 1999.

[89] T. Sayadi and P. Moin, "A comparative study of subgrid scale models for the prediction of transition in turbulent boundary layers," Center for Turbulence Research Annual Research Briefs, 2010.

[90] U. Piomelli, W. H. Cabot, P. Moin and S. Lee, "Subgrid-scale backscatter in turbulent and transitional flows," *Physics of Fluids A,* vol. 3, pp. 1766-1771, 1991.

[91] M. Germano, "Turbulence: the filtering approach," *Journal of Fluid Mechanics,* vol. 238, pp. 325-336, 1992.

[92] P. Moin, K. Squires, W. Cabot and S. Lee, "A dynamic subgrid-scale model for compressible turbulence and scalar transport," *Physics of Fluids A,* vol. 3, no. 11, pp. 2746-2757, 1991.

[93] D. Spalding, "A Single Formula for the "Law of the Wall"," *Journal of Applied Mechanics,* pp. 455-458, 1961.

[94] C. Jayatilleke, "The Influence of Prandtl Number and Surface Roughness on the Resistance of the Laminar Sublayer to Momentum and Heat Transfer," *Progress in Heat and Mass Transfer,* vol. 1, pp. 193-321, 1969.

[95] M. Malin, "On the calculation of heat transfer rates in fully turbulent wall flows," *Appl. Math. Modelling,* vol. 11, pp. 281-284, 1987.

[96] J. Deardorff, "A numerical study of three-dimensional turbulent channel flow at large Reynolds numbers," *Journal of Fluid Mechanics,* vol. 41, pp. 453-480, 1970.

[97] U. Schumann, "Subgrid-scale model for finite difference simulation of turbulent flows in plane channels and annuli," *Journal of Computational Physics,* vol. 18, pp. 376-404, 1975.

[98] U. Piomelli, P. Moin, J. Freziger and J. Kim, "New approximate boundary conditions for large-eddy simulations of wall-bounded flows," *Physics of Fluids*

A, vol. 1, pp. 1061-1068, 1989.

[99] S. Rajagopalan and R. Antonia, "Some properties of the large structure in a fully developed turbulent duct flow," *Physics of Fluids,* vol. 22, no. 4, pp. 614-622, 1979.

[100] W. George and S. Capp, "A theory for natural convection turbulent boundary layers next to heated vertical surfaces," *International Journal of Heat and Mass Transfer,* vol. 22, pp. 813-826, 1979.

[101] M. Hölling and H. Herwig, "Asymptotic analysis of the near-wall region of turbulent natural convection flows," *Journal of Fluid Mechanics,* vol. 541, pp. 383-397, 2005.

[102] P. Kiš and H. Herwig, "The near wall physics and wall functions for turbulent natural convection," *International Journal of Heat and Mass Transfer,* vol. 55, pp. 2625-2635, 2012.

[103] C. Balaji, M. Holling and H. Herwig, "A temperature wall function for turbulent mixed convection from vertical parallel plate channels," *International Journal of Thermal Sciences,* vol. 47, pp. 723-729, 2008.

[104] T. Versteegh and F. Nieuwstadt, "A direct numerical simulation of natural convection between two infinite vertical differentially heated walls: scaling laws and wall functions," *International Journal of Heat and Mass Transfer,* vol. 42, pp. 3673-3693, 1999.

[105] S. Ghosal, "Analysis of discretization errors in LES," Center for Turbulence Research Annual Research Briefs, 1995.

[106] B. Vreman, B. Geurts and H. Kuerten, "Discretization Error Dominance Over Subgrid Terms in Large Eddy Simulations of Compressible Shear Layers in 2D," *Communications in Numerical Methods in Engineering,* vol. 10, pp. 785-790, 1994.

[107] B. Luca and M. Vergassola, "Isotropy vs anisotropy in small-scale turbulence," *Physics of Fluids,* vol. 13, no. 8, pp. 2139-2141, 2001.

[108] X. Shen and Z. Warhaft, "The anisotropy of the small scale structure in high Reynolds number turbulent shear flow," *Physics of Fluids,* vol. 12, no. 11, pp. 2976-2989, 2000.

[109] T. Hofbauer, J. Palma, L. Biferale and S. Gama, "Anisotropy in large eddy simulation determined from the SO(3) symmetry group," *Journal of Turbulence,* vol. 6, no. 9, pp. 1-11, 2005.

[110] J. A. Domaradzki and E. M. Saiki, "Backscatter Models for Large-Eddy Simulations," *Theoret. Comput. Fluid Dynamics,* vol. 9, pp. 75-83, 1997.

[111] C. Fureby, G. Tabor, H. Weller, A. Gosman, N. Sandham and M. Wolfshtein, "Large Eddy Simulation of Turbulent Channel Flows," *Turbulent Shear Flows,* vol. 11, pp. 1-6, 1997.

[112] J. S. Bagget, "Some modeling requirements for wall models in large eddy simulation," Center for Turbulence Research Annual Research Briefs, 1997.

[113] W. Cabot and P. Moin, "Approximate Wall Boundary Conditions in the Large-Eddy Simulation of High Reynolds Number Flow," *Flow, Turbulence and*

Combustion, vol. 63, pp. 269-291, 1999.

[114] A. Kravchenko and P. Moin, "On the Effect of Numerical Errors in Large Eddy Simulations of Turbulent Flows," *Journal of Computationall Physics,* vol. 131, pp. 310-322, 1997.

[115] F. K. Chow and P. Moin, "A further study of numerical errors in large-eddy simulations," *Journal of Computational Physics,* vol. 184, pp. 366-380, 2003.

[116] T. Lund and H.-J. Kaltenbach, "Experiments with explicit filtering for LES using a finite-difference method," Center for Turbulence Research Annual Research Briefs, 1995.

[117] G. D. Stefano and O. V. Vasilyev, "Sharp Cutoff versus smooth filtering in large eddy simulation," *Physics of Fluids,* vol. 14, no. 1, pp. 362-369, 2002.

[118] J. Gullbrand, "Explicit filtering and subgrid-scale models in turbulent channel flow," Center for Turbulence Research Annual Research Briefs, 2001.

[119] J. Gullbrand and F. K. Chow, "The effect of numerical errors and turbulence models in large-eddy simulations of channel flow, with and without explicit filtering," *Journal of Fluid Mechanics,* vol. 495, pp. 323-341, 2003.

[120] O. V. Vasilyev, T. S. Lund and P. Moin, "A General Class of Commutative Filters for LES in Complex Geometries," *Journal of Computational Physics,* vol. 146, pp. 82-104, 1998.

[121] C. Hirsch, Numerical Computation of Internal and External Flows: The Fundamentals of Computational Fluid Dynamics, 2nd Edition, Massachussets: Butterworth-Heinemann, 2007.

[122] Y. Morinishi, T. Lund, O. Vasilyev and P. Moin, "Fully Conservative Higher Order Finite Difference Schemes for Incompressible Flow," *Journal of Computational Physics,* vol. 143, pp. 90-124, 1998.

[123] K. Mahesh, "A Family of High Order Finite Difference Schemes with Good Spectral Resolution," *Journal of Computational Physics,* vol. 145, pp. 332-358, 1998.

[124] Y. Xing and C.-W. Shu, "High order finite difference WENO schemes with the exact conservation property for the shallow water equations," *Journal of Computational Physics,* vol. 208, pp. 206-227, 2008.

[125] Y.-H. Choi and C. Merkle, "The Application of Preconditioning in Viscous Flows," *Journal of Computational Physics,* vol. 105, pp. 207-223, 1993.

[126] H. Jasak, "Numerical Solution Algorithms for Compressible Flows," Faculty of Mechanical Engineering and Naval Architecture University of Zagreb, Croatia, 2007.

[127] T. Chung, Computational Fluid Dynamics, NewYork: Cambridge University Press, 2002.

[128] M. Peric, "A Finite Volume method for the prediction of three-dimensional fluid flow in complex ducts," 1985.

[129] J. Ferziger and M. Peric, Computational Methods for Fluid Dynamics, New York: Springer, 2002.

[130] Y. Saad, Iterative Methods for Sparse Linear Systems 2nd Edition, Society of

Industrial and Applied Mathematics, 2003.

[131] S. V. Patankar, Numerical Heat Transfer and Fluid Flow, Washington : Hemisphere Publishing Corporation, 1980.

[132] R. Issa, "Solution of the Implicitly Discretized Fluid Flow Equations by Operator-Splitting," *Journal of Computational Physics,* vol. 62, pp. 40-65, 1985.

[133] K. McGrattan, S. Hostikka, J. Floyd, H. Baum and R. Rehm, "Fire Dynamics Simulator (Version 5) Technical Reference Guide," NIST Special Publication U.S. Department of Commerce, 2005.

[134] J. Larsson and S. Kawai, "Wall-modeling in large eddy simulation: length scales, grid resolution and accuracy," *Center for Turbulence Research, Annual Research Briefs,* pp. 39-46, 2010.

[135] W. Cabot, J. Jimenez and J. Baggett, "On wakes and near-wall behavior in coarse large-eddy simulation of channel flow with wall models and second-order finite-difference methods," Center for Turbulence Research, 1999.

[136] W. George, "Lectures for Turbulence for the 21st Century," Department of Thermo and Fluid Engineering, Chalmers University of Technology, Gothernberg, Sweden, 2005.

[137] P. J. Larsson, Interviewee, *Large Eddy Simulations and Wall Modeling.* [Interview]. 25 September 2013.

[138] T. Tsuji, Y. Nagano and M. Tagawa, "Thermally Driven Turbulent Boundary Layers," in *Turbulent Shear Flows, Technical University of Munich*, Munich, 1991.

[139] M. Z. Abedin, T. Tsuji and J. Lee, "Turbulence characteristics and vortical structures in combined-convection boundary layers along a heated vertical flat plate," *International Journal of Heat and Mass Transfer,* vol. 55, pp. 3995-4002, 2012.

[140] V. Carey and B. Gebhart, "The stability and disturbance amplification characteristics of vertical mixed convection flows," *Journal of Fluid Mechanics,* vol. 127, pp. 185-201, 1983.

[141] D. Bernard, Interviewee, *Intercomponent turbulent energy transfer.* [Interview]. 27 September 2013.

[142] H. Schlichting and K. Gersten, Boundary Layer Theory, 8th edition, Springer, 2000.

[143] I. Tani, "Production of Longitudinal Vortices in the Boundary Layer along a Concave Wall," *Journal of Geophysical Research,* vol. 67, pp. 3075-3080, 1962.

[144] W. S. Saric, "Görtler Vortices," *Annual Review of Fluid Mechanics,* vol. 26, pp. 379-409, 1994.

[145] A. Vouros and T. Panidis, "Statistical analysis of turbulent thermal free convection over a horizontal heated plate in an open top cavity," *Experimental Thermal and Fluid Science,* vol. 36, pp. 44-55, 2012.

[146] A. Belmonte, A. Tilgner and A. Libchaber, "Boundary Layer Length Scales in

Thermal Turbulence," *Physical Review Letters*, vol. 70, no. 26, pp. 4067-4070, 1993.

[147] R. D. Puits, C. Resagk, A. Tilgner, F. Busse and A. Thess, "Structure of thermal boundary layers in turbulent Rayleigh-Benard convection," *Journal of Fluid Mechanics*, vol. 572, pp. 231-254, 2007.

[148] A. Vouros and T. Panidis, "Turbulent free convection over a horizontal heated plate in an open top cavity," in *6th European Thermal Sciences Conference (Eurotherm 2012)*, 2012.

[149] S. Menon and W.-W. Kim, "High Reynolds number flow simulations using the localized dynamic subgrid-scale model," in *AIAA 34th Aerospace Sciences Meeting and Exhibit*, Reno, 1996.